

**DOCTORAL THESIS**

# Synthesis and Characterization of $\text{Sb}_{1-x}\text{Bi}_x\text{SeI}$ for Optoelectronic Applications

Marc Dolcet Sadurni

TALLINNA TEHNIKAÜLIKOO  
TALLINN UNIVERSITY OF TECHNOLOGY  
TALLINN 2026

TALLINN UNIVERSITY OF TECHNOLOGY  
DOCTORAL THESIS  
37/2026

# Synthesis and Characterization of $\text{Sb}_{1-x}\text{Bi}_x\text{SeI}$ for Optoelectronic Applications

MARC DOLCET SADURNI



TALLINN UNIVERSITY OF TECHNOLOGY

School of Engineering

Department of Materials and Environmental Technology

This dissertation was accepted for the defense of the degree 12/05/2026

**Supervisor:** Dr. Kristi Timmo  
School of Engineering  
Tallinn University of Technology  
Tallinn, Estonia

**Co-supervisor:** Prof. Marit Kauk-Kuusik  
School of Engineering  
Tallinn University of Technology  
Tallinn, Estonia

**Opponents:** Prof. Edgardo Ademar Saucedo Silva  
Department of Electronic Engineering  
Polytechnic University of Catalonia (UPC)  
Barcelona, Spain

Prof. Vambola Kisand  
Institute of Physics  
University of Tartu  
Tartu, Estonia

**Defence of the thesis:** 30/06/2026, Tallinn

**Declaration:**

Hereby I declare that this doctoral thesis, my original investigation and achievement, submitted for the doctoral degree at Tallinn University of Technology has not been submitted for doctoral or equivalent academic degree.

Marc Dolcet Sadurni

-----  
signature



European Union  
European Regional  
Development Fund



Investing  
in your future

Copyright: Marc Dolcet Sadurni, 2026

ISSN 2585-6898 (publication)

ISBN 978-9916-80-516-9 (publication)

ISSN 2585-6901 (PDF)

ISBN 978-9916-80-507-7 (PDF)

<https://doi.org/10.23658/taltech.37/2026>

Printed by Koopia Niini & Rauam

Dolcet Sadurni, M. (2026). *Synthesis and Characterization of Sb<sub>1</sub> xBixSe<sub>1</sub> for Optoelectronic Applications* [TalTech Press]. <https://doi.org/10.23658/taltech.37/2026>

TALLINNA TEHNIKAÜLIKOOL  
DOKTORITÖÖ  
37/2026

# **Sb<sub>1-x</sub>Bi<sub>x</sub>SeI süntees ja iseloomustamine optoelektronilisteks rakendusteks**

MARC DOLCET SADURNI





# Contents

List of Publications .....	7
Author's Contribution to the Publications .....	8
Introduction .....	9
Abbreviations .....	11
Symbols .....	12
1 Literature review .....	13
1.1 Heavy pnictogen chalcogenides for photovoltaic and energy applications .....	13
1.2 Crystal structure and quasi-1D nature of SbSeI and BiSeI .....	14
1.3 Phase diagrams of SbSeI and BiSeI .....	16
1.4 Synthesis methods of pnictogen chalcogenide materials .....	18
1.4.1 Bulk crystals and nanostructures .....	18
1.4.2 Thin film deposition techniques .....	19
1.5 Solid solutions in pnictogen chalcogenides .....	20
1.6 Optoelectronic properties .....	21
1.6.1 Band gaps of SbSeI and BiSeI .....	21
1.6.2 Optical absorption and dielectric properties of SbSeI and BiSeI .....	22
1.6.3 Effective masses and charge transport properties .....	22
1.7 Defect structure of pnictogen chalcogenides .....	23
1.8 Summary of the literature review and aim of the study .....	25
2 Experimental .....	28
2.1 Preparation of SbSeI thin films .....	28
2.2 Synthesis of $Sb_{1-x}Bi_xSeI$ ( $x = 0-1$ ) microcrystalline solid solutions .....	30
2.3 Applied characterization methods .....	31
2.3.1 X-ray diffraction spectroscopy .....	31
2.3.2 Room temperature micro-Raman spectroscopy .....	31
2.3.3 X-ray photoelectron spectroscopy .....	31
2.3.4 Ultraviolet photoelectron spectroscopy .....	31
2.3.5 Photoluminescence .....	32
2.3.6 Scanning Kelvin probe .....	32
2.3.7 Ultraviolet-Visible-Near-Infrared spectroscopy .....	32
2.3.8 Scanning electron microscopy .....	33
2.3.9 Transmission electron microscopy .....	33
2.3.10 Energy dispersive X-ray spectroscopy .....	33
3 Results and discussion .....	35
3.1 SbSeI thin films .....	35
3.1.1 Formation of SbSeI from c-Sb <sub>2</sub> Se <sub>3</sub> .....	35
3.1.2 Formation of SbSeI from a-Sb <sub>2</sub> Se <sub>3</sub> .....	39
3.2 $Sb_{1-x}Bi_xSeI$ ( $x = 0-1$ ) microcrystalline solid solutions .....	41
3.2.1 Morphology of $Sb_{1-x}Bi_xSeI$ microcrystals .....	41
3.2.2 Chemical composition of $Sb_{1-x}Bi_xSeI$ microcrystals .....	43
3.2.3 Structural properties of $Sb_{1-x}Bi_xSeI$ microcrystals .....	45
3.2.4 Electronic band structure of $Sb_{1-x}Bi_xSeI$ .....	49
3.3 Defect study of the (Sb,Bi)SeI system .....	53
3.3.1 Photoluminescence study of SbSeI thin films .....	53

3.3.2 Photoluminescence study of $\text{Sb}_{1-x}\text{Bi}_x\text{SeI}$ microcrystals .....	56
3.3.3 Photoluminescence study of BiSeI microcrystals .....	56
Conclusions .....	62
References .....	64
Acknowledgements.....	73
Abstract.....	74
Lühikokkuvõte.....	76
Appendix 1 .....	79
Appendix 2 .....	91
Appendix 3 .....	105
Curriculum vitae.....	121
Elulookirjeldus.....	125

## List of Publications

The list of author's publications, on the basis of which the thesis has been prepared:

- I **M. Dolcet Sadurni**, K. Timmo, V. Mikli, O. Volobujeva, I. Mengü, J. Krustok, M. Grossberg-Kuusk, M. Kauk-Kuusik, "Preparation and characterization of SbSeI thin films" *Journal of Science: Advanced Materials and Devices* 9 (2024) 100664, <https://doi.org/10.1016/j.jsamd.2023.100664>.
- II **M. Dolcet Sadurni**, J. Krustok, K. Timmo, V. Mikli, R. Kondrotas, M. Grossberg-Kuusk, M. Kauk-Kuusik, "Radiative recombination model for BiSeI microcrystals: unveiling deep defects through photoluminescence" *Journal of Physics: Energy* 6 (2024) 045004, <https://doi.org/10.1088/2515-7655/ad8377>.
- III **M. Dolcet Sadurni**, K. Timmo, V. Mikli, J. Krustok, M. Danilson, A. Suchodolskis, C. Radu, A. Bocirnea, A. Galca, M. Grossberg-Kuusk, M. Kauk-Kuusik, "Effects of cationic substitution on the properties of  $Sb_{1-x}Bi_xSeI$  ( $x = 0-1$ ) compounds" *Journal of Alloys and Compounds* 1037 (2025) 182292, <https://doi.org/10.1016/j.jallcom.2025.182292>.

## Author's Contribution to the Publications

Contributions to the papers in this thesis are:

- I Preparation of SbSeI thin films by annealing Sb<sub>2</sub>Se<sub>3</sub> thin films; material characterization by scanning electron microscopy, energy dispersive X-ray spectroscopy, Raman spectroscopy, room temperature photoluminescence, UV-Vis-NIR spectroscopy; analysis of the results and major part of the writing.
- II Synthesis of BiSeI microcrystals; material characterization by scanning electron microscopy, energy dispersive X-ray spectroscopy, Raman spectroscopy and photoluminescence (room temperature, temperature and laser power-dependent); analysis of the results and major part of the writing.
- III Synthesis of Sb<sub>1-x</sub>Bi<sub>x</sub>SeI (x = 0–1) solid solutions, material characterization by scanning electron microscopy, energy dispersive X-ray spectroscopy, Raman spectroscopy, scanning Kelvin probe microscopy, and room temperature photoluminescence; analysis of the results and major part of the writing.

## Introduction

One of the greatest challenges of the 21<sup>st</sup> century is ensuring sustainable production and efficient management of energy. Global electricity consumption continues to increase, driven by structural transformations in both advanced and emerging economies. According to the International Energy Agency, global electricity consumption grew by ~3.3% in 2025 and is projected to rise by ~3.7% in 2026 [1]. This sustained growth is associated with several converging developments, including the electrification of industrial processes [2], the rapid expansion of electrified mobility [3], rising demand for cooling and heating associated with a warming climate [4], and the continuous expansion of digital infrastructure, such as data centers supporting artificial intelligence and cloud computing applications [5].

At the same time, the global electricity supply is shifting towards low-carbon energy sources. In 2024, renewable technologies generated ~32% of global electricity, and this share is projected to increase to ~43% by 2030 [6].

Among the various renewable energy technologies, solar photovoltaic (PV) systems play a central role, due to their scalability, modularity, and rapidly declining costs. Solar PV devices convert sunlight directly into electricity through semiconductor absorbers, without direct generation of carbon emissions. In addition, solar energy is decentralized, widely accessible, and practically inexhaustible. Between 2020 and 2025, solar PV has been responsible for ~80% of the global increase in renewable power capacity and is expected to remain the dominant source of new renewable installations in the coming decades [6].

Crystalline silicon (c-Si) solar cells continue to dominate the PV market, representing ~98% of the total global production in 2024 [7]. Silicon benefits from high abundance, low toxicity, and a mature industrial ecosystem supported by decades of technological development and a well-established global manufacturing infrastructure. State-of-the-art c-Si devices combine high power conversion efficiencies (PCE) with long operational lifetimes and low degradation rates. However, the energy-intensive manufacturing processes and substantial material requirements associated with wafer-based technologies motivate the exploration of alternative absorber materials that can be processed at lower temperatures and potentially lower cost [8,9].

Several emerging PV technologies are currently under active investigation, including chalcogenide thin films, kesterites, organic semiconductors, and metal halide perovskites. Among these, lead halide perovskites have demonstrated remarkable optoelectronic properties such as strong optical absorption, long carrier diffusion lengths, defect tolerance, and tunable band gaps, enabling certified PCE exceeding 26% [10]. Despite these advantages, large-scale commercialization remains limited due to concerns regarding long-term operational stability and the presence of toxic lead [11]. This motivates the search for alternative absorber materials that combine favorable optoelectronic properties with improved environmental compatibility, stability, and scalable synthesis.

Pnictogen chalcogenides have recently emerged as a promising class of inorganic semiconductors that may address several of these challenges. These compounds, typically composed of group V elements (Sb, Bi) combined with chalcogen and halogen anions, exhibit attractive properties for PV applications, including suitable band gaps in the range of 1–2 eV, high absorption coefficients ( $>10^5 \text{ cm}^{-1}$ ), and  $ns^2$  lone-pair electronic configurations analogous to those found in lead halide perovskites. Such electronic

configurations are associated with defect tolerance and favorable charge-carrier transport properties [12]. Furthermore, pnictogen chalcogenides can be processed as thin films using solution-based or vapor-phase deposition techniques, making them compatible with scalable and potentially cost-effective device fabrication.

Among this material class, SbSeI has attracted particular interest as a potential PV absorber. SbSeI-based solar cells have reached PCE of up to 4.1%, representing the highest reported performance within pnictogen chalcogenide PV to date [13]. However, several challenges remain, including difficulties in controlling thin film morphology, anisotropic crystal growth arising from its quasi-1D crystal structure, and a relatively wide band gap (~1.7 eV) [13–15], which is slightly larger than the optimum for single-junction devices in PV applications.

Alloying strategies provide a potential pathway to tune the electronic and structural properties of SbSeI. In particular, partial substitution of Sb with Bi, leading to  $\text{Sb}_{1-x}\text{Bi}_x\text{SeI}$  solid solutions, may enable band gap engineering, modification of the defect structure, and changes in optoelectronic properties. Nevertheless, this alloy system remains largely unexplored. Experimental data concerning band alignment, photoluminescence (PL) behavior, defect physics, and charge-carrier transport mechanisms are scarce. Additionally, the fundamental properties of the end members SbSeI and BiSeI, including their defect structure and recombination pathways, remain insufficiently understood.

The novelty of this doctoral thesis lies in addressing several key knowledge gaps that have limited the development of Sb- and Bi-based chalcogenides for optoelectronic applications. First, it establishes a route for the preparation of compact and vertically oriented SbSeI thin films by controlling the crystallinity of the  $\text{Sb}_2\text{Se}_3$  precursor, thereby addressing the lack of reliable fabrication strategies for high-quality absorber layers with favorable orientation. Second, it provides a systematic experimental investigation of the  $\text{Sb}_{1-x}\text{Bi}_x\text{SeI}$  ( $x = 0-1$ ) solid-solution series over the full compositional range, clarifying the effects of Sb/Bi ratio on crystal structure, band gap, energy-band alignment, and conductivity type. Third, it advances the understanding of defect-related radiative recombination in SbSeI and BiSeI, helping to address the gap between the predicted defect-tolerant nature of these materials and their experimentally observed recombination behavior.

This thesis is divided into three chapters. Chapter 1 provides a review of the relevant literature and introduces the fundamental concepts underlying this work, together with the objectives of this study. Chapter 2 describes the experimental methods, including the synthesis procedures for SbSeI thin films and  $\text{Sb}_{1-x}\text{Bi}_x\text{SeI}$  microcrystalline solid solutions, as well as the characterization techniques employed. In Chapter 3, the summarized results and discussion of the published Papers I-III are presented.

## Abbreviations

a-Sb <sub>2</sub> Se <sub>3</sub>	Amorphous antimony selenide
BB	Band-to-band
CBM	Conduction band minimum
CPD	Contact potential difference
c-Sb <sub>2</sub> Se <sub>3</sub>	Crystalline antimony selenide
c-Si	Crystalline silicon
DD–DA	Deep donor–deep acceptor
DFT	Density functional theory
DOS	Density of states
DTA	Differential thermal analysis
EDX	Energy dispersive X-ray spectroscopy
FWHM	Full width at half maximum
hQSGW	Hybrid quasiparticle self-consistent GW method
HSE06	Range-separated hybrid functional
IPV	Indoor photovoltaic
PCE	Power conversion efficiency
PL	Photoluminescence
PV	Photovoltaics
PVD	Physical vapor deposition
PVT	Physical vapor transport
RT	Room temperature
SAED	Selected area electron diffraction
SEM	Scanning electron microscopy
SKP	Scanning Kelvin probe
SLG	Soda lime glass
SOC	Spin–orbit coupling
SQ	Shockley-Queisser
TEM	Transmission electron microscopy
UPS	Ultraviolet photoelectron spectroscopy
UV-Vis-NIR	Ultraviolet-Visible-Near-Infrared spectroscopy
VBM	Valence band maximum
XPS	X-ray photoelectron spectroscopy
XRD	X-ray diffraction

## Symbols

$E_A^0$	Ionization acceptor energy
$E_D^0$	Ionization donor energy
$E_a$	Thermal activation energy
$E_{cutoff}$	Secondary electron cutoff energy
$E_F$	Fermi level
$E_g$	Optical band gap
$E_U$	Urbach energy
$E_{VAC}$	Vacuum level
$E_{VBM}$	Valence band maximum
$h$	Planck's constant
$k$	Boltzmann's constant
$m_0$	Free electron rest mass
$r$	Distance donor-acceptor
$R_\infty$	Absolute diffuse reflectance
$T_c$	Carrier temperature
$\alpha$	Absorption coefficient
$\epsilon_0$	Vacuum permittivity
$\epsilon$	Dielectric constant
$\lambda$	Wavelength
$\nu$	Photon frequency
$\Phi$	Work function
$\phi$	Integrated PL intensity
$\Gamma$	Highest frequency mode

# 1 Literature review

This chapter provides an overview of the current state of research on heavy pnictogen chalcogenide materials, with particular emphasis on their potential for PV, optoelectronics, sensors, and other energy applications such as thermoelectricity, piezoelectricity, and photocatalysis. It covers the main properties of SbSeI and BiSeI, including their structure, phase, and optoelectronic characteristics. This review also discusses their main synthesis methods, focusing on single crystals, nanostructures, and thin film technologies.

## 1.1 Heavy pnictogen chalcogenides for photovoltaic and energy applications

Heavy pnictogen chalcogenides are an emerging class of inorganic semiconductors composed of group V-VI-VII elements. These materials were first intensively studied in the 1960s due to their optical and ferroelectric properties [16]. They follow the general formula  $MChX$ , where M is a pnictogen (Sb or Bi), the heaviest elements in group V. The chalcogen (Ch) is a group VI element (S or Se), and the halogen (X) is a group VII element (I or Br). Among these compounds, SbSI was the first material found to exhibit ferroelectric behavior [17], followed by BiSI and SbSBr [18]. During this early period, Sb- and Bi-based chalcogenides were widely investigated for their multifunctional properties, including photoconductivity [19,20], thermoelectricity and piezoelectricity [21], as well as their electronic and optical characteristics [22]. Despite their promising multifunctional properties, chalcogenides did not transition into widespread technological applications at that time.

During the last decade, however, heavy pnictogen chalcogenides have regained significant attention due to advances in computational materials design that showed the theoretical potential of these stable and non-toxic semiconductors to be used in different energy applications, opto- and microelectronic devices [23–28]. For example, Caño *et al.* demonstrated a photoelectrochemical water-splitting device based on SbSeI and reported the use of BiSeI for photocatalytic applications [29]. Other chalcogenides, such as BiSI [30] and SbSI [31,32], have also been explored as photocatalysts, while SbSI has found applications in piezoelectric and self-powered sensing systems [33].

One of the main applications in which pnictogen chalcogenides have recently been investigated is in PV. In the search for new PV absorbers, materials combining strong optical absorption, suitable band gaps, and chemical stability are of particular interest. Pnictogen chalcogenides share several characteristics with lead-halide perovskites, one of the most successful emerging PV absorbers. Lead-halide perovskite solar cells have achieved a PCE of 26% [10]. Despite their exceptional performance, the highest-performing perovskites still contain toxic lead and suffer from long-term instability under ambient conditions. Lead-free perovskite alternatives are actively being developed, but they have not yet reached comparable efficiencies [34].

The exceptional optoelectronic performance and defect tolerance of lead-halide perovskites are attributed to their electronic structure, particularly the presence of stereochemically active  $ns^2$  lone pairs on  $Pb^{2+}$  cations. This electronic configuration results in antibonding valence band maxima, which suppresses the formation of deep defect states. Notably,  $Sb^{3+}$  and  $Bi^{3+}$  cations possess analogous  $ns^2$  electronic configuration ( $5s^2$  and  $6s^2$ , respectively), suggesting that heavy pnictogen chalcogenides may exhibit similar defect-tolerant behavior and high charge carrier mobilities. As a

result, modern research has re-evaluated these materials as potential lead-free, ferroelectric semiconductors that bridge the chemistry and physics of chalcogenides and halide perovskites, offering new opportunities for PV and other energy-related applications.

In 2012, Mullins *et al.* reported the first solid-state heterojunction solar cell based on a heavy pnictogen chalcogenide, using *n*-type BiSI as the absorber and *p*-type CuSCN as the window layer. Despite demonstrating device feasibility, the solar cell exhibited a very low PCE of approximately 0.01% [35]. A breakthrough followed in 2018, when Nie *et al.* reported the first efficient pnictogen chalcogenide solar cell, based on SbSI grown within mesoporous TiO<sub>2</sub> via a solution-based process, achieving a PCE of 3.05% [36]. Two years later, the same research group improved device PCE to 3.62% using SbSI synthesized by a vapor-phase process. However, the relatively wide band gap of SbSI (~1.80 eV) [37] limits its maximum achievable efficiency in single-junction solar cells. BiSI exhibits a narrower band gap (~1.6 eV), and partial substitution of Sb with Bi enabled further performance enhancement. By forming the mixed composition Sb<sub>0.67</sub>Bi<sub>0.33</sub>SI, Nie *et al.* achieved a remarkable PCE of 4.07% [38]. In 2021, the same group fabricated the first solar cell based on SbSeI, a chalcogenide with a band gap closer to the Shockley–Queisser (SQ) optimal value for single-junction solar cells [39] than that of SbSI, thereby offering greater potential for high PCE. SbSeI was grown within mesoporous TiO<sub>2</sub> using a similar process as reported in [36], achieving a PCE of 4.1% [13]. Importantly, these devices exhibited good operational stability, retaining approximately 90% of their initial performance after prolonged exposure to humidity, elevated temperature, and continuous illumination.

To date, SbSeI-based devices exhibit the highest reported PCE among single-junction solar cells based on a pure heavy-metal chalcogenide absorber, however, their performance remains well below the SQ theoretical limit (~28%) [40]. This gap highlights significant opportunities for further improvement through enhanced control over film morphology and crystallographic orientation, optimized band alignment with charge-transport layers, and suppression of defect-related recombination losses. Motivated by these considerations, this thesis focuses on optimizing the synthesis conditions of SbSeI thin films to achieve improved morphology, crystallographic orientation and film compactness, thereby enhancing PV-relevant properties. In parallel, Bi incorporation is investigated as a strategy to tune the band gap and study the optoelectronic properties of the Sb<sub>1-x</sub>Bi<sub>x</sub>SeI solid-solution series, with the goal of identifying compositions for different PV applications.

## 1.2 Crystal structure and quasi-1D nature of SbSeI and BiSeI

In general, MChX pnictogen chalcogenides adopt a closely related orthorhombic crystal structure with space group *Pnma* or *Pnam*. Both SbSeI and BiSeI crystallize in the orthorhombic *Pnma*62 structure, with lattice parameters  $a = 8.7080 \text{ \AA}$ ,  $b = 4.1314 \text{ \AA}$ ,  $c = 10.4223 \text{ \AA}$  for SbSeI and  $a = 8.7074 \text{ \AA}$ ,  $b = 4.2202 \text{ \AA}$ ,  $c = 10.5837 \text{ \AA}$  for BiSeI [41]. The overall unit cell volume of SbSeI (374.96 Å<sup>3</sup>) is smaller than in BiSeI (388.92 Å<sup>3</sup>) due to the smaller radii of Sb.

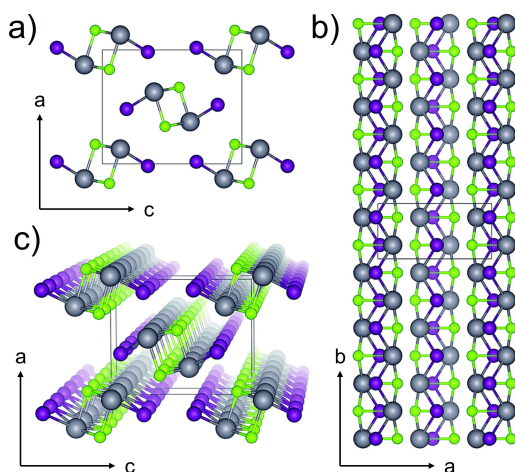


Figure 1. Crystal structure of BiSeI as viewed along a) the [100] direction, b) the [001] direction, and c) a three-dimensional view, highlighting the 1D chains. Bi, Se, and I atoms are denoted by grey, green, and purple spheres, respectively [42].

The crystal structure of these compounds consists of double chains of  $(M_2Ch_2X_2)_n$ -units, commonly referred to as ribbons. Figure 1 illustrates the crystal structure of BiSeI (SbSeI exhibits a similar crystal structure). Atoms along the ribbon axis share strong M-Ch and M-X covalent bonds, forming a stiff, chemically bonded backbone. Perpendicular to the ribbon axis, the ribbons stack in parallel and are held together by weak van der Waals forces [43,44]. This strong anisotropy in bonding, also sometimes named quasi-1D (covalent along the ribbon, van der Waals between ribbons), is the origin of the enhancement of many of the materials' optoelectronic properties. Charge carrier transport is typically much higher along the ribbon axis than perpendicular to it, as observed in chalcogenides with the similar quasi-1D structure like  $Sb_2Se_3$  [45,46]. Because strong bonding is concentrated along the ribbon axis, these compounds preferentially grow as rod-like crystals with the long axis parallel to the ribbon (conventionally, the crystallographic b direction in reported unit cells).

While this anisotropic growth facilitates the formation of high-quality single crystals with low defect density [41], it poses significant challenges for thin film applications. In thin films, device performance strongly depends on the orientation of the ribbons. When grains are oriented with ribbons vertically, device architectures can benefit from the high axial mobility, on the other hand, randomly oriented or incorrectly oriented films show poorer carrier collection and increased recombination losses. Consequently, controlling ribbon orientation is a key requirement for PV applications.

Experimental studies report pronounced anisotropic growth rates in pnictogen chalcogenides, with growth parallel to the ribbon axis occurring orders of magnitude faster than growth perpendicular to it. This behavior explains the columnar or needle-like morphologies commonly observed in vapor-, solution-, and flux-grown samples [41]. This anisotropic growth behavior has been extensively studied in related chalcogenide systems such as  $Sb_2Se_3$ , where control over ribbon orientation has been shown to be critical for efficient charge collection. Vertically oriented  $Sb_2Se_3$  thin films, obtained through techniques like radio-frequency magnetron sputtering and combined sputtering-selenization processes, have shown enhanced charge transport and reduced

carrier recombination compared to randomly oriented films [45,47–49]. Given the strong structural analogy between  $\text{Sb}_2\text{Se}_3$  and pnictogen chalcogenides, it is reasonable to expect that achieving a similar vertical alignment of ribbons in  $\text{SbSeI}$  or  $\text{BiSeI}$  thin films would improve the PV performance. However, the fabrication of high-quality  $\text{SbSeI}$  or  $\text{BiSeI}$  thin films remains relatively immature and insufficiently studied. In the context of thin-film PV absorbers, the term “high quality” refers to a combination of high crystallinity, phase purity, and optoelectronic properties that are suitable for efficient solar cell operation. For pnictogen chalcogenides, high-quality films should exhibit low density of grain boundaries, vertical crystal orientation, high morphological uniformity and compactness, all of which are critical for efficient charge transport and collection [50]. To date, however, reported films often suffer from random ribbon orientation, limited compactness, inhomogeneous morphology, and poorly controlled grain sizes. Addressing these challenges is therefore essential for advancing chalcogenide-based PV. Accordingly, this thesis focuses on the synthesis of high-quality  $\text{SbSeI}$  thin films, with the objective of improving crystal orientation, film homogeneity, and overall morphology, thereby advancing toward higher-efficiency  $\text{SbSeI}$ -based solar cells.

### 1.3 Phase diagrams of $\text{SbSeI}$ and $\text{BiSeI}$

Phase diagrams are fundamental to design suitable growth strategies to obtain single crystals or thin films, to identify temperature-composition windows where the desired phase is stable, and to anticipate decomposition or the formation of secondary phases. The phase diagrams of the ternary  $\text{Sb-Se-I}$  and  $\text{Bi-Se-I}$  systems have been mapped through experimental phase-equilibrium studies combined with differential thermal analysis (DTA).

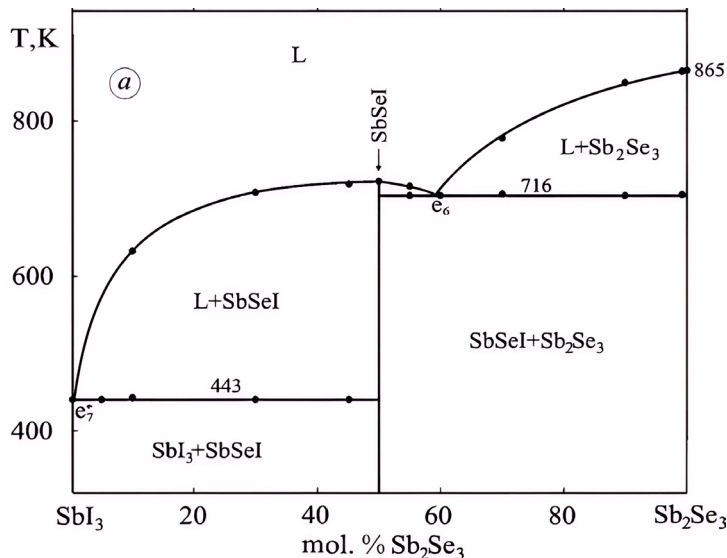


Figure 2. Phase diagram of the quasi-binary system  $\text{SbI}_3$ - $\text{Sb}_2\text{Se}_3$ . Adapted from [51].

The phase diagram of the quasi-binary  $\text{SbI}_3$ - $\text{Sb}_2\text{Se}_3$  [51] system is presented in Figure 2. Although the original diagram is presented in Kelvin, the corresponding temperatures are also given in degrees Celsius in the text for clarity. Only one ternary

stoichiometric compound, SbSel, forms in this system. SbSel exists as a single homogeneous phase at 50 mol% Sb<sub>2</sub>Se<sub>3</sub> and 50 mol% SbI<sub>3</sub>, and its formation can be described by the following chemical reaction:



SbSel melts congruently at 725 K (452 °C). On the SbI<sub>3</sub>-rich side and below 443 K (170 °C), the system consists of a two-phase region comprising SbI<sub>3</sub> and SbSel. A peritectic reaction occurs at 170 °C, producing a liquid phase and solid SbSel. On the Sb<sub>2</sub>Se<sub>3</sub>-rich side, SbSel coexists with Sb<sub>2</sub>Se<sub>3</sub> below 716 K (443 °C). When the Sb<sub>2</sub>Se<sub>3</sub> content exceeds 58 mol%, a second peritectic reaction occurs at 443 °C, yielding a liquid phase and solid Sb<sub>2</sub>Se<sub>3</sub>. Pure Sb<sub>2</sub>Se<sub>3</sub> melts at 865 K (592 °C). Two eutectic points have been reported in this quasi-binary system: (i) on the SbI<sub>3</sub>-rich side at 170 °C (e<sub>7</sub>), essentially degenerate with the melting point of SbI<sub>3</sub>; and (ii) on the Sb<sub>2</sub>Se<sub>3</sub>-rich side at 58 mol% Sb<sub>2</sub>Se<sub>3</sub> and 716 K (443 °C) (e<sub>6</sub>).

In the BiI<sub>3</sub>–Bi<sub>2</sub>Se<sub>3</sub> quasi-binary system (Figure 3), Petasch *et al.* reported BiSel as the only thermodynamically stable ternary compound [52]. BiSel forms at an equimolar composition of 50 mol% of Bi<sub>2</sub>Se<sub>3</sub> and 50 mol% BiI<sub>3</sub> via the following reaction:



A eutectic point (E) exists between BiSel and BiI<sub>3</sub> at 95 mol% BiI<sub>3</sub> and 400 °C, slightly below the melting point of pure BiI<sub>3</sub> (S<sub>1</sub>) at 408 °C. Pure Bi<sub>2</sub>Se<sub>3</sub> (S<sub>2</sub>) melts at 706 °C. Although early studies reported congruent melting at 535 °C [53] and 540 °C [54], modern DTA and total pressure measurements indicate that BiSel exhibits a peritectic melting point (P) at 545 °C.

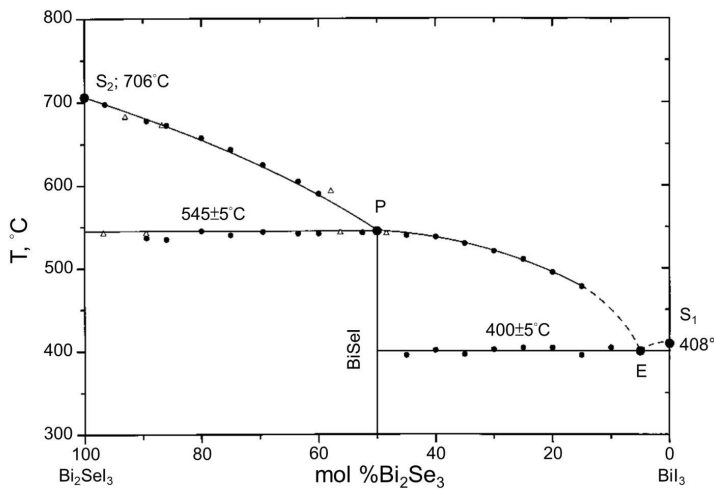


Figure 3. Phase diagram of the quasi-binary system Bi<sub>2</sub>Se<sub>3</sub>–BiI<sub>3</sub>. Black dots denote DTA measurements [52].

Unlike SbSel, BiSel does not melt directly into a stoichiometric liquid. Instead, it decomposes into a liquid phase together with solid Bi<sub>2</sub>Se<sub>3(s)</sub> and gaseous BiI<sub>3(g)</sub>, which

significantly complicates direct melt-growth strategies. During synthesis, the high volatility of  $\text{BiI}_3$  can readily shift the composition outside the single-phase stability region, leading to the formation of secondary phases of  $\text{Bi}_2\text{Se}_3$  and  $\text{BiI}_3$ . This behavior represents a recurring challenge in the synthesis of these materials and highlights the importance of detailed phase-diagram knowledge for optimizing growth processes and ensuring phase purity.

## 1.4 Synthesis methods of pnictogen chalcogenide materials

Historically, research on Sb- and Bi-based chalcogenides initially focused on the synthesis of bulk or single crystals, primarily to determine their structural, optical, electrical, and fundamental physical properties. Only at the later stage did scientific interest expand toward thin-film processing and device integration. Accordingly, this section reviews and compares the major crystal-growth approaches employed for heavy pnictogen chalcogenides, discussing their respective advantages and limitations and highlighting representative examples from the literature.

### 1.4.1 Bulk crystals and nanostructures

One of the most widely used methods for heavy pnictogen chalcogenides is growth from the melt. In this technique, high-purity elemental or binary precursors are sealed, typically in evacuated or inert gas-filled quartz ampoules and heated until the mixture melts completely. After equilibration at elevated temperature, controlled cooling or directional solidification is used to obtain crystalline ingots. Nitsche *et al.* [19] employed this method to synthesize several heavy pnictogen chalcogenides and investigated their photoconductive properties [4]. Aliev *et al.* [51] later employed a similar melt-growth method to synthesize  $\text{SbSeI}$  for phase diagram studies.

The vertical Bridgman technique has also been widely used to grow single crystals of  $\text{SbSI}$ ,  $\text{SbSeI}$ ,  $\text{BiSI}$ , and  $\text{BiSeI}$  for investigations of their optical and ferroelectric properties [55,56]. In particular, the Bridgman–Stockbarger method, which introduces a well-defined temperature gradient - often implemented via dual-zone furnaces or a baffle - enables more precise control of the crystallization front. This approach reduces thermal stress and improves compositional homogeneity. In [57], the photoelectric response of  $\text{BiSI}$  was examined, while Sereika *et al.* synthesized  $\text{BiSBr}$  via the Bridgman–Stockbarger technique to investigate its structural and optoelectronic properties [58]. These melt-grown crystals are typically very high-quality, large, well-oriented boules with low defect densities, making them well-suited for fundamental studies of charge transport, optical absorption, and ferroelectric switching. However, their fabrication requires high-temperature furnaces capable of maintaining uniform thermal gradients, which limits scalability and leads to high energy consumption.

As an alternative to melt-based growth, gas-phase growth via physical vapor transport (PVT) enables the preparation of high-quality single crystals without melting.  $\text{BiSeI}$  single crystals have been successfully grown using PVT in several studies [41,59,60]. Beyond these high-temperature solid-state routes, chemical synthesis methods have gained increasing attention, particularly for producing nanostructured materials, seed crystals, or when low-temperature processing is desirable. For instance,  $\text{SbSeI}$  has been prepared in gel or nanowire forms via a sonochemical route [61,62], which offers significantly reduced reaction times and lower synthesis temperatures compared with melt-based or vapor transport methods. Similarly, Zhu *et al.* demonstrated the synthesis of rod-like

BiSeI crystals through a mild solvothermal reaction between  $\text{Bi}_2\text{Se}_3$  and  $\text{BiI}_3$  in ethanol at 200 °C [63], while Fa *et al.* obtained BiSI nanowires using a comparable solvothermal approach [64]. The solvothermal method has been widely used for synthesizing Bi-based compounds, particularly in the context of photocatalytic applications [65–67]. In addition, mechanochemical synthesis via high-energy ball milling has been reported for BiSI and BiSeI, providing a rapid, solvent-free, and scalable alternative to conventional high-temperature synthesis routes [68].

#### 1.4.2 Thin film deposition techniques

While early work on heavy pnictogen chalcogenides focused primarily on bulk crystals and nanostructured materials, recent research has increasingly shifted toward thin-film fabrication for energy-related applications, particularly PV. Thin films have been investigated as potential absorber layers in solar cells, with many studies employing solution-based deposition techniques [28]. These methods typically involve one- or two-step spin-coating of precursor solutions followed by annealing, which enables deposition at relatively low temperatures and offers good scalability.

Nie *et al.* prepared several solution-based thin films by a similar two-step spin-coating and annealing method, where chalcogen and halide precursors were deposited onto mesoporous  $\text{TiO}_2$  substrates [13,69]. By this approach, SbSeI thin films were fabricated by applying multiple spin-coating cycles of  $\text{SbI}_3$  and annealing in Ar atmosphere at 150 °C for 2 min, onto pre-deposited  $\text{Sb}_2\text{Se}_3$  layers, achieving a PCE of 4.1% [13]. Although with this synthesis method, the reported solar cells achieved promising high efficiencies, the morphology of the absorber layer remains sub-optimal. SbSeI grown within mesoporous  $\text{TiO}_2$  resulted in randomly oriented crystals that filled the mesoporous network, and no preferred crystallographic orientation was achieved. An alternative route was reported in [70], where SbSeI thin films were obtained by spin-coating a solution in ethylenediamine and 1,2-ethanedithiol, followed by annealing. Two transformation strategies were examined: (i) solution casting of  $\text{SbI}_3$  in dimethylformamide with subsequent thermal annealing, and (ii) exposing  $\text{Sb}_2\text{Se}_3$  films to  $\text{SbI}_3$  vapors at 70 °C followed by annealing at 150 °C, demonstrating a topotactic solid-state reaction in which SbSeI preserves the crystal orientation of  $\text{Sb}_2\text{Se}_3$ . Although solution-based films are cost-effective and compositionally tunable, vapor-phase techniques offer better film uniformity, composition control, and often higher crystallinity [71].

Caño *et al.* [29] introduced a high-pressure physical vapor deposition (PVD) method to synthesize all combinations of (Sb,Bi)(S,Se)(Br,I) chalcogenides as absorber layers for solar cells. The process involved co-evaporation of the chalcogenide from elemental sources onto Mo/glass substrates, followed by annealing under halogen vapor at pressures above 1 atm in an argon atmosphere. SbSeI thin films were obtained by annealing  $\text{Sb}_2\text{Se}_3$  in the presence of  $\text{SbI}_3$  at 450 °C for 15 min, whereas BiSeI films were synthesized from  $\text{Bi}_2\text{Se}_3$  and  $\text{BiI}_3$  at 500 °C for 15 min. In both cases, the resulting films exhibited the characteristic quasi-1D needle-like morphology. Although the needles were randomly oriented for both compositions, the BiSeI films displayed a more uniform and densely packed columnar microstructure [29]. Vapor-phase deposition techniques eliminate the multiple spin-coating and annealing cycles required in solution-processed methods and generally yield films with higher uniformity and crystallinity. Nevertheless, SbSeI thin films produced by PVD remain challenging to control in terms of film compactness and crystallographic orientation. In addition, incomplete surface coverage will lead to the formation of pinholes and voids. In solar cells, such defects can create

direct electrical pathways between adjacent layers, resulting in shunting and leakage currents, which severely degrade device performance. The random orientation observed in chalcogenide thin films, including SbSeI and BiSeI, can be attributed to the fact that their growth occurs through structural inheritance from the underlying binary precursor. The crystallographic orientation of the chalcogenide reflects that of the precursor, regardless of whether the initial layer is deposited by solution-based methods, co-evaporation, or by any other method. Consequently, if the precursor film lacks preferential orientation, the resulting film will also grow with a random orientation. This highlights the importance of achieving a proper morphology in the precursor layer to obtain highly oriented chalcogenide thin films. Despite recent progress, the fabrication of dense and crystallographically oriented SbSeI thin films remains an unresolved challenge. Addressing these limitations requires a systematic investigation to define the synthesis conditions that promote the formation of dense, homogeneous, and pinhole-free SbSeI absorber layers, which are a key prerequisite for achieving high-performance SbSeI-based PV devices.

In this thesis, SbSeI thin films were fabricated via PVT using magnetron-sputtered  $\text{Sb}_2\text{Se}_3$  precursor layers deposited at different substrate temperatures. An investigation of the effects of annealing temperature and duration on the formation of the SbSeI phase was conducted. The study focused on controlling film morphology, crystallographic orientation, and compactness to enable the formation of homogeneous and dense SbSeI absorber layers suitable for PV device integration.

## 1.5 Solid solutions in pnictogen chalcogenides

Theoretical work has predicted the optoelectronic properties of heavy pnictogen chalcogenide solid solutions. For example, López *et al.* [72] used a combined machine learning and first-principles method to estimate band gaps, electronic band structures, and absorption coefficients of MChX solid solutions. Another recent study [73] examined  $\text{Sb}_{1-x}\text{Bi}_x\text{SeI}$  solid solutions using density functional theory (DFT).

Experimentally, several chalcogenide solid solutions have been synthesized to investigate compositional effects, with materials prepared both as thin films [35,38] for device applications and as crystals [74–80] for fundamental characterization. Substitution on the pnictogen site (Sb, Bi) [74,76–78], the chalcogen site (S, Se) [35,75], and the halogen site (I, Br) [79,80] has been reported to modify the band structure while preserving the parent orthorhombic lattice. In the  $\text{Sb}_{1-x}\text{Bi}_x\text{SI}$  system, for instance, the partial substitution of Sb with Bi resulted in a gradual reduction of the band gap from approximately 1.86 eV to 1.55 eV, while the orthorhombic crystal structure remained stable across the entire compositional range [74]. Kanchana *et al.* studied the  $\text{SbBiS}_x\text{Se}_{1-x}\text{I}$  series and observed shifts in Raman and infrared vibrational modes upon replacing Se with S, indicating local structural modifications that correlate with the band gap variations [75]. Consistent with these findings, solid solution compositions such as  $\text{Sb}_{0.67}\text{Bi}_{0.33}\text{SI}$  have enabled improved PV performance, underscoring the relevance of compositional engineering for device optimization [38].

Biskunets *et al.* [78] synthesized  $\text{Sb}_{1-x}\text{Bi}_x\text{SeI}$  solid solutions with compositional increments of  $x = 0.1$  and, by X-ray diffraction (XRD), confirmed their orthorhombic crystal structure across the investigated compositions, and the variation in lattice parameters with increasing Bi content. Sereika *et al.* synthesized  $\text{Sb}_{0.5}\text{Bi}_{0.5}\text{SeI}$  single crystals by the Bridgman-Stockbarger technique and performed temperature-dependent resistivity, PL, and Raman spectroscopy measurements. The results revealed two

electronic transitions at 146 K and 62 K, suggesting that compositional disorder can induce complex electronic behavior beyond simple band gap tuning [76]. Despite these studies, the influence of Bi-Sb substitution on the optical and electronic properties of  $\text{Sb}_{1-x}\text{Bi}_x\text{SeI}$  remains insufficiently understood, and systematic investigations across the full compositional range are still lacking. Accordingly, Section 3.1 of this thesis presents a systematic experimental investigation of the  $\text{Sb}_{1-x}\text{Bi}_x\text{SeI}$  solid solution series, synthesized with controlled compositional increments of  $x = 0.2$ , focusing on the resulting structural and optoelectronic properties.

## 1.6 Optoelectronic properties

The optical and electronic properties of pnictogen chalcogenides have been investigated using both experimental and theoretical approaches. From a theoretical perspective, these properties are typically examined through first-principles calculations based on DFT and its extensions. DFT enables access to key parameters that are difficult to determine experimentally, including the electronic band structure, density of states (DOS), and dielectric constants. These parameters are essential for predicting carrier effective masses, evaluating band alignment, and gaining insight into charge transport-related characteristics like carrier lifetime and mobility.

### 1.6.1 Band gaps of SbSeI and BiSeI

In semiconductors, the band gap energy is a fundamental parameter that determines the range of photon energies a material can absorb to generate electron-hole pairs. For PV applications, the optimal band gap depends on the illumination conditions and the specific device architecture. Under standard solar illumination (AM1.5G), the SQ limit establishes the optimal band gap range of approximately 1.0 and 1.5 eV for single-junction solar cells, with a maximum theoretical efficiency of about 33% occurring at a band gap of 1.34 eV [39,40]. In contrast, for indoor photovoltaic (IPV) applications, where illumination is dominated by LED light sources, higher band gaps in the range of 1.7–1.9 eV are preferred, as they better match the photon energy distribution of artificial lighting [81].

The band gaps of pnictogen chalcogenides have been reported to span a wide range, typically between 1 and 2 eV [29,82]. This tunability arises from their compositional flexibility, whereby substitution on either the cations or anion sublattice enables systematic control of the electronic structure. In general, replacing Sb with Bi, S with Se, or Br with I results in a reduction of the band gap due to the heavier atomic mass and increased orbital overlap of the constituent elements. This broad band gap tunability makes these compounds attractive for a variety of optoelectronic applications, including PV, photodetectors, and light-emitting devices.

Experimentally, SbSeI exhibits a room temperature band gap of  $\sim 1.7$  eV [13–15], while BiSeI shows a smaller value of  $\sim 1.29$  eV [41,59,68]. While wider band gap materials like SbSeI are well-suited for IPV applications or as top absorbers in tandem solar cell architectures, their band gap exceeds the optimal value for single-junction solar cells under standard solar illumination. For this reason, this thesis explores Bi incorporation into SbSeI to form solid solutions, with the aim of narrowing the band gap toward a range associated with higher theoretical efficiency limits.

An additional aspect of the electronic structure of pnictogen chalcogenides is the nature of the band gap, namely, whether it is direct or indirect. Theoretical studies

consistently predict that both Sb- and Bi-based chalcogenides exhibit indirect fundamental band gaps, although the energy difference between the indirect and direct transitions is relatively small. For example, SbSeI is reported to exhibit a calculated energy difference of about 0.2 eV between the indirect and direct transitions [82,83], while BiSeI exhibits a smaller difference of around 0.1 eV [42,84]. Owing to this small energy separation, these materials can simultaneously exhibit strong optical absorption along with reduced electron–hole recombination. In other words, they combine characteristics of both direct and indirect semiconductors [83]. Notably, despite the consistent theoretical prediction of indirect band gaps, several experimental studies report apparently direct optical band gaps for SbSeI and BiSeI [85], indicating that the nature of the band gap remains an open and experimentally relevant question.

### 1.6.2 Optical absorption and dielectric properties of SbSeI and BiSeI

The ability of a material to absorb photons is quantified by its absorption coefficient ( $\alpha$ ). A high absorption coefficient is essential for efficient light harvesting, as it determines how effectively incident photons are absorbed within a given material thickness, an especially important requirement for PV absorber layers. Theoretical studies have demonstrated that pnictogen chalcogenides exhibit remarkably high absorption coefficients, reaching values of up to  $10^5 \text{ cm}^{-1}$  near the band edge. Ganose *et al.* [84] investigated BiSI and BiSeI using the empirical hybrid quasiparticle self-consistent GW method (hQSGW), while Caño *et al.* [29] performed first-principles calculations for all eight pnictogen chalcogenide compounds based on DFT employing the range-separated hybrid functional HSE06, including spin–orbit coupling (HSE06+SOC). Both studies predicted strong optical absorption close to the band edge across this materials family, a finding that was later confirmed experimentally by Nielsen *et al.* [85].

Within this group, the Bi-based compounds display absorption coefficients on the order of  $10^5 \text{ cm}^{-1}$ , whereas Sb-based compounds show slightly lower values, typically ranging between  $10^4$  and  $10^5 \text{ cm}^{-1}$ . These absorption coefficients are comparable to those of established PV absorber materials, highlighting pnictogen chalcogenides as promising candidates for light-harvesting and other optoelectronic applications.

In addition to their strong optical absorption, pnictogen chalcogenides exhibit relatively high dielectric constants. Reported theoretical values are in the range of 20 to 100, depending on the computational methods used [86]. Among these compounds, SbSeI and BiSeI exhibit dielectric constants in the range of 43.9–57.2 [82,83], and 26.8–35.8 [12,42,82], respectively. A high dielectric constant is associated with effective screening of ionized defects, reduced grain boundary scattering, and lower recombination rates [12,70], all of which are beneficial for PV performance and charge transport in optoelectronic devices.

Taken together, the strong optical absorption and high dielectric constants of pnictogen chalcogenides provide favorable conditions for efficient photogeneration. However, the practical performance of these materials also depends on how effectively photogenerated charge carriers are transported. The influence of carrier effective masses and transport anisotropy in SbSeI and BiSeI is therefore discussed in the following section.

### 1.6.3 Effective masses and charge transport properties

The effective masses of charge carriers in pnictogen chalcogenides have been widely investigated using DFT and beyond-DFT approaches, consistently revealing strong

anisotropy. Ganose *et al.* [84] employed hQSGW and the BoltzTraP Code to study the carrier transport properties of BiSI and BiSeI. They reported strongly anisotropic electronic bands, with relatively light electron effective masses along the ribbon direction ( $\approx 0.3 m_0$ , where  $m_0$  is the free electron rest mass) for both BiSeI and BiSI and significantly heavier hole effective masses ( $0.79 m_0$  and  $0.84 m_0$ , respectively), indicating a clear preference for *n*-type transport. Similar trends were reported by Peng *et al.* [23] for SbSI, SbSeI, and SbSBr, where electrons consistently exhibit smaller effective masses than holes. More recently, Caño *et al.* [29] surveyed a wide range of (Sb,Bi)(S,Se)(Br,I) compounds and reported electron effective masses spanning from 0.34 to 3.3  $m_0$ , reinforcing the general observation that substitution with heavier chalcogens or halogens leads to increased carrier masses.

Overall, both Bi- and Sb-based chalcogenides exhibit directionally dependent and relatively low electron effective masses, supporting their potential as efficient and environmentally friendly semiconductors for PV applications. The pronounced asymmetry between light electrons and significantly heavier holes suggests that these materials may preferentially support electron transport and could function as selective charge-transport layers, thereby reducing recombination losses. Furthermore, vertically oriented crystals are expected to further enhance carrier mobilities by aligning the preferred transport direction with the device architecture [16].

Consistent with their quasi-1D crystal structure, the electrical conductivity of heavy pnictogen chalcogenides is also highly anisotropic. Experimental measurements on single SbSeI crystals grown by PVT reveal resistivities on the order of  $10^6 \Omega\text{-cm}$  [41], indicating highly resistive behavior. In contrast, BiSeI exhibits significantly lower resistivity of approximately  $28.3 \Omega\text{-cm}$  under comparable growth conditions [41]. This difference is primarily attributed to the narrower band gap of BiSeI and its higher intrinsic carrier concentration. For PV applications, the high resistivity of SbSeI limits charge transport and consequently reduces device efficiency. Incorporating Bi into SbSeI to form solid solutions, therefore, represents a promising strategy to enhance electrical conductivity and improve the overall performance of SbSeI-based solar absorbers.

Despite the favorable intrinsic optoelectronic properties of SbSeI and BiSeI—including suitable band gaps, strong optical absorption, and low electron effective masses—these characteristics alone do not guarantee high PV performance. In practical devices, non-radiative recombinations at defects, grain boundaries, and interfaces often dominate carrier dynamics. Therefore, a comprehensive understanding of defect formation and recombination mechanisms is essential for translating the intrinsic material properties discussed in this section into efficient PV devices. These aspects are addressed in the following section, which focuses on the defect physics and recombination behavior of pnictogen chalcogenide materials.

## 1.7 Defect structure of pnictogen chalcogenides

Defects in crystalline materials can be classified according to their dimensionality. Point defects include vacancies, interstitials, antisites, and substitutional impurities. Line defects correspond to dislocations, while planar defects include grain boundaries, and volume defects may involve secondary phases or inclusions. Defects can also be categorized based on their electronic character. Shallow defects, located near the conduction band minimum (CBM) or valence band maximum (VBM), generally have a limited impact on carrier transport and may even contribute to electrical doping. Such

doping can be intentional or unintentional, originating from intrinsic point defects or unavoidably incorporated impurities.

In contrast, deep defects introduce electronic states well within the band gap, acting as traps or recombination centers that reduce carrier lifetime and overall device efficiency. Materials are considered defect-tolerant when their optoelectronic performance remains largely unaffected by a high density of defects. The origin of this tolerance lies primarily in the electronic structure of the material. In most conventional semiconductors used in solar cells, like GaAs and CdTe, the VBM is bonding and the CBM antibonding (Figure 4 left), promoting the formation of deep defect states far from the band edges and resulting in a strong degradation of optoelectronic properties even at relatively low defect concentrations. Defect-tolerant semiconductors typically exhibit an antibonding VBM and a bonding CBM (Figure 4, right). This electronic configuration favors the formation of shallow defect states upon the creation of vacancies or antisites. This defect-tolerant configuration is well established in lead-halide perovskites, where the stereochemically active  $ns^2$  lone pair of  $Pb^{2+}$  (originated from the  $6s^2$  configuration) causes strong orbital hybridization with the halide p-states, resulting in an antibonding VBM. A similar electronic structure is predicted for pnictogen chalcogenides, which contain cations with analogous  $ns^2$  lone-pair configurations ( $Sb^{3+}$ :  $5s^2$ ,  $Bi^{3+}$ :  $6s^2$ ).

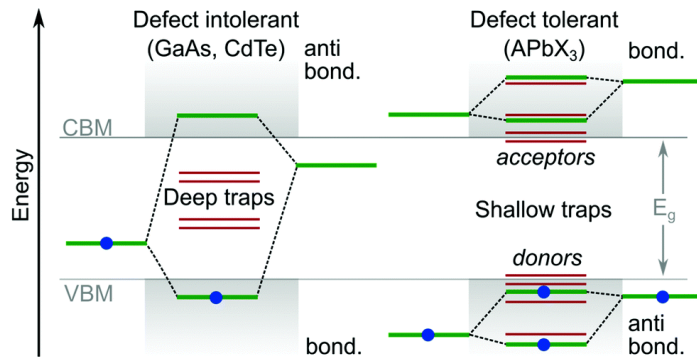


Figure 4. Comparison of the electronic structure of defect intolerant and defect tolerant semiconductors [87].

In SbSeI, the VBM is composed of the hybridization of Sb-5s, Se-4p, and I-5p orbitals, while the CBM mainly originates from Sb-5p states. The dominant intrinsic point defects are the antisite acceptor  $Se_I$  and the donor  $I_{Se}$ , both of which are shallow defects with a relatively high concentration, and tend to compensate each other, resulting in weak  $p$ -type or  $n$ -type conductivity. In contrast, the formation and concentration of deep defects such as  $Se_{Sb}$  antisites and iodine vacancies ( $V_I$ ) are strongly dependent on the growth conditions [88]. Experimental studies on SbSeI and SbSI have revealed carrier lifetimes of 6 and 3.2 ns, respectively, suggesting that recombination is not ultrafast and that these materials can maintain photogenerated carriers, indicating their potential for PV [89]. Nevertheless, these lifetime values remain lower than those observed in lead-halide perovskites [89]. In thin film PV absorbers, carrier lifetimes on the order of tenths to hundreds of nanoseconds are generally desired for efficient carrier collection [90,91]. Therefore, further optimization of synthesis conditions and careful defect control is still required to suppress deep defects and reduce recombination losses.

For BiSeI, the VBM primarily originates from the antibonding hybridization between Bi-6s and anion p orbitals (Se-4p and I-5p), while the CBM is mainly derived from Bi-6p states. The antibonding nature of the VBM is expected to reduce the formation of deep defects [92]. Nevertheless, the defect landscape of BiSeI is strongly influenced by synthesis conditions, as changes in chemical composition alter the formation energy of intrinsic point defects. Anion-rich (Se- and I-rich) and cation-poor (Bi-poor) growth conditions favor the formation of acceptor-type intrinsic defects, leading to *p*-type self-doping, while anion-poor and cation-rich (Bi-rich) conditions promote donor-type intrinsic defects and *n*-type self-doping. Importantly, this behavior arises from native defects rather than extrinsic dopants. According to Ganose *et al.* [84], BiSeI is therefore classified as an intrinsic semiconductor.

The lowest defect concentrations and recombination rates in BiSeI are obtained near stoichiometric composition, but it generally exhibits strong recombination, which has been attributed to the presence of ultradeep defect levels. These include acceptor-type defects such as  $Se_{Bi}$  and  $V_{Bi}$ , which are favored under Bi-poor (nominally *p*-type) growth conditions, as well as donor-type defects such as  $V_{Se}$ ,  $Bi_{Se}$ , and  $V_I$ , which are promoted under Bi-rich (nominally *n*-type) conditions [84]. López *et al.* [93] demonstrated through DFT calculations that  $V_{Se}$  and  $Bi_{Se}$  deep defects act as dominant non-radiative recombination centers, reducing the theoretical efficiency by approximately 6% relative to the maximum theoretical limit [93]. They further proposed that Bi-poor growth conditions increase the formation energies of these defects, thereby mitigating recombination and improving carrier lifetimes.

Despite these theoretical insights, experimental investigations of defect-related recombination processes in SbSeI and BiSeI have remained limited. To address this gap, temperature- and excitation power-dependent PL measurements were performed on SbSeI thin films and BiSeI microcrystals, on the basis of which a recombination model for BiSeI is proposed for the first time and possible defect states in SbSeI and BiSeI are identified through analysis of their activation energies.

## 1.8 Summary of the literature review and aim of the study

Global energy demand is rapidly increasing due to electrification, digital infrastructure expansion, climate-related needs, and the growth of electric mobility. At the same time, electricity generation is transitioning toward low-carbon sources, with renewable energy expected to reach about 43% of global electricity by 2030. Solar PV technology plays a key role in this transition because of its scalability, decreasing costs, and ability to generate electricity without direct carbon emissions. Currently, the PV market is dominated by c-Si solar cells, however, their energy-intensive manufacturing motivates the search for alternative materials and technologies, such as thin film solar cells, which require significantly less material. Among emerging PV materials, lead-halide perovskites show remarkable PCEs, low-temperature processing, and intrinsic defect tolerance. On the other hand, their instability under ambient conditions and the presence of toxic lead in the highest-performing compositions motivate the search for alternative absorber materials. These alternatives must combine excellent optoelectronic properties with long-term stability, consist of abundant elements, and exhibit low toxicity.

Heavy pnictogen chalcogenides were originally studied for their ferroelectric and optoelectronic properties. Over the last decade, they have been identified as promising semiconductors for optoelectronic devices and energy-conversion applications, including PV. These materials exhibit high absorption coefficients and a wide range of

compositionally tunable band gaps. In addition, their stereochemically active  $ns^2$  lone-pair cations have been proposed to promote defect tolerance. These characteristics make pnictogen chalcogenides attractive candidates for next-generation PV and optoelectronic technologies.

SbSeI has recently attracted significant attention as a potential PV absorber, and SbSeI-based solar cells with efficiencies of up to 4.1% have been reported, along with high stability. However, this performance remains far below the theoretical efficiency limit of about 28%, indicating substantial room for further improvement.

One of the main challenges arises from the quasi-1D crystal structure of SbSeI. The material grows in ribbon-like units with strong covalent bonding along the ribbon axis and weak van der Waals interactions between adjacent ribbons. This anisotropic bonding leads to highly directional crystal growth and is a major obstacle for thin-film fabrication, as crystals tend to form needle-like morphologies with random orientations. The resulting structural anisotropy strongly affects charge transport and limits device performance when grains are not favorably aligned.

To date, fabrication routes for high-quality SbSeI thin films remain underdeveloped. Therefore, it is necessary to develop and optimize synthesis strategies to produce compact, densely packed SbSeI thin films with preferentially oriented crystallites to improve solar cell efficiencies. SbSeI thin-film fabrication has relied on both solution processing and PVD, but orientation control remains challenging in both approaches. Since chalcogenide growth often inherits the crystallographic orientation of the precursor layer, controlling the morphology and crystallinity of the precursor is critical for achieving highly oriented crystallites in SbSeI films with improved optoelectronic performance.

SbSeI exhibits a band gap of approximately  $\sim 1.7$  eV. Although this value is suitable for IPV applications and as a top absorber in tandem solar cell architectures, it is higher than optimal for single-junction solar cells operating under standard solar illumination and could therefore benefit from further band gap optimization.

Compositional engineering through solid solutions ( $Sb_{1-x}Bi_xSeI$ ) enables band gap tuning while preserving the orthorhombic crystal structure. The incorporation of Bi reduces the band gap, modifies the electronic structure, and can enhance electrical conductivity, making alloying an attractive strategy for PV optimization. However, systematic experimental studies covering the full compositional range remain limited, providing strong motivation for the investigations presented in this thesis.

Defect physics plays a crucial role in determining PV performance. Due to antibonding valence band maxima arising from  $ns^2$  lone pairs on  $Sb^{3+}$  and  $Bi^{3+}$  cations, pnictogen chalcogenides are predicted to exhibit defect-tolerant behavior, favoring the formation of shallow intrinsic defects under appropriate growth conditions. Nevertheless, despite these theoretical predictions, experimental investigations of defect-related recombination processes in SbSeI and BiSeI remain scarce, and a deeper understanding of their defect structure is necessary for translating intrinsic material properties into efficient optoelectronic devices.

The overall aim of this study is to experimentally investigate the structural, optical, electronic, and defect-related properties of heavy pnictogen chalcogenides, in order to address key gaps in the fundamental understanding of these materials.

The main objectives of this thesis are:

- To establish processing–structure relationships for SbSeI thin films synthesized via physical vapor transport by investigating the influence of the precursor crystallinity, annealing temperature, and duration on the phase formation,

morphology, crystallographic orientation, and optoelectronic properties. The aim is to identify processing conditions that enable the formation of dense, phase-pure SbSeI layers with vertically orientated crystallites for PV applications.

- To synthesize and systematically characterize the complete  $\text{Sb}_{1-x}\text{Bi}_x\text{SeI}$  ( $x = 0-1$ ) solid solution series using a solid-state method, and to determine how the Bi incorporation modifies the crystal structure, band gap, band alignment, and conductivity type.
- To elucidate the defect structure and radiative recombination mechanisms in SbSeI and BiSeI using excitation power- and temperature-dependent PL spectroscopy. These measurements aim to identify dominant defect levels, establish recombination pathways, and develop an experimental defect-assisted recombination model.

## 2 Experimental

This chapter presents the methodologies employed for the synthesis of the materials investigated in this thesis, including the preparation of SbSeI thin films and the synthesis of microcrystalline SbSeI, BiSeI, and their solid solution series. Subsequently, the characterization techniques used throughout this work, together with a description of the instrumentation utilized for each method, are presented.

### 2.1 Preparation of SbSeI thin films

SbSeI thin films used in Paper I were prepared through a two-step process involving the sputtering of  $\text{Sb}_2\text{Se}_3$  onto molybdenum (Mo)-coated soda lime glass (SLG) substrate, followed by annealing with  $\text{SbI}_3$  (Figure 5).

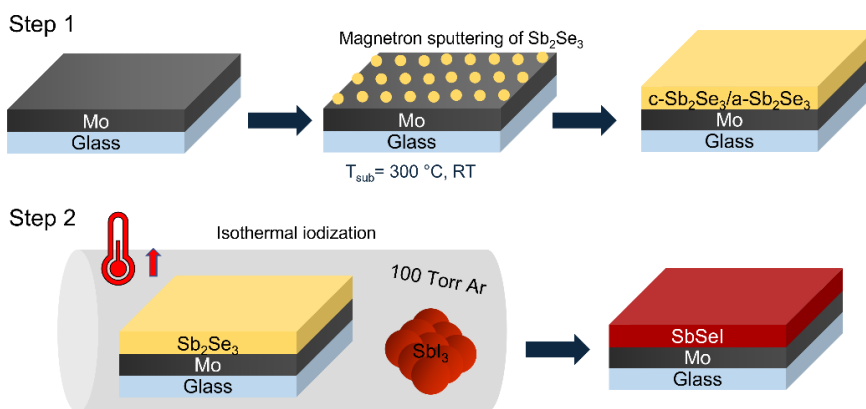


Figure 5. Schematic illustration of the two-step process for the preparation of SbSeI thin films.

$\text{Sb}_2\text{Se}_3$  layers on Mo/SLG substrates were prepared by Dr. Olga Volobujeva at Tallinn University of Technology. The  $\text{Sb}_2\text{Se}_3$  thin films were deposited by radio-frequency magnetron sputtering using an  $\text{Sb}_2\text{Se}_3$  target. Two different substrate temperatures were employed during deposition:  $300\text{ }^\circ\text{C}$  and room temperature (RT,  $25\text{ }^\circ\text{C}$ ), resulting in two distinct types of  $\text{Sb}_2\text{Se}_3$  layers (Figures 6 and 7). Structural analysis by XRD revealed that the RT-deposited films were amorphous, while films deposited at  $300\text{ }^\circ\text{C}$  were crystalline and exhibited a preferred orientation along the (061) plane [94]. No preferential orientation was observed for the  $\text{Sb}_2\text{Se}_3$  films deposited at RT. Raman spectroscopy corroborated the XRD results, confirming the crystalline nature of  $\text{Sb}_2\text{Se}_3$  deposited at  $300\text{ }^\circ\text{C}$  and the amorphous structure of the  $\text{Sb}_2\text{Se}_3$  films deposited at RT. Hereafter,  $\text{Sb}_2\text{Se}_3$  films deposited at  $300\text{ }^\circ\text{C}$  and RT are referred to as crystalline  $\text{Sb}_2\text{Se}_3$  (c- $\text{Sb}_2\text{Se}_3$ ) and amorphous  $\text{Sb}_2\text{Se}_3$  (a- $\text{Sb}_2\text{Se}_3$ ), respectively. The film thickness was approximately 800 nm and was controlled by adjusting the sputtering duration.

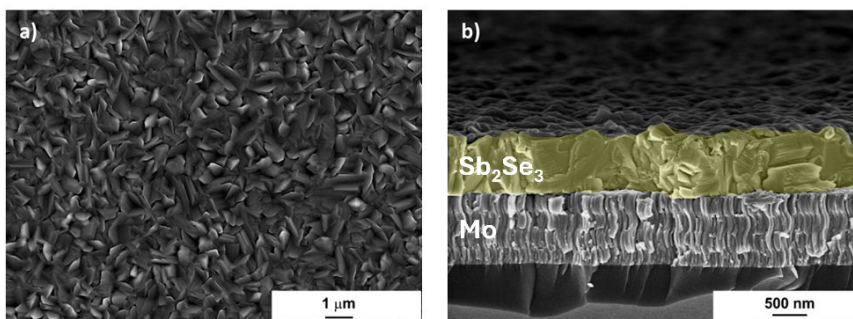


Figure 6. SEM images of a) top view and b) cross-section of crystalline  $Sb_2Se_3$  thin film.

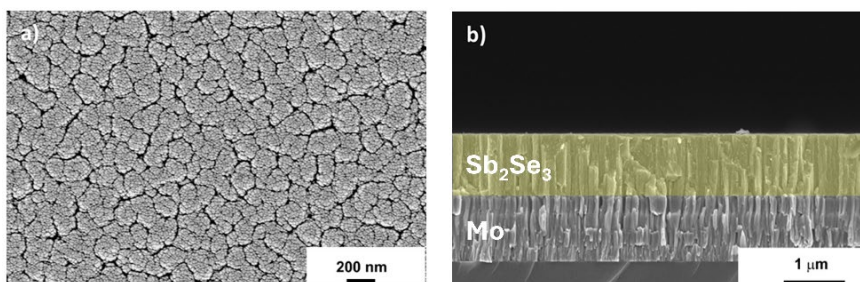


Figure 7. SEM images of a) top view and b) cross-section of amorphous  $Sb_2Se_3$  thin film.

$SbSeI$  thin films were synthesized from the as-deposited  $Sb_2Se_3$  layers by isothermal annealing in sealed quartz ampoules containing  $SbI_3$ . The  $SbI_3$  used in this work was self-synthesized from the constituent elements Sb (Alfa Aesar, 99.999%) and  $I_2$  (Реахим, 99.999%) by isothermal annealing in an evacuated quartz ampoule. The synthesis was carried out by heating at 180–200 °C for one month to ensure complete reaction and formation of a single-phase. For iodization, the  $Sb_2Se_3$  thin film substrates together with approximately 0.1 g of  $SbI_3$  were loaded into quartz ampoules with a length of 7 cm and an inner diameter of 12 mm. This process was carried out in an argon-filled glove box to avoid moisture exposure, owing to the hygroscopic nature of  $SbI_3$ . The ampoules were subsequently degassed under dynamic vacuum and filled with 100 Torr of argon pressure prior to sealing (Figure 8). The introduction of argon mitigates  $Sb_2Se_3$  decomposition by preventing Se loss and suppressing the rapid evaporation of  $SbI_3$  during annealing.



Figure 8.  $Sb_2Se_3$  thin film and  $SbI_3$  powder inside a sealed quartz ampoule.

The sealed ampoules were then annealed isothermally in a preheated chamber furnace under controlled conditions. For the c- $Sb_2Se_3$  samples, the annealing temperature was varied from 150 to 300 °C and the duration from 1 to 20 min (Table 1). In contrast, a- $Sb_2Se_3$  samples were iodized at 200, 225, and 250 °C for 5 min, based on

the optimized annealing parameters identified for the *c*-Sb<sub>2</sub>Se<sub>3</sub> samples. After iodization, the samples were removed from the furnace and allowed to cool down naturally to RT.

Table 1. Annealing conditions used for *c*-Sb<sub>2</sub>Se<sub>3</sub> thin films.

Temperature, °C	150	175	200	225	250	300
Time, min	-	-	-	1	1	1
	-	-	-	3	3	3
	5	5	5	5	5	5
	10	10	10	10	-	-
	15	15	15	15	-	-
	20	20	20	20	-	-

## 2.2 Synthesis of Sb<sub>1-x</sub>Bi<sub>x</sub>Sel (x = 0–1) microcrystalline solid solutions

BiSel (Paper II) and Sb<sub>1-x</sub>Bi<sub>x</sub>Sel (x = 0; 0.2; 0.4; 0.6; 0.8; 1) solid solutions (Paper III) were synthesized through a solid-state reaction route using self-prepared binary precursors Bi<sub>2</sub>Se<sub>3</sub> (99.999%), Sb<sub>2</sub>Se<sub>3</sub> (99.99%), SbI<sub>3</sub> (99.999%), and commercially available BiI<sub>3</sub> (Aldrich, 99%). Due to its hygroscopic nature, SbI<sub>3</sub> was stored and handled exclusively in an argon-filled glove box to prevent exposure to air and moisture.

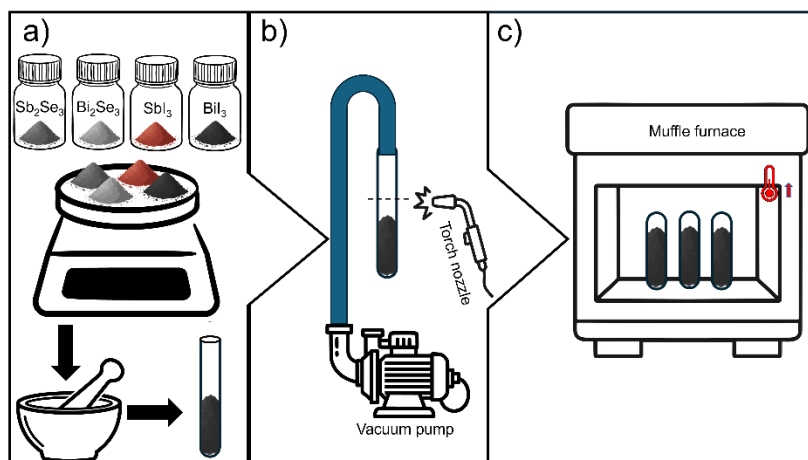


Figure 9. Schematic representation of the preparation of Sb<sub>1-x</sub>Bi<sub>x</sub>Sel microcrystals. a) Weighing, mixing, and loading of the precursor materials in ampoules. b) Evacuation and sealing of the ampoules. c) Annealing in a muffle furnace.

For the preparation of the solid solutions, the required amount of SbI<sub>3</sub> was taken from the glove box and mixed with the remaining binary precursors under ambient conditions. The appropriate ratios of the precursors were weighed, thoroughly mixed in an agate mortar, and loaded into quartz ampoules (Figure 9a). The ampoules were immediately evacuated under dynamic vacuum and sealed to minimize oxidation and volatilization losses (Figure 9b). All materials were heated in a muffle furnace (Figure 9c) from RT to 225 °C within 3 h, and the temperature was maintained for 24 h to promote initial reactions. Subsequently, the temperature of the samples with Bi contents of x = 0, 0.2, and 0.4 was increased to 440 °C within 5 h, remaining below the melting point of SbSel (452 °C) [51] and maintained for 256 h. Samples with Bi contents of x = 0.6, 0.8, and 1

were annealed at a higher temperature of 480 °C, since the melting temperature of BiSeI is 545 °C [52], and were also maintained at this temperature for 256 h. Finally, all samples were cooled down naturally to RT in air. Alternative synthesis routes starting from elemental Bi, Sb, Se, and I were also explored; however, these approaches resulted in inhomogeneous materials containing secondary phases. Consequently, the synthesis strategy was restricted to routes based on binary precursors, and multiple solid solution series were prepared using this approach.

## **2.3 Applied characterization methods**

### **2.3.1 X-ray diffraction spectroscopy**

The crystal structure and phase composition of thin films and microcrystalline materials were analyzed by XRD. Measurements were performed using a Rigaku Ultima IV diffractometer operated at 40 kV and 40 mA, equipped with a silicon strip detector (D/teX Ultra) and employing monochromatic Cu K $\alpha$  radiation ( $\lambda = 1.5406 \text{ \AA}$ ). This setup was used to study SbSeI thin films, BiSeI microcrystals, and Sb $_{1-x}$ Bi $_x$ SeI ( $x = 0-1$ ) solid solutions. Phase identification and lattice parameter calculations were carried out using the PDXL2 Rigaku software. All XRD measurements were conducted by Dr. Arvo Mere at Tallinn University of Technology, Tallinn, Estonia.

### **2.3.2 Room temperature micro-Raman spectroscopy**

The phase composition of thin films and microcrystalline materials (Papers I–III) was further investigated by room-temperature micro-Raman (RT  $\mu$ -Raman) spectroscopy. Raman spectra were acquired using a Horiba LabRAM HR 800 spectrometer equipped with an 1800 l/mm diffraction grating. The 532 nm Nd:YAG laser with a power of 0.42 mW was used as the excitation source and focused on the sample using an  $\times 50$  objective lens, resulting in a laser spot size of 3–5  $\mu\text{m}$  in diameter. The Raman signal was collected in a backscattering configuration and detected using a CCD detector.

### **2.3.3 X-ray photoelectron spectroscopy**

The elemental composition of the crystal surface of Sb $_{1-x}$ Bi $_x$ SeI microcrystals (Paper III) was studied by X-ray photoelectron spectroscopy (XPS). Measurements were performed using a Kratos Ultra DLD spectrometer operated under ultrahigh vacuum conditions, with a base pressure of  $10^{-9}$  mbar, with a monochromatized Al K $\alpha$  anode with a photon energy of 1486.6 eV. The surface charging effects were compensated using an electron flood gun during measurement, and binding energies were subsequently calibrated to the surface carbon C-C contamination peak at 284.6 eV. XPS measurements were conducted by Dr. Amelia Elena Bocirnea at the National Institute of Materials Physics, Magurele, Romania.

### **2.3.4 Ultraviolet photoelectron spectroscopy**

The work function and VBM energies of Sb $_{1-x}$ Bi $_x$ SeI microcrystals (Paper III) were determined by ultraviolet photoelectron spectroscopy (UPS). Measurements were carried out using an Axis Ultra DLD photoelectron spectrometer (Kratos Analytical) equipped with a helium discharge lamp operating at the He(I) resonance line ( $h\nu = 21.21 \text{ eV}$ ). Measurements were made on freshly synthesized selected microcrystals to minimize surface contamination and degradation. UPS measurements were conducted by Dr. Mati Danilson at Tallinn University of Technology, Tallinn, Estonia.

### 2.3.5 Photoluminescence

PL measurements were carried out to investigate the optoelectronic properties of the different materials studied in this thesis. Room temperature micro-photoluminescence (RT-PL) was performed on SbSeI thin films (Paper I), BiSeI microcrystals (Paper II), and  $Sb_{1-x}Bi_xSeI$  solid solutions (Paper III). RT-PL measurements were performed in the 1.1–1.9 eV range using the same equipment and experimental setup as for RT Raman.

Temperature and laser power-dependent PL measurements were performed on SbSeI thin films (Paper I) and BiSeI microcrystals (Paper II). For temperature-dependent measurements, the samples were mounted on the cold finger of a closed-cycle helium cryostat (Janis CCS-150), and the temperature decreased to 8 K. A LakeShore Model 335 temperature controller was used to adjust the temperature to 80 K for SbSeI thin films and 200 K for BiSeI crystals. The PL excitation source used was a continuous-wave laser (Cobolt 08-DPL) with a wavelength of 532 nm. For laser power-dependent measurements, the power of the incident laser beam was altered via neutral density filters. An optical chopper was used for modulating the laser beam, and the PL signal was detected using a lock-in amplifier (Stanford SR810 DSP). The emitted light was filtered using a cut-off low-pass filter and focused onto a computer-controlled single grating monochromator (600 lines/mm, focal length  $f = 0.64$  m; Horiba Jobin Yvon FHR640). The spectrally dispersed PL signal was detected using R632 and/or InGaAs photomultiplier tube, depending on the spectral range of interest. Temperature and laser power-dependent PL measurements were conducted by the author himself and Dr. Idil Mengü at Tallinn University of Technology, Tallinn, Estonia.

### 2.3.6 Scanning Kelvin probe

Scanning Kelvin probe (SKP) measurements were performed to evaluate the photosensitivity and to estimate the conductivity type of  $Sb_{1-x}Bi_xSeI$  ( $x = 0-1$ ) solid solutions investigated in Paper III. The measurements were carried out using an SKP system (SKP5050, KP Technology Ltd., UK) equipped with a 2 mm gold-coated vibrating probe. Illumination-induced variations in surface potential were investigated using a red semiconductor laser with a wavelength of 670 nm and an output power of 1 mW. For sample preparation,  $Sb_{1-x}Bi_xSeI$  microcrystalline powders were placed onto double-sided carbon tape fixed to the metallic sample holder of the system. The powder was gently pressed to ensure good electrical contact, and excess material was removed to obtain a thin, continuous layer suitable for SKP measurements.

### 2.3.7 Ultraviolet-Visible-Near-Infrared spectroscopy

The optical band gaps of all materials investigated in this thesis were determined by Ultraviolet-Visible-Near-Infrared (UV-Vis-NIR) diffuse reflectance spectroscopy. Two different experimental setups were employed. For SbSeI thin films (Paper I), measurements were performed at RT using a Cary500 spectrophotometer, with spectra collected in the 400–1100 nm wavelength range. For BiSeI microcrystals (Paper II) and  $Sb_{1-x}Bi_xSeI$  solid solutions (Paper III), a double-beam Shimadzu UV-3600 spectrometer equipped with an MPC-3100 multi-purpose compartment was used. In this case, diffuse reflectance spectra were recorded over the 260–2600 nm wavelength range. UV-Vis-NIR measurements were conducted by Dr. Rokas Kondrotas (Paper II) and Dr. Artūras Suchodolskis (Paper III) at the Center for Physical Sciences and Technology, Vilnius, Lithuania.

The optical band gap energies can be extracted using the Kubelka–Munk theory [95,96]. The Kubelka–Munk function is defined as:

$$F(R_{\infty}) = \frac{(1-R_{\infty})^2}{2R_{\infty}} \sim \alpha \quad (3)$$

where  $R_{\infty}$  is the absolute diffuse reflectance, and  $\alpha$  is the absorption coefficient. For optically thick samples, the reflectance becomes independent of sample thickness, and  $F(R_{\infty})$  can be approximated to the absorption coefficient. The optical band gap energy can be estimated by using the Tauc equation:

$$(\alpha h\nu)^{1/n} = A(h\nu - E_g) \quad (4)$$

where  $h$  is Planck's constant,  $\nu$  is the photon frequency,  $A$  is a constant, and  $E_g$  is the optical band gap. The exponent  $n$  depends on the nature of the optical transition, with  $n = 1/2$  corresponding to a direct and  $n = 2$  to an indirect transition. By substituting  $F(R_{\infty})$  for  $\alpha$ , the band gap can be determined by drawing a tangent line in the linear region that intersects the energy axis, and we obtain:

$$(F(R_{\infty})h\nu)^{1/n} = A(h\nu - E_g) \quad (5)$$

where  $E_g$  is obtained by extrapolating the linear region of the Tauc plot to the energy axis.

### 2.3.8 Scanning electron microscopy

The morphology of SbSeI thin films and  $Sb_{1-x}Bi_xSeI$  solid solutions was studied using a high-resolution scanning electron microscope (HR-SEM) Zeiss Ultra 55 and Merlin. The instrument was equipped with a high-resolution in-lens secondary electron detector for high-contrast surface imaging and an energy-selective backscattered electron detector for compositional contrast. High-resolution secondary electron SEM imaging was performed at an accelerating voltage of 4 keV, and 20 kV was used for back-scattered electrons. For SbSeI thin films, both top-view and cross-sectional morphology were analyzed. SEM measurements were conducted by the author himself and Dr. Valdek Mikli at Tallinn University of Technology, Tallinn, Estonia.

### 2.3.9 Transmission electron microscopy

High-resolution transmission electron microscopy (HR-TEM) images were acquired using a JEOL JEM-2100F transmission electron microscope. Selected area electron diffraction (SAED) was used to confirm the crystal structure of  $Sb_{1-x}Bi_xSeI$  microcrystals. TEM measurements were conducted by Cristian Radu at the National Institute of Materials Physics, Magurele, Romania.

### 2.3.10 Energy dispersive X-ray spectroscopy

The chemical composition of thin films and microcrystals was analyzed using energy-dispersive X-ray spectroscopy (EDX) integrated into a HR-SEM Zeiss Ultra 55 and Merlin systems. A Bruker Esprit 1.82 (Ultra 55) and 1.9 (Merlin) EDX systems equipped with an XFlash 3001 detector were employed for all measurements. For bulk compositional analysis of microcrystals, samples had to be prepared in advance. Crystals were

embedded in liquid epoxy resin. After curing for 48 h, the embedded crystals were sequentially polished using SiC sandpapers with decreasing grit size (from P400, corresponding to  $\sim 35 \mu\text{m}$ , to P4000,  $\sim 5 \mu\text{m}$ ), followed by final polishing with diamond suspensions ( $3 \mu\text{m}$  and  $1 \mu\text{m}$ ) and  $\text{Al}_2\text{O}_3$  ( $0.05 \mu\text{m}$ ) suspended particles. Polished samples embedded into epoxy resin were examined at an accelerating voltage of 20 kV. Additionally, the chemical composition of  $\text{Sb}_{1-x}\text{Bi}_x\text{SeI}$  solid solutions was analyzed by TEM-based EDX (EDX-TEM) using a JEOL JEM-2100F microscope equipped with a JEOL JED-2300T Dry SDD detector. The acceleration voltage was set to 200 keV. EDX measurements were conducted by the author himself and Dr. Valdek Mikli at Tallinn University of Technology, Tallinn, Estonia.

## 3 Results and discussion

### 3.1 SbSeI thin films

This section presents the results on the preparation and optimization of SbSeI thin films prepared via a two-step process consisting of sputtering deposition of  $\text{Sb}_2\text{Se}_3$  precursor layers followed by isothermal iodization in an  $\text{SbI}_3$  atmosphere (Paper I). The primary objective was to identify processing conditions that ensure complete phase conversion, near-stoichiometric composition, and a favorable micro-columnar morphology with controlled crystal orientation. Particular emphasis was placed on understanding the influence of annealing temperature, duration, and precursor crystallinity on the structural and compositional evolution of the films.

Two types of  $\text{Sb}_2\text{Se}_3$  precursor layers were investigated: crystalline  $\text{Sb}_2\text{Se}_3$  deposited at 300 °C and amorphous  $\text{Sb}_2\text{Se}_3$  deposited at room temperature. The results obtained for both precursor types are discussed separately.

#### 3.1.1 Formation of SbSeI from c- $\text{Sb}_2\text{Se}_3$

The formation of SbSeI thin films from crystalline  $\text{Sb}_2\text{Se}_3$  (c- $\text{Sb}_2\text{Se}_3$ ) precursor layers was systematically investigated as a function of annealing temperature (150–350 °C) and duration (1–20 min) in  $\text{SbI}_3$  vapor in an Ar-filled ampoule (initial Ar pressure of 100 Torr at RT). The objective was to determine the conditions required for complete phase conversion while maintaining a compact morphology and controlled crystal orientation.

The as-deposited c- $\text{Sb}_2\text{Se}_3$  precursor layer exhibited a compact, fully covered surface morphology, with good adhesion to the Mo substrate and no visible gaps at the film-substrate interface (Figure 6).

Figure 10a-c presents cross-sectional SEM images of SbSeI thin films obtained by iodization of c- $\text{Sb}_2\text{Se}_3$  at 150 °C for 5, 10, and 20 min. Corresponding SEM images for iodization at 175 °C for 5–20 min are presented in Paper I. In both cases, the annealed layers consist of SbSeI micro-columnar structures with column length, diameter, and density increasing systematically with annealing duration. However, despite this morphological evolution, all films annealed at 150–175 °C exhibited a residual unreacted  $\text{Sb}_2\text{Se}_3$  layer beneath the SbSeI micro-columns, regardless of the annealing duration. This indicates that temperatures in the range of 150–175 °C are insufficient to achieve complete conversion to a single-phase SbSeI thin film.

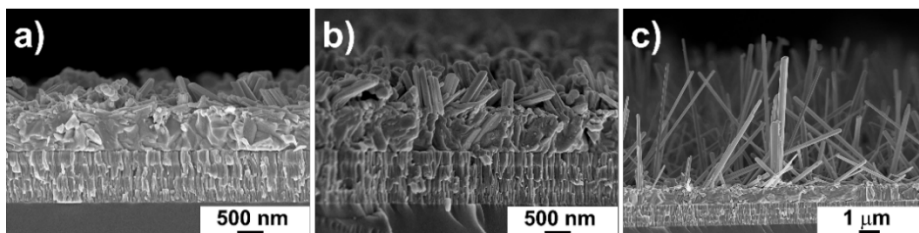


Figure 10. SEM images of the cross-section of SbSeI thin films annealed in  $\text{SbI}_3+\text{Ar}$  atmosphere at 150 °C for a) 5, b) 10, and c) 20 min.

A similar behavior was observed for shorter annealing times (3 min) at higher temperatures (225–300 °C) (Figure 11a-b), indicating that elevated temperature alone does not ensure complete transformation. The persistence of unreacted  $\text{Sb}_2\text{Se}_3$  suggests

that the iodization process may be diffusion-limited, with the formation of a SbSeI layer partially hindering further transport of iodine compounds towards the reaction interface. In contrast, increasing the annealing duration to 5 min at temperatures between 200 and 300 °C, complete formation of the SbSeI layer was achieved. Although two distinct layers are visible in the cross-section (Figure 12), both correspond to the SbSeI phase, and no residual Sb<sub>2</sub>Se<sub>3</sub> was detected.

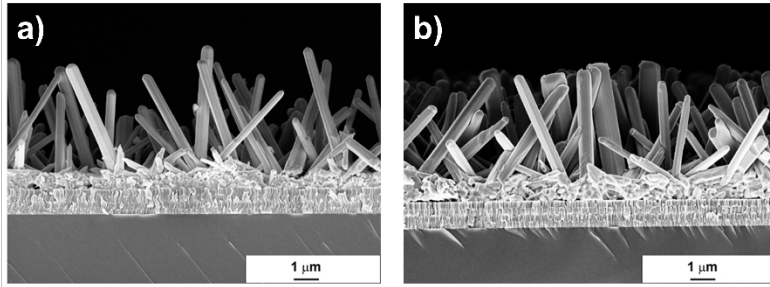


Figure 11. SEM images of the cross-section of SbSeI thin films annealed in SbI<sub>3</sub>+Ar atmosphere during 3 min at a) 225 °C and b) 300 °C.

Analysis of the cross-sectional SEM images shows that both the length and diameter of the SbSeI micro-columns increase with increasing annealing temperature and duration. For an annealing duration of 5 min, the SbSeI columns formed at 150 °C were barely distinguishable from the underlying Sb<sub>2</sub>Se<sub>3</sub> layer (Figure 10a). At 175 °C, the column length increases from ~0.8 μm to ~5 μm, and the morphology became more uniform. At higher annealing temperatures (≥200 °C), the reaction proceeded more efficiently: column lengths of ~17 μm were obtained at 250 °C, increasing further to ~37 μm at 300 °C (Figure 12a-c).

In addition to length, the column diameter also increased with the annealing temperature. After annealing at 250 °C for 5 min, ~0.5 μm of diameter was observed, while at 300 °C for the same duration, the diameter increased to ~2 μm. However, at 300 °C, the micro-columns became less homogeneous, exhibiting a broad distribution of lengths and diameters, indicating coarsening and non-uniform growth at elevated temperatures.

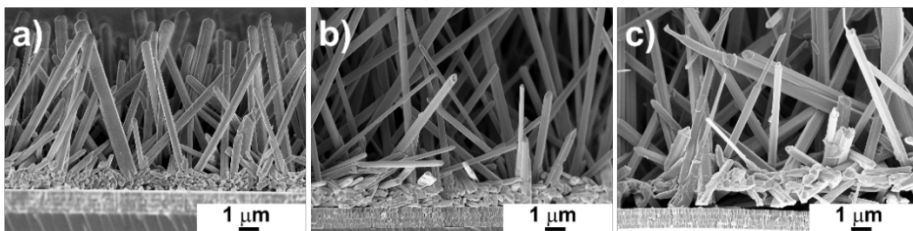


Figure 12. SEM images of the cross-section of SbSeI thin films annealed in SbI<sub>3</sub>+Ar atmosphere during 5 min at a) 200 °C, b) 250 °C, and c) 300 °C.

At an annealing temperature of 350 °C, the characteristic micro-columnar morphology disappeared, resulting in a non-uniform, irregular, and relatively flat SbSeI layer. Annealing temperatures above 350 °C were not investigated further due to the pronounced deterioration of the film morphology.

The elemental composition of the SbSeI thin films was analyzed by EDX. As summarized in Table 2, the chemical composition of the thin films is strongly dependent on both the annealing temperature and duration.

Table 2. Elemental composition of SbSeI thin films annealed at different temperatures and durations measured by EDX.

Annealing temperature, °C	Annealing duration, min	Sb, at%	Se, at%	I, at%	Proposed phases
150	5	35.2	55.2	9.6	SbSeI, Sb <sub>2</sub> Se <sub>3</sub> , Se
	10	36.8	48.2	15.0	SbSeI, Sb <sub>2</sub> Se <sub>3</sub>
	15	36.9	46.5	17.6	SbSeI, Sb <sub>2</sub> Se <sub>3</sub>
	20	35.4	51.4	13.3	SbSeI, Sb <sub>2</sub> Se <sub>3</sub> , Se
175	5	36.7	36.9	26.4	SbSeI, Sb <sub>2</sub> Se <sub>3</sub>
	10	36.0	37.4	26.6	SbSeI, Sb <sub>2</sub> Se <sub>3</sub>
	15	35.2	30.1	34.7	SbSeI, SbI <sub>3</sub>
	20	37.0	27.9	35.2	SbSeI, SbI <sub>3</sub>
200	5	34.5	32.6	32.9	SbSeI
	10	36.6	37.1	26.4	SbSeI, Sb <sub>2</sub> Se <sub>3</sub>
	15	37.8	38.7	23.5	SbSeI, Sb <sub>2</sub> Se <sub>3</sub>
225	1	36.6	57.7	5.7	SbSeI, Sb <sub>2</sub> Se <sub>3</sub> , Se
	3	35.4	35.3	29.3	SbSeI, Sb <sub>2</sub> Se <sub>3</sub>
	5	34.2	32.7	33.1	SbSeI
250	1	37.1	55.0	8.0	SbSeI, Sb <sub>2</sub> Se <sub>3</sub> , Se
	3	35.9	33.8	30.2	SbSeI, Sb <sub>2</sub> Se <sub>3</sub>
	5	34.1	32.8	33.1	SbSeI
300	1	39.3	48.8	11.9	SbSeI, Sb <sub>2</sub> Se <sub>3</sub>
	3	34.7	29.7	35.6	SbSeI, SbI <sub>3</sub>
	5	34.4	29.7	35.9	SbSeI, SbI <sub>3</sub>

Films annealed at lower temperatures (150 °C for 5–20 min and 175 °C for 5–10 min) exhibited iodine-deficient compositions. Similar I-poor composition was observed for samples annealed for short durations at higher temperatures, namely 225 °C (1–3 min), 250 °C (1–3 min), and 300 °C (1 min). These compositional deviations are consistent with the presence of an unreacted Sb<sub>2</sub>Se<sub>3</sub> interlayer observed in the corresponding cross-sectional SEM images (Figures 10 and 11). In contrast, films annealed at 175 °C for longer durations (15–20 min) and at 300 °C for 3–5 min exhibited Sb-rich and I-rich compositions. This can be attributed to the coexistence of SbI<sub>3</sub> with the SbSeI phase, likely due to excess iodine incorporation and/or incomplete desorption of volatile SbI<sub>3</sub> under these conditions.

SbSeI thin films with composition close to the stoichiometric ratio (Sb : Se : I = 1 : 1 : 1) were obtained by annealing Sb<sub>2</sub>Se<sub>3</sub> precursor in the presence of SbI<sub>3</sub>+Ar atmosphere for 5 min at 200–250 °C. Thus, this temperature range represents the optimal conditions for achieving near-stoichiometric SbSeI thin films.

Raman spectroscopy was used to investigate the phase composition of the thin films and to provide complementary information for the possible presence of secondary phases (Sb<sub>2</sub>Se<sub>3</sub>, SbI<sub>3</sub>, Se) detected by EDX. RT Raman spectra of as-deposited c-Sb<sub>2</sub>Se<sub>3</sub> thin film and of films annealed at 150, 175, and 200 °C for 5 min are shown in Figure 13. As

for the samples discussed in Section 3.1, all spectra were fitted using a Lorentzian function to resolve individual peaks.

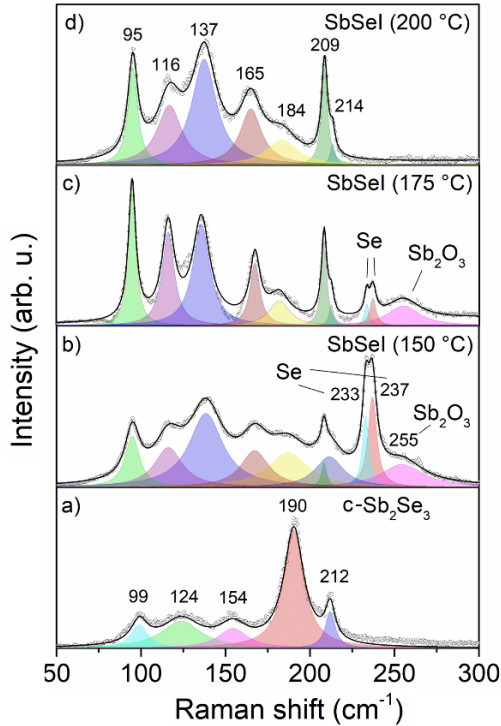


Figure 13. RT Raman spectra of a) as-deposited  $c\text{-Sb}_2\text{Se}_3$  and SbSel films formed by annealing at b) 150, c) 175, and d) 200 °C for 5 min.

The Raman spectrum of the as-deposited  $c\text{-Sb}_2\text{Se}_3$  film exhibited a dominant peak at  $190\text{ cm}^{-1}$ , along with less intense peaks at  $99$ ,  $124$ ,  $154$ , and  $212\text{ cm}^{-1}$  (Figure 13a). These peak positions are consistent with reported Raman modes of  $\text{Sb}_2\text{Se}_3$  [97]. SbSel exhibits characteristic Raman peaks at  $96$  and  $115\text{ cm}^{-1}$ , which are attributed to Sb–I vibrational modes [44], and at  $209\text{ cm}^{-1}$ , corresponding to Sb–Se bond vibrations [70]. The Raman spectrum of the SbSel film formed by annealing at  $150\text{ °C}$  for 5 min (Figure 13b), revealed peaks at  $95$ ,  $116$ ,  $137$ ,  $165$ ,  $184$ ,  $209$ ,  $211$ ,  $233$ ,  $237$ , and  $255\text{ cm}^{-1}$ . The peak at  $211\text{ cm}^{-1}$  can be attributed to residual  $\text{Sb}_2\text{Se}_3$ , while the peak at  $255\text{ cm}^{-1}$  corresponds to  $\text{Sb}_2\text{O}_3$  [98], indicating the presence of secondary phases. The presence of  $\text{Sb}_2\text{O}_3$  is likely related to the susceptibility of Sb-containing compounds to photo-induced oxidation or degradation during Raman measurements [98,99]. In addition, two intense peaks observed at  $233$  and  $237\text{ cm}^{-1}$  are attributed to trigonal Se [44]. Although Raman modes associated with SbSel are present, they appear broader and less intense compared to the Se peaks, suggesting incomplete conversion and limited crystallinity.

For the SbSel film formed by annealing at  $175\text{ °C}$  for 5 min (Figure 13c), the  $\text{Sb}_2\text{O}_3$ -related peak at  $255\text{ cm}^{-1}$  is still observed, while trigonal Se peaks at  $233$  and  $237\text{ cm}^{-1}$  persist, but with reduced intensity. In this case, however, the dominant Raman peaks correspond to the ternary SbSel phase. Compared to the sample annealed at  $150\text{ °C}$ , the SbSel-related peaks appear noticeably narrower, indicating improved crystallinity. The presence of  $\text{Sb}_2\text{O}_3$  in films annealed at  $150$  and  $175\text{ °C}$  is attributed to the higher susceptibility of incompletely

reacted films to the laser power used during Raman measurements compared to films annealed at higher temperatures. This behavior suggests that the reaction between  $\text{Sb}_2\text{Se}_3$  and  $\text{SbI}_3$  remains incomplete at 150 and 175 °C.

In contrast, the Raman spectrum of the thin film formed by annealing at 200 °C for 5 min (Figure 13d), shows peaks at 95, 116, 137, 165, 184, 209, and 214  $\text{cm}^{-1}$ . Peaks previously assigned to  $\text{Sb}_2\text{O}_3$  and trigonal Se are no longer observed, confirming the complete formation of the SbSeI phase. All observed Raman modes can be attributed to SbSeI and are in good agreement with literature reports [44,70]. Overall, the Raman spectroscopy results are consistent with the compositional analysis presented in Table 2 and confirm the presence of secondary phases in films formed at temperatures below 200 °C. Films formed at higher temperatures exhibit similar Raman peaks to the sample annealed at 200 °C, with the main difference being an increased intensity ratio of 95 and 209  $\text{cm}^{-1}$  peaks relative to the other SbSeI modes.

In conclusion, SbSeI thin films prepared from c- $\text{Sb}_2\text{Se}_3$  precursor layers under the investigated conditions (150–350 °C, 1–20 min) did not exhibit densely packed and vertically oriented micro-columnar structures. Although a complete conversion to SbSeI was achieved under optimized annealing conditions (200–250 °C for 5 min). As the crystallographic orientation of the precursor layer plays a critical role in the growth of the SbSeI phase, an  $\text{Sb}_2\text{Se}_3$  precursor layer without a preferred crystalline orientation is therefore employed in the following subsection.

### 3.1.2 Formation of SbSeI from a- $\text{Sb}_2\text{Se}_3$

Given the morphological limitations of SbSeI thin films prepared from crystalline  $\text{Sb}_2\text{Se}_3$  precursor layers, amorphous  $\text{Sb}_2\text{Se}_3$  substrates deposited at RT were employed to improve crystal alignment and packing density in the resulting SbSeI films. Based on the optimal annealing conditions identified in the previous section, under which complete conversion to SbSeI was achieved, a- $\text{Sb}_2\text{Se}_3$  substrates were annealed in an  $\text{SbI}_3+\text{Ar}$  atmosphere at 200, 225, and 250 °C for 5 min.

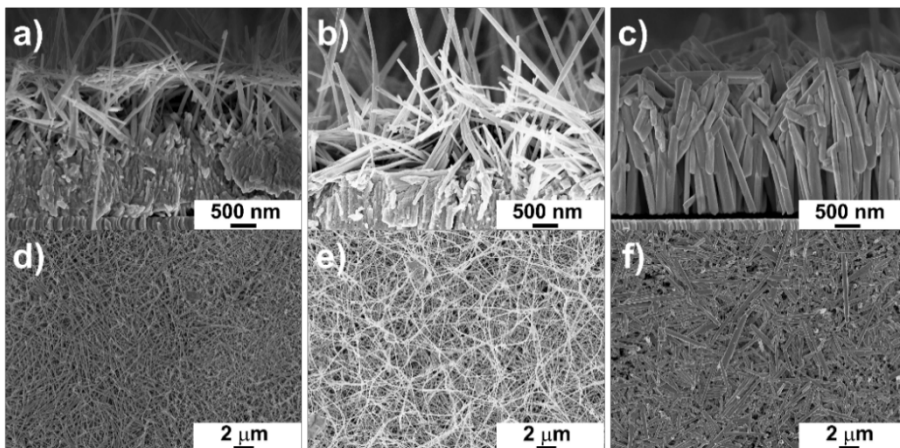


Figure 14. SEM images of cross-section (a–c) and top-view (d–f) of SbSeI thin films formed by annealing a- $\text{Sb}_2\text{Se}_3$  in an  $\text{SbI}_3+\text{Ar}$  atmosphere for 5 min at (a, d) 200 °C, (b, e) 225 °C, and (c, f) 250 °C.

Figure 14 presents cross-sectional and top-view SEM images of the SbSeI thin films obtained by iodization of *a*-Sb<sub>2</sub>Se<sub>3</sub> at 200, 225, and 250 °C for 5 min. SEM analysis shows that annealing at 200-225 °C resulted in a non-uniform double-layer structure consisting of an SbSeI top layer and unreacted *a*-Sb<sub>2</sub>Se<sub>3</sub>. The SbSeI crystals formed under these conditions exhibited significant variations in length, thickness, and orientation. Crystals appear elongated and curved (Figure 14a, d, and 14b, e) instead of exhibiting the expected straight columnar shape. The persistence of a double-layer structure containing unreacted Sb<sub>2</sub>Se<sub>3</sub>, similar to that observed for *c*-Sb<sub>2</sub>Se<sub>3</sub> precursors, indicates that the annealing temperature and/or duration were insufficient to achieve complete conversion to SbSeI under these conditions. In contrast, annealing at 250 °C yielded a uniform SbSeI thin film composed of well-oriented, densely packed micro-columnar crystals, as shown in Figure 14c. No residual Sb<sub>2</sub>Se<sub>3</sub> was detected at this temperature, demonstrating that the use of *a*-Sb<sub>2</sub>Se<sub>3</sub> precursors, in combination with sufficiently high annealing temperatures, enables complete conversion and yields improved film morphology.

EDX analysis indicated that the resulting SbSeI thin film was slightly Sb- and I-rich, suggesting the presence of residual SbI<sub>3</sub>. The elemental composition of Sb : Se : I was 35.2 : 29.7 : 35.1 at%.

To further assess the phase composition, the SbSeI thin film formed at 250 °C for 5 min was analyzed by Raman spectroscopy and XRD (Figure 15a and 15b). The Raman spectrum exhibited only the characteristic vibrational modes of SbSeI at 96, 117, 138, 168, 180, 209, and 214 cm<sup>-1</sup>, with no detectable signals from secondary phases (Figure 15a). The spectrum is comparable to that of SbSeI formed from *c*-Sb<sub>2</sub>Se<sub>3</sub> annealed at 200 °C (Figure 13d). However, the Raman peaks are noticeably sharper and narrower than those of the other SbSeI thin films shown in Figure 12, indicating a higher level of crystallinity. The main Raman peak at 209 cm<sup>-1</sup> exhibits a full width at half maximum (FWHM) of 3.82 cm<sup>-1</sup>.

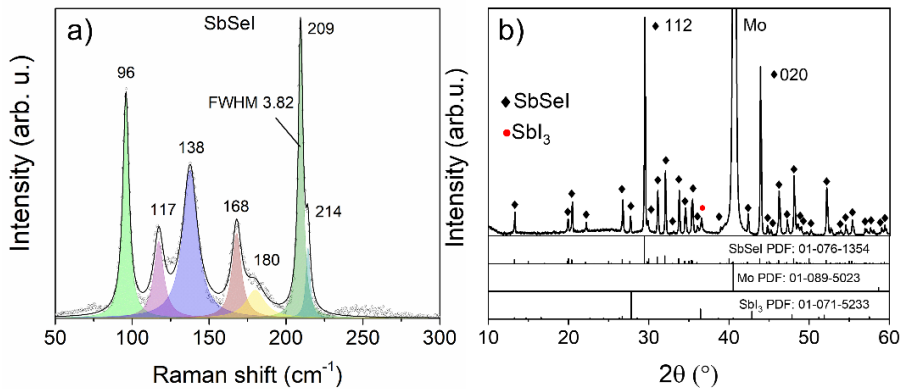


Figure 15. a) Raman spectrum and b) XRD pattern of SbSeI thin film formed by annealing *a*-Sb<sub>2</sub>Se<sub>3</sub> at 250 °C for 5 min in SbI<sub>3</sub>+Ar atmosphere.

XRD analysis confirmed an orthorhombic crystal structure with SbSeI as the predominant phase, while a minor SbI<sub>3</sub> secondary phase was detected at 2θ = 36.5°, in agreement with the EDX results (Figure 15b). In addition, a reflection at 2θ = 40.6° was observed, which corresponds to the (110) plane of the Mo substrate. The XRD pattern exhibited two intense SbSeI reflections at 2θ = 29.4° (112) and 43.9° (020), indicating the

presence of two preferred crystallographic orientations. These reflections correspond to predominantly vertically oriented SbSeI crystallites, with a fraction of horizontally oriented crystallites located on top of the vertical columns (Figure 14f). The lattice parameters of SbSeI were determined as  $a = 8.671 \text{ \AA}$ ,  $b = 4.118 \text{ \AA}$ , and  $c = 10.382 \text{ \AA}$ , in good agreement with the values reported in [41].

Compared with SbSeI films derived from c-Sb<sub>2</sub>Se<sub>3</sub>, SbSeI thin films prepared from a-Sb<sub>2</sub>Se<sub>3</sub> precursor layer and annealed in an SbI<sub>3</sub> at 250 °C for 5 min exhibited significantly improved vertical orientation and a higher packing density of micro-columns. These morphological features make such films more promising candidates for use as absorber layers in solar cell devices. The results demonstrate that the morphology and crystallinity of the chalcogen precursor layer (Sb<sub>2</sub>Se<sub>3</sub>) strongly influence the formation of the resulting chalcohalide thin film, affecting crystal orientation, column density, and overall film compactness. Consequently, careful selection and control of the chalcogenide precursor properties are crucial to obtaining chalcohalide thin films with morphologies optimized for PV applications. These results suggest that this approach is among the most promising reported strategies for obtaining vertically aligned and densely packed SbSeI thin films.

Considering that the optical band gap of SbSeI has been reported to be too large for efficient single-junction solar cells, and that it can be reduced by incorporating Bi into SbSeI, as discussed in Chapter 1, (Sb,Bi)SeI thin films were subsequently investigated using a similar approach and processing conditions. Specifically, Sb<sub>2</sub>Se<sub>3</sub> thin films were iodized in a BiI<sub>3</sub> atmosphere [100]. However, this method did not enable precise control of the Sb/Bi ratio in the resulting films. Therefore, an alternative synthesis approach was used to obtain Sb<sub>1-x</sub>Bi<sub>x</sub>SeI solid solutions with controlled composition.

### 3.2 Sb<sub>1-x</sub>Bi<sub>x</sub>SeI (x = 0–1) microcrystalline solid solutions

In this section, a complete series of Sb<sub>1-x</sub>Bi<sub>x</sub>SeI microcrystalline solid solutions synthesized by a solid-state reaction, with compositional steps  $x = 0.2$  (Papers II and III) is presented, including SbSeI and BiSeI end members. The morphological, compositional, structural, and optoelectronic properties of the Sb<sub>1-x</sub>Bi<sub>x</sub>SeI system are discussed.

#### 3.2.1 Morphology of Sb<sub>1-x</sub>Bi<sub>x</sub>SeI microcrystals

The synthesized microcrystalline materials were first visually inspected while remaining sealed in transparent quartz ampoules (Figure 16). All samples contained needle-like

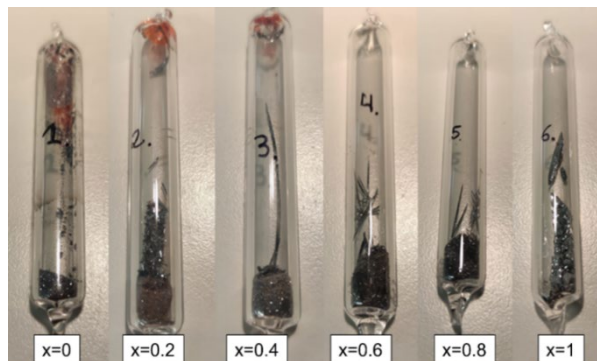


Figure 16. Sb<sub>1-x</sub>Bi<sub>x</sub>SeI (x = 0–1) materials in sealed quartz ampoules after synthesis.

crystals with a grey, metallic appearance and a reflective surface, with the microcrystals grown at the bottom of the ampoules. The needle-like crystals are clearly visible to the naked eye, ranging from small crystallites to elongated structures reaching several centimeters in length. For samples with compositions  $x = 0, 0.2,$  and  $0.4,$  a distinct reddish coloration was observed near the upper region of the ampoules, indicating the presence of residual  $\text{SbI}_3$ .

The morphology of the synthesized materials was further investigated by SEM. Top-view SEM images of  $\text{Sb}_{1-x}\text{Bi}_x\text{SeI}$  ( $x = 0-1$ ), shown in Figure 17, reveal that the samples consist predominantly of cylindrical or prismatic, needle-shaped crystals with a broad size distribution. The largest crystals exceed 1 mm in length and several hundred micrometers in diameter, often forming well-defined, regular columnar structures. SEM images show that needles consist of multiple parallel-aligned layers that are interconnected along the  $a$ -axis. This growth behavior is consistent with previous reports on one-dimensional  $\text{SbSI}$  crystals, in which the formation of needle-like morphologies is attributed to strongly anisotropic growth mechanisms in  $\text{A}^{\text{V}}\text{B}^{\text{VI}}\text{C}^{\text{VII}}$  compounds, characterized by a significantly faster growth rate along the  $b$ -axis. The observed layered crystal structure connected along the  $a$ -axis is also comparable to that reported for  $\text{BiSeI}$  crystals [59]. In addition to the larger crystals, smaller needle-shaped crystals are present, with lengths of tens of micrometers and a diameter of a few micrometers, while maintaining a similar cylindrical elongated morphology. Furthermore, the needle-shaped crystals coexist with clusters of smaller and irregularly shaped crystals that are partially covered with nanometer-sized particles (Figure 17f).

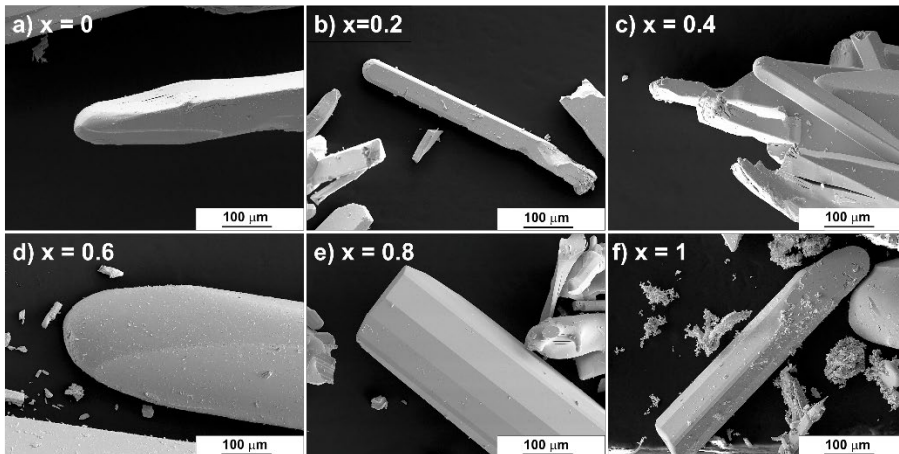


Figure 17. (a-f) SEM images of the surface morphology of  $\text{Sb}_{1-x}\text{Bi}_x\text{SeI}$  microcrystals ( $x = 0-1$ ).

TEM was used to further study the crystals' morphology and internal structure. TEM analysis confirmed that all samples consist of large, elongated microcrystals (Figure 18a) with straight, well-defined edges (facets) indicating growth along specific crystallographic directions. As shown in Figure 18b, the ribbon-like structural units characteristic of these materials are aligned parallel to the long axis of the columnar crystals. A magnified image of the region highlighted in Figure 18b reveals a continuous crystalline layer without visible grain boundaries and structural defects such as dislocations (Figure 18c). Figure 18d presents the SAED pattern of the  $\text{Sb}_{0.2}\text{Bi}_{0.8}\text{SeI}$  crystal. The diffraction spots can be indexed to the (010), (11-1), and (10-1) lattice planes, with

corresponding interplanar spacings of 4.22 Å, 3.57 Å, and 6.72 Å, respectively. A single set of diffraction spots is observed for all investigated solid solutions, confirming their high crystallinity.

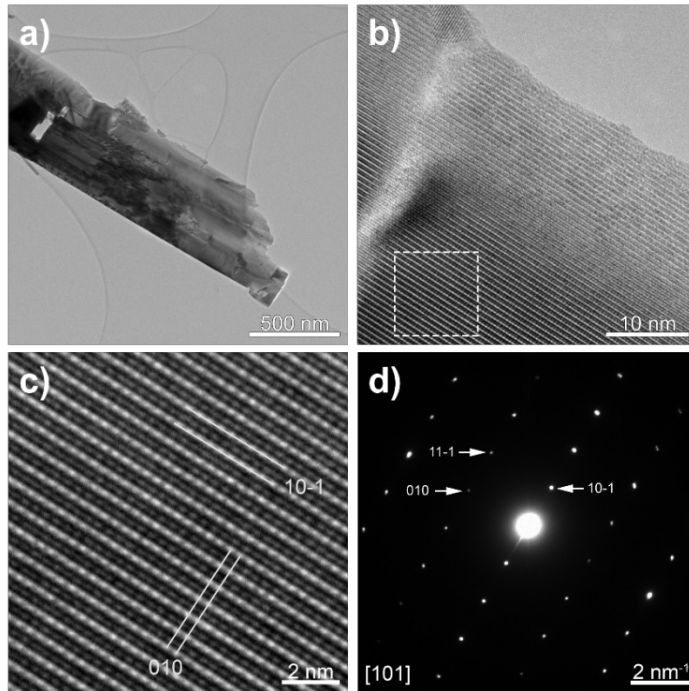


Figure 18. a) Low magnification TEM image, b) TEM image indicating the area that was magnified in c), where the lattice planes (10-1) and (010) were illustrated, and d) SAED corresponding to  $Sb_{1-x}Bi_xSeI$  with  $x = 0.8$ .

### 3.2.2 Chemical composition of $Sb_{1-x}Bi_xSeI$ microcrystals

The bulk composition of the solid solutions (Paper III), including BiSeI crystals (Paper II), was investigated. The exposed cross-sections were analyzed by SEM-EDX to assess the

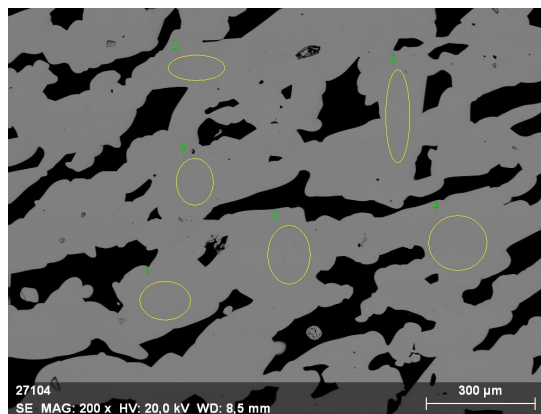


Figure 19. SEM-EDX image of a polished sample of  $Sb_{1-x}Bi_xSeI$  with  $x = 0.8$ .

elemental composition and spatial distribution of the constituent elements. For each sample, SEM-EDX measurements were performed on 6-7 different regions across multiple crystals (Figure 19), and the atomic percentages of each element were calculated by averaging these analyses. The results were consistent across all measured regions and crystals, indicating a homogeneous composition and good compositional uniformity of the samples.

In addition to the SEM-EDX measurements, TEM-EDX analyses were performed on microcrystals of solid solutions. Elemental mapping by TEM-EDX confirmed a uniform distribution of all constituent elements throughout the crystals (Figure 20).

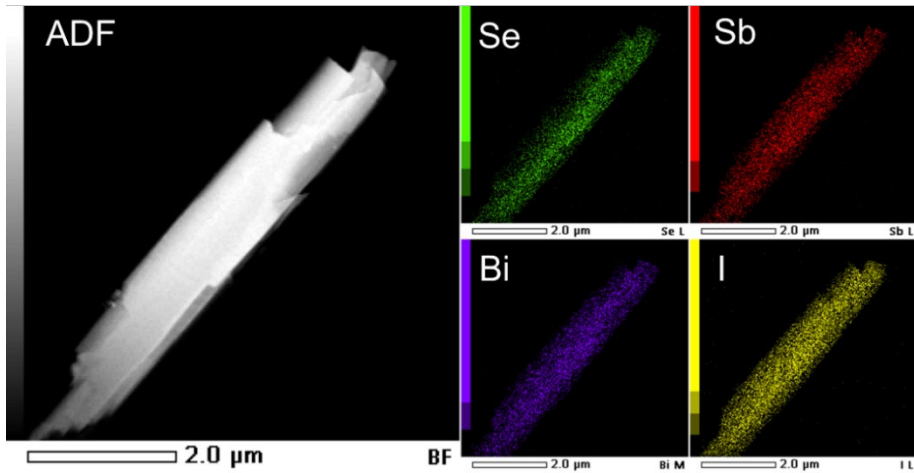


Figure 20. Dark-field STEM image and EDX elemental mapping of  $Sb_{1-x}Bi_xSeI$  with  $x = 0.4$ .

The values reported in Table 3 represent the atomic percentages derived from SEM-EDX and TEM-EDX analyses. In addition, the elemental composition of the solid solutions was investigated by XPS, and these results are also included in Table 3 for comparison. According to the SEM-EDX data, the measured elemental composition is consistent with the nominal stoichiometry of the  $Sb_{1-x}Bi_xSeI$  system, corresponding to a target atomic ratio of (Sb+Bi) : Se : I = 33.33 : 33.33 : 33.33 at% (denoted as “Stoichiometric” in Table 3 for clarity). The TEM-EDX results are consistent with the expected stoichiometric ratio and show good agreement with the SEM-EDX results. However, as the Bi molar fraction increases, discrepancies between SEM-EDX and TEM-EDX measurements become apparent. Specifically, the Bi content measured by TEM-EDX is systematically higher than that obtained by SEM-EDX. This discrepancy can be attributed to the different acceleration voltages used in the two techniques (20 keV for SEM-EDX and 200 keV for TEM-EDX). In particular, SEM-EDX has higher sensitivity to the Bi M-line at 2.3 keV compared to TEM-EDX, which may account for the observed variation in Bi quantification. Consequently, SEM-EDX is considered more reliable for determining Bi content in this system. When considering XPS results, some discrepancies arise between EDX and XPS data due to the fundamentally different probing depths of the techniques. While EDX is bulk-sensitive, XPS probes only the near-surface region (~5-10 nm). Moreover, the quantitative interpretation of XPS data is limited by several factors, including surface geometry effects, uncertainties in peak intensities, the accuracy of relative sensitivity factors, surface volume homogeneity, and potential sample

degradation during analysis. Additional challenges arise from the heterogeneous nature of the polycrystalline samples, local variations in surface composition, and possible surface contamination [101]. Despite these limitations, the XPS data qualitatively confirms the presence of all constituent elements and shows reasonable agreement with the stoichiometric trends observed by EDX. Overall, these results support the proposed elemental composition and confirm the compositional consistency across the solid solution series.

Table 3. EDX elemental composition of  $Sb_{1-x}Bi_xSeI$  ( $x = 0-1$ ) solid solutions determined by SEM-EDX, TEM-EDX, and XPS.

Composition	Method	Sb, at%	Bi, at%	Se, at%	I, at%
SbSeI	SEM-EDX	34.1	-	32.6	33.3
	Stoichiometric	33.33	-	33.33	33.33
$Sb_{0.8}Bi_{0.2}SeI$	SEM-EDX	27.0	6.7	32.7	33.6
	TEM-EDX	27.1	8.4	32.6	31.8
	XPS	28.1	8.3	36.1	27.5
	Stoichiometric	26.67	6.66	33.33	33.33
$Sb_{0.6}Bi_{0.4}SeI$	SEM-EDX	20.5	13.7	31.3	34.5
	TEM-EDX	18.6	17.0	33.6	30.6
	XPS	22.4	17.4	31.7	27.5
	Stoichiometric	20.00	13.33	33.33	33.33
$Sb_{0.4}Bi_{0.6}SeI$	SEM-EDX	13.0	21.1	32.3	33.6
	TEM-EDX	12.3	24.7	32.3	30.6
	XPS	17.8	26.1	29.5	26.6
	Stoichiometric	13.33	20.00	33.33	33.33
$Sb_{0.2}Bi_{0.8}SeI$	SEM-EDX	6.6	27.5	32.5	33.4
	TEM-EDX	6.1	32.9	30.8	30.2
	XPS	7.6	33.3	33.3	25.8
	Stoichiometric	6.66	26.67	33.33	33.33
BiSeI	SEM-EDX	-	34.2	32.6	33.2
	Stoichiometric	-	33.33	33.33	33.33

### 3.2.3 Structural properties of $Sb_{1-x}Bi_xSeI$ microcrystals

The phase composition of  $Sb_{1-x}Bi_xSeI$  solid solutions (Paper III), including the end member BiSeI (Paper II), was investigated by Raman spectroscopy. Raman spectra of  $Sb_{1-x}Bi_xSeI$  ( $x = 0-1$ ) were measured from multiple individual microcrystals and from different regions within each crystal to ensure reproducibility. All spectra were fitted using a Lorentzian function and are presented in Figure 21. The Raman spectrum of SbSeI single crystals is consistent with previously reported data and is in good agreement with that obtained from SbSeI thin films (Figure 15a) (Paper I). The characteristic Raman modes at 95, 115, 137, 167, 187, 209, and 213  $cm^{-1}$  were identified and attributed to SbSeI. Vibrational modes at 95 and 115  $cm^{-1}$  are assigned to Sb-I bonds [44], whereas the highest frequency mode at 209  $cm^{-1}$  ( $\Gamma_{Sb}$ ), observed in both SbSeI single crystals and thin films, corresponds to the Sb-Se vibration [70]. Importantly, the Raman spectrum of SbSeI does not exhibit characteristic peaks of possible secondary phases, such as  $Sb_2Se_3$ , which has a dominant Raman mode at 190  $cm^{-1}$  (Figure 13a) (Paper I), or  $SbI_3$ , characterized by

peaks at 73, 138, and 160  $\text{cm}^{-1}$  [102] [91]. These observations confirm the phase purity of the synthesized SbSel crystals.

The Raman spectrum of BiSel (Figure 21) exhibits its highest frequency mode at 182  $\text{cm}^{-1}$  ( $\Gamma_{Bi}$ ), corresponding to Bi-Se vibrations. Additional Raman peaks were observed at 75, 96, 106, 115, 137, 153, 159, 182, and 186  $\text{cm}^{-1}$ , in good agreement with previous reports [75]. Analogously to SbSel, the low wavenumber modes at 75 and 96  $\text{cm}^{-1}$  are attributed to Bi-I vibrations, while higher wavenumber modes at 153, 159, 182, and 186  $\text{cm}^{-1}$  correspond to Bi-Se vibrations [103–105]. As shown in Figure 21, the substitution of Sb by Bi significantly influences the Raman spectra of the  $\text{Sb}_{1-x}\text{Bi}_x\text{Sel}$  solid-solution series, reflecting systematic changes in the local bonding and vibrational dynamics induced by pnictogen-site substitution.

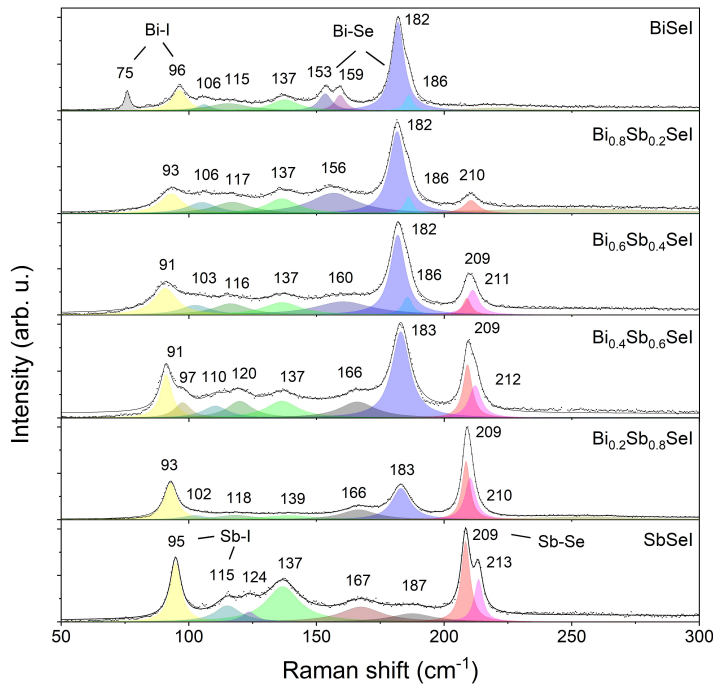


Figure 21. Normalized Raman spectra of  $\text{Sb}_{1-x}\text{Bi}_x\text{Sel}$  ( $x = 0-1$ ) microcrystals with Lorentzian peak fitting.

Variations in Bi content cause systematic changes in the relative intensities of the  $\Gamma_{Sb}$  and  $\Gamma_{Bi}$  vibrational modes. The coexistence of two distinct modes in solid solutions with  $x = 0.2-0.8$ , rather than a single averaged mode, indicates two-mode Raman behavior. This behavior is analogous to that observed in the  $\text{Sb}_{1-x}\text{Bi}_x\text{SI}$  system [74] and has also been reported for  $\text{Sb}_{0.5}\text{Bi}_{0.5}\text{Sel}$  crystals [76]. With increasing Bi content, the relative intensities of the two main Raman modes associated with SbSel and BiSel change systematically (Figure 22a). This monotonic and linear trend ( $m = 0.97$ ) enables the estimation of the content of metal cation composition in the solid solutions with relatively high accuracy ( $R^2 = 0.975$ ) using Raman spectroscopy. To exclude potential effects of microcrystal orientation on the measured spectra, polarization-dependent Raman measurements

were conducted by varying the alignment of individual microcrystals relative to the incident polarized laser beam. The relative intensities of the Bi–Se and Sb–Se main vibrational modes remained constant, confirming that the observed intensity variations are intrinsic and independent of polarization effect (Figure 22b).

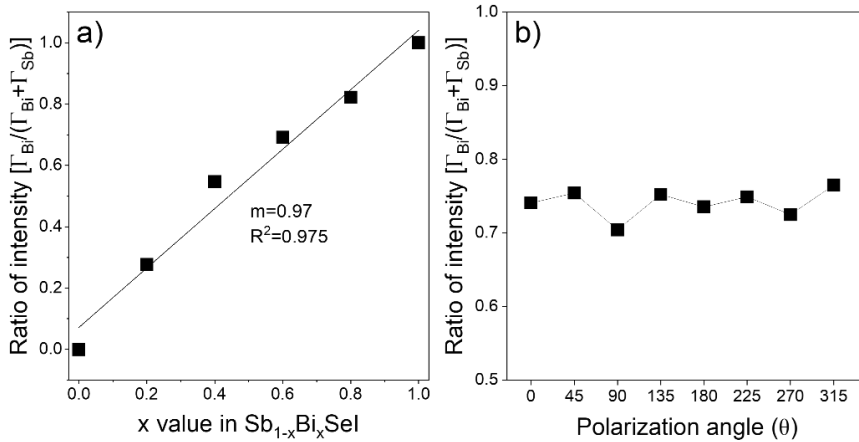


Figure 22. a) Ratio of the intensities of the main Raman peaks corresponding to the Sb–Se ( $209\text{ cm}^{-1}$ ) and Bi–Se ( $182\text{ cm}^{-1}$ ) modes. b) Ratio of the Raman peak intensities corresponding to Bi–Se and Sb–Se bonds as a function of polarization angle.

XRD patterns of the  $\text{Sb}_{1-x}\text{Bi}_x\text{SeI}$  solid solutions (Paper III) are presented in Figure 23a. The measured diffraction patterns were compared with reference data cards of SbSeI (ICSD # 01–076–1354), BiSeI (ICSD # 01–070–4693),  $\text{Sb}_{0.7}\text{Bi}_{0.3}\text{SeI}$  (ICDD # 00–065–0522), and  $\text{Sb}_{0.3}\text{Bi}_{0.7}\text{SeI}$  (ICDD # 00–066–0065). All observed reflections are consistent with the peak positions expected from the corresponding reference data, confirming the formation of single-phase solid solutions across the investigated compositional range. With increasing the Bi content, the diffraction peaks gradually shift toward lower  $2\theta$  angles, reflecting lattice expansion associated with the substitution of smaller  $\text{Sb}^{3+}$  ions by larger  $\text{Bi}^{3+}$  ions. For instance, the (112) reflection shifts from  $29.4^\circ$  for SbSeI to  $28.9^\circ$  for BiSeI (Figure 23b). Similar behavior has been reported for  $\text{BiSb}_{1-x}\text{I}_x$  solid solutions [79]. Differences in relative peak intensities are observed when comparing the experimental XRD patterns with reference data, in particular, the low intensity of the (112) reflection and the dominance of the (301) reflection. This discrepancy can be attributed to preferred orientation effects arising from sample preparation. The microcrystals used in the XRD measurements were not finely ground, instead, they were pressed directly onto the sample holder. Due to their needle-like morphology, the crystallites tend to align parallel to the sample holder, which enhances reflections such as (301) and (101) while suppressing others, including (112). This interpretation is supported by TEM observations, indicating that a significant fraction of the crystallites lies horizontally. In contrast, the SbSeI thin films discussed in Section 3.1 exhibit an intense (112) reflection corresponding to vertically aligned columns (Figure 15b) and consistent with reference data.

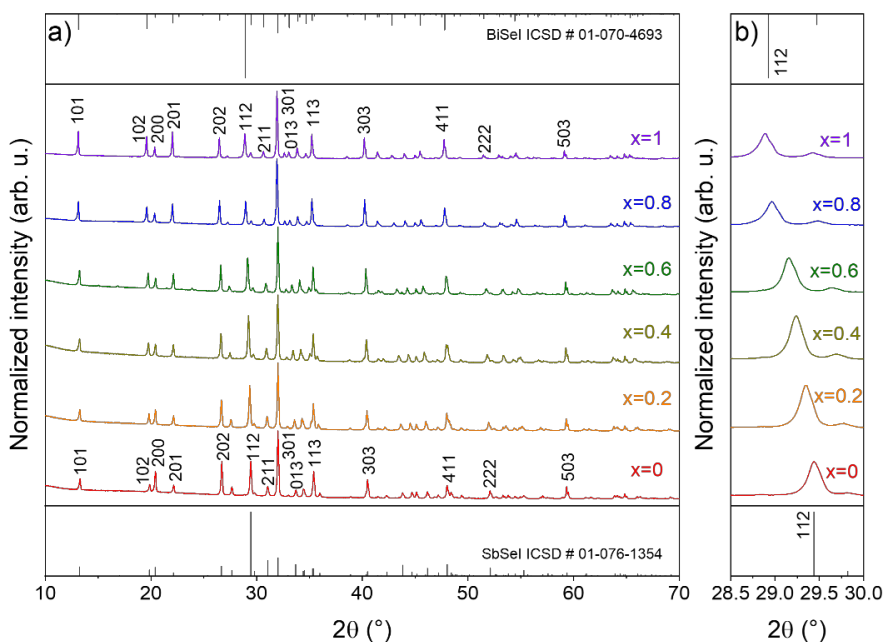


Figure 23. a) XRD pattern of  $Sb_{1-x}Bi_xSe$  ( $x = 0-1$ ) powders. b) The enlarged XRD pattern shows a shift of the distance between (112) planes.

The lattice parameters of  $Sb_{1-x}Bi_xSe$  solid solutions ( $x = 0-1$ ) were calculated from XRD data using PDXL2 Rigaku's software and are presented in Figure 24. All compositions have an orthorhombic crystal structure with space group  $Pnma$ , consistent with the SbSe and BiSe end members. Complete replacement of Sb with Bi results in an approximately 3.4% increase in unit-cell volume, which can be attributed to the larger ionic radius of  $Bi^{3+}$  compared to  $Sb^{3+}$  and is consistent with previous studies [42,71,76]. The lattice expansion is anisotropic: the lattice parameters  $b$  and  $c$  increase systematically with increasing Bi content, while  $a$  remains nearly constant (Figure 24). Both parameters  $b$  and  $c$  follow Vegard's law [106], showing a linear dependence on Bi concentration. SAED measurements for  $Sb_{1-x}Bi_xSe$  solid solutions ( $x = 0.2, 0.4, 0.6, 0.8$ ) are also included in Figure 24. SAED results confirmed the orthorhombic crystal structure and  $Pnma$  space group identified by XRD. Minor discrepancies between the lattice parameters derived from SAED and XRD can be attributed to the different sampling volumes and measurement conditions: SAED probes individual microcrystals, whereas XRD averages over ensembles of ground powder samples. The orthorhombic space group  $Pnma$  was also identified by XRD for BiSe microcrystals (Paper II) and SbSe thin films (Paper I), further supporting the structural consistency across all compositions and morphologies studied in this work.

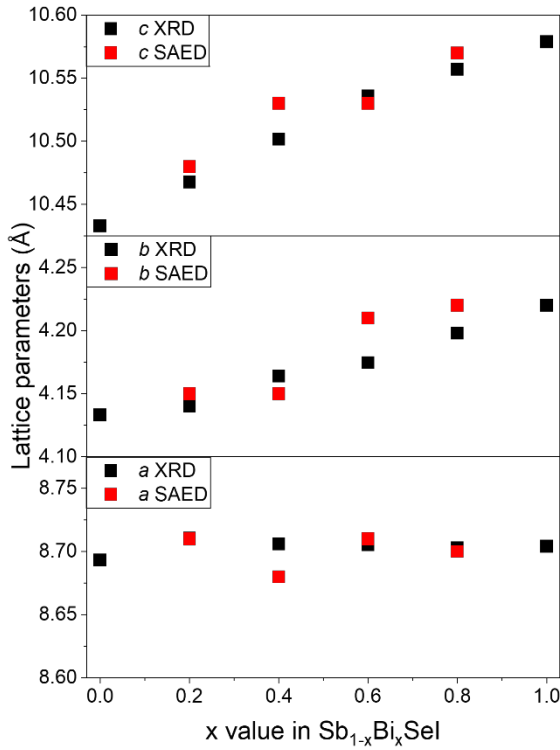


Figure 24. Comparison of lattice parameters obtained from XRD and SAED.

### 3.2.4 Electronic band structure of $\text{Sb}_{1-x}\text{Bi}_x\text{SeI}$

The optical band gap of SbSeI thin films (Paper I), BiSeI microcrystals (Paper II), and  $\text{Sb}_{1-x}\text{Bi}_x\text{SeI}$  ( $x = 0-1$ ) microcrystals (Paper III) was determined experimentally by UV-Vis-NIR diffuse reflectance spectroscopy using the method described in Section 2.3.7. For SbSeI thin films, a direct band gap of 1.72 eV was obtained (Figure 25a) and is in good

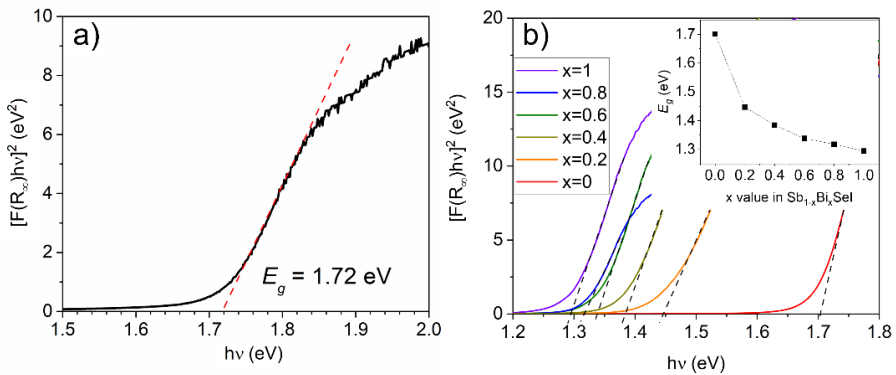


Figure 25. Optical band gap determination from Tauc plots: extrapolation of the linear least squares fit of  $[F(R_{\infty})hv]^2$  vs  $hv$  for a) SbSeI thin films and for b)  $\text{Sb}_{1-x}\text{Bi}_x\text{SeI}$  ( $x = 0-1$ ) microcrystals. Inset graph: Extracted band gap energies.

agreement with literature values [14,71]. For the microcrystalline samples, measurements were performed on pressed microcrystalline powders. The optical band gap of the  $\text{Sb}_{1-x}\text{Bi}_x\text{SeI}$  solid solutions can be continuously tuned by varying the Bi/Sb ratio, with experimentally determined values ranging from 1.70 eV for SbSeI to 1.29 eV for BiSeI (Figure 25b). The measured band gap of BiSeI is consistent with previously reported values [59]. The band gaps for all compositions (including SbSeI thin films) were determined using  $n=1/2$ .

Earlier studies have reported an approximately linear decrease in the band gap with increasing Bi content [77]. However, it should be noted that this study dates back to 1975 and reported results should therefore be interpreted with caution. In contrast, the results obtained in the present work reveal a non-linear dependence of the band gap on composition, indicating the presence of a band gap bowing effect. The composition dependence of the band gap energy can be described by:

$$E_g(x) = xE_g(A) + (1-x)E_g(B) - bx(1-x) \quad (6)$$

where  $x$  represents the Bi content,  $E_g(A)$  and  $E_g(B)$  are the band gap energies of the end member compounds SbSeI and BiSeI, respectively, and  $b$  denotes the band bowing parameter, for which a moderate value of 0.6 eV was calculated. Similar bowing behavior has been reported for other chalcogenide and chalcogenide solid solution systems, including  $\text{Sb}_{1-x}\text{Bi}_x\text{SI}$  [74],  $\text{Sb}_2(\text{S}_x\text{Se}_{1-x})_3$  [107], and  $\text{Ag}_x\text{Cu}_{1-x}\text{GaSe}_2$  [108]. This nonlinear behavior is often attributed to local structural distortions induced by alloying, including atomic displacements, clustering, and/or formation of localized states within the band gap. It may also result from increased SOC when heavier atoms replace lighter ones. More generally, the optical bowing effect in semiconductor alloys is related to differences in atomic electronegativities and internal structural relaxation, i.e., composition-dependent changes in bond lengths and bond angles.

Among the investigated compositions,  $\text{Sb}_{0.4}\text{Bi}_{0.6}\text{SeI}$  exhibits an optical band gap of 1.34 eV (Figure 25b), which is close to the optimum for a single-junction solar cell absorber. In contrast, the wider band gap of 1.7–1.72 eV observed for SbSeI microcrystals and thin films makes this composition more suitable for IPV applications or as a top absorber in tandem solar cell architecture.

To address the limited experimental investigation of the electronic band structure of the (Sb,Bi)SeI system, UPS was used to examine the effect of Bi incorporation and to determine the energy difference between the valence band maximum and the Fermi level ( $E_{VBM}$ ) and the work function ( $\Phi$ ) of the  $\text{Sb}_{1-x}\text{Bi}_x\text{SeI}$  solid solutions. All measurements were carried out on freshly synthesized microcrystals to minimize surface contamination and degradation. The  $\Phi$  was determined from the secondary-electron cutoff energy ( $E_{cutoff}$ ) using He(I) excitation, as described by Equation 7.

$$\Phi = h\nu - E_{cutoff} \quad (7)$$

where  $h\nu$  is the photon energy of the He(I) excitation line (21.21 eV), and  $E_{cutoff}$  corresponds to the secondary-electron cutoff energy. The value of  $E_{cutoff}$  was obtained by linear extrapolation of the high binding energy edge of the UPS spectrum (Figure 26a). The  $\Phi$  is defined as the minimum energy required to remove an electron from the Fermi level ( $E_F$ ) to the vacuum level ( $E_{VAC}$ ) [109]. The energy difference between the valence band maximum and  $E_F$  can be determined by linear fitting of the lower energy site

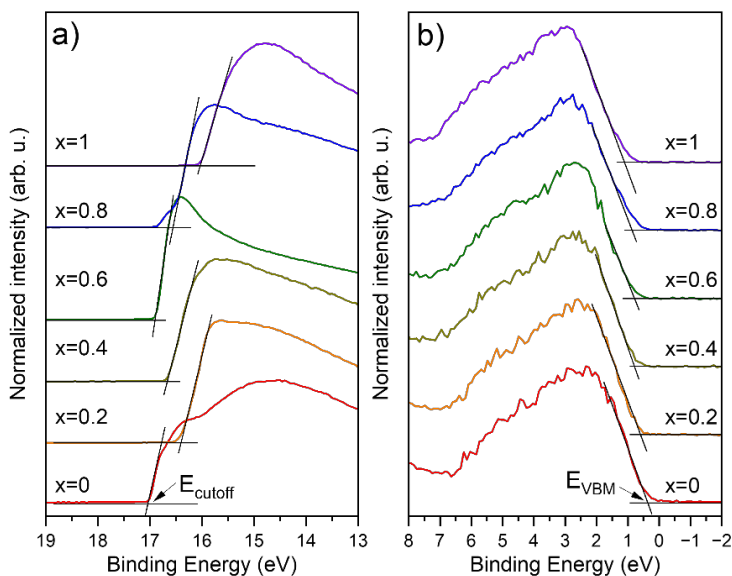


Figure 26. UPS spectra of  $Sb_{1-x}Bi_xSeI$  ( $x = 0-1$ ) shown in the binding energy scale. a) High binding energy region highlighting the secondary electron cutoff. b) Low binding energy region showing the valence band onset used to determine the difference between the valence band maximum and the Fermi level.

of the UPS spectrum (Figure 26b). By combining  $\Phi$  and  $E_{VBM}$  with the optical band gap values obtained from UV-Vis-NIR measurements, the absolute position of the valence band relative to the vacuum level can be estimated, enabling the construction of an experimental energy band diagram for the  $Sb_{1-x}Bi_xSeI$  system (Figure 27).

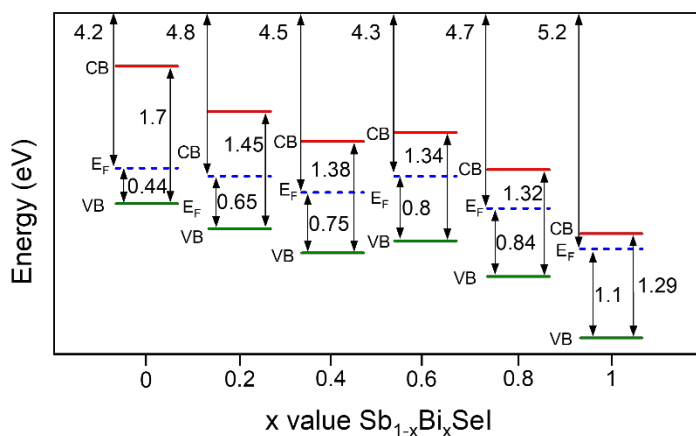


Figure 27. Experimentally determined band diagram of  $Sb_{1-x}Bi_xSeI$  ( $x = 0-1$ ) solid solutions, illustrating the compositional dependence of work function, valence band maximum, and band gap energy.

UPS results show that increasing Bi content in  $Sb_{1-x}Bi_xSeI$  leads to a systematic increase in  $E_{VBM}$  from 0.44 eV to 1.1 eV, consistent with an upward shift of the  $E_F$  toward the

conduction band. A similar composition-dependent shift of  $E_{VBM}$  has been observed in other semiconductor solid solutions, such as CZTSSe [110]. In contrast, the work function does not exhibit a clear dependence on composition and varies between 4.2 and 5.2 eV across the investigated series. A key observation is that UPS-derived band positions suggest a possible transition in conductivity type from  $p$ -type to  $n$ -type at Bi contents between  $x = 0.2$  and  $x = 0.4$ . Although  $n$ -type conductivity has previously been reported for SbSeI [71] and BiSeI [59], the present results indicate that the conductivity type in the (Sb,Bi)SeI system is strongly influenced by composition. Comparable work function and optical band gap values have been reported for SbSeI in [15], although the  $E_{VBM}$  values obtained in that study are considerably lower than those obtained here. While experimental data for BiSeI remain scarce, theoretical calculations predict a comparable band gap (1.29 eV) and  $E_{VBM}$ , which differs by approximately 0.1 eV from the experimental values determined in this work [42].

To further investigate the conductivity type of the  $Sb_{1-x}Bi_xSeI$  solid solutions, SKP measurements were performed for all compositions. The samples were prepared by grinding microcrystals in an agate mortar to obtain a clean and homogeneous surface. Due to the potentially hygroscopic nature of iodine-containing materials, all measurements were conducted immediately after grinding to minimize moisture adsorption. The freshly ground powder was then evenly distributed on a carbon tape mounted on an aluminium substrate and gently flattened with a glass slide to form a smooth and continuous layer, thereby improving measurement accuracy and reproducibility. SKP measurements were carried out under both dark conditions and red laser illumination ( $\lambda = 670$  nm).

Illumination-induced changes in the surface potential arise from photo-generated charge carriers and their redistribution near the surface. The sign and magnitude of the surface photovoltage provide qualitative information about the dominant charge carriers, enabling discrimination between  $p$ -type and  $n$ -type conductivity.

Although the quantitative interpretation of the contact potential difference (CPD) is limited, because the measurements are performed under ambient conditions, this technique provides valuable qualitative insight into the photosensitivity and conductivity type of the materials. All six solid solutions exhibit a clear photosensitive response under red laser illumination (Figure 28). Upon illumination, Sb-rich compositions ( $x = 0-0.4$ ) show increased CPD, while Bi-rich compositions ( $x = 0.6-1$ ) show decreased CPD, revealing a distinct transition across the series from  $p$ -type to  $n$ -type conductivity, with the end members clearly exhibiting  $p$ - and  $n$ -type behavior, respectively, in agreement with UPS results; to our knowledge, this is the first systematic experimental demonstration of this evolution in the (Sb,Bi)SeI system. Based on these observations, Sb-rich compositions are likely to be more suitable PV absorbers in conventional heterojunction architectures employing an  $n$ -type buffer layer, where  $p$ -type absorber behavior is advantageous for junction formation and carrier-selective collection. However,  $n$ -type compositions could still be viable in inverted device architecture with appropriate contact and buffer-layer selection.

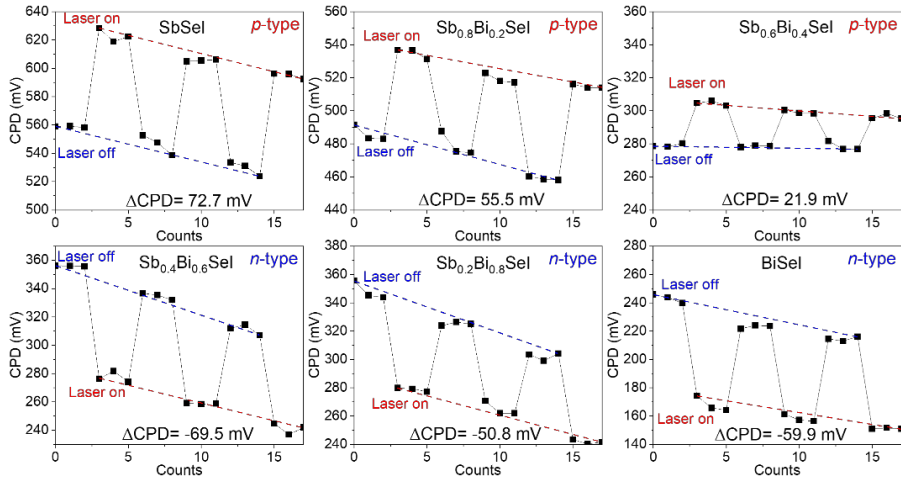


Figure 28. CPD of  $Sb_{1-x}Bi_xSe$  ( $x = 0-1$ ) measured under dark and illuminated conditions using the SKP technique.

### 3.3 Defect study of the (Sb,Bi)Se system

Although the defect physics of pnictogen chalcogenides has been investigated through first-principles calculations, experimental investigations remain limited, as discussed in Section 1.7. In particular, the defect structure and associated recombination mechanisms in (Sb,Bi)Se systems, including the end members SbSe and BiSe, have not been systematically investigated experimentally. This section presents a comprehensive PL study of SbSe thin films (Paper I) and BiSe microcrystals (Paper II), with the aim of identifying dominant radiative recombination pathways and correlating them with possible intrinsic defect states. RT-PL measurements have been performed on  $Sb_{1-x}Bi_xSe$  solid solutions (Paper III).

#### 3.3.1 Photoluminescence study of SbSe thin films

The defect structure of SbSe thin films prepared from  $\alpha-Sb_2Se_3$  precursors (annealed at 250 °C for 5 min) was investigated by RT-PL, temperature- and excitation power-dependent PL spectroscopy. At RT, SbSe exhibits a single broad, asymmetric emission band with a maximum at 1.67 eV (Figure 29). The spectrum was fitted using a Split Voigt function, confirming the presence of one dominant emission peak.

At RT, electron-phonon interactions lead to thermal broadening, and thermally activated non-radiative processes reduce PL intensity, making individual transitions difficult to resolve. In particular, the luminescence yield of transitions involving localized states decreases with increasing temperature due to thermal emission of trapped carriers into the conduction or valence band (thermal quenching). As a result, impurity- and defect-related transitions can become weak at RT. Therefore, low-temperature PL measurements are performed to suppress thermal quenching and reduce broadening, allowing impurity-related recombination mechanisms that are not visible at RT to be clearly resolved.

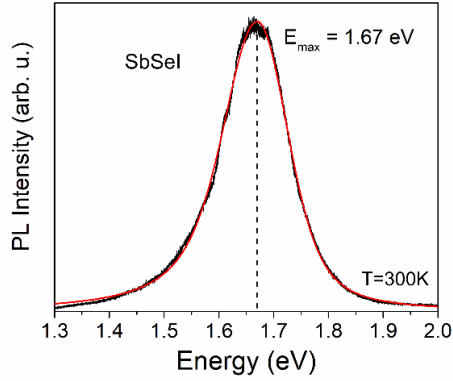


Figure 29. RT-PL spectrum of the Sb<sub>2</sub>Se<sub>3</sub> thin film (black line). Experimental data was fitted using the Split Voigt function (red line).

Figure 30a shows the temperature-dependent PL spectra recorded in the range of 10–80 K. At low temperatures, a broad and asymmetric emission band centered at ~1.4 eV is observed. A decrease in PL intensity is observed near 1.32 eV; however, this originates from the absorption of water vapor and complicates the precise determination of the peak position at higher temperatures. Temperature-dependent measurements show rapid thermal quenching of the PL band (Figure 30a).

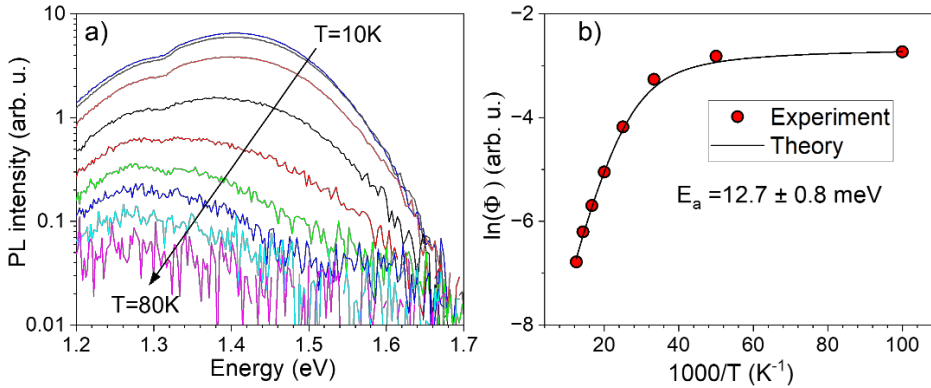


Figure 30. a) Temperature dependence of the deep PL band of the Sb<sub>2</sub>Se<sub>3</sub> thin film. b) Temperature dependence of integral intensity, the fitting result with Eq. 8 is given as a black curve.

The Arrhenius plot shown in Figure 30b presents the natural logarithm of the integrated PL intensity ( $\ln\Phi$ ) as a function of  $1000/T$ , where  $T$  is the absolute temperature. The data were fitted using a theoretical model describing recombination via discrete defect levels [111]:

$$\Phi(T) = \Phi_0 / (1 + \alpha_1 T^{3/2} + \alpha_2 T^{3/2} \exp(-E_a/kT)) \quad (8)$$

where  $\Phi$  is the integrated PL intensity,  $\alpha_1$  and  $\alpha_2$  are process rate parameters,  $E_a$  is the thermal activation energy, and  $k$  is the Boltzmann constant. An activation energy of  $12.7 \pm 0.8$  meV was obtained. This relatively small thermal activation energy explains the rapid quenching of the PL band with increasing temperature. Comparison of the low-

temperature PL peak position ( $T = 8$  K) with the RT band gap energy of SbSeI ( $E_g = 1.72$  eV) shows that the PL emission occurs significantly below the band edge. The extracted activation energy suggests that the 1.4 eV emission band originates from recombination involving deep donor–deep acceptor (DD–DA) pairs [112,113], similar to the mechanism reported for polycrystalline Sb<sub>2</sub>Se<sub>3</sub> [97].

The emission energy from a donor-acceptor pair separated by a distance  $r$  can be described by [114]:

$$h\nu_{max} = E_g - (E_A^0 + E_D^0) + \frac{e^2}{4\pi\epsilon_0\epsilon r} \quad (9)$$

where  $E_g$  is the band gap energy,  $E_A^0$  and  $E_D^0$  are the ionization energies of the acceptor and donor, respectively,  $\epsilon_0$  is the vacuum permittivity,  $\epsilon$  is the static dielectric constant, and  $r$  is the distance between the donor and acceptor.

The final term in Equation 9 describes the Coulomb interaction between donor and acceptor defects. This contribution becomes significant only at short distances. Therefore, radiative recombination occurs predominantly between closely spaced pairs, where sufficient overlap of the electron and hole wave functions is possible. When single acceptor and donor defect levels are coupled, they tend to shift closer to the band boundaries, resulting in a reduced thermal activation energy. As reported in [115], DD–DA recombination typically shows an approximately linear dependence of PL intensity on excitation power. This behavior is consistent with the experimental results observed in the present study.

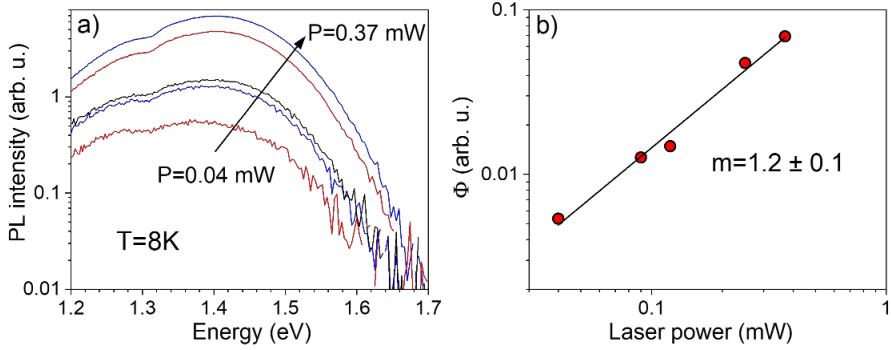


Figure 31. a) Laser power dependence of the deep PL band of the SbSeI thin film. b) Integral PL intensity versus laser power. The fitting result is given as a black line.

Figure 31a shows the excitation power-dependent PL spectra measured at low temperature (8 K). Increasing the excitation power results in a slight blueshift of the PL band. Figure 31b presents the integrated PL intensity as a function of excitation power. According to the power law, the integrated PL intensity  $\Phi$  is proportional to  $P^m$ , where  $P$  is the excitation power and the exponent  $m$  provides information about the recombination mechanism associated with the PL band. Fitting the experimental data yields  $m = 1.2 \pm 0.1$ . Values close to unity are commonly associated with excitonic or band-to-band (BB) emissions [116]. However, the DD–DA model has been proposed in the case of Cu<sub>2</sub>ZnSnS<sub>4</sub>, where values of  $m$  close to 1 have been reported [115].

### 3.3.2 Photoluminescence study of $\text{Sb}_{1-x}\text{Bi}_x\text{SeI}$ microcrystals

The evolution of radiative recombination processes across the  $\text{Sb}_{1-x}\text{Bi}_x\text{SeI}$  ( $x = 0-1$ ) solid solution series was investigated by RT-PL spectroscopy. The objective was to determine how Bi incorporation influences PL emission behavior.

RT-PL spectra of  $\text{Sb}_{1-x}\text{Bi}_x\text{SeI}$  ( $x = 0-1$ ) solid solutions exhibit a single asymmetric emission band for all compositions (Figure 32a). The band shape is characteristic of BB recombination. The high-energy side of the emission band is governed by the Fermi distribution, while the low-energy side is dominated by the DOS function.

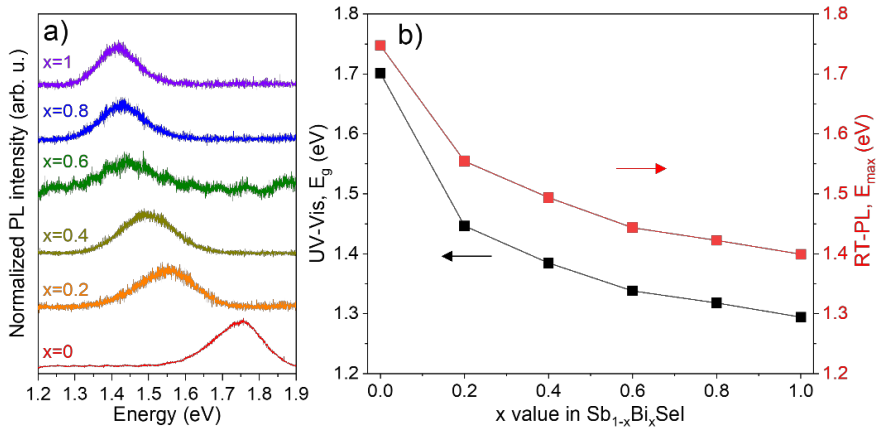


Figure 32. a) RT-PL spectra of  $\text{Sb}_{1-x}\text{Bi}_x\text{SeI}$  ( $x = 0-1$ ) microcrystals; b)  $E_g$  values (black squares) along with the maximum emission energy ( $E_{max}$ ) from PL spectra (red squares) for  $\text{Sb}_{1-x}\text{Bi}_x\text{SeI}$  ( $x = 0-1$ ) microcrystals.

The PL peak maxima were determined by fitting the spectra using Split Pseudo-Voigt functions. The position of the PL maximum shifts systematically toward lower energies with increasing Bi content (Figure 32b, red squares), decreasing from 1.75 eV for SbSeI to 1.41 eV for BiSeI. The PL maxima obtained for the end members is in good agreement with the values reported by Nielsen in [85]. This compositional dependence closely follows the variation of the optical band gap determined from diffuse reflectance measurements (Figure 32b, black squares). Both the PL peak position and the band gap energy exhibit a non-linear dependence on Bi concentration, confirming the presence of band gap bowing in the  $\text{Sb}_{1-x}\text{Bi}_x\text{SeI}$  system.

Although the PL peak energy tracks the band gap trend, a noticeable offset between the maximum emission and the optical band gap is observed. This offset increases with Bi content, from approximately 0.05 eV for SbSeI to about 0.11 eV for BiSeI. The increasing difference suggests enhanced band tailing and defect-related broadening as Bi concentration increases. This behavior has been observed in different semiconductors [117,118] and is commonly associated with alloy-induced disorder, which can introduce localized states and modify the defect landscape.

### 3.3.3 Photoluminescence study of BiSeI microcrystals

The PL properties of BiSeI microcrystals were investigated to elucidate the dominant radiative recombination mechanisms and identify possible defect-related transitions. Both RT and low-temperature PL measurements were performed.

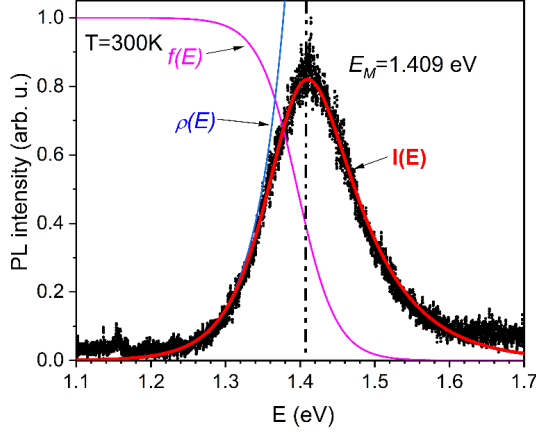


Figure 33. RT-PL spectrum of BiSeI microcrystal. The spectrum is fitted using the product of a Fermi distribution (magenta line) and the density of states function (blue line). The fitting result is given as a red line.

The RT-PL spectrum of BiSeI microcrystals (Paper II) is shown in Figure 33. The spectrum exhibits a single asymmetric emission band. The PL intensity remains relatively low even at high laser power densities ( $\sim 13 \text{ kW cm}^{-2}$ ). The laser power density was limited to avoid possible sample modification during the measurements. The shape of the PL band is characterized by a steeper slope on the low-energy side and a more gradual decay on the high-energy side. This asymmetric profile is typical of BB recombination influenced by band tail states. The high-energy side of the emission is determined by the Fermi distribution function:

$$f(E) = [1 + \exp((E - E_F)/kT_c)]^{-1} \quad (10)$$

where  $E_F$  is the Fermi energy and  $T_c$  the carrier temperature. The low-energy side is determined by the DOS near the band edge [119–121]. The nearly exponential shape of the low-energy side suggests the presence of Urbach tail states, indicating a relatively high density of localized defect states. In this case, the DOS function can be described as:

$$\rho(E) = \rho_0 \exp[(E - E_g)/E_U] \quad (11)$$

where  $E_g$  is the band gap energy,  $E_U$  is the characteristic Urbach energy that describes the extent of the Urbach tail density of localized defect states in the gap, and  $\rho_0$  is an amplitude factor [119]. To model the RT emission band, the product of the Fermi distribution and the exponential DOS function was used:

$$I(E) = f(E) * \rho(E) \quad (12)$$

In Figure 33, the Fermi function is shown as a continuous pink line, the DOS function as a blue continuous line, and their product  $I(E)$  as a continuous red line, which fits the experimental spectrum well.

The best fit was obtained using the following parameters:  $E_F = 1.396 \text{ eV}$ ,  $E_g = 1.336 \text{ eV}$ , and  $E_U = 41 \text{ meV}$ . The peak position of the BB-band is located at  $E_M = 1.409 \text{ eV}$ . Although the maximum of the BB band shifts with temperature and excitation power, it is still

commonly employed to estimate the band gap energy,  $E_g$ . In this case, the BB emission peak lies at slightly higher energy than the band gap obtained from diffuse reflectance measurements (Section 3.2.4). This shift is attributed to the relatively high excitation power of the laser used during the PL measurements.

Since the DOS near the band edge may be more complex than assumed in the simplified model, the estimation of  $E_g$  from the shape of the BB band should be treated with caution. Nevertheless, the extracted RT band gap value (1.336 eV) is close to the theoretically calculated value of 1.31 eV [84]. The band gap energy determined from the RT-PL measurements is approximately 46 meV higher than that obtained from reflectance measurements. This difference can be explained by filling of band edge states at high excitation power, where band-edge states become partially occupied, leading to a blueshift of the emission peak. A similar excitation-induced blueshift of the BB band has been reported by Fang *et al.* [122].

Low-temperature PL spectra of BiSeI microcrystals measured at  $T = 8$  K reveal four distinct emission peaks. The experimental spectra and corresponding fits are shown in Figure 34. Using an InGaAs photomultiplier tube (PMT) detector, two prominent bands at 0.903 eV and 1.108 eV were detected. Measurements performed with an R632 detector, which is sensitive in the visible-near-infrared (400–1200 nm) spectral range, revealed two additional but much weaker bands. All observed bands were fitted using Gaussian functions except the H-band, which was fitted using the asymmetric double sigmoidal function.

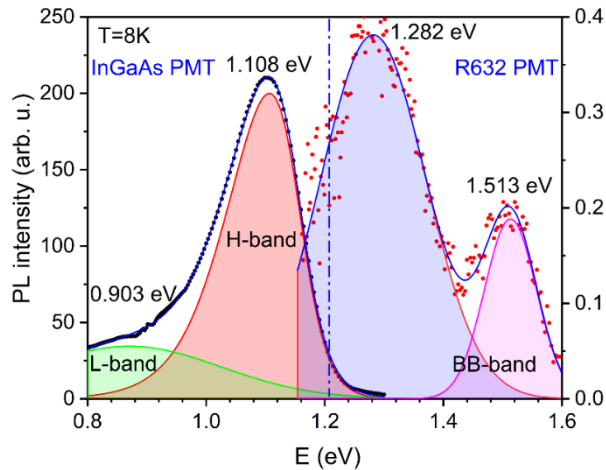


Figure 34. Low temperature PL spectra of BiSeI microcrystals. Near band edge spectra were measured with an R632 PMT, while deep PL bands were measured with an InGaAs PMT. Solid lines present the fitting of the experimental data.

The highest-energy PL band located at 1.513 eV closely matches the theoretical band gap value of  $E_g = 1.52$  eV at  $T = 0$  K reported in [84]. Therefore, this band is attributed to a BB recombination. Using the RT band gap value of  $E_g = 1.336$  eV and the temperature dependence of the band gap described in [123], a low-temperature band gap of approximately 1.52 eV is obtained, further supporting this assignment. Because the PL bands detected with the R632 PMT were weak, a more detailed analysis was not possible, and the origin of the band at 1.282 eV remains unclear.

In contrast, the two bands detected with the InGaAs PMT are significantly more intense. These bands, located at 1.108 eV and 0.903 eV, are referred to as the H-band and L-band, respectively. Due to its asymmetric shape, the H-band was fitted using a double sigmoidal function, while the L-band, which is weaker and more symmetric, was fitted with a Gaussian function.

Figure 35a and 35b present the laser power- and temperature-dependent PL spectra measured with the InGaAs PMT detector. Due to their higher intensity, only the H- and L-bands are observed in these measurements. The shape of both bands, as well as the peak position of the H-band, remains unchanged with increasing laser power (Figure 35a), indicating that the underlying recombination mechanism does not vary with excitation density.

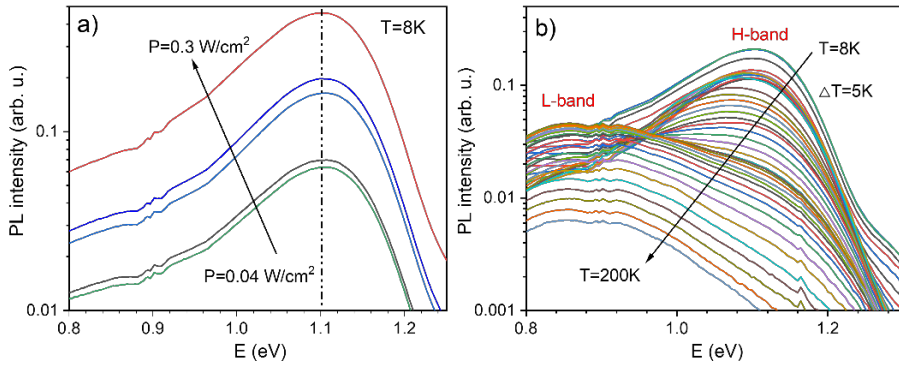


Figure 35. a) Laser power dependence and b) temperature dependence of PL spectra of the BiSeI microcrystals.

Temperature-dependent PL measurements show that the H-band dominates at low temperatures, while the L-band becomes dominant at higher temperatures. This behavior suggests different thermal quenching characteristics for the two bands. Figure 36 shows the Arrhenius plots for the integrated PL intensity for both bands. The high-temperature region was fitted using

$$\Phi = \Phi_0 / [1 + C \exp(E_a/kT)] \quad (13)$$

where  $E_a$  is a thermal activation energy,  $\phi$  is the integral intensity, and  $C$  is a fitting constant. The extracted activation energies are similar for both bands. However, the H-band exhibits more rapid quenching, indicating a larger value of  $C$ . The parameter  $C$  is proportional to the probability of electronic transition from a localized donor level to a delocalized band, and a higher value of  $C$  results in faster PL quenching [111]. The obtained values are  $7.8 \cdot 10^6$  for the H-band and  $2.2 \cdot 10^5$  for the L-band. These differences suggest that the two emissions involve different donor defects of DD–DA pairs.

The peak positions of both deep PL bands are distant from the band gap energy. Conventional recombination via distant donor-acceptor pairs involving Urbach tail states can be excluded, as the extracted  $E_a$  values are relatively low and no peak shift is observed with increasing excitation power. Similar behavior has been reported in other semiconductor compounds, where recombination between discrete deep levels has been identified as the dominant mechanism. The temperature and laser power dependencies of both bands suggest that both bands originate from DD–DA complexes.

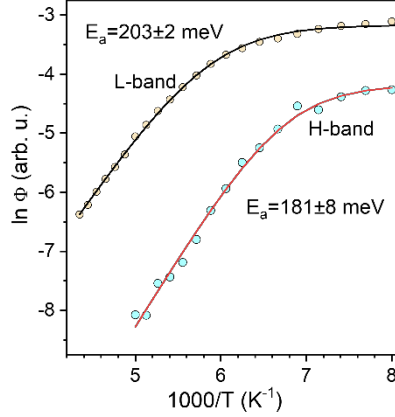


Figure 36. Arrhenius plots derived from the temperature dependence of PL spectra together with the obtained thermal activation energy values ( $E_a$ ).

The DD–DA recombination model was originally proposed to explain deep-level PL bands in CdTe [113] and has since been applied to various chalcopyrite semiconductors [112,124,125]. In this mechanism, the electron and hole wave functions are localized in deep levels, and radiative recombination occurs primarily between closely spaced donor-acceptor pairs. The emission energy of a donor-acceptor pair separated by a distance  $r$  is given by [112]:

$$E(r) = E_g - (E_A^0 + E_D^0) + \frac{e^2}{\epsilon r} - \Gamma(r) \quad (14)$$

where  $E_A^0$  and  $E_D^0$  are ionization energies of the acceptor and donor, respectively,  $\epsilon$  is the dielectric constant, and  $\Gamma(r)$  refers to interactions that are only important at extremely short distances. As shown by Williams [114], for extremely short donor-acceptor distances, the magnitude of  $\Gamma(r)$  may be greater than or equal to 25 meV.

Consequently, the Coulomb energy estimated theoretically is typically slightly larger than the experimentally observed recombination energy. Although the precise value of the dielectric constant in BiSeI is unknown, estimates place it at approximately 35 [92]. Considering the shortest lattice distance in BiSeI (Bi-Se bond length of 2.74 Å [42]), the Coulomb term is estimated to be on the order of 150 meV. This value supports the possibility of strong Coulomb interaction between closely spaced defect pairs.

Several defects may occur in BiSeI, including antisites ( $I_{Se}$ ,  $Se_{Bi}$ ,  $I_{Bi}$ ,  $Se_I$ ,  $Bi_{Se}$ , and  $Bi_I$ ), vacancies ( $V_I$ ,  $V_{Se}$ , and  $V_{Bi}$ ), and interstitials ( $Bi_I$ ,  $Se_I$ ,  $I_I$ ) [84]. Although experimental studies on defect states in BiSeI remain limited, theoretical calculations by Ganose *et al.* [84] provide insight into their formation energies and electronic levels. The PL results obtained in this work suggest that both the H-band and L-band may be associated with the same deep acceptor defect with an activation energy of  $\sim 0.2$  eV. The weak edge emission band at 1.282 eV is also most likely associated with the same acceptor defect. According to theoretical predictions, a bismuth vacancy ( $V_{Bi}$ ) is a plausible candidate for this deep acceptor level. In contrast, the donor states involved in the H- and L-band transitions are likely different, indicating distinct DD–DA pairs. Possible donor candidates include  $Se_{Bi}$  antisites and interstitial  $I_I$  defects. However, further experimental and

theoretical studies are required to determine the exact origin of the DD defects. Based on these findings, a radiative recombination model for BiSel microcrystals is proposed in Figure 37.

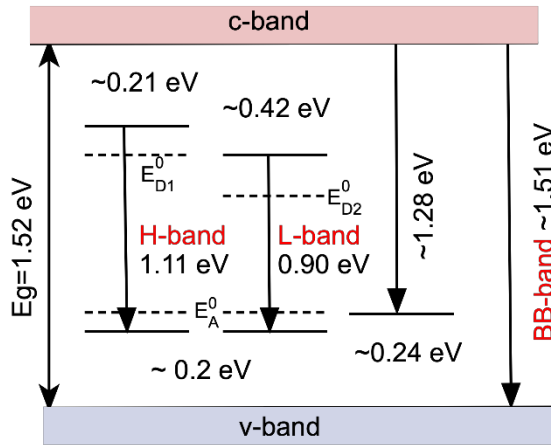


Figure 37. Radiative recombination model for BiSel microcrystal at  $T = 8$  K.

In summary, this work provides the first comprehensive low-temperature PL investigation of SbSel-based materials, revealing a broad asymmetric emission in SbSel thin films centered at  $\sim 1.4$  eV and identifying DD–DA pair recombination with a low thermal quenching activation energy of  $12.7 \pm 0.8$  meV. For the first time, Bi incorporation effects were systematically examined, showing a non-linear red shift of the RT-PL maximum from 1.75 eV (SbSel) to 1.41 eV (BiSel), consistent with band gap evolution. Most notably, detailed low-temperature PL analysis of BiSel microcrystals uncovers a previously unreported complex defect landscape with four distinct emission bands, including BB recombination at 1.51 eV and dominant deep-level DD–DA transitions involving a common deep acceptor, likely  $V_{Bi}$ , with multiple donor states such as  $Se_{Bi}$  antisites or  $I_i$  interstitials. These findings establish new insight into defect-assisted recombination mechanisms in pnictogen chalcogenides. Importantly, the relative concentration of dominant defects involved in the identified DD–DA pairs can be tuned through synthesis conditions and compositional engineering. For instance, Bi-poor growth conditions are expected to favor the formation of  $V_{Bi}$  acceptors, whereas Bi-rich conditions can suppress their formation. Adjusting towards certain compositions may reduce the density of deep-level defects and shift the defect landscape to more benign, shallower states. Suppressed recombination losses are expected to increase carrier lifetimes and overall PV performance.

## Conclusions

The aim of this thesis was to experimentally investigate the structural, optical, electronic, and defect-related properties of heavy pnictogen chalcogenides and to address key gaps in their fundamental understanding. This work demonstrates clear processing-structure-property relationships in  $\text{Sb}_{1-x}\text{Bi}_x\text{SeI}$ , showing that their optoelectronic properties can be systematically tuned through controlled synthesis and compositional engineering, while these properties are also determined by intrinsic defect states. The most important findings and resulting conclusions of this work are summarized as follows:

- Processing conditions were identified as the key factor controlling the formation of high-quality SbSeI thin films. It was established that iodization of amorphous  $\text{Sb}_2\text{Se}_3$  at 250 °C for 5 minutes enables the formation of dense and compact SbSeI layers with predominantly vertically oriented crystallites. These findings provide a clear pathway for controlled thin-film growth and directly address the challenges associated with achieving highly oriented SbSeI absorbers. The formation of a single-phase orthorhombic SbSeI thin film with a direct band gap of 1.72 eV confirms the intrinsic suitability of this material as a PV absorber, particularly in tandem and IPV applications.
- The  $\text{Sb}_{1-x}\text{Bi}_x\text{SeI}$  system was demonstrated to be a compositionally tunable semiconductor material. Raman analysis showed that the relative intensities of Sb–Se and Bi–Se vibrational modes enable reliable determination of the Sb/Bi ratio in  $\text{Sb}_{1-x}\text{Bi}_x\text{SeI}$  solid solutions, providing a novel and practical method for compositional analysis. A nonlinear band gap reduction from 1.7 eV to 1.29 eV confirms effective band gap engineering, with  $\text{Sb}_{0.4}\text{Bi}_{0.6}\text{SeI}$  ( $E_g = 1.34$  eV) emerging as a near-optimal composition for single-junction PV applications. With increasing Bi content, a systematic shift of the Fermi level from the valence band maximum toward the conduction band was observed, consistent with the transition from *p*-type to *n*-type conductivity. This confirms that charge carrier type and electronic structure can be controlled through alloying.
- PL analysis demonstrated that radiative recombination in SbSeI and BiSeI is dominated by deep defect-assisted processes. In SbSeI thin films, a broad and asymmetric PL band at 1.67 eV at RT, while low-temperature (8 K) measurements revealed a dominant emission band at 1.4 eV. The large energy separation from the band edge, together with a low thermal quenching activation energy ( $12.7 \pm 0.8$  meV), indicates that this emission originates from DD–DA recombination.
- BiSeI exhibits a more complex defect landscape, with four distinct emission bands at low temperatures. The H-band (0.903 eV) and L-band (1.108 eV) are attributed to DD–DA recombination, while the emission at 1.282 eV corresponds to a deep defect level with an ionization energy of 240 meV. These three bands are associated with a deep acceptor defect ( $V_{\text{Bi}}$ ).  $\text{Se}_{\text{Bi}}$  antisites and interstitial  $\text{I}_i$  defects are proposed as possible deep donor defects contributing to the H- and L-bands. A higher-energy band at  $\sim 1.51$  eV is attributed to BB recombination.

In conclusion, this study provides new insight into how the interplay of synthesis parameters, material composition, and defects influences the behavior of heavy pnictogen chalcogenides. The results highlight that the optoelectronic properties of  $\text{Sb}_{1-x}\text{Bi}_x\text{SeI}$  can be effectively tuned through compositional control. Overall, this work advances the fundamental understanding of these materials and underlines the importance of precise material design strategies for their integration into next-generation PV and optoelectronic devices.

## References

- [1] International Energy Agency, Electricity Mid-Year Update 2025, (2025). [www.iea.org](http://www.iea.org) (accessed February 26, 2026).
- [2] The long march of electrification | Ember, (n.d.). <https://ember-energy.org/latest-insights/the-long-march-of-electrification/> (accessed February 26, 2026).
- [3] International Energy Agency, Global EV Outlook 2025, (2025). [www.iea.org](http://www.iea.org) (accessed February 26, 2026).
- [4] World Meteorological Organization, International Renewable Energy Agency, 2024 Year in Review: Climate-driven Global Renewable Energy Resources and Energy Demand, (2025).
- [5] S. Chen, Data centres will use twice as much energy by 2030 — driven by AI, *Nature* (2025). <https://doi.org/10.1038/d41586-025-01113-z>.
- [6] International Energy Agency, Renewables 2025, (2025). [www.iea.org](http://www.iea.org) (accessed February 26, 2026).
- [7] Fraunhofer Institute for Solar Energy Systems ISE, Photovoltaics Report, (2025).
- [8] M. Fan, Z. Yu, W. Ma, L. Li, Life Cycle Assessment of Crystalline Silicon Wafers for Photovoltaic Power Generation, *Silicon* 13 (2021) 3177–3189. <https://doi.org/10.1007/s12633-020-00670-4>.
- [9] C. Zhang, N.-G. Park, Materials and methods for cost-effective fabrication of perovskite photovoltaic devices, *Commun. Mater.* 5 (2024) 194. <https://doi.org/10.1038/s43246-024-00636-8>.
- [10] M.A. Green, E.D. Dunlop, M. Yoshita, N. Kopidakis, K. Bothe, G. Siefer, X. Hao, J.Y. Jiang, Solar Cell Efficiency Tables (Version 66), *Progress in Photovoltaics: Research and Applications* 33 (2025) 795–810. <https://doi.org/10.1002/pip.3919>.
- [11] M. Abulikemu, J. Barbé, A. El Labban, J. Eid, S. Del Gobbo, Planar heterojunction perovskite solar cell based on CdS electron transport layer, *Thin Solid Films* 636 (2017) 512–518. <https://doi.org/10.1016/j.tsf.2017.07.003>.
- [12] R.E. Brandt, V. Stevanović, D.S. Ginley, T. Buonassisi, Identifying defect-tolerant semiconductors with high minority-carrier lifetimes: beyond hybrid lead halide perovskites, *MRS Commun.* 5 (2015) 265–275. <https://doi.org/10.1557/mrc.2015.26>.
- [13] R. Nie, M. Hu, A.M. Risqi, Z. Li, S. Il Seok, Efficient and Stable Antimony Seleniodide Solar Cells, *Advanced Science* 8 (2021) 1–8. <https://doi.org/10.1002/advs.202003172>.
- [14] A.C. Wibowo, C.D. Malliakas, Z. Liu, J.A. Peters, M. Sebastian, D.Y. Chung, B.W. Wessels, M.G. Kanatzidis, Photoconductivity in the Chalcogenide Semiconductor, SbSeI: a New Candidate for Hard Radiation Detection, *Inorg. Chem.* 52 (2013) 7045–7050. <https://doi.org/10.1021/ic401086r>.
- [15] Y.C. Choi, K.-W. Jung, One-Step Solution Deposition of Antimony Seleniodide Films via Precursor Engineering for Lead-Free Solar Cell Applications, *Nanomaterials* 11 (2021) 3206. <https://doi.org/10.3390/nano11123206>.
- [16] U. V. Ghorpade, M.P. Suryawanshi, M.A. Green, T. Wu, X. Hao, K.M. Ryan, Emerging Chalcogenide Materials for Energy Applications, *Chem. Rev.* 123 (2023) 327–378. <https://doi.org/10.1021/acs.chemrev.2c00422>.

- [17] E. Fatuzzo, G. Harbeke, W.J. Merz, R. Nitsche, H. Roetschi, W. Ruppel, Ferroelectricity in SbSI, *Physical Review* 127 (1962) 2036–2037. <https://doi.org/10.1103/PhysRev.127.2036>.
- [18] R. Nitsche, H. Roetschi, P. Wild, NEW FERROELECTRIC V. VI. VII COMPOUNDS OF THE SbSI TYPE, *Appl. Phys. Lett.* 4 (1964) 210–211. <https://doi.org/10.1063/1.1753944>.
- [19] R. Nitsche, W.J. Merz, Photoconduction in ternary V-VI-VII compounds, *Journal of Physics and Chemistry of Solids* 13 (1960) 154–155. [https://doi.org/10.1016/0022-3697\(60\)90136-0](https://doi.org/10.1016/0022-3697(60)90136-0).
- [20] Y. Sasaki, Photoconductivity of a Ferroelectric Photoconductor BiSI, *Jpn. J. Appl. Phys.* 4 (1965) 614. <https://doi.org/10.1143/JJAP.4.614>.
- [21] D. Berlincourt, H. Jaffe, W.J. Merz, R. Nitsche, PIEZOELECTRIC EFFECT IN THE FERROELECTRIC RANGE IN SbSI, *Appl. Phys. Lett.* 4 (1964) 61–63. <https://doi.org/10.1063/1.1753963>.
- [22] J.F. Alward, C.Y. Fong, M. El-Batanouny, F. Wooten, Electronic and optical properties of SbSBr, SbSI and SbSeI, *Solid State Commun.* 25 (1978) 307–310. [https://doi.org/10.1016/0038-1098\(78\)90964-X](https://doi.org/10.1016/0038-1098(78)90964-X).
- [23] B. Peng, K. Xu, H. Zhang, Z. Ning, H. Shao, G. Ni, J. Li, Y. Zhu, H. Zhu, C.M. Soukoulis, 1D SbSeI, SbSI, and SbSBr with High Stability and Novel Properties for Microelectronic, Optoelectronic, and Thermoelectric Applications, *Adv. Theory Simul.* 1 (2018) 1–7. <https://doi.org/10.1002/adts.201700005>.
- [24] K. Li, Y. Gao, Z. Dong, H. Zhang, X. Fan, L. Xu, J. Huang, F. Teng, H. Fan, J. Song, C. Zhang, X. He, P. Hu, SbSeI for high-efficient photocatalytic degradation of multiple pollutants, *Environ. Res.* 263 (2024) 120209. <https://doi.org/10.1016/j.envres.2024.120209>.
- [25] M.D. Ali, M. Jesionek, A. Starczewska, T. Zeeshan, M. Zubko, Doping-induced structural and electrical modifications in SbSI nanowires embedded in graphene oxide for enhanced optoelectronic applications, *J. Alloys Compd.* 1043 (2025) 184183. <https://doi.org/10.1016/j.jallcom.2025.184183>.
- [26] P. Govindaraj, K. Venugopal, Intrinsic ultra-low lattice thermal conductivity in orthorhombic BiSI: An excellent thermoelectric material, *J. Alloys Compd.* 929 (2022) 167347. <https://doi.org/10.1016/j.jallcom.2022.167347>.
- [27] G. Xiong, T. Liu, H. Huang, J. Wang, Thermoelectric properties of Janus BiXI (X = S and Se) monolayers: A first-principles study, *J. Appl. Phys.* 136 (2024). <https://doi.org/10.1063/5.0221109>.
- [28] D. Tiwari, F. Cardoso-Delgado, D. Alibhai, M. Mombrú, D.J. Fermín, Photovoltaic Performance of Phase-Pure Orthorhombic BiSI Thin-Films, *ACS Appl. Energy Mater.* 2 (2019) 3878–3885. <https://doi.org/10.1021/acsaem.9b00544>.
- [29] I. Caño, A. Navarro-Güell, E. Maggi, A. Gon Medaille, D. Rovira, A. Jimenez-Arguijo, O. Segura, A. Torrens, M. Jimenez, C. López, P. Benítez, C. Cazorla, Z. Jehl, Y. Gong, J. Asensi, L. Calvo-Barrio, L. Soler, J. Llorca, J. Tamarit, B. Galiana, M. Dimitrievska, N. Ruiz-Marín, H.Z. Chun, L. Wong, J. Puigdollers, M. Placidi, E. Saucedo, Ribbons of Light: Emerging (Sb,Bi)(S,Se)(Br,I) Van der Waals Chalcogenides for Next-Generation Energy Applications, *Small* 21 (2025) 1–23. <https://doi.org/10.1002/sml.202505430>.
- [30] C. Zhou, R. Wang, C. Jiang, J. Chen, G. Wang, Dynamically Optimized Multi-interface Novel BiSI-Promoted Redox Sites Spatially Separated n–p–n Double Heterojunctions BiSI/MoS<sub>2</sub>/CdS for Hydrogen Evolution, *Ind. Eng. Chem. Res.* 58 (2019) 7844–7856. <https://doi.org/10.1021/acs.iecr.9b00234>.

- [31] P. Kwolek, K. Pilarczyk, T. Tokarski, J. Mech, J. Irzmański, K. Szaciłowski, Photoelectrochemistry of *n*-type antimony sulfoiodide nanowires, *Nanotechnology* 26 (2015) 105710. <https://doi.org/10.1088/0957-4484/26/10/105710>.
- [32] M. Tamilselvan, A.J. Bhattacharyya, Antimony sulfoiodide (SbSI), a narrow band-gap non-oxide ternary semiconductor with efficient photocatalytic activity, *RSC Adv.* 6 (2016) 105980–105987. <https://doi.org/10.1039/C6RA23750A>.
- [33] B. Toroń, P. Szperlich, M. Nowak, A. Sobota, M.J. Kłos, S. Krawiec, W. Matysiak, Toward Self-Powered Sensors for Traffic Monitoring and Energy Harvesting – Comparison of Different SbSI-Based Nanocomposites, *ECS Sensors Plus* 4 (2025) 032601. <https://doi.org/10.1149/2754-2726/adfb8d>.
- [34] S. Ahmed, M.A. Gondal, A.S. Alzahrani, M. Parvaz, A. Ahmed, S. Hussain, Recent Trends and Challenges in Lead-Free Perovskite Solar Cells: A Critical Review, *ACS Appl. Energy Mater.* 7 (2024) 1382–1397. <https://doi.org/10.1021/acsaem.3c02327>.
- [35] N.T. Hahn, A.J.E. Rettie, S.K. Beal, R.R. Fullon, C.B. Mullins, n-BiSI Thin Films: Selenium Doping and Solar Cell Behavior, *The Journal of Physical Chemistry C* 116 (2012) 24878–24886. <https://doi.org/10.1021/jp3088397>.
- [36] R. Nie, H. Yun, M. Paik, A. Mehta, B. Park, Y.C. Choi, S. Il Seok, Efficient Solar Cells Based on Light-Harvesting Antimony Sulfoiodide, *Adv. Energy Mater.* 8 (2018) 1–7. <https://doi.org/10.1002/aenm.201701901>.
- [37] M. Nowak, B. Kauch, P. Szperlich, Determination of energy band gap of nanocrystalline SbSI using diffuse reflectance spectroscopy, *Review of Scientific Instruments* 80 (2009) 21–24. <https://doi.org/10.1063/1.3103603>.
- [38] R. Nie, J. Im, S. Il Seok, Efficient Solar Cells Employing Light-Harvesting  $\text{Sb}_{0.67}\text{Bi}_{0.33}\text{SI}$ , *Advanced Materials* 31 (2019) 1–8. <https://doi.org/10.1002/adma.201808344>.
- [39] W. Shockley, H.J. Queisser, Detailed Balance Limit of Efficiency of p-n Junction Solar Cells, *J. Appl. Phys.* 32 (1961) 510–519. <https://doi.org/10.1063/1.1736034>.
- [40] S. Rühle, Tabulated values of the Shockley–Queisser limit for single junction solar cells, *Solar Energy* 130 (2016) 139–147. <https://doi.org/10.1016/j.solener.2016.02.015>.
- [41] R. Bai, B. Xiao, F. Li, X. Liu, S. Xi, M. Zhu, W. Jie, B.-B. Zhang, Y. Xu, Growth of bismuth- and antimony-based chalcogenide single crystals by the physical vapor transport method, *CrystEngComm* 24 (2022) 1094–1099. <https://doi.org/10.1039/D1CE01602D>.
- [42] A.M. Ganose, K.T. Butler, A. Walsh, D.O. Scanlon, Relativistic electronic structure and band alignment of BiSI and BiSeI: candidate photovoltaic materials, *J. Mater. Chem. A Mater.* 4 (2016) 2060–2068. <https://doi.org/10.1039/C5TA09612J>.
- [43] Y.C. Choi, R. Nie, Heavy pnictogen chalcogenides for efficient, stable, and environmentally friendly solar cell applications, *Nanotechnology* 34 (2023) 142001. <https://doi.org/10.1088/1361-6528/acb05d>.
- [44] S.K. Balakrishnan, P.C. Parambil, L. Houben, M. Asher, O. Yaffe, E. Edri, Revealing hidden phases and self-healing in antimony trichalcogenides and chalcogenides, *Cell Rep. Phys. Sci.* 4 (2023) 101298. <https://doi.org/10.1016/j.xcrp.2023.101298>.
- [45] Y. Zhou, L. Wang, S. Chen, S. Qin, X. Liu, J. Chen, D.-J. Xue, M. Luo, Y. Cao, Y. Cheng, E.H. Sargent, J. Tang, Thin-film  $\text{Sb}_2\text{Se}_3$  photovoltaics with oriented one-dimensional ribbons and benign grain boundaries, *Nat. Photonics* 9 (2015) 409–415. <https://doi.org/10.1038/nphoton.2015.78>.

- [46] Z. Li, X. Liang, G. Li, H. Liu, H. Zhang, J. Guo, J. Chen, K. Shen, X. San, W. Yu, R.E.I. Schropp, Y. Mai, 9.2%-efficient core-shell structured antimony selenide nanorod array solar cells, *Nat. Commun.* 10 (2019) 125. <https://doi.org/10.1038/s41467-018-07903-6>.
- [47] G. Spaggiari, F. Pattini, D. Bersani, D. Calestani, A. De Iacovo, E. Gilioli, F. Mezzadri, A. Sala, G. Trevisi, S. Rampino, Growth and structural characterization of  $\text{Sb}_2\text{Se}_3$  solar cells with vertical  $\text{Sb}_4\text{Se}_6$  ribbon alignment by RF magnetron sputtering, *J. Phys. D Appl. Phys.* 54 (2021) 385502. <https://doi.org/10.1088/1361-6463/ac0eb5>.
- [48] K. Li, R. Tang, C. Zhu, T. Chen, Critical Review on Crystal Orientation Engineering of Antimony Chalcogenide Thin Film for Solar Cell Applications, *Advanced Science* 11 (2024) 1–21. <https://doi.org/10.1002/advs.202304963>.
- [49] Y.-D. Luo, R. Tang, S. Chen, J.-G. Hu, Y.-K. Liu, Y.-F. Li, X.-S. Liu, Z.-H. Zheng, Z.-H. Su, X.-F. Ma, P. Fan, X.-H. Zhang, H.-L. Ma, Z.-G. Chen, G.-X. Liang, An effective combination reaction involved with sputtered and selenized Sb precursors for efficient  $\text{Sb}_2\text{Se}_3$  thin film solar cells, *Chemical Engineering Journal* 393 (2020) 124599. <https://doi.org/10.1016/j.cej.2020.124599>.
- [50] Y.C. Choi, E. Hwang, Controlled Growth of BiSI Nanorod-Based Films through a Two-Step Solution Process for Solar Cell Applications, *Nanomaterials* 9 (2019) 1650. <https://doi.org/10.3390/nano9121650>.
- [51] Z.S. Aliev, S.S. Musaeva, D.M. Babanly, A.V. Shevelkov, M.B. Babanly, Phase diagram of the Sb–Se–I system and thermodynamic properties of SbSeI, *J. Alloys Compd.* 505 (2010) 450–455. <https://doi.org/10.1016/j.jallcom.2010.06.103>.
- [52] U. Petasch, H. Go, È.H. Oppermann, È. Das, Untersuchungen zum quasibina È ren System  $\text{Bi}_2\text{Se}_3/\text{BiI}_3$ , 624 (1998). [https://doi.org/10.1002/\(SICI\)1521-3749\(1998110\)624](https://doi.org/10.1002/(SICI)1521-3749(1998110)624).
- [53] Д.П. Белоцкий, В.Ф. Лапшин, Р.Ф. Бойчук, Система  $\text{Bi}_2\text{Se}_3\text{—BiI}_3$ , *Неорганические Материалы* 7 (1971) 1936–1938.
- [54] И. Д. Туряница, М. П. Заячковский, Н. Ф. Заячковская, К. И. И., Выращивание кристаллов BiSeI методом стокбаргера, *Неорганические Материалы* 10 (1974) 1884–1885.
- [55] Dong-Woon Shin, Seung-Cheol Hyun, Sang-an Park, Yoeng-Geun Kim, Chang-dae Kim, Wha-Tek Kim, Optical properties of undoped and Ni-doped VA-VIA-VIIA single crystals, *Journal of Physics and Chemistry of Solids* 55 (1994) 825–830. [https://doi.org/10.1016/0022-3697\(94\)90006-X](https://doi.org/10.1016/0022-3697(94)90006-X).
- [56] W.-T. Kim, Optical properties of undoped and cobalt-doped  $\text{I}_B\text{-Ga-IV}_A\text{-Se}_4$  single crystals, *Phys. Rev. B* 44 (1991) 8667–8671. <https://doi.org/10.1103/PhysRevB.44.8667>.
- [57] J. Horák, K. Čermák, Preparation and photoelectric properties of bismuth sulphidiodide, *Czechoslovak Journal of Physics* 15 (1965) 536–538. <https://doi.org/10.1007/BF01689287>.
- [58] R. Sereika, Š. Varnagiris, M. Urbonavičius, R. Žaltauskas, D. Milčius, Synthesis and properties of quasi-one-dimensional BiSBr crystals via the Bridgman-Stockbarger technique, *J. Cryst. Growth* 643 (2024) 127816. <https://doi.org/10.1016/j.jcrysgro.2024.127816>.
- [59] B. Xiao, M. Zhu, L. Ji, B.-B. Zhang, J. Dong, J. Yu, Q. Sun, W. Jie, Y. Xu, Centimeter size BiSeI crystal grown by physical vapor transport method, *J. Cryst. Growth* 517 (2019) 7–11. <https://doi.org/10.1016/j.jcrysgro.2019.04.003>.

- [60] R. Ganesha, D. Arivuoli, P. Ramasamy, Growth of some group V-VI-VII compounds from the vapour, *J. Cryst. Growth* 128 (1993) 1081–1085. [https://doi.org/10.1016/S0022-0248\(07\)80101-1](https://doi.org/10.1016/S0022-0248(07)80101-1).
- [61] M. Nowak, B. Kauch, P. Szperlich, M. Jesionek, M. Kępińska, Ł. Bober, J. Szala, G. Moskal, T. Rzychoń, D. Stróż, Sonochemical preparation of SbSeI gel, *Ultrason. Sonochem.* 16 (2009) 546–551. <https://doi.org/10.1016/j.ultsonch.2009.01.003>.
- [62] B. Toroń, W. Matysiak, A. Starczewska, J. Dec, P. Szperlich, M. Nowak, Electrospun Fabrication of 1–3-Type PVP/SbSI and PVP/SbSeI Nanocomposites with Excellent Piezoelectric Properties for Nanogenerators and Sensors, *Energies (Basel)*. 18 (2025) 5506. <https://doi.org/10.3390/en18205506>.
- [63] L. Zhu, X. Zheng, X. Yin, X. Liu, Y. Jia, Y. Xie, A Mild Solution Route to Bismuth Seleniodide Rod-like Crystals, *Chem. Lett.* 32 (2003) 350–351. <https://doi.org/10.1246/cl.2003.350>.
- [64] W.J. Fa, P.J. Li, Y.G. Zhang, L.L. Guo, J.F. Guo, F.L. Yang, The Competitive Growth of BiOI and BiSI in the Solvothermal Process, *Adv. Mat. Res.* 236–238 (2011) 1919–1922. <https://doi.org/10.4028/www.scientific.net/AMR.236-238.1919>.
- [65] L.-N. Fan, K. Han, Q. Lu, H.-J. Zhang, Y. Tian, W.-J. Gong, Two-dimensional Janus BiXY (X = Se, Te; Y I, Br, Cl) for photocatalytic water splitting, *Int. J. Hydrogen Energy* 150 (2025) 150113. <https://doi.org/10.1016/j.ijhydene.2025.150113>.
- [66] Y. Chen, G. Tian, T. Feng, W. Zhou, Z. Ren, T. Han, Y. Xiao, H. Fu, Single-crystalline Bi<sub>19</sub>Br<sub>3</sub>S<sub>27</sub> nanorods with an efficiently improved photocatalytic activity, *CrystEngComm* 17 (2015) 6120–6126. <https://doi.org/10.1039/C5CE00952A>.
- [67] Z. Wu, Y. Liu, S. Zhang, Z. Huang, Q. Jiang, T. Zhou, J. Hu, Biomimetic structure design and construction of cactus-like MoS<sub>2</sub>/Bi<sub>19</sub>Cl<sub>3</sub>S<sub>27</sub> photocatalysts for efficient hydrogen evolution, *J. Mater. Chem. A Mater.* 6 (2018) 21404–21409. <https://doi.org/10.1039/C8TA08834A>.
- [68] S.Z.M. Murtaza, P. Vaqueiro, Rapid synthesis of chalcogenides by ball milling: Preparation and characterisation of BiSI and BiSeI, *J. Solid State Chem.* 291 (2020) 121625. <https://doi.org/10.1016/j.jssc.2020.121625>.
- [69] R. Nie, S. Il Seok, Efficient Antimony-Based Solar Cells by Enhanced Charge Transfer, *Small Methods* 4 (2020) 1–10. <https://doi.org/10.1002/smt.201900698>.
- [70] S.K. Balakrishnan, P.C. Parambil, E. Edri, Mechanistic Insight into the Topotactic Transformation of Trichalcogenides to Chalcogenides, *Chemistry of Materials* 34 (2022) 3468–3478. <https://doi.org/10.1021/acs.chemmater.2c00306>.
- [71] I. Caño, A. Navarro-Güell, E. Maggi, M. Barrio, J.-L. Tamarit, S. Svatek, E. Antolín, S. Yan, E. Barrena, B. Galiana, M. Placidi, J. Puigdollers, E. Saucedo, SbSeI and SbSeBr micro-columnar solar cells by a novel high pressure-based synthesis process, *J. Mater. Chem. A Mater.* 11 (2023) 17616–17627. <https://doi.org/10.1039/D3TA03179A>.
- [72] C. López, I. Caño, D. Rovira, P. Benítez, J.M. Asensi, Z. Jehl, J. Tamarit, E. Saucedo, C. Cazorla, Machine-Learning Aided First-Principles Prediction of Earth-Abundant Pnictogen Chalcogenide Solid Solutions for Solar-Cell Devices, *Adv. Funct. Mater.* 34 (2024) 1–14. <https://doi.org/10.1002/adfm.202406678>.
- [73] J.T.S. Thakshila Jayawardane, D. Hu, P.K.W. Abeygunawardhana, G. Asha, Tuning of Optoelectronic Properties of Chalcogenides by Tailoring Pnictogen Composition for Sustainable Photovoltaics, *Adv. Theory Simul.* 8 (2025) 1–7. <https://doi.org/10.1002/adts.202500104>.

- [74] R.A. Groom, A. Jacobs, M. Cepeda, R. Drummey, S.E. Latturmer, Structural and Optical Properties of Sb-Substituted BiSI Grown from Sulfur/Iodine Flux, *Inorg. Chem.* 56 (2017) 12362–12368. <https://doi.org/10.1021/acs.inorgchem.7b01839>.
- [75] G. Kanchana, D. Arivuoli, Spectroscopic investigation of BiSeI, SbSeI compounds and BiSbS<sub>x</sub>Se<sub>1-x</sub> solid solutions, *Indian Journal of Engineering and Materials Sciences* 8 (2001) 373–376.
- [76] R. Sereika, R. Žaltauskas, S. Bandaru, F. Liu, A. Čerškus, Two-transition behavior in Bi<sub>0.5</sub>Sb<sub>0.5</sub>SeI crystals, *Journal of Physics and Chemistry of Solids* 154 (2021) 110031. <https://doi.org/10.1016/j.jpcs.2021.110031>.
- [77] Д. П. Белоцкий, Н.В. Гавриленко, Д.М. Катеринюк, Я.И. Кушнир, В.Ф. Лапшин, И.Б. Моик., Фотопроводимость и оптические свойства кристаллов и пленок SbSeI–BiSeI, *Неорганические Материалы* 9 (1973) 1142–1145.
- [78] Л. Віскунець, Л. Піскач, І. Олексеюк, Г. Яковлюк, Система SbSeI–BiSeI, *Науковий Вісник Східноєвропейського Національного Університету Імені Лесі Українки. Хімічні Науки* 24 (2013) 22–24.
- [79] H. Kunioku, M. Higashi, R. Abe, Low-Temperature Synthesis of Bismuth Chalcogenides: Candidate Photovoltaic Materials with Easily, Continuously Controllable Band gap, *Sci. Rep.* 6 (2016) 32664. <https://doi.org/10.1038/srep32664>.
- [80] A. Audzijonis, L. Žigas, A. Kvedaravičius, R. Žaltauskas, The experimental and theoretical investigation of vibration spectra in ferroelectric semiconductor SbSBr<sub>x</sub>I<sub>1-x</sub> crystals, *Physica B Condens. Matter* 404 (2009) 3941–3946. <https://doi.org/10.1016/j.physb.2009.07.162>.
- [81] S. Hwang, T. Yasuda, Indoor photovoltaic energy harvesting based on semiconducting π-conjugated polymers and oligomeric materials toward future IoT applications, *Polym. J.* 55 (2023) 297–316. <https://doi.org/10.1038/s41428-022-00727-8>.
- [82] Z. Ran, X. Wang, Y. Li, D. Yang, X.-G. Zhao, K. Biswas, D.J. Singh, L. Zhang, Bismuth and antimony-based oxyhalides and chalcogenides as potential optoelectronic materials, *NPJ Comput. Mater.* 4 (2018) 14. <https://doi.org/10.1038/s41524-018-0071-1>.
- [83] K.T. Butler, S. McKechnie, P. Azarhoosh, M. van Schilfgaarde, D.O. Scanlon, A. Walsh, Quasi-particle electronic band structure and alignment of the V-VI-VII semiconductors SbSI, SbSBr, and SbSeI for solar cells, *Appl. Phys. Lett.* 108 (2016). <https://doi.org/10.1063/1.4943973>.
- [84] A.M. Ganose, S. Matsumoto, J. Buckeridge, D.O. Scanlon, Defect Engineering of Earth-Abundant Solar Absorbers BiSI and BiSeI, *Chemistry of Materials* 30 (2018) 3827–3835. <https://doi.org/10.1021/acs.chemmater.8b01135>.
- [85] R.S. Nielsen, Á.L. Álvarez, A.G. Medaille, I. Caño, A. Navarro-Güell, C.L. Álvarez, C. Cazorla, D.R. Ferrer, Z.J. Li-Kao, E. Saucedo, M. Dimitrievska, Parallel exploration of the optoelectronic properties of (Sb,Bi)(S,Se)(Br,I) chalcogenides, *J. Mater. Chem. A Mater.* 13 (2025) 31727–31739. <https://doi.org/10.1039/D5TA05011A>.
- [86] E. Właźlak, A. Blachecki, M. Bisztyga-Szklarz, S. Klejna, T. Mazur, K. Mech, K. Pilarczyk, D. Przyczyna, M. Suchecki, P. Zawal, K. Szaciłowski, Heavy pnictogen chalcogenides: the synthesis, structure and properties of these rediscovered semiconductors, *Chemical Communications* 54 (2018) 12133–12162. <https://doi.org/10.1039/C8CC05149F>.

- [87] H. Jin, E. Debroye, M. Keshavarz, I.G. Scheblykin, M.B.J. Roeffaers, J. Hofkens, J.A. Steele, It's a trap! On the nature of localised states and charge trapping in lead halide perovskites, *Mater. Horiz.* 7 (2020) 397–410. <https://doi.org/10.1039/C9MH00500E>.
- [88] M. Huang, Z. Zheng, Z. Dai, X. Guo, S. Wang, L. Jiang, J. Wei, S. Chen, DASP: Defect and Dopant ab-initio Simulation Package, *Journal of Semiconductors* 43 (2022) 042101. <https://doi.org/10.1088/1674-4926/43/4/042101>.
- [89] R.E. Brandt, J.R. Poindexter, P. Gorai, R.C. Kurchin, R.L.Z. Hoye, L. Nienhaus, M.W.B. Wilson, J.A. Polizzotti, R. Sereika, R. Žaltauskas, L.C. Lee, J.L. MacManus-Driscoll, M. Bawendi, V. Stevanović, T. Buonassisi, Searching for “Defect-Tolerant” Photovoltaic Materials: Combined Theoretical and Experimental Screening, *Chemistry of Materials* 29 (2017) 4667–4674. <https://doi.org/10.1021/acs.chemmater.6b05496>.
- [90] S.D. Stranks, G.E. Eperon, G. Grancini, C. Menelaou, M.J.P. Alcocer, T. Leijtens, L.M. Herz, A. Petrozza, H.J. Snaith, Electron-Hole Diffusion Lengths Exceeding 1 Micrometer in an Organometal Trihalide Perovskite Absorber, *Science* (1979). 342 (2013) 341–344. <https://doi.org/10.1126/science.1243982>.
- [91] T. Ablekim, J.N. Duenow, C.L. Perkins, J. Moseley, X. Zheng, T. Bidaud, B. Frouin, S. Collin, M.O. Reese, M. Amarasinghe, E. Colegrove, S. Johnston, W.K. Metzger, Exceeding 200 ns Lifetimes in Polycrystalline CdTe Solar Cells, *Solar RRL* 5 (2021) 2100173. <https://doi.org/10.1002/solr.202100173>.
- [92] H. Shi, W. Ming, M.-H. Du, Bismuth chalcogenides and oxyhalides as optoelectronic materials, *Phys. Rev. B* 93 (2016) 104108. <https://doi.org/10.1103/PhysRevB.93.104108>.
- [93] C. López, S.R. Kavanagh, P. Benítez, E. Saucedo, A. Walsh, D.O. Scanlon, C. Cazorla, Chalcogen Vacancies Rule Charge Recombination in Pnictogen Chalcogenide Solar-Cell Absorbers, *ACS Energy Lett.* 10 (2025) 3562–3569. <https://doi.org/10.1021/acsenergylett.5c01267>.
- [94] J.O. Adegite, Post Deposition Thermal Treatment of Sputtered Antimony Selenide Thin Films, master's thesis, 2019.
- [95] A. Escobedo Morales, E. Sánchez Mora, U. Pal, Use of diffuse reflectance spectroscopy for optical characterization of unsupported nanostructures, *Revista Mexicana de Física S* 53 (2007) 18–22.
- [96] G.D. Gesesse, A. Gomis-Berenguer, M.-F. Barthe, C.O. Ania, On the analysis of diffuse reflectance measurements to estimate the optical properties of amorphous porous carbons and semiconductor/carbon catalysts, *J. Photochem. Photobiol. A Chem.* 398 (2020) 112622. <https://doi.org/10.1016/j.jphotochem.2020.112622>.
- [97] M. Grossberg, O. Volobujeva, A. Penezko, R. Kaupmees, T. Raadik, J. Krustok, Origin of photoluminescence from antimony selenide, *J. Alloys Compd.* 817 (2020) 152716. <https://doi.org/10.1016/j.jallcom.2019.152716>.
- [98] A. Shongalova, M.R. Correia, B. Vermang, J.M. V. Cunha, P.M.P. Salomé, P.A. Fernandes, On the identification of Sb<sub>2</sub>Se<sub>3</sub> using Raman scattering, *MRS Commun.* 8 (2018) 865–870. <https://doi.org/10.1557/mrc.2018.94>.
- [99] A. Kumar, V. Kumar, A. Romeo, C. Wiemer, G. Mariotto, Raman Spectroscopy and In Situ XRD Probing of the Thermal Decomposition of Sb<sub>2</sub>Se<sub>3</sub> Thin Films, *The Journal of Physical Chemistry C* 125 (2021) 19858–19865. <https://doi.org/10.1021/acs.jpcc.1c05047>.

- [100] M. Hovhannisyanyan, Synthesis and characterization of (Bi,Sb)SeI thin films, bachelor's thesis, 2024.
- [101] J.F. Moulder, W.F. Stickle, P.E. Sobol, K.D. Bomben, Handbook of X-ray Photoelectron Spectroscopy, Perkin-Elmer Corporation, Physical Electronics Division, 1992.
- [102] Z. Li, S. Chen, F. Tian, S. Fang, Q. Li, M. Du, B. Yuan, L. Kang, L. Zhang, B. Liu, Photoelectric properties surge driven by molecular-ionic crystal transition in layered antimony triiodide under high pressure, *Acta Mater.* 278 (2024) 120263. <https://doi.org/10.1016/j.actamat.2024.120263>.
- [103] L. Xu, M. Yang, Q. Lu, Y. Ren, Y. Chen, J. Guo, M. Cai, X. Miao, F. Teng, H. Fan, C. Zhang, X. He, P. Hu, 2D BiSeI Nanosheets for Broadband Self-Powered Photoelectrochemical Photodetector, *Physica Status Solidi (RRL) – Rapid Research Letters* 18 (2024) 1–9. <https://doi.org/10.1002/pssr.202300183>.
- [104] H. Hu, W. Zhen, Z. Yue, R. Niu, F. Xu, W. Zhu, K. Jiao, M. Long, C. Xi, W. Zhu, C. Zhang, A mixed-dimensional quasi-1D BiSeI nanowire-2D GaSe nanosheet p–n heterojunction for fast response optoelectronic devices, *Nanoscale Adv.* 5 (2023) 6210–6215. <https://doi.org/10.1039/D3NA00525A>.
- [105] Y. Li, S. Wang, J. Hong, N. Zhang, X. Wei, T. Zhu, Y. Zhang, Z. Xu, K. Liu, M. Jiang, H. Xu, Polarization-Sensitive Photodetector Based on High Crystallinity Quasi-1D BiSeI Nanowires Synthesized via Chemical Vapor Deposition, *Small* 19 (2023) 1–9. <https://doi.org/10.1002/sml.202302623>.
- [106] A.R. Denton, N.W. Ashcroft, Vegard's law, *Phys. Rev. A (Coll. Park)*. 43 (1991) 3161–3164. <https://doi.org/10.1103/PhysRevA.43.3161>.
- [107] E.A. Rueda Pérez, E. Regalado-Pérez, A. Cerdán-Pasarán, R.G. Avilez García, N.R. Mathews, Sb<sub>2</sub>(S<sub>x</sub>Se<sub>1-x</sub>)<sub>3</sub> thin films by electrodeposition: Role of deposition potential on the formation of the solid solution and photovoltaic performance via device simulation, *Current Applied Physics* 47 (2023) 44–53. <https://doi.org/10.1016/j.cap.2022.12.011>.
- [108] V. V. Rakitin, M. V. Gapanovich, D.S. Lutsenko, V.B. Nazarov, A. V. Stanchik, V.F. Gremenok, A. V. Kabyliatski, Studying the Effect of Composition on the Crystal Structure, Optical Properties, and Photogenerated Current Carriers Lifetimes in Ag<sub>x</sub>Cu<sub>1-x</sub>GaSe<sub>2</sub> (0 ≤ x ≤ 1) Solid Solutions, *High Energy Chemistry* 58 (2024) 492–498. <https://doi.org/10.1134/S0018143924700474>.
- [109] J.W. Kim, A. Kim, Absolute work function measurement by using photoelectron spectroscopy, *Current Applied Physics* 31 (2021) 52–59. <https://doi.org/10.1016/j.cap.2021.07.018>.
- [110] T. Olar, I. Lauermann, H. Xie, M. Neuschitzer, E. Saucedo, W. Calvet, A. Steigert, B. Ümsür, B. Chacko, V. Parvan, M. Gorgoi, B. Senkovskiy, M.C. Lux-Steiner, Assessment of Chemical and Electronic Surface Properties of the Cu<sub>2</sub>ZnSn(SSe)<sub>4</sub> After Different Etching Procedures by Synchrotron-based Spectroscopies, *Energy Procedia* 84 (2015) 8–16. <https://doi.org/10.1016/j.egypro.2015.12.289>.
- [111] J. Krustok, H. Collan, K. Hjelt, Does the low-temperature Arrhenius plot of the photoluminescence intensity in CdTe point towards an erroneous activation energy?, *J. Appl. Phys.* 81 (1997) 1442–1445. <https://doi.org/10.1063/1.363903>.
- [112] J. Krustok, J. Raudoja, J.-H. Schön, M. Yakushev, H. Collan, The role of deep donor–deep acceptor complexes in CIS-related compounds, *Thin Solid Films* 361–362 (2000) 406–410. [https://doi.org/10.1016/S0040-6090\(99\)00756-7](https://doi.org/10.1016/S0040-6090(99)00756-7).

- [113] J. Krustok, H. Collan, K. Hjelt, J. Mädasson, V. Valdna, Photoluminescence from deep acceptor-deep donor complexes in CdTe, *J. Lumin.* 72–74 (1997) 103–105. [https://doi.org/10.1016/S0022-2313\(97\)00061-6](https://doi.org/10.1016/S0022-2313(97)00061-6).
- [114] F. Williams, Donor—acceptor pairs in semiconductors, *Physica Status Solidi (b)* 25 (1968) 493–512. <https://doi.org/10.1002/pssb.19680250202>.
- [115] J. Krustok, T. Raadik, M. Grossberg, M. Kauk-Kuusik, V. Trifiletti, S. Binetti, Photoluminescence study of deep donor- deep acceptor pairs in  $\text{Cu}_2\text{ZnSnS}_4$ , *Mater. Sci. Semicond. Process.* 80 (2018) 52–55. <https://doi.org/10.1016/j.mssp.2018.02.025>.
- [116] T. Schmidt, K. Lischka, W. Zulehner, Excitation-power dependence of the near-band-edge photoluminescence of semiconductors, *Phys. Rev. B* 45 (1992) 8989–8994. <https://doi.org/10.1103/PhysRevB.45.8989>.
- [117] G. Martinez, B.A. Piot, M. Hakl, M. Potemski, Y.S. Hor, A. Materna, S.G. Strzelecka, A. Hruban, O. Caha, J. Novák, A. Dubroka, Č. Drašar, M. Orlita, Determination of the energy band gap of  $\text{Bi}_2\text{Se}_3$ , *Sci. Rep.* 7 (2017) 6891. <https://doi.org/10.1038/s41598-017-07211-x>.
- [118] M. Lang, C. Zimmermann, C. Krämmer, T. Renz, C. Huber, H. Kalt, M. Hetterich, Luminescence properties of  $\text{Cu}_2\text{ZnSn}(\text{S,Se})_4$  solar cell absorbers: State filling versus screening of electrostatic potential fluctuations, *Phys. Rev. B* 95 (2017) 155202. <https://doi.org/10.1103/PhysRevB.95.155202>.
- [119] J. Bleuse, S. Perret, Y. Curé, L. Grenet, R. André, H. Mariette, Optical determination of the band gap and band tail of epitaxial  $\text{Ag}_2\text{ZnSnSe}_4$  at low temperature, *Phys. Rev. B* 102 (2020) 195205. <https://doi.org/10.1103/PhysRevB.102.195205>.
- [120] A.P. Levanyuk, V. V. Osipov, Edge luminescence of direct-gap semiconductors, *Soviet Physics Uspekhi* 24 (1981) 187–215. <https://doi.org/10.1070/PU1981v024n03ABEH004770>.
- [121] J. Krustok, R. Kaupmees, N. Abbasi, K. Muska, I. Mengü, K. Timmo, Bandgap Fluctuations, Hot Carriers, and Band-to-Acceptor Recombination in  $\text{Cu}_2\text{ZnSn}(\text{S,Se})_4$  Microcrystals, *Physica Status Solidi (RRL) – Rapid Research Letters* 17 (2023) 1–5. <https://doi.org/10.1002/pssr.202300077>.
- [122] H.-H. Fang, S. Adjokatse, S. Shao, J. Even, M.A. Loi, Long-lived hot-carrier light emission and large blue shift in formamidinium tin triiodide perovskites, *Nat. Commun.* 9 (2018) 243. <https://doi.org/10.1038/s41467-017-02684-w>.
- [123] D. V. Chepur, D.M. Bercha, I.D. Turyanitsa, V.Y. Slivka, Peculiarities of the Energy Spectrum and Edge Absorption in the Chain Compounds AV BVI CVII, *Physica Status Solidi (b)* 30 (1968) 461–468. <https://doi.org/10.1002/pssb.19680300206>.
- [124] J. Krustok, J.H. Schön, H. Collan, M. Yakushev, J. Mädasson, E. Bucher, Origin of the deep center photoluminescence in  $\text{CuGaSe}_2$  and  $\text{CuInS}_2$  crystals, *J. Appl. Phys.* 86 (1999) 364–369. <https://doi.org/10.1063/1.370739>.
- [125] J. Krustok, J. Raudoja, M. Krunks, H. Mändar, H. Collan, Nature of the native deep localized defect recombination centers in the chalcopyrite and orthorhombic  $\text{AgInS}_2$ , *J. Appl. Phys.* 88 (2000) 205–209. <https://doi.org/10.1063/1.373644>.

## Acknowledgements

I would first like to express my sincere gratitude to my supervisors, Dr. Kristi Timmo and Prof. Marit Kauk-Kuusik, for their continuous support throughout my doctoral studies. Thank you for believing in me and for giving me this opportunity. Your guidance, ideas, and constant availability have been essential to this work. I am especially grateful for your support, for challenging me, and for encouraging me to persevere whenever it was needed.

I would like to extend my special thanks to Prof. Emer. Jüri Krustok for his invaluable support and expertise, particularly in photoluminescence. Your guidance, insightful discussions, and willingness to share your knowledge have significantly contributed to this work, even though you were not formally my supervisor.

I am deeply thankful to my colleagues from the Laboratory of Photovoltaic Materials for their help and collaboration. Thanks for creating a supportive and collaborative working environment. The positive atmosphere made my time here truly enjoyable. In particular, I would like to thank Dr. Katri Muska for assistance with ampoule preparation, Dr. Maris Pilvet for help with solar cell preparation, Dr. Olga Volobujeva for providing thin film substrates, Dr. Sergei Bereznev for his support with SKP measurements, Dr. Mati Danilson for his assistance with XPS and UPS measurements, Dr. Valdek Mikli for his assistance with SEM and EDX measurements, and Dr. Idil Mengü for her help with PL measurements. I would also like to thank Prof. Maarja Grossberg-Kuusk, Director of the Department of Materials and Environmental Technology, for her leadership and support.

My sincere thanks also go to Prof. Emer. Malle Krunks and Dr. Mai Uibu for their help in preparing me for the defence. I am grateful to Anu Green and Anne Käärt for their administrative support and assistance with documentation and organizational matters.

I would like to acknowledge Dr. Arvo Mere from the Laboratory of Thin Films for performing XRD measurements. I am also grateful to Dr. Rokas Kondrotas and Dr. Artūras Suchodolskis from the Center for Physical Sciences and Technology in Lithuania for conducting diffuse reflectance spectroscopy measurements and for hosting me. Furthermore, I thank Dr. Aurelian Catalin Galca, Dr. Amelia Elena Bocirnea, and Cristian Radu from the National Institute of Materials Physics in Romania for carrying out XRD, XPS, and TEM measurements and welcoming me to their institute.

I am especially grateful to my family for their unwavering support, even from afar. Your encouragement has been a constant source of strength. I also thank my friends and my fellow PhD colleagues for the time we shared and for making this journey more enjoyable.

Finally, I would like to express my gratitude to Dr. Marc Salleras, Dr. Luis Fonseca, Dr. Andrej Stranz, and Dr. İnci Dönmez from the Institute of Microelectronics of Barcelona for introducing me to the world of research and inspiring me to pursue this path. This research was supported by the Estonian Research Council under grant PRG1023 “Sustainable, cost-efficient, flexible, lightweight and semitransparent multinary chalcogenide-based solar cells for building-integrated photovoltaics”; by the Estonian Ministry of Education and Research with project TK210 “Center of Excellence in Sustainable Green Hydrogen and Energy Technologies (GREENTECH)”; by the European Regional Development Fund with project TK141 “Advanced materials and high-technology devices for sustainable energetics, sensorics and nanoelectronics”. The research was carried out using the NAMUR+ core facility, funded by the Estonian Research Council (Projects TT13, TTK26).

## Abstract

### Synthesis and Characterization of $\text{Sb}_{1-x}\text{Bi}_x\text{SeI}$ Pnictogen Chalcogenides

Pnictogen chalcogenides have emerged in recent years as a promising class of semiconductor materials for next-generation optoelectronic and energy conversion technologies. The combination of suitable optoelectronic properties, good chemical stability, relatively low toxicity, and constituent elements that are abundant in the Earth's crust makes these materials attractive alternatives to conventional absorber materials used in photovoltaic devices. Particular attention has been drawn to Sb- and Bi-based chalcogenides, whose  $ns^2$  electron configuration promotes the formation of an antibonding valence band maxima associated with defect tolerance and potentially efficient charge-carrier transport, similarly to lead halide perovskites.

Despite the significant potential of pnictogen chalcogenides for photovoltaic applications, their practical implementation is limited by strong structural anisotropy, the impact of which on device performance depends critically on the control of microstructure and crystallographic orientation. In particular, for SbSeI, the preparation of high-quality thin films with suitable morphology and preferred crystallite orientation remains insufficiently studied and technologically challenging. Furthermore, a comprehensive understanding of how composition influences energy band alignment and conductivity type across the entire  $\text{Sb}_{1-x}\text{Bi}_x\text{SeI}$  solid solution series is still lacking. In addition, defect-related recombination mechanisms remain insufficiently understood, despite their critical role in determining the optoelectronic properties of these materials.

This thesis aims to develop and optimize synthesis methods for  $\text{Sb}_{1-x}\text{Bi}_x\text{SeI}$  ( $x = 0-1$ ) and to investigate the influence of composition, structure, and defects on their optoelectronic properties, in order to enable their targeted application in high-efficiency photovoltaics and other optoelectronic devices. The first part of the work focused on the preparation of SbSeI thin films and the systematic optimization of their synthesis using amorphous and crystalline  $\text{Sb}_2\text{Se}_3$  precursor layers deposited on Mo-coated glass. SbSeI thin films were obtained by iodization of  $\text{Sb}_2\text{Se}_3$  in the vapor phase of  $\text{SbI}_3$  under controlled Ar pressure using the physical vapor transport method. The results show that precursor crystallinity, synthesis temperature, and duration determine the morphology, phase purity, and composition of the films. Using amorphous  $\text{Sb}_2\text{Se}_3$  precursors enables the formation of dense, compact SbSeI thin films with vertically oriented crystallites, which are single-phase and near-stoichiometric in composition compared to those derived from crystalline  $\text{Sb}_2\text{Se}_3$ , as confirmed by X-ray diffraction (XRD) and Raman spectroscopy. Optical measurements showed that the material has a direct band gap of 1.72 eV. Notably, this work demonstrates for the first time that deliberate control of  $\text{Sb}_2\text{Se}_3$  precursor crystallinity provides a viable strategy for controlling anisotropic growth in chalcogenide systems.

In the second part, microcrystalline  $\text{Sb}_{1-x}\text{Bi}_x\text{SeI}$  ( $x = 0-1$ ) solid solutions were synthesized in compositional steps of 0.2 from binary compounds in sealed quartz ampoules by solid-state reaction. Energy-dispersive spectroscopy confirmed the gradual substitution of Sb by Bi. XRD and Raman analyses showed that single-phase materials with an orthorhombic (*Pnma*) crystal structure were formed over the entire compositional range. With increasing Bi content, the diffraction peaks shifted systematically toward lower angles, indicating lattice expansion. The lattice parameters

*b* and *c* increased linearly with increasing Bi content, whereas the lattice parameter *a* remained nearly unchanged. Raman analysis showed for the first time that the relative intensities of the Sb–Se and Bi–Se vibrational modes enable reliable determination of the Sb/Bi ratio in the  $\text{Sb}_{1-x}\text{Bi}_x\text{Se}$  system, providing a novel and practical compositional analysis approach. Scanning electron microscopy and transmission electron microscopy revealed that the materials consist of rod-shaped microcrystals formed by ribbon-like structures aligned along the long axis. Ultraviolet-Visible-Near-Infrared (UV-Vis-NIR) spectroscopy showed that replacing Sb with Bi reduces the band gap nonlinearly from 1.7 eV for SbSe to 1.29 eV for BiSe. Ultraviolet photoelectron spectroscopy further revealed a systematic shift of the Fermi level from the valence band maximum towards the conduction band with increasing Bi content, accompanied by a transition in conductivity type from *p*-type conductivity in Sb-rich compositions to *n*-type conductivity in Bi-rich materials. These results highlight the wide tunability of the structural and electronic properties of the  $\text{Sb}_{1-x}\text{Bi}_x\text{Se}$  system and provide important insight into the role of compositional engineering in tailoring the optoelectronic properties of pnictogen chalcogenides.

In the third part of the work, photoluminescence studies were carried out to elucidate the defect structure and recombination mechanisms. In SbSe thin films, the room-temperature PL spectra exhibited a broad and asymmetric emission band with a maximum at 1.67 eV, whereas measurements performed at low temperature (8 K) showed a dominant emission band at 1.4 eV, significantly below the band gap. The large energy difference, together with the low activation energy of thermal quenching ( $12.7 \pm 0.8$  meV), indicates that radiative recombination is associated with deep donor-deep acceptor (DD–DA) pairs. Room-temperature PL analysis of  $\text{Sb}_{1-x}\text{Bi}_x\text{Se}$  microcrystals ( $x = 0-1$ ) showed that increasing Bi content shifts the emission band maximum from 1.75 eV to 1.41 eV, in agreement with the nonlinear band gap reduction determined from UV-Vis-NIR measurements. Low-temperature PL studies of BiSe microcrystals revealed the presence of multiple emission bands, indicating a complex defect structure and several radiative recombination channels. PL bands with maxima at 0.903 and 1.108 eV were assigned to DD–DA recombination. PL band at 1.282 eV was associated with recombination between a deep–acceptor and the conduction band. In addition, the emission band at 1.51 eV was assigned to band-to-band (BB) recombination. Based on the activation energies and spectral features, the most probable donor-type defects were identified as  $\text{Se}_{\text{Bi}}$  antisite defects and interstitial  $\text{I}_i$  defects, while  $\text{V}_{\text{Bi}}$  was identified as the most probable acceptor. These results represent the first comprehensive experimental investigation of defect-related radiative recombination processes in SbSe and BiSe, providing critical insight into their defect physics.

In summary, this doctoral thesis demonstrates that Sb- and Bi-based chalcogenides are promising materials for photovoltaic applications. Through controlled synthesis, deliberate precursor engineering, and systematic compositional tuning, key properties such as band gap, energy band alignment, and conductivity type can be precisely controlled. The findings establish new processing strategies, reveal previously unexplored structure–property relationships, and provide the first comprehensive experimental insights into defect-related processes in these materials, thereby laying a strong foundation for their further optimization and integration into optoelectronic devices.

## Lühikokkuvõte

### **Sb<sub>1-x</sub>Bi<sub>x</sub>SeI pniktogeen kalkohaliidide süntees ja iseloomustamine**

Pniktogeen kalkohaliidid on viimastel aastatel tõusnud esile paljulubavate pooljuhtmaterjalide klassina järgmise põlvkonna optoelektronika- ja energiamuundamise tehnoloogiate jaoks. Sobivate optoelektronsete omaduste, hea keemilise stabiilsuse, suhteliselt madala toksilisuse ning maakoos laialdaselt esinevate koostiselementide kombinatsioonist tõttu peetakse neid atraktiivseteks alternatiivideks tavapärastele fotovoltseadmete absorbermaterjalidele. Erilist tähelepanu on pälvinud Sb- ja Bi-põhised kalkohaliidid, mille ns<sup>2</sup>-elektronkonfiguratsioon soodustab mittesiduvat-tüüpi valentstsooni maksimumi kujunemist, mis on seotud defektitaluvuse ja potentsiaalselt tõhusa laengukandjate transpordiga, sarnaselt pliihaliid-perovskiididega.

Hoolimata pniktogeen kalkohaliidide märkimisväärsest potentsiaalset fotovoltseadmetes, piirab nende rakendatavust tugev struktuurne anisotroopia, mille mõju seadmete jõudlusele sõltub oluliselt SbSeI kile kristalliitide mikrostruktuuri ja kristallograafilise orientatsiooni kontrollist. Eelkõige SbSeI puhul on sobiva morfoloogia ja eelistatud orientatsiooniga kristalliitidega kvaliteetsete õhukeste kilede valmistamine endiselt vähe uuritud ning tehnoloogiliselt väljakutsuv. Samuti puudub terviklik teadmine sellest, kuidas koostis mõjutab energiatsoonide joondumist ja juhtivustüüpi kogu Sb<sub>1-x</sub>Bi<sub>x</sub>SeI tahkete lahuste ulatuses. Lisaks on defektidega seotud rekombinatsiooni mehhanismid jäänud ebapiisavalt selgitatuks, hoolimata nende kriitilisest rollist materjalide optoelektronsetele omadustele.

Käesoleva töö eesmärk oli arendada ja optimeerida Sb<sub>1-x</sub>Bi<sub>x</sub>SeI (x = 0–1) sünteesimeetodeid ning uurida koostise, struktuuri ja defektide mõju optoelektronilistele omadustele, et võimaldada nende sihipärast rakendamist päikeseelementides ja teistes optoelektronilistes seadmetes.

Töö esimeses osas keskenduti SbSeI õhukeste kilede valmistamisele ja nende sünteesitingimuste süstemaatilisele optimeerimisele, kasutades Mo-klaasile sadestatud amorfseid ja kristallilisi Sb<sub>2</sub>Se<sub>3</sub> kilesid. SbSeI õhukesed kiled sünteesiti suletud kvartsampullides Sb<sub>2</sub>Se<sub>3</sub> jodiseerimisel Sbl<sub>3</sub> aurufaasis kontrollitud Ar-rõhu all, kasutades füüsikalise aurutranspordi meetodit. XRD ja Raman analüüside tulemused näitasid, et Sb<sub>2</sub>Se<sub>3</sub> kile kristallilisus koos sünteesitemperatuuri ja -ajaga määravad tekkinud SbSeI kilede morfoloogia, faasilise puhtuse ja keemilise koostise. Amorfse Sb<sub>2</sub>Se<sub>3</sub> kasutamine võimaldab saavutada tihedad ja kompaktsed, vertikaalselt orienteeritud kristalliitidega SbSeI õhukesed kiled, mis on ühefaasilised ja stõhhiomeetria lähedase koostisega. Optiliste mõõtmiste põhjal määrati materjali otsese keelutsooni laiuseks 1,72 eV. Esmakordselt näidati, et Sb<sub>2</sub>Se<sub>3</sub> lähtekile kristallilisuse teadlik kontroll pakub toimiva strateegia anisotroopse kasvu juhtimiseks pniktogeen kalkohaliidide süsteemis.

Teises osas sünteesiti mikrokristallilised Sb<sub>1-x</sub>Bi<sub>x</sub>SeI (x = 0–1) tahked lahused sammuga 0,2 binaarsetest ühenditest kinnistes kvartsampullides tahkefaasilise reaktsiooni teel. Energia dispersioon-spektroskoopia kinnitas Sb järkjärgulist asendumist Bi-ga. XRD ja Raman analüüsi tulemused näitasid, et kogu koostise vahemikus moodustusid ühefaasilised ortorombilise (*Pnma*) kristallstruktuuriga materjalid. Bi sisalduse suurenemisel nihkusid difraktsioonipiigid süstemaatiliselt väiksemate nurkade suunas, viidates kristallvõre paisumisele. Võreparameetrid *b* ja *c* suurenesid lineaarselt Bi sisalduse kasvades, samas kui võreparameeter *a* jäi peaaegu muutumatuks. Ramani spektrite

analüüsil näidati esmakordselt, et Sb–Se ja Bi–Se võnkemoodide suhtelised intensiivsused võimaldavad usaldusväärselt määrata Sb ja Bi omavahelist suhet  $Sb_{1-x}Bi_xSe$  süsteemis, pakkudes uutset ja praktilist lähenemist koostise määramiseks. Skaneeriva elektronmikroskoopia ja transmissioonelektron-mikroskoopia uuringud näitasid, et materjalid koosnevad vardakujulistest mikrokristallidest, mis on moodustunud pika telje suunas joondunud kihilistest struktuuridest. Ultravioletne-nähtava spektrofotomeetria (UV-Vis-NIR) mõõtmistulemused näitasid, et Sb asendamisel Bi-ga väheneb materjali keelutsooni laius mittelineaarselt 1,7 eV-lt (SbSe) kuni 1,29 eV-ni (BiSe). Ultraviolettfotoelektronspektroskoopia tulemused näitasid lisaks Fermi taseme süstemaatilist nihkumist valentstsooni maksimumist Bi sisalduse suurenemisel, millega kaasnes juhtivustüübi üleminek  $p$ -tüüpi juhtivuselt Sb-rikastes koostistes  $n$ -tüüpi juhtivusele Bi-rikastes materjalides. Saadud tulemused rõhutavad  $Sb_{1-x}Bi_xSe$  süsteemi struktuursete ja elektrooniliste omaduste laialatuslikku varieeritavust ning selle potentsiaali võimaldada sihipärast optimeerimist erinevate fotovoltseadmete jaoks.

Töö kokkumandas osas viidi defektstruktuuri ja rekombinatsiooni mehhanismide välja selgitamiseks läbi fotoluminesentsi (PL) uuringud. SbSe õhukeste kiledede puhul ilmnis toatemperatuuril mõõdetud PL-spektrites lai ja asümmeetriline kiirgusriba maksimumiga 1,67 eV, samas kui madalal temperatuuril (8 K) tehtud mõõtmised näitasid domineerivat kiirgusriba 1,4 eV juures, oluliselt allpool keelutsooni. Suur energiavahe koos madala termilise kustumise aktivatsioonienergiaga ( $12,7 \pm 0,8$  meV) viitab sellele, et kiirguslik rekombinatsioon on seotud sügavate doonor–aktseptor (DD–DA) paaridega.  $Sb_{1-x}Bi_xSe$ -di ( $x = 0–1$ ) mikrokristallide toatemperatuurine PL-analüüs näitas, et Bi sisalduse suurenemisel nihkub kiirgusriba maksimum 1,75 eV-lt 1,41 eV-ni, olles kooskõlas UV-Vis-NIR mõõtmiste põhjal määratud keelutsooni mittelineaarse vähenemisega. BiSe mikrokristallide madaltemperatuurine PL-uuring näitas mitme kiirgusriba olemasolu, viidates keerukale defektstruktuurile ning mitmele kiirgusliku rekombinatsiooni kanalile. Luminesentsribad maksimumidega 0,903 ja 1,108 eV omistati DD–DA rekombinatsioonile. PL kiirgusriba 1,282 eV juures seostati sügava aktseptori ja juhtivustsooni rekombinatsiooniga. Lisaks leiti, et 1,51 eV juures paiknev kiirgusriba on seotud tsoonidevahelise (BB) rekombinatsiooniga. Aktivatsioonienergiate ja spektraalsete tunnuste põhjal tuvastati kõige tõenäolisemateks doonortüüpi defektideks  $Se_{Bi}$  asendusdefektid ja võrevahelised  $I_i$  defektid, samas kui  $V_{Bi}$  määratleti kõige tõenäolisemaks aktseptoriks. Käesolev töö esitab esmakordselt põhjaliku eksperimentaalse analüüsi SbSe ja BiSe defektidega seotud kiirguslike rekombinatsioonide kohta.

Kokkuvõtteks näitab doktoritöö, et Sb- ja Bi-põhised kalkohaliidid on paljulubavad materjalid fotovoltseadmete rakendusteks. Kontrollitud sünteesi ja koostise sihipärase muutmise kaudu on võimalik süstemaatiliselt varieerida mitmeid olulisi omadusi, sealhulgas keelutsooni laiust (1,29–1,7 eV), energiatsoonide joondust, juhtivustüüpi ning defektidega seotud rekombinatsiooni mehhanisme. Tulemused toovad välja uued tehnoloogilised strateegiad, avavad seni uurimata koostise, struktuuri ja optoelektooniliste omaduste seosed ning pakuvad esmakordselt põhjalikku eksperimentaalset ülevaadet defektidega seotud protsessidest nendes materjalides, luues tugeva aluse nende edasiseks optimeerimiseks ja rakendamiseks optoelektronilistes seadmetes.



# Appendix 1

## Publication I

**M. Dolcet Sadurni**, K. Timmo, V. Mikli, O. Volobujeva, I. Mengü, J. Krustok, M. Grossberg-Kuusk, M. Kauk-Kuusik, "Preparation and characterization of SbSeI thin films" *Journal of Science: Advanced Materials and Devices* 9 (2024) 100664, <https://doi.org/10.1016/j.jsamd.2023.100664>.





Contents lists available at ScienceDirect

Journal of Science: Advanced Materials and Devices

journal homepage: [www.elsevier.com/locate/jسامd](http://www.elsevier.com/locate/jسامd)

## Preparation and characterization of SbSeI thin films

Marc Dolcet Sadurni<sup>\*</sup>, Kristi Timmo, Valdek Mikli, Olga Volobujeva, Idil Mengü, Jüri Krustok, Maarja Grossberg-Kuusik, Marit Kauk-Kuusik

Department of Materials and Environmental Technology, Tallinn University of Technology, Ehitajate tee 5, 19086, Tallinn, Estonia

### ARTICLE INFO

#### Keywords:

Antimony selenoiodide  
Pnictogen chalcogenides  
Thin films  
Photoluminescence  
SbSeI

### ABSTRACT

Metal chalcogenides are promising candidates for next-generation technologies that include energy conversion, information storage, and quantum computing. Among them, antimony selenoiodide (SbSeI) has received rising interest for different optoelectronic devices, including photovoltaics, due to its bandgap energy, strong optical absorption, stability, and earth abundant, low-cost, and low toxicity constituents. In this work, SbSeI thin films were prepared through a two-step process. At first, antimony selenide ( $\text{Sb}_2\text{Se}_3$ ) thin films were deposited at 300 °C ( $\text{Sb}_2\text{Se}_3$ -300) and at room temperature ( $\text{Sb}_2\text{Se}_3$ -RT) onto molybdenum covered soda-lime glass substrates by a magnetron sputtering method. The formation of SbSeI thin films was performed by isothermally annealing the as-deposited  $\text{Sb}_2\text{Se}_3$  thin films in sealed quartz ampoules in the atmosphere of antimony iodide ( $\text{SbI}_3$ ) with the presence of 100 Torr of argon pressure. The influence of the annealing temperature and time during the iodization of different types of substrates on the morphology and composition of SbSeI thin films was investigated. The well-oriented and dense single-phase SbSeI thin films with stoichiometric composition and single-crystal micro-columnar structures were achieved by annealing  $\text{Sb}_2\text{Se}_3$ -RT in  $\text{SbI}_3$  atmosphere at 250 °C for 5 min under 100 Torr of Ar pressure. The room temperature photoluminescence (RT-PL) of SbSeI exhibited a broad asymmetric PL band with a maximum at 1.67 eV. The low-temperature ( $T = 8$  K) PL study of SbSeI showed a broad and asymmetric PL band at 1.4 eV, being quite distant from the bandgap. This PL band at 1.4 eV with obtained small thermal quenching activation energy of 12.7 meV is proposed to originate from the deep donor-deep acceptor pair (DD-DA) recombination.

### 1. Introduction

Emerging photovoltaic technologies, such as kesterite, Sb-chalcogenide, dye-sensitized solar cells, organic solar cells, and perovskite solar cells, are currently under research as alternatives to traditional silicon solar cells [1]. Perovskites, among these candidates, exhibit exceptional optoelectronic properties [2]. Notably, Pb-based perovskite solar cells have already achieved a power conversion efficiency (PCE) of 25.7 % [3], making them very attractive for solar energy applications. Although remarkable progress has been made in the development of perovskite-based photovoltaic technology, the commercialization of these solar cells has significant limitations due to their instability and toxicity issues [4]. Exposure to humid conditions, heat or light tends to induce rapid degradation of perovskite materials [5]. Moreover, during the fabrication and operation of devices, Pb-perovskites have a tendency to decompose into components

containing lead, posing potential environmental and health hazards [6]. Therefore, there is a critical need to explore and identify more stable and Pb-free materials that could be considered as promising alternatives to Pb-perovskites as an absorber layer in solar cell applications. Antimony selenide ( $\text{Sb}_2\text{Se}_3$ ) solar cells have gained extensive research attention in recent years. While demonstrating enhanced stability compared to Pb-perovskites [7],  $\text{Sb}_2\text{Se}_3$  solar cells suffer from a large open circuit voltage ( $V_{oc}$ ) deficit associated with its complex defect chemistry. Despite recent efforts aimed at enhancing  $V_{oc}$  [8,9], the efficiency record of  $\text{Sb}_2\text{Se}_3$  solar cells has reached around 10 % [10], leaving plenty of room for improvement considering the theoretical Shockley–Queisser (S-Q) limit for  $\text{Sb}_2\text{Se}_3$ , which stands at 30 %.

The defect tolerance observed in Pb-perovskites is closely related to the  $ns^2$  electronic configuration of  $\text{Pb}^{2+}$  ( $5s^2$ ). Metallic cations like  $\text{Sb}^{3+}$  or  $\text{Bi}^{3+}$  share the same  $ns^2$  electronic configuration, offering a high dielectric constant, low effective masses and anti-bonding character of

Peer review under responsibility of Vietnam National University, Hanoi.

<sup>\*</sup> Corresponding author.

E-mail address: [marc.dolcet@taltech.ee](mailto:marc.dolcet@taltech.ee) (M. Dolcet Sadurni).

<https://doi.org/10.1016/j.jsamd.2023.100664>

Received 20 September 2023; Received in revised form 30 November 2023; Accepted 17 December 2023

Available online 21 December 2023

2468-2179/© 2023 Vietnam National University, Hanoi. Published by Elsevier B.V. This is an open access article under the CC BY-NC-ND license (<http://creativecommons.org/licenses/by-nc-nd/4.0/>).

the valence band. These properties collectively contribute to defect-tolerant transport properties [11]. One potential group of materials displaying the  $ns^2$  electronic configuration is metal chalcogenides. These compounds consist of a trivalent heavy pnictogen cation, a divalent chalcogenide and monovalent halide anions. They are typically represented by the general chemical formula  $MXY$ , where  $M = Bi$  or  $Sb$ ;  $X = S, Se, \text{ or } Te$ ; and  $Y = Cl, Br, \text{ or } I$ .

While heavy pnictogen chalcogenides have historically received less attention compared to other materials, there has been a recent surge in interest aimed at exploring their potential as absorber materials in solar cells [12–17]. Among them, antimony selenide ( $Sb_2Se_3$ ) has received rising interest for different optoelectronic devices including photovoltaics [18,19].  $Sb_2Se_3$  has an orthorhombic crystal structure with the space group  $Pnma$  62 [20]. It has a high absorption coefficient ( $\sim 10^5 \text{ cm}^{-1}$ ) and an indirect bandgap of 1.67 eV [21]. Theoretical calculations have shown that dominant defects in  $Sb_2Se_3$  are  $Se_i$  acceptors and  $Se_v$  donors, leading to an electrical conductivity that can only exhibit weak  $n$ -type or weak  $p$ -type characteristics [22]. Defects play a major role in determining the performance of photovoltaics and therefore careful investigation is needed.

$Sb_2Se_3$  has been synthesized through different methods—by melting at high temperatures from elements in sealed ampoules [23], by the sonochemical method using pure elements [24] and by the Bridgman technique [25].  $Sb_2Se_3$  thin films have been deposited using multiple techniques: from previously deposited antimony selenide ( $Sb_2Se_3$ ), from an Ethane dithiol/Ethylene diamine solution followed by casting an antimony iodide ( $SbI_3$ ) solution or thermal formation and then, by iodization of the  $Sb_2Se_3$  with iodine vapors produced by heating iodine pellets in a closed gas chamber [26]. Nie et al. fabricated  $Sb_2Se_3$ -based solar cells by depositing  $Sb_2Se_3$  onto mesoporous titanium oxide ( $TiO_2$ ) using multiple spin-coating cycles of  $SbI_3$  solutions onto  $Sb_2Se_3$ , previously formed through thermal decomposition and crystallization. These solar cells demonstrated remarkable stability regardless of humidity, temperature, and light, while achieving a power conversion efficiency of 4.1% [18]. Although  $Sb_2Se_3$  has very promising properties, there are few studies where this material has been used as an absorber layer in solar cells, and the obtained efficiency is still far from the theoretical 28% [25].

$Sb_2Se_3$  crystallizes into the  $(M_2X_2Y_2)_n$  double-chained system, that are covalently linked along the chain axis direction, while at out-of-chain-axis directions, the adjacent chains are joined together by van der Waals forces. The pseudo-1D crystal structure of these materials and growth rate anisotropy can be problematic for the formation of dense thin films in a planar photovoltaic device [27]. On the other hand, the optimization of the grain orientation in materials with similar 1D crystal structure as  $Sb_2Se_3$  has been proved critical to enhance the performance of solar cells [28,29]. Careful control of annealing parameters, such as temperature, pressure, and duration, significantly influences the characteristics of the resulting  $Sb_2Se_3$  films, including crystal structure, composition, and optical and electrical properties. Therefore, specific annealing conditions must be optimized to obtain  $Sb_2Se_3$  films with desirable properties for various applications.

The objective of this research is to fabricate  $Sb_2Se_3$  thin films using physical vapor transport to achieve homogeneous material with well-oriented crystals, with the aim to obtain morphology and optoelectronic properties suitable for high-performance solar cells. In this work,  $Sb_2Se_3$  was prepared by iodizing sputtered  $Sb_2Se_3$  thin films. The study investigates the influence of annealing temperature and time during the iodization on various types of substrates, exploring their impact on the morphology, composition, and optical properties of the resulting  $Sb_2Se_3$  thin films.

## 2. Experimental

### 2.1. Preparation of $Sb_2Se_3$ thin films

$Sb_2Se_3$  thin films were deposited by radio frequency magnetron sputtering from  $Sb_2Se_3$  target onto molybdenum covered soda-lime glass substrate. The thickness of the 800 nm  $Sb_2Se_3$  thin films was adjusted by the sputtering time. The formation of  $Sb_2Se_3$  thin films was carried out by isothermal annealing of as-deposited  $Sb_2Se_3$  thin films in sealed quartz ampoules in the  $SbI_3$  atmosphere. In this study, two different types of  $Sb_2Se_3$  thin films were used: 1) sputtered at a substrate temperature of 300 °C (hereafter referred to as samples  $Sb_2Se_3$ -300), and 2) sputtered at a substrate temperature of 25 °C (hereafter referred to as samples  $Sb_2Se_3$ -RT). The used  $SbI_3$  compound was self-synthesized isothermally in evacuated quartz ampoule.  $Sb_2Se_3$  thin film substrates and a piece of  $SbI_3$  were introduced into quartz ampoules. Then ampoules were degassed under dynamic vacuum, filled with 100 Torr of argon (Ar), sealed, and heated isothermally at different temperatures and time periods. For  $Sb_2Se_3$ -300 substrates, the iodization process was carried out at annealing temperatures from 150 to 350 °C for 1–20 min. For  $Sb_2Se_3$ -RT substrates, the iodization process was carried out at annealing temperatures of 200, 225 and 250 °C for 5 min.

### 2.2. Characterization

The morphology of the  $Sb_2Se_3$  thin films was characterized by a high-resolution scanning electron microscope (HR-SEM Zeiss Merlin), equipped with a high-efficiency In-lens secondary electron detector for high-contrast surface imaging and an energy-selective backscattered electrons detector for compositional contrast. The chemical composition of the deposited  $Sb_2Se_3$  thin films was analyzed by energy dispersive X-ray spectroscopy (EDX) on a Bruker Esprit 1.82 EDX system equipped with an EDX-XFlash 3001 detector with an accelerating voltage of 20 kV. The crystal structure of the formed  $Sb_2Se_3$  thin films was characterized by X-ray diffraction (XRD) using a Rigaku Ultima IV diffractometer at 40 kV and 40 mA operating with the silicon strip detector D/teX Ultra with monochromatic  $Cu K\alpha$  ( $\lambda = 1.5406 \text{ \AA}$ ) radiation. Phase analysis and lattice parameters were calculated by using PDXL2 Rigaku's software. Room temperature micro-Raman spectroscopy was used to determine the phase composition of  $Sb_2Se_3$  thin films. Raman spectra were recorded by a Horiba LabRam HR 800 spectrometer equipped with a multichannel CCD detection system in the backscattering configuration. A laser with wavelength 532 nm with a power intensity of 0.42 mW was used. The same equipment was used to perform the room temperature micro-photoluminescence (RT-PL) measurements in visible spectral region. Ultraviolet–Visible–Near-Infrared (UV–Vis–NIR) Spectrophotometer Cary5000 was used to obtain the optical diffuse reflectance spectra of  $Sb_2Se_3$  thin films at room temperature. Measurements were recorded between 400 and 1100 nm. For temperature dependent PL measurements, the samples were mounted on the cold finger of the closed-cycle helium cryostat (Janis CCS-150) and cooled down to 8 K. The temperature was adjusted up to 80 K via a temperature controller (LakeShore Model 335). The Cobolt 08-DPL laser with a wavelength of 532 nm was used for PL excitation. The power of the incident laser beam was altered via neutral density filters between 0.04 and 0.37 mW. An optical chopper was used for modulating the laser light. The emitted light was conditioned using a cut-off low-pass filter and focused on the computer-controlled single grating (600 lines/mm) monochromator ( $f = 0.64 \text{ m}$ ) (Horiba Jobin Yvon FHR640). Luminescence was dispersed by the monochromator and detected by the R632 photomultiplier tube. Stanford SR810 DSP lock-in amplifier was used for amplifying the PL signal.

### 3. Results and discussion

#### 3.1. Effect of annealing time and temperature on the $Sb_2Se_3$ -300 morphology and composition

The morphology of iodized  $Sb_2Se_3$  thin films was investigated as a function of the growth temperature and time. In this part of the study, the  $Sb_2Se_3$ -300 substrates with crystalline structure were used (see Fig. 1).

Fig. 2 a-c show the SEM images of SbSeI thin films formed by iodization of  $Sb_2Se_3$ -300 at 150 °C. SEM analysis showed significant changes in the morphology of formed SbSeI thin films depending on annealing temperature and time. The thin films iodized at 150 °C for 5–20 min (Fig. 2a–c) consist of SbSeI micro-columns. The length, thickness, and density of these columns increase with the annealing time. Nevertheless, regardless of the heating duration, all films exhibited a layer of unreacted  $Sb_2Se_3$  beneath the layer of these micro-columns. This suggests that the annealing temperature of 150 °C is not enough for the complete formation of a single phase SbSeI thin film.

Elevating the growth temperature to 175 °C accelerates the reaction between  $Sb_2Se_3$  with  $SbI_3$ , leading to the formation of regularly shaped micro-columnar crystals with length of 5–6  $\mu\text{m}$  (Fig. 3a–c) regardless of annealing time (5–20 min). Nevertheless, the bottom of the film consists of smaller grains with a porous structure, indicating the present of unreacted  $Sb_2Se_3$ . A similar layer was also seen after annealing for 20 min at 175 °C (see Fig. 3c).

Annealing at higher temperatures ( $\geq 200$  °C) for shorter times (3 min) resulted also in the formation of double layer structure of the thin films. For example, Fig. 4a and b shows the cross-sectional SEM images after annealing for 3 min at 225 °C and at 300 °C, respectively. Increasing the reaction duration to 5 min at annealing temperature 200–300 °C, results in complete formation of SbSeI thin films. Although the double-layer structure remains, but both layers contain only SbSeI phase (see Fig. 5a–c). At an annealing temperature of 350 °C, the formation of micro-columnar crystals stopped, and instead a non-uniform, irregular and flat SbSeI layer was observed.

The cross-sectional SEM images of the SbSeI thin film revealed that the thickness of the films increased with the annealing temperature as the length of the micro-columnar crystals increased. After annealing at 300 °C for 5 min, the length of the crystals increased to  $\sim 37$   $\mu\text{m}$ . In comparison, the initial thickness of the  $Sb_2Se_3$  film was  $\sim 0.8$   $\mu\text{m}$  (see Fig. 1b). Not only the length but also the diameter of the SbSeI micro-columns depended on the annealing temperature. Micro-columnar crystals with a diameter of  $\sim 500$  nm and a length of  $\sim 17$   $\mu\text{m}$  were formed by annealing at 250 °C for 5 min, while annealing at 300 °C for 5 min results in crystals with a diameter of  $\sim 2$   $\mu\text{m}$ . In the latter case, the thin film morphology was non-uniform, the random distribution of thicker micro-columns with sharp needles can also be seen in Fig. 5c. With a further increase in the annealing temperature to 350 °C and higher, the micro-columnar crystals were no longer formed, and instead a non-uniform, irregular and flat SbSeI layer was observed.

According to EDX analysis (Table 1), the chemical composition of the formed thin films is strongly influenced by the annealing temperature and time. At lower temperatures (150 °C for  $t = 5$ –20 min and 175 °C for  $t = 5$ –10 min), the resulting films were iodine poor. The deficiency of iodine was also detected in the samples that were annealed for shorter times at temperature 225 °C ( $t = 1$ –3 min), 250 °C ( $t = 1$ –3 min) and 300 °C ( $t = 1$  min). This result indicates an unreacted  $Sb_2Se_3$  layer that was also seen in SEM images in Figs. 3 and 4. EDX analysis showed that film annealed at temperature 175 °C ( $t = 15$ –20 min) and 300 °C ( $t = 3$ –5 min) had Sb-rich and I-rich composition. This could be attributed to coexistence of the  $SbI_3$  phase alongside the main SbSeI compound. SbSeI thin films with composition close to stoichiometry (Sb:Se:I = 1 : 1 : 1) formed by annealing  $Sb_2Se_3$  films in  $SbI_3$  at 100 Torr of Ar atmosphere for 5 min within the temperature range of 200–250 °C.

Raman spectroscopy analysis was carried out to investigate the phase composition of the thin films and to confirm the presence of possible secondary phases proposed by EDX. Raman spectra of as-deposited  $Sb_2Se_3$ , and after annealing at 150, 175 and 200 °C for 5 min are shown in Fig. 6. All Raman spectra were fitted using Lorentzian functions to resolve the peaks. The Raman spectrum of as-deposited  $Sb_2Se_3$  showed a dominating peak at 190  $\text{cm}^{-1}$  and less intense peaks at 99, 124, 154 and 212  $\text{cm}^{-1}$  (see Fig. 6a). These Raman frequencies are attributed to  $Sb_2Se_3$  and are in good correlation with the literature [30]. The fitting results of the Raman spectrum of the thin film, annealed at 150 °C for 5 min (Fig. 6b), revealed peaks at 95, 116, 137, 165, 184, 209, 211, 233, 237 and 255  $\text{cm}^{-1}$  showing the mixture of different phases. The peaks at 211  $\text{cm}^{-1}$  and 255  $\text{cm}^{-1}$  could be attributed to the  $Sb_2Se_3$  [31] and  $Sb_2O_3$  [32], respectively. The origin of the  $Sb_2O_3$  formation could be due to the sensitivity of the Sb-containing compounds to the potential photo-induced transformation or degradation during the Raman measurements [32,33]. The most intensive peaks at 233 and 237  $\text{cm}^{-1}$  belong to the trigonal Se [34]. The Raman spectrum of the thin film annealed for 5 min at 200 °C (Fig. 6d), exhibited peaks at 95, 116, 137, 165, 184, 209, and 214  $\text{cm}^{-1}$ . The identified peaks are characteristic to SbSeI and have been previously reported in the literature [26, 35]. Peaks below 200  $\text{cm}^{-1}$  are assigned to Sb–I bonds and 209  $\text{cm}^{-1}$  is assigned to the Sb–Se heteropolar vibration [26,36]. The Raman spectrum analysis of the film annealed at 175 °C (Fig. 6c) revealed, in addition to the SbSeI peaks, the presence of weaker peaks at 233, 237 and 255  $\text{cm}^{-1}$  (attributed to Se and  $Sb_2O_3$ ), which indicates non-uniform growth of SbSeI crystals. The SbSeI layers formed at 150 °C and 175 °C, exhibited higher sensitivity to the laser power of Raman equipment when compared to the sample prepared at 200 °C. This is probably due to the incomplete reactions in the  $Sb_2Se_3 + SbI_3$  system. All Raman analysis results are in a good correlation with the data presented in Table 1 and confirm the presence of secondary phases at annealing temperatures lower than 200 °C. Annealing the thin films at temperatures higher than 200 °C (up to 300 °C) for 5 min resulted in unchanged positions of the Raman peaks (spectra not presented here). However, there was observed increase in the intensity ratio of the peaks at 95 and 209  $\text{cm}^{-1}$  compared to the other peaks.

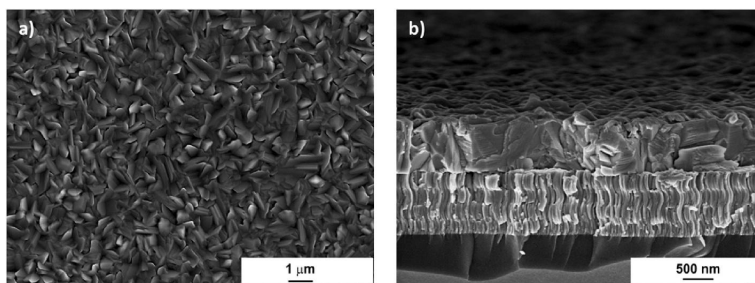


Fig. 1. SEM images of a) top view and b) cross-section of  $Sb_2Se_3$  thin film sputtered at 300 °C.

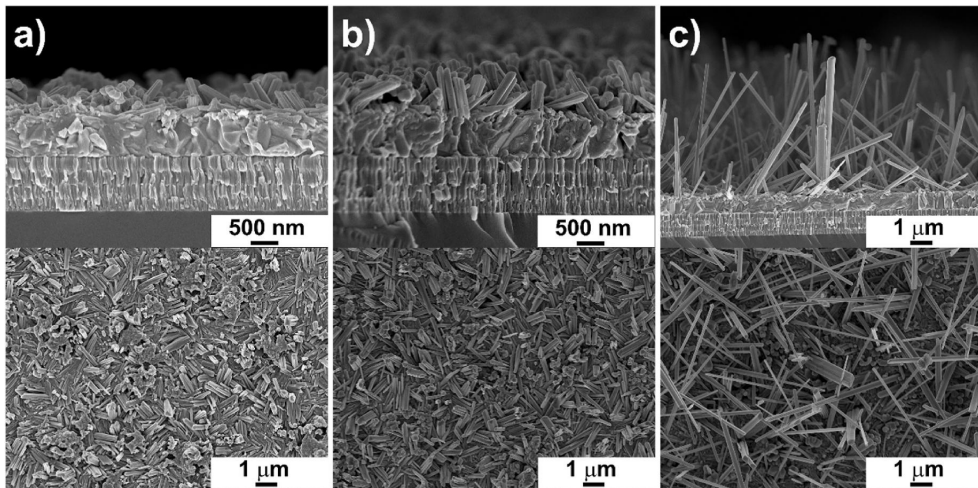


Fig. 2. SEM images of cross-section and surface of SbSeI thin films annealed in  $\text{SbI}_3$  and 100 Torr of Ar atmosphere at 150 °C for a) 5, b) 10, and c) 20 min.

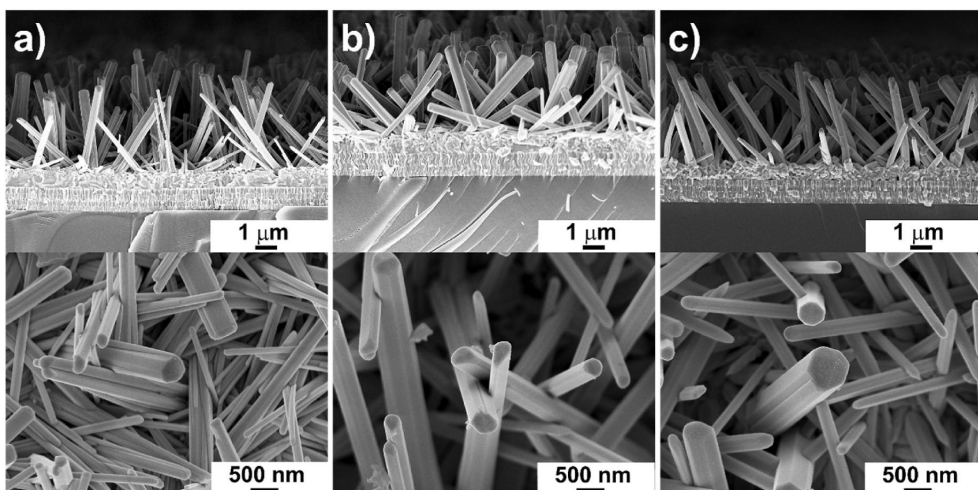


Fig. 3. SEM images of cross-section and surface of SbSeI thin films annealed in  $\text{SbI}_3$  and 100 Torr of Ar atmosphere at 175 °C for a) 5, b) 10, and c) 20 min.

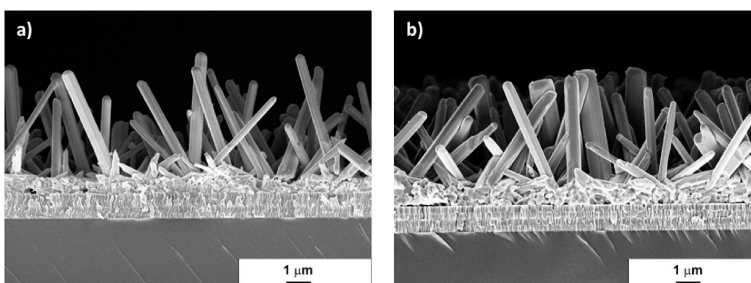


Fig. 4. SEM images of cross-section of SbSeI thin films annealed in  $\text{SbI}_3$  and 100 Torr of Ar atmosphere: a) at 225 °C for 3 min and b) at 300 °C for 3 min.

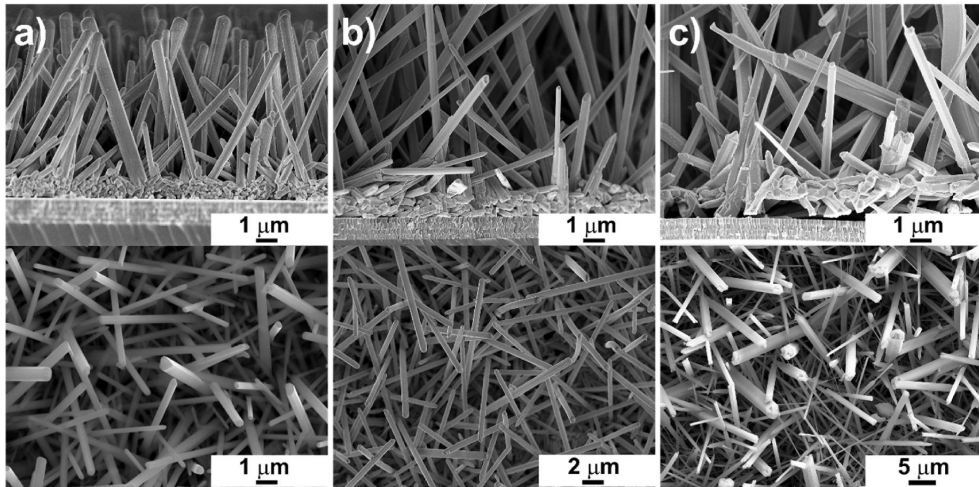


Fig. 5. SEM images of cross-section and surface of Sb<sub>2</sub>Se<sub>3</sub> thin films annealed in SbI<sub>3</sub> and 100 Torr of Ar atmosphere during 5 min at a) 200 °C. b) 250 °C and c) 300 °C.

**Table 1**  
Chemical composition of Sb<sub>2</sub>Se<sub>3</sub> thin films annealed at different temperatures and times measured by EDX.

Annealing temperature, °C	Annealing time, min	Sb, at %	Se, at %	I, at %	Proposed phases
150	5	35.2	55.2	9.6	Sb <sub>2</sub> Se <sub>3</sub> , Sb <sub>2</sub> Se <sub>3</sub> , Se
	10	36.8	48.2	15.0	Sb <sub>2</sub> Se <sub>3</sub> , Sb <sub>2</sub> Se <sub>3</sub>
	15	36.9	46.5	17.6	Sb <sub>2</sub> Se <sub>3</sub> , Sb <sub>2</sub> Se <sub>3</sub>
175	20	35.4	51.4	13.3	Sb <sub>2</sub> Se <sub>3</sub> , Sb <sub>2</sub> Se <sub>3</sub> , Se
	5	36.7	36.9	26.4	Sb <sub>2</sub> Se <sub>3</sub> , Sb <sub>2</sub> Se <sub>3</sub>
	10	36.0	37.4	26.6	Sb <sub>2</sub> Se <sub>3</sub> , Sb <sub>2</sub> Se <sub>3</sub>
200	15	35.2	30.1	34.7	Sb <sub>2</sub> Se <sub>3</sub> , SbI <sub>3</sub>
	20	37.0	27.9	35.2	Sb <sub>2</sub> Se <sub>3</sub> , SbI <sub>3</sub>
	5	34.5	32.6	32.9	Sb <sub>2</sub> Se <sub>3</sub> , Sb <sub>2</sub> Se <sub>3</sub>
225	10	36.6	37.1	26.4	Sb <sub>2</sub> Se <sub>3</sub> , Sb <sub>2</sub> Se <sub>3</sub>
	15	37.8	38.7	23.5	Sb <sub>2</sub> Se <sub>3</sub> , Sb <sub>2</sub> Se <sub>3</sub>
	1	36.6	57.7	5.7	Sb <sub>2</sub> Se <sub>3</sub> , Sb <sub>2</sub> Se <sub>3</sub> , Se
250	3	35.4	35.3	29.3	Sb <sub>2</sub> Se <sub>3</sub> , Sb <sub>2</sub> Se <sub>3</sub>
	5	34.2	32.7	33.1	Sb <sub>2</sub> Se <sub>3</sub> , Sb <sub>2</sub> Se <sub>3</sub>
	1	37.1	55.0	8.0	Sb <sub>2</sub> Se <sub>3</sub> , Sb <sub>2</sub> Se <sub>3</sub> , Se
300	3	35.9	33.8	30.2	Sb <sub>2</sub> Se <sub>3</sub> , Sb <sub>2</sub> Se <sub>3</sub>
	5	34.1	32.8	33.1	Sb <sub>2</sub> Se <sub>3</sub> , Sb <sub>2</sub> Se <sub>3</sub>
	1	39.3	48.8	11.9	Sb <sub>2</sub> Se <sub>3</sub> , Sb <sub>2</sub> Se <sub>3</sub>
	3	34.7	29.7	35.6	Sb <sub>2</sub> Se <sub>3</sub> , SbI <sub>3</sub>
	5	34.4	29.7	35.9	Sb <sub>2</sub> Se <sub>3</sub> , SbI <sub>3</sub>

In summary, the single layer micro-columnar structured Sb<sub>2</sub>Se<sub>3</sub> films with stoichiometric composition were obtained by annealing Sb<sub>2</sub>Se<sub>3</sub>-300 in SbI<sub>3</sub> atmosphere at 200–250 °C for 5 min under 100 Torr of Ar pressure. However, the thin film layer consisted of randomly oriented and not tightly packed crystals. Most probably, the orientation of the as-deposited Sb<sub>2</sub>Se<sub>3</sub>-300 thin film crystals determines the properties of the

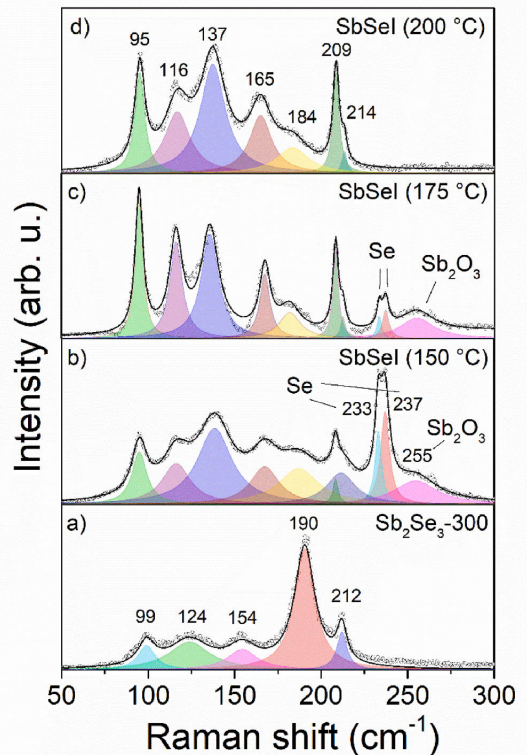


Fig. 6. RT Raman spectra of: a) Sb<sub>2</sub>Se<sub>3</sub>-300 sputtered at 300 °C and Sb<sub>2</sub>Se<sub>3</sub> annealed at b) 150, c) 175 and d) 200 °C respectively for 5 min under 100 Torr of Ar pressure.

formed SbSeI.

### 3.2. Effect of annealing temperature on the $Sb_2Se_3$ -RT morphology and composition

To improve the alignment and packing density of the SbSeI thin film crystals, amorphous  $Sb_2Se_3$  substrates (sputtered at RT) were used. SEM images of the cross-section and top view of an amorphous  $Sb_2Se_3$  substrates is shown in Fig. 7. Based on the knowledge gathered from previous experimental series, the  $Sb_2Se_3$ -RT films were annealed in  $SbI_3$  atmosphere at temperatures of 200, 225 and 250 °C for 5 min under 100 Torr of Ar pressure.

Fig. 8 shows SEM images of cross-section and top-view of the formed SbSeI thin films after iodization of  $Sb_2Se_3$ -RT at temperature ranging from 200 to 250 °C for 5 min. According to SEM studies, annealing at 200–225 °C for 5 min led to an ununiform double layer structure comprising unreacted  $Sb_2Se_3$ -RT and SbSeI crystals that exhibited irregularities in length, thickness, and orientation, as shown in Fig. 8a and b. At a temperature of 250 °C, a uniform thin film characterized by well-oriented, densely packed, and micro-columnar structured crystals was successfully obtained, as seen in Fig. 8c. Under these conditions, no unreacted antimony selenide was detected. The EDX analysis revealed that the chemical composition of formed SbSeI thin film is Sb- and I-rich, suggesting the presence of  $SbI_3$ . The atomic percentage ratio of Sb:Se:I was determined to be 35.2:29.7:35.1 (at%).

The phase composition and crystal structure of the SbSeI thin films formed at 250 °C were investigated by Raman spectroscopy and XRD (Fig. 9a and b). In Fig. 9a, the Raman spectra of the SbSeI show distinct peaks at 96, 117, 138, 168, 180, 209, and 214  $cm^{-1}$ , which are attributed to SbSeI phase [26,35]. The Raman spectra of the thin films did not reveal the presence of secondary phases. The width of Raman peak is an indicator of the crystallinity and structural distribution, with crystalline materials exhibiting sharper and narrower Raman peaks compared to amorphous materials. For the SbSeI thin film, formed through the annealing process of  $Sb_2Se_3$ -RT at 250 °C for 5 min in  $SbI_3$  atmosphere under 100 Torr of Ar pressure, the Raman peaks were sharper and narrower in comparison to other produced thin films. This indicates a higher level of crystallinity within the SbSeI structure. The full width at half maximum (FWHM) of the main Raman peak at 209  $cm^{-1}$  is 3.82  $cm^{-1}$ .

In Fig. 9b, the XRD pattern of the SbSeI thin film crystals formed by annealing of  $Sb_2Se_3$ -RT at 250 °C for 5 min is shown. According to XRD pattern, the SbSeI film consists of orthorhombic crystal structure of SbSeI phase with the space group  $Pnma$  62 (ICSD 01-076-1354) as the primary phase. Additionally, there is a presence of  $SbI_3$ , identified as a minor secondary phase (diffraction peak at  $2\theta = 36.5^\circ$ ). Furthermore, the sharp peak at  $2\theta = 40.6^\circ$  corresponds to the (110) reflection of the Mo substrate. The determined lattice parameters for SbSeI  $a = 8.671 \text{ \AA}$ ,  $b = 4.118 \text{ \AA}$  and  $c = 10.382 \text{ \AA}$  are in good agreement with the literature data [37]. Two strong and sharp reflections at  $2\theta$  angles of  $29.4^\circ$  (112) and  $43.9^\circ$  (020) reveal that the SbSeI crystals have two preferred orientations. It is also seen in SEM image of SbSeI thin film (Fig. 8c top

view) that some crystals are grown horizontally on top of the well-oriented vertical crystals. Further research is needed to develop a growth methodology for highly c-axis-oriented SbSeI thin films with (112) reflections.

### 3.3. Characterization of SbSeI thin films' optical properties

UV-Vis spectroscopy is a widely used technique to determine the optical bandgap of thin film materials. The Kubelka-Munk theory is commonly used to evaluate the optical bandgap from reflectance spectra [38,39]. The reflectance spectra of the SbSeI thin film after using Kubelka-Munk function are shown in Fig. 10a. By extrapolating the linear least squares fit of  $[F(R_\infty)/h\nu]^2$  versus  $h\nu$  using linear fitting, where  $R_\infty$  is absolute diffuse reflectance,  $h$  is the Planck's constant and  $\nu$  is the photon frequency, estimated direct optical bandgap was found to be 1.72 eV. This value is consistent with previously reported value [40].

Optical properties of SbSeI thin films were characterized by RT-PL and LT-PL. In Fig. 10b, the RT-PL spectrum of SbSeI shows a broad asymmetric band with a maximum around 1.67 eV.

In Fig. 11a and b, the dependence of low-temperature PL emission on laser power and temperature is presented, respectively. PL observations at low temperatures show a broad and asymmetric PL band at roughly 1.4 eV.

Unfortunately, we were unable to measure the entire PL spectrum because of the detector sensitivity limitation. Despite this, we can see that the peak position of the PL band exhibits a noticeable redshift as temperature increases. This shift can be attributed to the temperature dependence of the bandgap energy. Additionally, a minor blueshift is observed with increasing laser power. The measurement system created a spectral characteristic at about 1.32 eV, which made it more challenging to pinpoint the peak position at higher temperatures. According to the power law  $\sim P^m$ , where  $P$  is the excitation power and  $m$  is the exponent, the excitation power dependence of the intensity of the integrated PL band is shown in Fig. 12a. The linear fitting enabled the extraction of the  $m$  value, indicating the type of recombination, and resulted in a value of 1.2. Usually, excitonic or band-to-band emission is associated with these high exponent values [41].

The temperature dependence of the PL band showed very fast quenching. The thermal activation energy for this band was obtained from the Arrhenius plot (Fig. 12b), where the dependence of  $\ln(\Phi)$  versus  $1000/T$  was fitted by using a theoretical expression for discrete energy levels [42]:

$$\Phi(T) = \Phi_0 / (1 + \alpha_1 T^{3/2} + \alpha_2 T^{3/2} \exp(-E_a / kT)) \quad (1)$$

where  $\Phi$  is integrated PL intensity,  $\alpha_1$  and  $\alpha_2$  are the process rate parameters and  $E_a$  is the thermal activation energy. As predicted by the fast quenching of the PL spectra with temperature, very small thermal activation energy for the PL band was obtained, see Fig. 12b. Considering the room temperature band gap of SbSeI ( $E_g = 1.72 \text{ eV}$ ) [18], the observed PL band position at  $T = 8 \text{ K}$  appears significantly distant from the band gap. The obtained small thermal activation energy of 12.7 meV

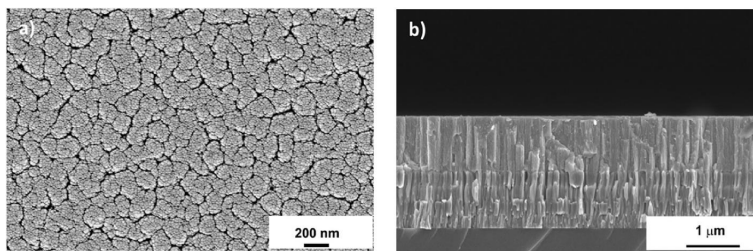


Fig. 7. SEM images of a) top view and b) cross-section of  $Sb_2Se_3$  thin film sputtered at room temperature.

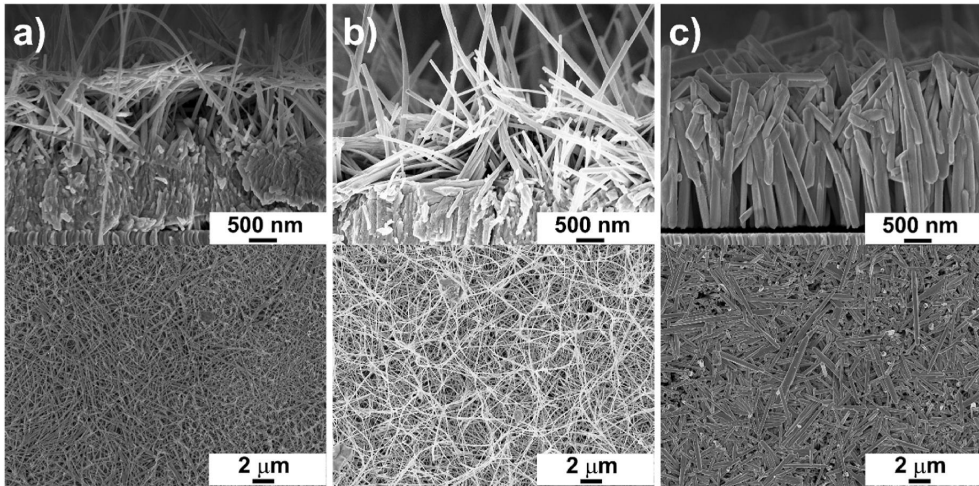


Fig. 8. SEM images of cross-section and surface of Sb<sub>2</sub>Se<sub>3</sub> thin films annealed in SbI<sub>3</sub> and 100 Torr of Ar atmosphere during 5 min at a) 200 °C, b) 225 °C and c) 250 °C.

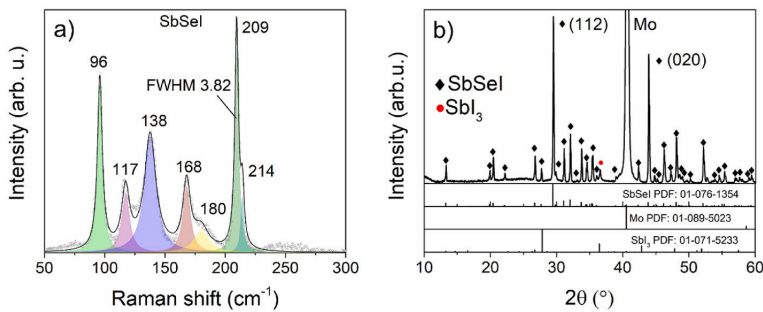


Fig. 9. a) RT Raman spectra and b) XRD pattern of Sb<sub>2</sub>Se<sub>3</sub> thin film formed by annealing Sb<sub>2</sub>Se<sub>3</sub>-RT at 250 °C for 5 min in SbI<sub>3</sub> atmosphere under 100 Torr of Ar pressure.

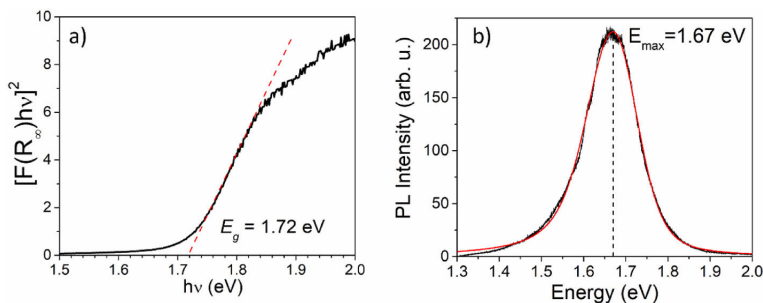


Fig. 10. a) Calculation of the optical bandgap from extrapolation of the linear least squares fit of  $[F(R_{\infty})h\nu]^2$  vs  $h\nu$  using linear fitting in the Tauc representation of Sb<sub>2</sub>Se<sub>3</sub>. Experimental data (black line); fitted range (red line). b) Room temperature photoluminescence spectrum of the Sb<sub>2</sub>Se<sub>3</sub> thin film (black line). Experimental data was fitted using SplitVoigt function (red line).

may suggest that the PL band at 1.4 eV possibly originates from the recombination of a deep donor-deep acceptor pair (DD-DA) [43,44]. The same model was also suggested for the PL bands in polycrystalline Sb<sub>2</sub>Se<sub>3</sub> [30].

The following equation can be used to determine the emission energy

from a donor-acceptor pair that is separated from one another by a distance  $r$  [45]:

$$h\nu_{max} = E_g - (E_d + E_a) + \frac{e^2}{4\pi\epsilon_0\epsilon r} \quad (2)$$

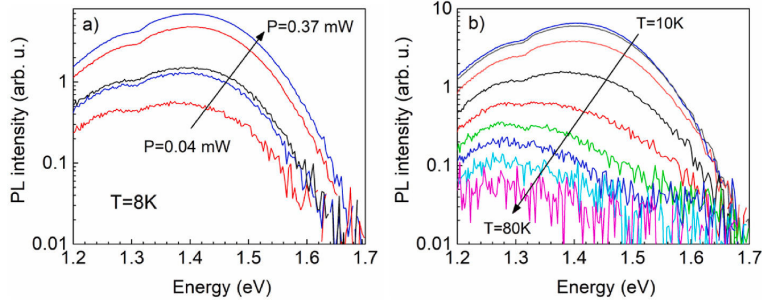


Fig. 11. a) Laser power dependence and b) temperature dependence of deep PL band.

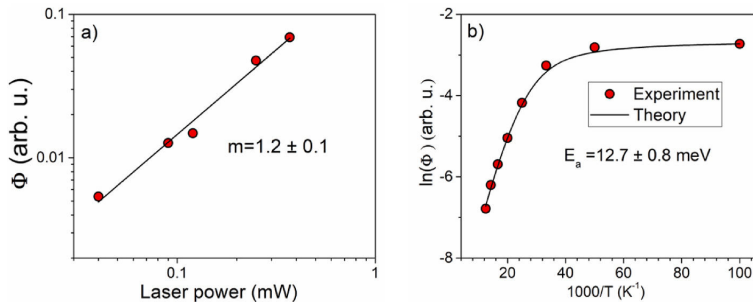


Fig. 12. a) Integral PL intensity versus laser power. The fitting result is given as a black line; b) temperature dependence of integral intensity, the fitting result with Eq. (1) is given as a black curve.

where  $E_g$  is the bandgap energy,  $E_a$  and  $E_d$  are the ionization energies of the acceptor and donor, respectively,  $r$  is the distance between the donor and acceptor,  $e$  is the electron charge,  $\epsilon$  is the static dielectric constant, and  $\epsilon_0$  is the permittivity of the vacuum. The Coulomb interaction between the donor and acceptor defects is described in Eq. (2)'s last term. The deep donor (acceptor) level's electron (hole) wave function is very confined. Therefore, only very close donor-acceptor pairs can show recombination due to overlapping of carriers wave function. When single acceptor and donor defect levels are coupled, they tend to shift closer to the band boundaries. Consequently, the thermal activation energy associated with these complexes decreases significantly. As outlined in Ref. [46], it has been observed that when the laser power is increased, the PL intensity, particularly in case of DD-DA pairs, demonstrates a near-linear increase. Future research is required to fully understand the characteristics of this deep PL band.

#### 4. Conclusions

In the present work, SbSeI thin films were prepared through a two-step process.  $Sb_2Se_3$  thin films, prepared via sputtering at 300 °C and RT, were iodized isothermally within sealed quartz ampoules in the  $SbI_3$  atmosphere under 100 Torr of argon pressure. The investigation focused on understanding the influence of technological parameters—specifically, annealing temperature and duration—during the iodization process involving various substrate types. The aim was to evaluate their impact on the morphology, composition, structural, and optical properties of the obtained SbSeI thin films. EDX and SEM analyses indicated a significant correlation between the chemical composition and the morphology of formed thin films with the annealing temperature, time and the initial  $Sb_2Se_3$  thin film substrate used. Achieving well-oriented, dense SbSeI thin films with stoichiometric composition and single-

crystal micro-columnar structures was successful by annealing  $Sb_2Se_3$ -RT in  $SbI_3$  atmosphere at 250 °C for 5 min. Raman and XRD analysis confirmed the formation of mainly single-phase high crystallinity SbSeI. The direct band gap energy value of 1.72 eV was determined by UV-Vis spectroscopy. The room-temperature PL of SbSeI exhibited a broad asymmetric PL band with a maximum at around 1.67 eV. The low-temperature ( $T = 8$  K) PL analysis revealed a distinct broad and asymmetric PL band at 1.4 eV, being quite distant from the bandgap. This PL band at 1.4 eV, coupled with a low thermal quenching activation energy of 12.7 meV, is proposed to originate from the deep donor-deep acceptor pair recombination.

#### CRedit authorship contribution statement

Marc Dolcet Sadurni: Methodology, Writing – original draft, Data curation, Investigation, Formal analysis. Kristi Timmo: Supervision, Project administration, Writing – review & editing, Investigation, Data curation, Formal analysis. Valdek Mikli: Investigation, Formal analysis. Olga Volobujeva: Investigation, Resources. Idil Mengu: Investigation, Formal analysis. Jüri Krustok: Writing – review & editing, Investigation, Formal analysis. Maarja Grossberg-Kuusik: Funding acquisition. Marit Kauk-Kuusik: Supervision, Project administration, Writing – review & editing, Funding acquisition.

#### Declaration of competing interest

The authors declare that they have no known competing financial interests or personal relationships that could have appeared to influence the work reported in this paper.

## Acknowledgements

This work was supported by European Union through the European Regional Development Fund, Project TK141 and "NAMUR+ (2020.4.01.16-0123)", and by the Estonian Research Council grant PRG1023.

## References

- [1] M. Giannouli, Current status of emerging PV technologies: a comparative study of dye-sensitized, organic, and perovskite solar cells, *Int. J. Photoenergy* 2021 (2021) 1–19, <https://doi.org/10.1155/2021/6692858>.
- [2] A.K. Jena, A. Kulkarni, T. Miyasaka, Halide perovskite photovoltaics: background, status, and future prospects, *Chem. Rev.* 119 (2019) 3036–3103, <https://doi.org/10.1021/acs.chemrev.8b00539>.
- [3] H. Min, D.Y. Lee, J. Kim, G. Kim, K.S. Lee, J. Kim, M.J. Paik, Y.K. Kim, K.S. Kim, M. G. Kim, T.J. Shin, S. Il Seok, Perovskite solar cells with atomically coherent interlayers on SnO<sub>2</sub> electrodes, *Nature* 598 (2021) 444–450, <https://doi.org/10.1038/s41586-021-03964-8>.
- [4] A. Babayigit, A. Ethirajan, M. Muller, B. Conings, Toxicity of organometal halide perovskite solar cells, *Nat. Mater.* 15 (2016) 247–251, <https://doi.org/10.1038/nmat4572>.
- [5] D. Zhang, D. Li, Y. Hu, A. Mei, H. Han, Degradation pathways in perovskite solar cells and how to meet international standards, *Commun. Mater.* 3 (2022), <https://doi.org/10.1038/s43246-022-00281-z>.
- [6] M. Ren, X. Qian, Y. Chen, T. Wang, Y. Zhao, Potential lead toxicity and leakage issues on lead halide perovskite photovoltaics, *J. Hazard Mater.* 426 (2022) 127848, <https://doi.org/10.1016/j.jhazmat.2021.127848>.
- [7] R. Tang, Z.H. Zheng, Z.H. Su, X.J. Li, Y.D. Wei, X.H. Zhang, Y.Q. Fu, J.T. Luo, P. Fan, G.X. Liang, Highly efficient and stable planar heterojunction solar cell based on sputtered and post-selenized Sb<sub>2</sub>Se<sub>3</sub> thin film, *Nano Energy* 64 (2019) 103929, <https://doi.org/10.1016/j.nanoen.2019.103929>.
- [8] R. Tang, S. Chen, Z.H. Zheng, Z.H. Su, J.T. Luo, P. Fan, X.H. Zhang, J. Tang, G. X. Liang, Heterojunction annealing enabling record open-circuit voltage in antimony triselenide solar cells, *Adv. Mater.* 34 (2022) 1–11, <https://doi.org/10.1002/adma.202109078>.
- [9] G. Liang, M. Chen, M. Ishaq, X. Li, R. Tang, Z. Zheng, Z. Su, P. Fan, X. Zhang, S. Chen, Crystal growth promotion and defects healing enable minimum open-circuit voltage deficit in antimony selenide solar cells, *Adv. Sci.* 9 (2022) 1–15, <https://doi.org/10.1002/advs.202105142>.
- [10] Y. Zhao, S. Wang, C. Li, B. Che, X. Chen, H. Chen, R. Tang, X. Wang, G. Chen, T. Wang, J. Gong, T. Chen, X. Xiao, J. Li, Regulating deposition kinetics via a novel additive-assisted chemical bath deposition technology enables fabrication of 10.57%-efficiency Sb<sub>2</sub>Se<sub>3</sub> solar cells, *Energy Environ. Sci.* 15 (2022) 5118–5128, <https://doi.org/10.1039/d2ee02261c>.
- [11] R.E. Brandt, V. Stevanovic, D.S. Ginley, T. Buonassisi, Identifying defect-tolerant semiconductors with high minority-carrier lifetimes: beyond hybrid lead halide perovskites, *MRS Commun* 5 (2015) 265–275, <https://doi.org/10.1557/mrc.2015.26>.
- [12] Y.C. Choi, R. Nie, Heavy pnictogen chalcogenides for efficient, stable, and environmentally friendly solar cell applications, *Nanotechnology* 34 (2023) 142001, <https://doi.org/10.1088/1361-6528/acb055>.
- [13] U.V. Ghorpade, M.P. Suryawanshi, M.A. Green, T. Wu, X. Hao, K.M. Ryan, Emerging chalcogenide materials for energy applications, *Chem. Rev.* 123 (2023) 327–378, <https://doi.org/10.1021/acs.chemrev.2c00422>.
- [14] R. Nie, K.S. Lee, M. Hu, M.J. Paik, S. Il Seok, Heteroleptic tin-antimony sulfide for stable and lead-free solar cells, *Matter* 3 (2020) 1701–1713, <https://doi.org/10.1016/j.matt.2020.08.020>.
- [15] R. Nie, B. Kim, S.T. Hong, S. Il Seok, Nanostructured heterojunction solar cells based on Pb<sub>2</sub>Sb<sub>2</sub>S<sub>2</sub>: linking lead halide perovskites and metal chalcogenides, *ACS Energy Lett.* 3 (2018) 2376–2382, <https://doi.org/10.1021/acsenergylett.8b01332>.
- [16] R. Nie, H.S. Yun, M.J. Paik, A. Mehta, B.W. Park, Y.C. Choi, S. Il Seok, Efficient solar cells based on light-harvesting antimony sulfide, *Adv. Energy Mater.* 8 (2018) 1–7, <https://doi.org/10.1002/aenm.201701901>.
- [17] R. Nie, J. Im, S. Il Seok, Efficient solar cells employing light-harvesting Sb<sub>0.67</sub>Bi<sub>0.33</sub>Sn, *Adv. Mater.* 31 (2019) 1–8, <https://doi.org/10.1002/adma.201808344>.
- [18] R. Nie, M. Hu, A.M. Risqi, Z. Li, S. Il Seok, Efficient and stable antimony selenide solar cells, *Adv. Sci.* 8 (2021) 1–8, <https://doi.org/10.1002/advs.202003172>.
- [19] I. Caño, A. Navarro-Güell, E. Maggi, M. Barrio, J.L. Tamarit, S. Svatek, E. Antolín, S. Yan, E. Barrena, B. Galiana, M. Placidi, J. Puigdollers, E. Saucedo, SbSeI and SbSeBr micro-columnar solar cells by a novel high pressure-based synthesis process, *J. Mater. Chem. A* (2023) 17616–17627, <https://doi.org/10.1039/d3ta03179a>.
- [20] P.I. Rentzperis, Crystal growth and structure of chalcogenides and chalcogenides of the general formulae A<sub>m</sub>B<sub>n</sub>C<sub>3</sub> and A<sub>2</sub>B<sub>3</sub> with A = As, Sb, Bi; B = S, Se, Te and C = Cl, Br, I, *Prog. Cryst. Growth Char. Mater.* 21 (1991) 113–138, [https://doi.org/10.1016/0960-8974\(91\)90010-A](https://doi.org/10.1016/0960-8974(91)90010-A).
- [21] E. Wlazlak, A. Blachecki, M. Biszyta-Szklarz, S. Klejna, T. Mazur, K. Mech, K. Pilarczyk, D. Przyczyna, M. Suchecki, P. Zawal, K. Szaciowski, Heavy pnictogen chalcogenides: the synthesis, structure and properties of these rediscovered semiconductors, *Chem. Commun.* 54 (2018) 12133–12162, <https://doi.org/10.1039/c8cc05149f>.
- [22] M. Huang, Z. Zheng, Z. Dai, X. Guo, S. Wang, L. Jiang, J. Wei, S. Chen, DASP: defect and dopant ab-initio simulation package, *J. Semiconduct.* 43 (2022), <https://doi.org/10.1088/1674-4926/43/4/042101>.
- [23] Z.S. Aliev, S.S. Musaeva, D.M. Babanly, A.V. Shevelkov, M.B. Babanly, Phase diagram of the Sb-Se-I system and thermodynamic properties of SbSeI, *J. Alloys Compd.* 505 (2010) 450–455, <https://doi.org/10.1016/j.jallcom.2010.06.103>.
- [24] M. Nowak, Photoferroelectric Nanowires, 2010, <https://doi.org/10.5772/39496>.
- [25] S. Jeon, G. Cho, W. Kim, S.-I. Kwon, Optical properties of SbSi: Co and SbSeI: Co single crystals, *Solid State Commun.* 68 (1988) 1043–1046, [https://doi.org/10.1016/0038-1098\(88\)90422-X](https://doi.org/10.1016/0038-1098(88)90422-X).
- [26] S.K. Balakrishnan, P.C. Parambil, E. Edri, Mechanistic insight into the topotactic transformation of trichalcogenides to chalcogenides, *Chem. Mater.* 34 (2022) 3468–3478, <https://doi.org/10.1021/acs.chemmater.2c00306>.
- [27] F. Palazon, Metal chalcogenides: next generation photovoltaic materials? *Sol. RRL* 6 (2022) <https://doi.org/10.1002/solr.202100829>, 1–9.
- [28] Y. Zhou, L. Wang, S. Chen, S. Qin, X. Liu, J. Chen, D.J. Xue, M. Luo, Y. Cao, Y. Cheng, E.H. Sargent, J. Tang, Thin-film Sb<sub>2</sub>Se<sub>3</sub> photovoltaics with oriented one-dimensional ribbons and benign grain boundaries, *Nat. Photonics* 9 (2015) 409–415, <https://doi.org/10.1038/nphoton.2015.78>.
- [29] Y. Di Luo, R. Tang, S. Chen, J.G. Hu, Y.K. Liu, Y.F. Li, X.S. Liu, Z.H. Zheng, Z.H. Su, X.F. Ma, P. Fan, X.H. Zhang, H.L. Ma, Z.G. Chen, G.X. Liang, An effective combination reaction involving with sputtered and selenized Sb precursors for efficient Sb<sub>2</sub>Se<sub>3</sub> thin film solar cells, *Chem. Eng. J.* 393 (2020) 124599, <https://doi.org/10.1016/j.cej.2020.124599>.
- [30] M. Grossberg, O. Volobujeva, A. Penezko, R. Kaupmees, T. Raadik, J. Krustok, Origin of photoluminescence from antimony selenide, *J. Alloys Compd.* 817 (2020) 1–5, <https://doi.org/10.1016/j.jallcom.2019.152716>.
- [31] S. Li, H. Shen, J. Chen, Y. Jiang, L. Sun, A. Raza, Y. Xu, Effect of selenization temperature on the properties of Sb<sub>2</sub>Se<sub>3</sub> thin films and solar cells by two-step method, *J. Mater. Sci. Mater. Electron.* 30 (2019) 19871–19879, <https://doi.org/10.1007/s10854-019-02354-1>.
- [32] A. Shongalova, M.R. Correia, B. Vermang, J.M.V. Cunha, P.M.P. Salomé, P. A. Fernandes, On the identification of Sb<sub>2</sub>Se<sub>3</sub> using Raman scattering, *MRS Commun* 8 (2018) 865–870, <https://doi.org/10.1557/mrc.2018.94>.
- [33] A. Kumar, V. Kumar, A. Romeo, C. Wiemer, G. Mariotto, Raman spectroscopy and in situ XRD probing of the thermal decomposition of Sb<sub>2</sub>Se<sub>3</sub> thin films, *J. Phys. Chem. C* 125 (2021) 19858–19865, <https://doi.org/10.1021/acs.jpcc.1c05047>.
- [34] G. Lucovsky, A. Mooradian, W. Taylor, G.B. Wright, R.C. Keezer, Identification of the fundamental vibrational modes of trigonal,  $\alpha$ -monoclinic and amorphous selenium, *Solid State Commun.* 5 (1967) 113–117, [https://doi.org/10.1016/0038-1098\(67\)90006-3](https://doi.org/10.1016/0038-1098(67)90006-3).
- [35] S.K. Balakrishnan, P.C. Parambil, L. Houben, M. Asher, O. Yaffe, E. Edri, Revealing hidden phases and self-healing in antimony trichalcogenides and chalcogenides, *Cell Reports Phys. Sci.* 4 (2023) 101298, <https://doi.org/10.1016/j.xcrp.2023.101298>.
- [36] G. Kanchana, D. Arivuoli, Spectroscopic investigation of BiSeI, SbSeI compounds and BiSb<sub>2</sub>Se<sub>3</sub> solid solutions, *Indian J. Eng. Mater. Sci.* 8 (2001) 373–376.
- [37] R. Bai, B. Xiao, F. Li, X. Liu, S. Xi, M. Zhu, W. Jie, B. Bin Zhang, Y. Xu, Growth of bismuth- and antimony-based chalcogenide single crystals by the physical vapor transport method, *CrystEngComm* 24 (2022) 1094–1099, <https://doi.org/10.1039/d1ce01602d>.
- [38] A. Escobedo Morales, E. Sánchez Mora, U. Pal, Use of diffuse reflectance spectroscopy for optical characterization of un-supported nanostructures, *Rev. Mexic. Fisica* 53 (2007) 18–22, <https://www.redalyc.org/articulo.oa?id=57028299004>.
- [39] G.D. Gesesse, A. Gomis-Berenguer, M.F. Barthe, C.O. Ania, On the analysis of diffuse reflectance measurements to estimate the optical properties of amorphous porous carbons and semiconductor/carbon catalysts, *J. Photochem. Photobiol. Chem.* 398 (2020), <https://doi.org/10.1016/j.jphotochem.2020.112622>.
- [40] A.C. Wibowo, C.D. Malliakas, Z. Liu, J.A. Peters, M. Sebastian, D.Y. Chung, B. W. Wessels, M.G. Kanatzidis, Photoconductivity in the chalcogenide semiconductor, SbSeI: a new candidate for hard radiation detection, *Inorg. Chem.* 52 (2013) 7045–7050, <https://doi.org/10.1021/ic401086r>.
- [41] T. Schmidt, K. Lischka, W. Zulehner, Excitation-power dependence of the near-band-edge photoluminescence of semiconductors, *Phys. Rev. B* 45 (1992) 8989–8994, <https://doi.org/10.1103/PhysRevB.45.8989>.
- [42] J. Krustok, H. Collan, K. Hjelt, Does the low-temperature Arrhenius plot of the photoluminescence intensity in CdTe point towards an erroneous activation energy? *J. Appl. Phys.* 81 (1997) 1442–1445, <https://doi.org/10.1063/1.363903>.
- [43] J. Krustok, J. Raudoja, J.H. Schön, M. Yakushev, H. Collan, Role of deep donor-deep acceptor complexes in CIS-related compounds, *Thin Solid Films* 361 (2000) 406–410, [https://doi.org/10.1016/S0022-2313\(97\)00756-7](https://doi.org/10.1016/S0022-2313(97)00756-7).
- [44] J. Krustok, H. Collan, K. Hjelt, J. Madsöon, V. Valnda, Photoluminescence from deep acceptor-deep donor complexes in CdTe, *J. Lumin.* 72–74 (1997) 103–105, [https://doi.org/10.1016/S0022-2313\(97\)00061-6](https://doi.org/10.1016/S0022-2313(97)00061-6).
- [45] F. Williams, Donor-acceptor pairs in semiconductors, *Phys. Status Solidi.* 25 (1968) 493–512, <https://doi.org/10.1002/psbb.19680250202>.
- [46] J. Krustok, T. Raadik, M. Grossberg, M. Kauk-Kuusik, V. Trifiletti, S. Binetti, Photoluminescence study of deep donor- deep acceptor pairs in Cu<sub>2</sub>ZnSnS<sub>4</sub>, *Mater. Sci. Semicond. Process.* 80 (2018) 52–55, <https://doi.org/10.1016/j.mssp.2018.02.025>.



## Appendix 2

### Publication II

**M. Dolcet Sadurni**, J. Krustok, K. Timmo, V. Mikli, R. Kondrotas, M. Grossberg- Kuusk, M. Kauk-Kuusik, “Radiative recombination model for BiSeI microcrystals: unveiling deep defects through photoluminescence” *Journal of Physics: Energy* 6 (2024) 045004, <https://doi.org/10.1088/2515-7655/ad8377>.



PAPER • OPEN ACCESS

## Radiative recombination model for BiSeI microcrystals: unveiling deep defects through photoluminescence

To cite this article: Marc Dolcet Sadurni *et al* 2024 *J. Phys. Energy* **6** 045004

View the [article online](#) for updates and enhancements.

You may also like

- [Optical, electrical, structural and magnetic properties of BiSe thin films produced by CBD on different substrates for optoelectronics applications](#)  
Fatih Aydın, Fatma Meydaneri Tezel and Afın Kariper
- [Observation of Dirac-like surface state bands on the top surface of BiSe](#)  
H. Lohani, K. Majhi, R. Ganesan et al.
- [Electronic properties of BiSeI and BiSeBr](#)  
C Y Fong, C Perlov and F Wooten



## PAPER

## OPEN ACCESS

RECEIVED  
6 August 2024REVISED  
26 September 2024ACCEPTED FOR PUBLICATION  
4 October 2024PUBLISHED  
15 October 2024

Original content from  
this work may be used  
under the terms of the  
[Creative Commons  
Attribution 4.0 licence](#).

Any further distribution  
of this work must  
maintain attribution to  
the author(s) and the title  
of the work, journal  
citation and DOI.



# Radiative recombination model for BiSeI microcrystals: unveiling deep defects through photoluminescence

Marc Dolcet Sadurni<sup>1,\*</sup>, Jüri Krustok<sup>1</sup>, Kristi Timmo<sup>1</sup>, Valdek Mikli<sup>1</sup>, Rokas Kondrotas<sup>2</sup>,  
Maarja Grossberg-Kuusik<sup>1</sup> and Marit Kauk-Kuusik<sup>1</sup>

<sup>1</sup> Department of Materials and Environmental Technology, Tallinn University of Technology, Ehitajate tee 5, Tallinn 19086, Estonia

<sup>2</sup> Department of Characterisation of Materials Structure, Center for Physical Sciences and Technology, Saulėtekio av. 3, Vilnius 10257, Lithuania

\* Author to whom any correspondence should be addressed.

E-mail: [marc.dolcet@taltech.ee](mailto:marc.dolcet@taltech.ee)

**Keywords:** bismuth selenoiodide, pnictogen chalcogenides, photoluminescence, BiSeI

## Abstract

Pnictogen chalcogenides are semiconductors that have emerged as promising materials for energy conversion due to their exceptional optoelectronic properties. Their electronic configuration ( $ns^2$ ), particularly for Bi- and Sb-based compounds, can be a key factor in efficient carrier transport and defect tolerance, similarly, to Pb-perovskites. In the present study, the Bi-containing chalcogenide, bismuth selenoiodide (BiSeI) was synthesized via isothermal heat treatment of binary precursors in evacuated quartz ampoules. The synthesized BiSeI microcrystals exhibited a characteristic needle-like morphology and a near-stoichiometric composition. Both indirect and direct band gap energies of BiSeI were determined by ultraviolet–visible–near-infrared diffuse reflectance spectroscopy, with room temperature values of 1.17 eV and 1.29 eV, respectively. This study presents the first experimental investigation of the photoluminescence properties of BiSeI microcrystals resulting in a recombination model involving multiple defect states. This work provides valuable insights into the defect structure and recombination mechanisms within BiSeI, paving the way for further exploration of its potential in optoelectronic devices.

## 1. Introduction

The escalating global energy demand and the detrimental effects of climate change have highlighted the necessity for sustainable energy solutions. Among these, photovoltaic (PV) energy stands out as a viable and promising alternative. The development of efficient and cost-effective solar cell materials is crucial in the growth of PV technologies [1, 2]. New solar absorbers must exhibit excellent optoelectronic properties, a tunable band gap ideally between 1.1–1.5 eV [3], a high absorption coefficient, high carrier mobility and defect tolerance. These materials should also demonstrate stability under ambient conditions (including temperature, humidity, and light exposure) and must be non-toxic.

Heavy pnictogen chalcogenides represent a class of inorganic ternary semiconductors characterized by the general formula  $A^V B^VI C^{VII}$ , where  $A = \text{Bi, Sb}$ ;  $B = \text{S, Se}$ ;  $C = \text{Br, I}$ . These materials are formed by the combination of a pnictogen cation (A) and two anions, a chalcogen (B) and a halogen (C). They share a similar  $ns^2$  outer electronic configuration ( $\text{Bi}^{3+}$ ,  $\text{Sb}^{3+}$ ) with perovskites [4, 5]. This electronic structure is believed to be closely linked to efficient carrier transport and good defect tolerance, which are key factors contributing to the high performance of perovskite solar cells [6]. Consequently, Bi and Sb-based chalcogenides are expected to exhibit similar optoelectronic properties, making them promising absorbers. They have been recently investigated and applied not only in PV applications [7–11] but also in photocatalysis, photodetectors [12], thermoelectric devices [13], and piezoelectric nanogenerators [11, 12, 14, 15] among other potential applications.

Among heavy pnictogen chalcogenides, bismuth selenoiodide (BiSeI) possess a high absorption coefficient ( $\sim 10^5 \text{ cm}^{-1}$ ) [16] and a narrow band gap of 1.29 eV [17]. Density functional theory

calculations indicate a small difference between the direct and indirect band gap energies of BiSeI, reported as 0.02 eV in [18] and 0.1 eV in [19]. This material crystallizes in the orthorhombic crystal structure [20] with *Pnma* (62) space group [4]. Similarly to other pnictogen chalcogenides, the structure of BiSeI consists of double chains of  $(\text{Bi}_2\text{Se}_2\text{I}_2)_n$ . Within these ribbons, Bi and Se atoms exhibit strong covalent bonding, while iodine ions are bonded ionically with a covalently bound bridge [21]. Neighboring ribbons are linked by weak van der Waals forces [17], resulting in a layered structure.

Several synthesis methods have been explored for BiSeI materials, including physical vapor transport [17, 21–23], solution-based growth [24], ball milling [25] etc. The used synthesis method significantly influences the electrical conductivity type and defect structure of BiSeI crystals. The stoichiometry during growth plays a crucial role in determining the nature and concentration of defects within the crystal lattice of BiSeI. Anion-rich conditions (excess of Se and I) are likely to promote the formation of acceptor-like defects, such as  $\text{Se}_{\text{Bi}}$ ,  $V_{\text{Bi}}$ , while Bi-rich environments favor the creation of donor-like defects, such as  $\text{Bi}_{\text{Se}}$ ,  $V_{\text{I}}$ ,  $V_{\text{Se}}$  and  $\text{Bi}_i$  [18].

Despite the promising optoelectronic properties of BiSeI, no experimental data is currently available regarding its defect structure. In this study, the optical properties of BiSeI, particularly the band gap energies, were determined. Due to the limited understanding of BiSeI's defect structure and recombination mechanisms, a photoluminescence (PL) study was conducted at different temperatures and laser excitation powers to experimentally investigate these aspects.

## 2. Experimental details

BiSeI microcrystals used in this study were synthesized via a solid-state method, using self-prepared  $\text{Bi}_2\text{Se}_3$  and commercially available  $\text{BiI}_3$  (Aldrich, 99%). The precursors were used in a molar ratio of Bi : Se : I = 1 : 1 : 1, calculated based on the masses of the binary precursors and weighed to achieve a total mass of 1 g according to the reaction formula:  $\text{Bi}_2\text{Se}_3 + \text{BiI}_3 \rightarrow 3\text{BiSeI}$ .

The mixture of precursors was finely ground in an agate mortar to achieve uniformity and facilitate the reaction. The homogeneous mixture was transferred into a quartz ampoule with dimensions of 6.5 cm in length and 1.2 cm in diameter. The ampoule was then subjected to dynamic vacuum degassing and sealed. It was gradually heated from room temperature (RT) to 225 °C within 3 h. After maintaining this temperature for 24 h, the temperature was further increased from 225 °C to 440 °C within 5 h. The material was held at 440 °C for 256 h before being cooled down to RT by removing the ampoule from the furnace to ambient conditions.

The morphology of BiSeI microcrystals was investigated using a high-resolution scanning electron microscope (HR-SEM Zeiss Merlin). For detailed surface imaging, a high-efficiency In-lens secondary electron detector was used. To achieve compositional contrast, an energy-selective backscattered electron detector was utilized. The chemical composition of individual crystals was analyzed using x-ray dispersive spectroscopy (EDX) with a Bruker Esprit 1.82 system with an EDX-XFlash 3001 detector. Polished samples revealing the bulk of the crystals was examined using an accelerating voltage of 20 kV. X-ray diffraction (XRD) was the technique selected to characterize the crystal structure of BiSeI microcrystals. A Rigaku Ultima IV diffractometer utilizing monochromatic Cu  $K\alpha$  radiation ( $\lambda = 1.5406 \text{ \AA}$ , 40 kV, 40 mA and a silicon strip detector (D/teX Ultra) was used. Phase identification and calculation of lattice parameters were performed using PDXL2 Rigaku software. The phase composition of BiSeI microcrystals was further investigated by RT micro-Raman spectroscopy. A Horiba's LabRam HR 800 spectrometer equipped with a cooled multichannel CCD detector in a backscattering configuration was utilized to carry out the measurements. The YAG: Nd 532 nm laser with a power density of  $13 \text{ kW cm}^{-2}$  was focused on the individual crystals. The same equipment was used to perform RT-PL measurements. ultraviolet–visible–near-infrared (UV–Vis–NIR) diffuse reflectance was measured using Shimadzu UV-3600 two-beam spectrometer equipped with a multi-purpose compartment MPC-3100. Samples were placed in a 60 mm integrating sphere and a barium sulphate target was used for calibration. Measurements were recorded between 260 and 2600 nm. For temperature-dependent PL measurements, BiSeI single crystals were placed on the cold finger of the closed-cycle helium cryostat (Janis CCS-150). Then its temperature was decreased to 8 K. The temperature was adjusted up to 200 K via a temperature controller (LakeShore Model 335). PL excitation was achieved using a 532 nm Cobolt 08-DPL laser. The power density of the incident laser beam was altered via neutral density filters between  $0.04$  and  $0.3 \text{ W cm}^{-2}$ . An optical chopper was used for modulating the laser light. The resulting luminescence was filtered through a cut-off low-pass filter and then directed towards a computer-controlled single grating ( $600 \text{ lines mm}^{-1}$ ) monochromator ( $f = 0.64 \text{ m}$ ) (Horiba Jobin Yvon FHR640). Two different detectors were used, R632 and InGaAs photomultiplier tubes (PMT). A Stanford SR810 DSP lock-in amplifier was employed to amplify the PL signal.

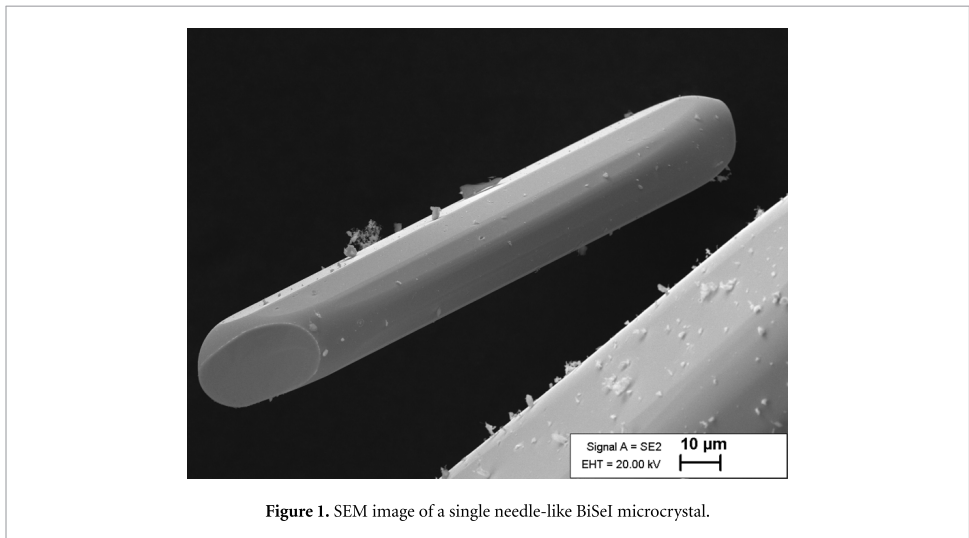


Figure 1. SEM image of a single needle-like BiSeI microcrystal.

### 3. Results and discussion

#### 3.1. Elemental and phase composition of BiSeI microcrystals

SEM studies of the synthesized microcrystals (figure 1) showed the formation of needle-like crystals, consistent with previous reports on BiSeI [17] and similar to other pnictogen chalcogenides [26, 27]. These crystals exhibit variations in both thickness and length, reflecting the anisotropic growth behaviour of BiSeI. Crystal lengths range from tens of micrometers to several centimeters, while their thickness typically remains below 500  $\mu\text{m}$ . EDX analysis of the bulk of the microcrystals revealed an average composition of 34.1 at% of Bi, 32.7 at% of Se, and 33.2 at% of I. This composition closely corresponds to the expected stoichiometric ratio of 1:1:1 (33.3 at% for each element), confirming the successful synthesis of BiSeI.

In figure 2(a), the XRD pattern of the synthesized BiSeI microcrystals is shown. The diffraction peaks were compared to the reference pattern of BiSeI (ICDD 01-070-4693). The analysis indicated that the majority of the observed diffraction peaks align with the orthorhombic crystal structure with the space group  $Pnma$  (62). This excellent agreement with the reference pattern confirms that BiSeI is the predominant phase present in the synthesized microcrystals. However, to some extent, the presence of  $\text{Bi}_2\text{Se}_3$  (ICDD 01-077-7147) as a secondary phase was identified. These secondary phase peaks were located at  $2\theta$  values of  $18.6^\circ$ ,  $28.1^\circ$  and  $37.7^\circ$ . Calculated lattice parameters of BiSeI were following:  $a = 8.6956(5) \text{ \AA}$ ,  $b = 4.2155(9) \text{ \AA}$ ,  $c = 10.5715(5) \text{ \AA}$ , which are in agreement with previous reports [25, 28]. The phase composition of individual BiSeI microcrystals was also investigated using Raman spectroscopy. The Raman spectrum, shown in figure 2(b), was fitted using Lorentzian functions to resolve the peaks. The analysis revealed Raman peaks at 75, 96, 105, 115, 137, 153, 159, 182 and  $186 \text{ cm}^{-1}$ , which are in a good agreement with previously reported Raman data of BiSeI [29]. Raman peaks at 153, 159, 182 and  $186 \text{ cm}^{-1}$  are associated with Bi-Se, while peaks at 75 and  $96 \text{ cm}^{-1}$  with Bi-I vibration modes [30–32]. Raman measurements were done from different grains and different spots. No secondary phase peaks corresponding to  $\text{Bi}_2\text{Se}_3$  [33, 34] could be detected in the Raman spectrum. Although minor residual amounts of  $\text{Bi}_2\text{Se}_3$  were detected in the final product by XRD, the overall composition of the synthesized BiSeI microcrystals remains predominantly pure, as confirmed by EDX and Raman analyses. This discrepancy may be attributed to the use of a polycrystalline form of BiSeI powder material for the XRD analysis, while single, carefully selected crystals were used for the Raman and PL measurements. Consequently, the presence of traces of  $\text{Bi}_2\text{Se}_3$  is unlikely to significantly impact the bulk PL response. Furthermore, the band gap energy of  $\text{Bi}_2\text{Se}_3$  single crystals has been reported to be between 0.22 eV [35] and 0.33 eV [36]. This significant difference in band gap makes it highly unlikely that any PL band observed in the PL spectra of BiSeI can be attributed to  $\text{Bi}_2\text{Se}_3$ .

#### 3.2. Optical properties of BiSeI microcrystals

UV–Vis–NIR diffuse reflectance measurements were performed on BiSeI microcrystals to determine the optical band gap. The band gap energy of BiSeI microcrystals was determined using the Kubelka–Munk

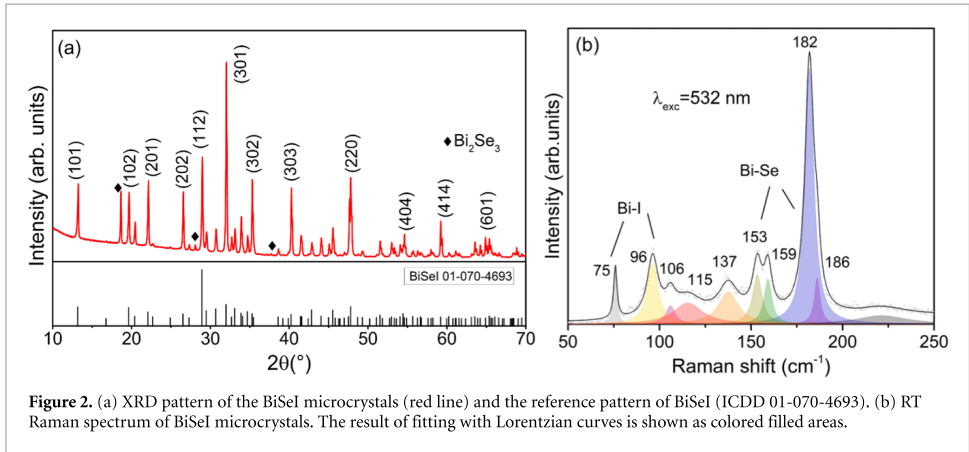


**Figure 2.** (a) XRD pattern of the BiSeI microcrystals (red line) and the reference pattern of BiSeI (ICDD 01-070-4693). (b) RT Raman spectrum of BiSeI microcrystals. The result of fitting with Lorentzian curves is shown as colored filled areas.

theory [37]. The band gap energy was estimated by fitting the data according to the Tauc equation:

$$(\alpha h\nu)^{1/n} = A(h\nu - E_g) \quad (1)$$

where  $\alpha$  is the absorption coefficient,  $h$  is the Planck constant,  $\nu$  is the photon's frequency of vibration,  $A$  is a proportional constant,  $E_g$  is the band gap energy and the value of the  $n$  exponent indicates the nature of the optical transition,  $1/2$  for direct and  $2$  for indirect transition. The diffuse reflectance spectrum can be converted to Kubelka–Munk function by quantifying  $F(R_\infty)$ , in the limiting case of an infinitely thick sample, which is proportional to  $\alpha$  [37],

$$F(R_\infty) = \frac{(1 - R_\infty)^2}{2R_\infty} \sim \alpha \quad (2)$$

where  $R_\infty$  is the absolute diffuse reflectance. Then,

$$(F(R_\infty) h\nu)^{1/n} = A(h\nu - E_g). \quad (3)$$

A tangent line can be drawn from the linear part of the function to zero to determine the band gap energy of BiSeI, as shown in figure 3. Direct band gap value of  $E_g = 1.29$  eV and indirect band gap value of  $E_g = 1.17$  eV were obtained. The determined indirect band gap aligns well with previous report [30]. However, it should be noted that  $[F(R_\infty) h\nu]^{1/2}$  does not converge to 0 when  $h\nu$  decreases. This limitation suggests that it is not possible to be completely certain about the precise value of the indirect band gap energy. Nevertheless, the observed difference of 0.12 eV between the direct and indirect band gaps is consistent with prior theoretical calculations for BiSeI [19].

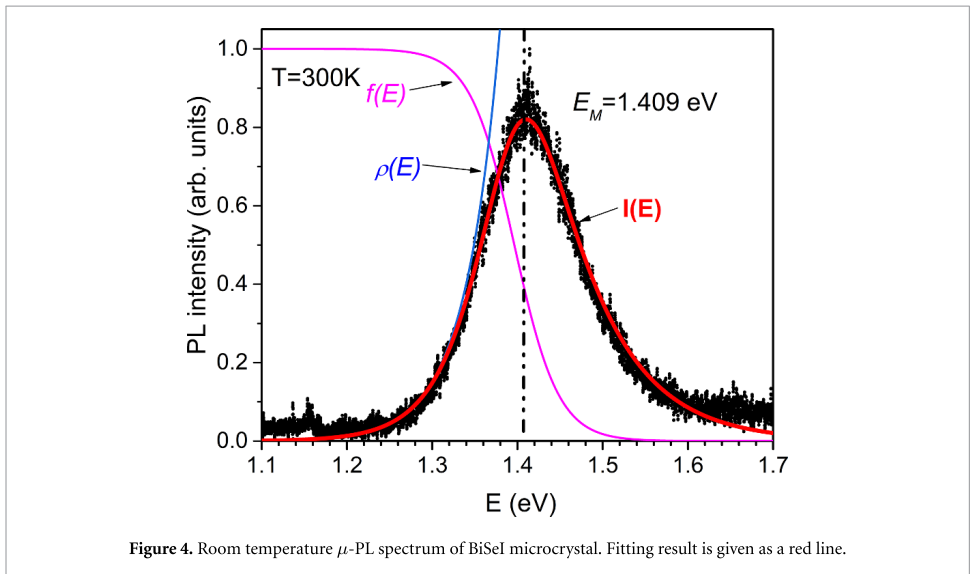
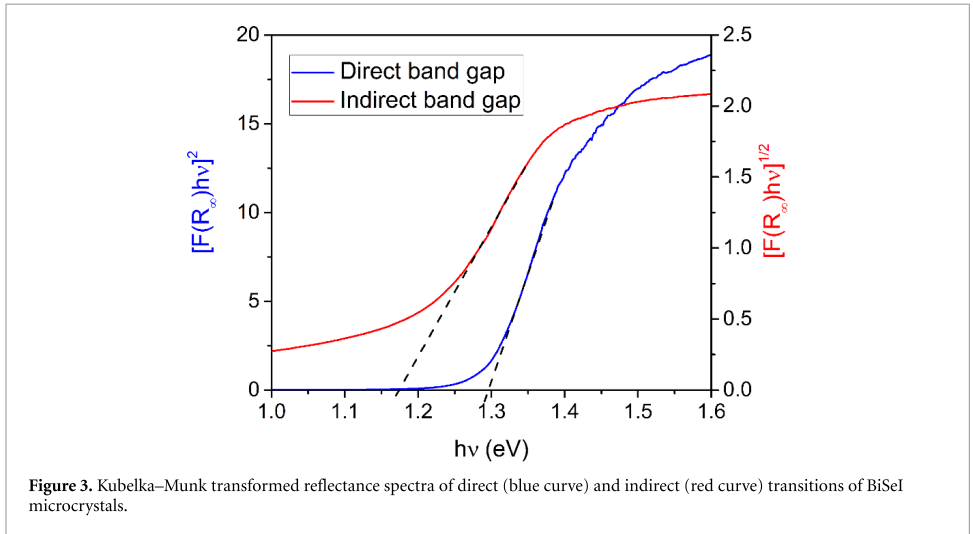
The room-temperature  $\mu$ -PL spectrum of the BiSeI microcrystal showed only one slightly asymmetric band (see figure 4). The PL intensity of this band was quite low even at very high laser power density ( $\sim 13$  kW cm $^{-2}$ ). This maximum laser power density was selected to ensure that the Raman or PL spectra of the sample remained unchanged. The rise in intensity from the high energy side of the band is rather gentle compared to the more abrupt fall from the low energy side. This type of PL band shape is typical for band-to-band (BB) recombination, where the shape of the high energy side is determined by the Fermi distribution function

$$f(E) = [1 + \exp((E - E_F)/kT)]^{-1} \quad (4)$$

and the shape of the low energy side is related to the density of states function  $\rho(E)$  [38–40]. The nearly exponential low energy side of the BB-band of studied crystal suggests that the defect density is quite large, resulting in the creation of exponential Urbach-like tail states. Therefore, the  $\rho(E)$  function has a form

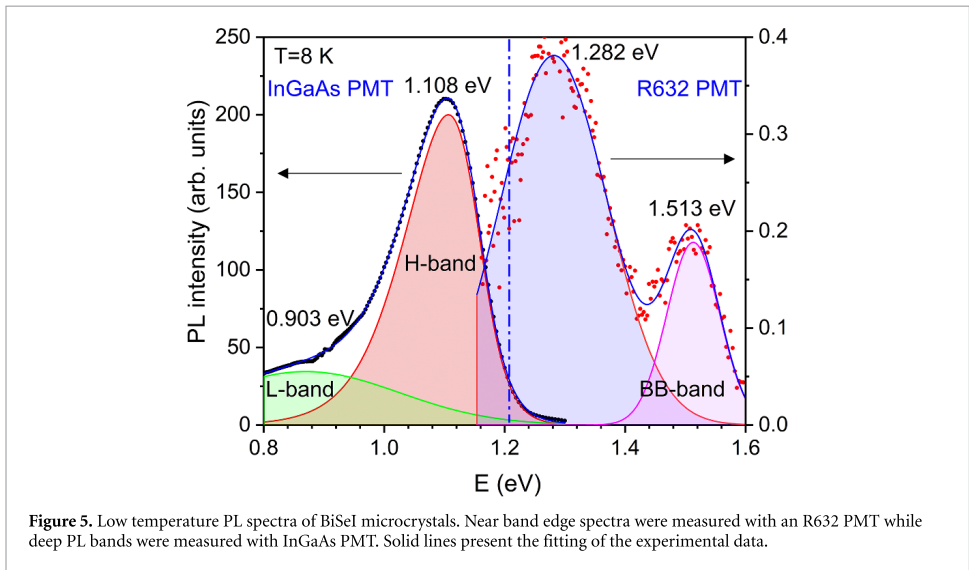
$$\rho(E) = \rho_0 \exp[(E - E_g)/E_u], \quad (5)$$

where  $E_g$  is the band gap energy, and  $E_u$  is the characteristic Urbach energy that scales the extent of the Urbach tail density of localized defect states in the gap;  $\rho_0$  is an amplitude factor [40]. Consequently,



$I(E) = f(E) * \rho(E)$  function was used to fit RT BB-band shape. The result of this fitting is given in figure 4 as a continuous line. The best fit was obtained using the following values:  $E_F = 1.396$  eV,  $E_g = 1.336$  eV,  $E_U = 41$  meV, and  $T = 300$  K. The peak position of the BB-band is measured at  $E_M = 1.409$  eV. Even though the peak position of the BB-band varies with temperature and excitation intensity, it is frequently used to calculate the band gap energy  $E_g$ . In this case, due to the quite high excitation intensity, it is expected that the real band gap energy is lower than the peak position  $E_M$ . Although there is a 73 meV difference between these values, it must be considered that the density of states function could have a more complex structure. As a result, the shape of BB-band can only provide a rough estimation of the value of  $E_g$ . Moreover, the intensity of this BB-band was very weak, which can be attributed to the presence of both indirect and direct band gaps. In that case, the low energy side of the BB-band may have an even more intricate shape. Nevertheless, the RT band gap value obtained from the fitting is very close to the theoretically calculated value  $E_g = 1.31$  eV [18].

However, the band gap energy obtained from the RT-PL measurements is higher (about 46 meV) than the same energy obtained from reflectance measurements. In this case, state-filling of band edge states occurs due to very high excitation power. A similar effect was observed by Fang *et al* where the BB-band exhibited a blueshift with increasing laser power [41].



As shown in figure 5, low temperature ( $T = 8$  K) PL measurements identified four distinct PL bands. BB emission was measured using an R632 PMT and two very weak PL bands were detected. Both bands were fitted using Gaussian function. The PL band at 1.513 eV is nearly identical to the 0 K direct band gap value of  $E_g = 1.52$  eV calculated in [18], indicating that BB recombination is associated with this band. Anticipating that the BB peak position will now be closer to the band gap value due to the relatively low laser power density ( $\sim 0.3$  W cm<sup>2</sup>). Using the RT value of  $E_g = 1.336$  eV and the experimentally determined rate of temperature dependence of  $E_g$  ( $dE_g/dT = -6.5 \times 10^{-4}$  eV K<sup>-1</sup>) [42], it is also possible to derive the low temperature  $E_g$  value of 1.52 eV.

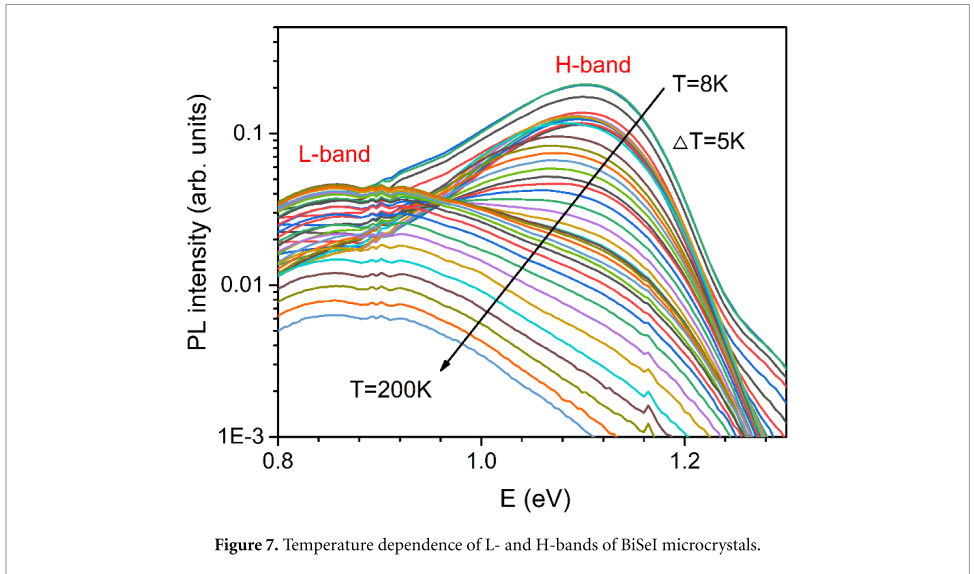
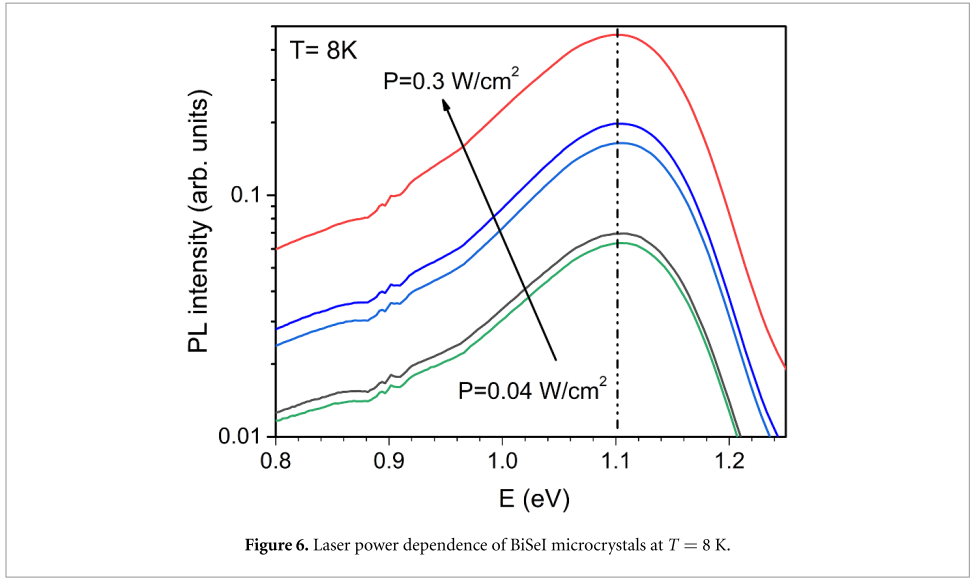
Unfortunately, a thorough examination of this BB-band was hindered by its extremely low intensity. The deeper PL band at 1.282 eV also exhibited the same issue. Unfortunately, the origin of this band cannot be determined.

Two deeper bands with relatively high intensity were observed by using the InGaAs PMT. They are referred to as the H-band ( $E_M = 1.108$  eV) and L-band ( $E_M = 0.903$  eV). It is evident that these bands are associated with different types of recombination. Due to the asymmetric shape of the H-band, the data was fitted using the asymmetric double sigmoidal function. Since the L-band was less pronounced, it was fitted with a Gaussian function. All the fitting results are shown in figure 5.

The laser power and temperature dependence of synthesized BiSeI microcrystals could be measured due to the high PL starting intensity. Figure 6 shows the laser power dependence. It is evident that both the general shape of the L- and H-bands and the peak position of the H-band remain unchanged with increasing laser power. This suggests that both bands have similar origins.

The H- and L-band temperature dependence is displayed in figure 7. At lower temperatures, the H-band predominates, whereas at higher temperatures, the L-band begins to dominate. It indicates that the thermal activation energies of the two PL bands are not the same. Indeed, figure 8 shows the Arrhenius plot for both PL bands. The higher temperature part was fitted using a simple function  $\Phi = \Phi_0 / [1 + \alpha \exp(E_a/kT)]$ , where  $E_a$  is a thermal activation energy,  $\Phi$  is the integral intensity of PL band, and  $\alpha$  is a fitting constant. The activation energies that were obtained are relatively close to each other, see figure 8. At the same time, there is more rapid quenching of the H-band, as shown in figure 7. This is possible if the values of parameter  $\alpha$  are different for both PL bands. The parameter  $\alpha$  is proportional to the probability of electronic transition from a localized donor level to a delocalized band, and a higher value of  $\alpha$  leads to more rapid quenching of the PL band [43]. Indeed, the  $\alpha$  values are  $7.8 \times 10^6$  and  $2.2 \times 10^5$  for the H- and L-band, respectively. Different values of  $\alpha$  are probably related to different donor defects of DD-DA pairs.

The peak positions of both deep PL bands are distant from the band gap energy. General distant donor-acceptor pair recombination model and recombination involving Urbach tail states can be ruled out due to the relatively low  $E_a$  values and the absence of peak position shift with increasing laser intensity. Similar conditions have been found in many other semiconductor compounds, and recombination between discrete levels that are far from band edges is frequently cited as the cause. The temperature and laser power



dependencies of both bands suggest that these bands may be related to deep donor-deep acceptor (DD-DA) complexes. The DD-DA pair model was initially proposed to explain similar behavior of deep PL bands in CdTe [44] and in various chalcopyrites [45–47]. Because the electron and hole wave functions are localized in these deep levels, PL emissions from these DA pairs can only be seen at smallest separation between donor and acceptor defects. In this model the emission energy from a DA pair separated by a distance  $r$  is obtained from [47]

$$E(r) = E_g - (E_A^0 + E_D^0) + \frac{e^2}{\epsilon r} - \Gamma(r), \quad (6)$$

where  $E_g$  is the band gap energy,  $E_A^0$  and  $E_D^0$  are the acceptor and donor ionization energies,  $\epsilon$  is the dielectric constant, and  $\Gamma(r)$  refers to interactions that are only important at extremely short distances. However, as Williams [48] demonstrated, in the case of extremely short donor-acceptor distances, the magnitude of  $\Gamma(r)$  may be greater than or equal to 25 meV.

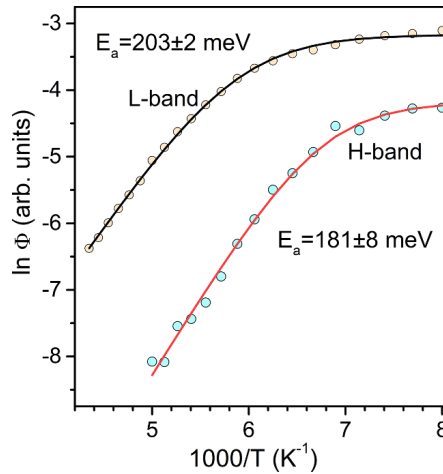


**Figure 8.** Arrhenius plots derived from the temperature dependence of PL spectra together with the obtained thermal activation energy values,  $E_a$ .

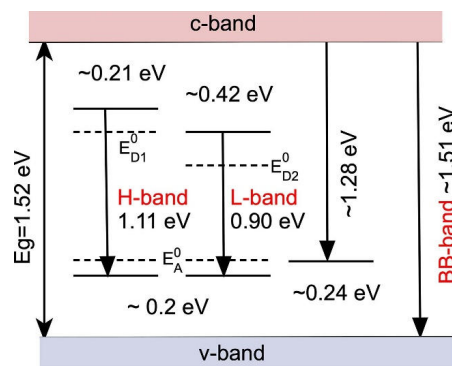


**Figure 9.** Radiative recombination model for BiSeI microcrystal at  $T = 8$  K.

As a result, the Coulombic energy determined theoretically typically tends to be slightly higher than the energy observed experimentally. Although the precise value of the dielectric constant in BiSeI is unknown, estimates place it at approximately 35 [6]. The shortest distance between different lattice sites in BiSeI is between Bi and Se sites, where  $r = 2.74 \text{ \AA}$  [19]. So, the highest value of the Coulomb term in BiSeI is about 150 meV. Moreover, in the spaces between the one-dimensional ribbons, two interstitial defect sites are present: one penta-coordinated site and one octa-coordinated site. So, iodine on chalcogen antisite ( $I_{Se}$ ), anion on bismuth antisites ( $Se_{Bi}$  and  $I_{Bi}$ ), anion vacancies ( $V_I$  and  $V_{Se}$ ), bismuth interstitial ( $Bi_i$ ), a bismuth vacancy ( $V_{Bi}$ ), Se on iodine antisite ( $Se_I$ ), bismuth on Se and I antisites ( $Bi_{Se}$  and  $Bi_I$ ), and anion interstitials ( $Se_i$  and  $I_i$ ) can be found in BiSeI crystals [18]. Unfortunately, there is a lack of experimental information on potential defects in BiSeI; however, theoretical defect energy calculations were carried out by Ganose *et al* [18]. The PL data from this study indicates that the H-band and L-band may be associated with the same DA defect, which has an activation energy of approximately 0.2 eV. A weak edge emission band at 1.282 eV, is also most likely associated with the same acceptor defect. According to the computation results provided by Ganose *et al*, the most suitable acceptor defect is  $V_{Bi}$ . At the same time, DD defects for the H- and L-bands are different. There are several DD defects present in BiSeI crystals. The most appropriate defects are  $Se_{Bi}$  and interstitial  $I_i$  with both coordination symmetry [18]. Further research will be necessary to determine the exact origin of the DD defects in the H- and L-bands, as there is currently significant uncertainty in this area. As a result of this study, the radiative recombination model for BiSeI crystals is presented in figure 9.

## 4. Conclusion

BiSeI microcrystals with a needle-like morphology were successfully synthesized via a solid-state method using  $\text{Bi}_2\text{Se}_3$  and  $\text{BiI}_3$  precursors. The formation of BiSeI predominantly as a single phase was confirmed by Raman spectroscopy and XRD. The synthesized material exhibited a composition close to stoichiometric ( $\text{Bi} : \text{Se} : \text{I} = 1 : 0.96 : 0.97$ ) and crystallized in an orthorhombic structure with the  $Pnma$  (62) space group. RT indirect band gap of 1.17 and direct band gap of 1.29 eV were determined from the UV–Vis–NIR reflectance spectra of BiSeI microcrystals. The comprehensive PL study revealed a complex defect structure in BiSeI microcrystals. At 8 K, four distinct PL bands have been observed. The H- and L-bands are attributed to DD-DA pairs, while the band at 1.282 eV is likely related to a deep defect with an ionization energy of 240 meV. These three bands may be associated with a bismuth vacancy defect. Additionally, DD defects contributing to the H- and L-bands could be identified as  $\text{Se}_{\text{Bi}}$  and interstitial  $\text{I}_i$ . Finally, BB-band is attributed to a BB recombination. The identification of these defect states provides crucial insights into the radiative recombination pathways, which is essential for optimizing material performance. However, further research is needed to accurately identify the origin of DD defects in the H- and L-bands.

## Data availability statement

All data that support the findings of this study are included within the article (and any supplementary files).

## Acknowledgment

This work was supported by European Union through the European Regional Development Fund, Project TK210, by the Estonian Research Council Grant PRG1023 and the research was conducted using the NAMUR+ core facility funded by the Estonian Research Council (TT13).

## Conflict of interest

The authors declare that they have no known competing financial interests or personal relationships that could have appeared to influence the work reported in this paper.

## ORCID iDs

Marc Dolcet Sadurni  <https://orcid.org/0000-0003-0821-1550>

Jüri Krustok  <https://orcid.org/0000-0002-4671-2332>

Kristi Timmo  <https://orcid.org/0000-0001-6054-6783>

Valdek Mikli  <https://orcid.org/0000-0002-2406-3562>

Rokas Kondrotas  <https://orcid.org/0000-0002-1751-7909>

Maarja Grossberg-Kuusk  <https://orcid.org/0000-0003-3357-189X>

Marit Kauk-Kuusik  <https://orcid.org/0000-0003-0071-8568>

## References

- [1] Wang K, Xu Z, Guo Z, Wang H, Qaid S M H, Yang K and Zang Z 2024 Phosphonate diacid molecule induced crystallization manipulation and defect passivation for high-performance inverted MA-free perovskite solar cells *Adv. Energy Mater.* **14** 2402249
- [2] He T, Jiang Y, Xing X and Yuan M 2020 Structured perovskite light absorbers for efficient and stable photovoltaics *Adv. Mater.* **32** 1–17
- [3] Bremner S P, Yi C, Almansouri I, Ho-Baillie A and Green M A 2016 Optimum band gap combinations to make best use of new photovoltaic materials *Sol. Energy* **135** 750–7
- [4] Brandt R E, Stevanović V, Ginley D S and Buonassisi T 2015 Identifying defect-tolerant semiconductors with high minority-carrier lifetimes: beyond hybrid lead halide perovskites *MRS Commun.* **5** 265–75
- [5] Grandhi G K, Hardy D, Krishnaiah M, Vargas B, Al-Anesi B, Suryawanshi M P, Solis-Ibarra D, Gao F, Hoye R L Z and Vivo P 2023 Wide-bandgap perovskite-inspired materials: defect-driven challenges for high-performance optoelectronics *Adv. Funct. Mater.* **2307441**
- [6] Shi H, Ming W and Du M H 2016 Bismuth chalcogenides and oxyhalides as optoelectronic materials *Phys. Rev. B* **93** 1–7
- [7] Hahn N T, Self J L and Mullins C B 2012 BiSI micro-rod thin films: efficient solar absorber electrodes? *J. Phys. Chem. Lett.* **3** 1571–6
- [8] Choi Y C and Jung K W 2020 Recent progress in fabrication of antimony/bismuth chalcogenides for lead-free solar cell applications *Nanomaterials* **10** 1–15
- [9] Nie R, Hu M, Risqi A M, Li Z and Seok S I 2021 Efficient and stable antimony selenide solar cells *Adv. Sci.* **8** 1–8
- [10] Nie R, Im J and Seok S I 2019 Efficient solar cells employing light-harvesting Sb 0.67 Bi 0.33 SI *Adv. Mater.* **31** 1–8
- [11] Nie R and Seok S I 2020 Efficient antimony-based solar cells by enhanced charge transfer *Small Methods* **4** 1–10
- [12] Farooq S, Feeney T, Mendes J O, Krishnamurthi V, Walia S, Della Gaspera E and van Embden J 2021 High gain solution-processed carbon-free BiSI chalcogenide thin film photodetectors *Adv. Funct. Mater.* **31** 1–13

- [13] Peng B, Xu K, Zhang H, Ning Z, Shao H, Ni G, Li J, Zhu Y, Zhu H and Soukoulis C M 2018 1D SbSeI, SbSI, and SbSBr with high stability and novel properties for microelectronic, optoelectronic, and thermoelectric applications *Adv. Theory Simul.* **1** 1–7
- [14] Purusothaman Y, Alluri N R, Chandrasekhar A and Kim S J 2018 Photoactive piezoelectric energy harvester driven by antimony sulfide (SbSI): a AVBVCVII class ferroelectric–semiconductor compound *Nano Energy* **50** 256–65
- [15] Toroń B, Mistewicz K, Jesionek M, Koziol M, Zubko M and Stróż D 2022 A new hybrid piezo/triboelectric SbSeI nanogenerator *Energy* **238** 122048
- [16] Shin D-W, Hyun S-C, Park S-A, Kim Y-G, Chang-dae K and Kim W-T 1994 Optical properties of undoped and Ni-doped VA-VIA-VIIA single crystals *J. Phys. Chem. Solids* **55** 825–30
- [17] Xiao B, Zhu M, Ji L, Zhang B B, Dong J, Yu J, Sun Q, Jie W and Xu Y 2019 Centimeter size BiSeI crystal grown by physical vapor transport method *J. Cryst. Growth* **517** 7–11
- [18] Ganose A M, Matsumoto S, Buckridge J and Scanlon D O 2018 Defect engineering of earth-abundant solar absorbers BiSI and BiSeI *Chem. Mater.* **30** 3827–35
- [19] Ganose A M, Butler K T, Walsh A and Scanlon D O 2016 Relativistic electronic structure and band alignment of BiSI and BiSeI: candidate photovoltaic materials *J. Mater. Chem. A* **4** 2060–8
- [20] Wlazlak E et al 2018 Heavy pnictogen chalcogenides: the synthesis, structure and properties of these rediscovered semiconductors *Chem. Commun.* **54** 12133–62
- [21] Audzjonis A, Gaigalas G, Žigas L, Sereika R, Žaltauskas R, Balnionis D and Reza A 2009 Electronic structure and optical properties of BiSeI crystal *Phys. Status Solidi b* **246** 1702–8
- [22] Arivuoli D, Gnanam F D and Ramasamy P 1987 Growth of bismuth seleno iodide single crystals from the vapour *J. Mater. Sci.* **22** 981–4
- [23] An C, Du X, Chen X, Zhou Y, Zhang M, Zhou Y, Zhou J and Yang Z 2023 Pressure-induced superconductivity in the photoelectric semiconductor BiSeI *Phys. Rev. B* **107** 1–8
- [24] Hahn N T, Rettie A J E, Beal S K, Fullon R R and Mullins C B 2012 N-BiSI thin films: selenium doping and solar cell behavior *J. Phys. Chem. C* **116** 24878–86
- [25] Murtaza S Z M and Vaqueiro P 2020 Rapid synthesis of chalcogenides by ball milling: preparation and characterisation of BiSI and BiSeI *J. Solid State Chem.* **291** 121625
- [26] Dolcet Sadurni M, Timmo K, Mikli V, Volobujeva O, Mengü I, Krustok J, Grossberg-Kuusik M and Kauk-Kuusik M 2024 Preparation and characterization of SbSeI thin films *J. Sci. Adv. Mater. Devices* **9** 100664
- [27] Caño I et al 2023 SbSeI and SbSeBr micro-columnar solar cells by a novel high pressure-based synthesis process *J. Mater. Chem. A* **11** 17616–27
- [28] Bai R, Xiao B, Li F, Liu X, Xi S, Zhu M, Jie W, Zhang B B and Xu Y 2022 Growth of bismuth- and antimony-based chalcogenide single crystals by the physical vapor transport method *CrystEngComm* **24** 1094–9
- [29] Kanchana G and Arivuoli D 2001 Spectroscopic investigation of BiSeI, SbSeI compounds and BiSb<sub>2</sub>Se<sub>1-x</sub>I solid solutions *Indian J. Eng. Mater. Sci.* **8** 373–6 (available at: <http://nopr.niscair.res.in/handle/123456789/24465>)
- [30] Xu L et al 2024 2D BiSeI nanosheets for broadband self-powered photoelectrochemical photodetector *Phys. Status Solidi* **18** 1–9
- [31] Hu H et al 2023 A mixed-dimensional quasi-1D BiSeI nanowire-2D GaSe nanosheet p-n heterojunction for fast response optoelectronic devices *Nanoscale Adv.* **5** 6210–5
- [32] Li Y et al 2023 Polarization-sensitive photodetector based on high crystallinity quasi-1D BiSeI nanowires synthesized via chemical vapor deposition *Small* **19** 1–9
- [33] Rawat D, Singh A, Singh N K and Soni A 2023 Anisotropic light-matter interactions in the single-crystal topological insulator bismuth selenide *Phys. Rev. B* **107** 2–7
- [34] Deshpande M P, Bhatt S V, Sathé V, Rao R and Chaki S H 2014 Pressure and temperature dependence of Raman spectra and their anharmonic effects in Bi<sub>2</sub>Se<sub>3</sub> single crystal *Physica B* **433** 72–78
- [35] Martinez G et al 2017 Determination of the energy band gap of Bi<sub>2</sub>Se<sub>3</sub> *Sci. Rep.* **7** 1–5
- [36] Nechaev I A et al 2013 Evidence for a direct band gap in the topological insulator Bi<sub>2</sub>Se<sub>3</sub> from theory and experiment *Phys. Rev. B* **87** 1–5
- [37] Escobedo Morales A, Sánchez Mora E and Pal U 2007 Use of diffuse reflectance spectroscopy for optical characterization of un-supported nanostructures *Rev. Mex. Fis.* **53** 18–22
- [38] Levanyuk A P and Osipov V V 1981 Edge luminescence of direct-gap semiconductors *Sov. Phys.-Usp.* **24** 187–215
- [39] Krustok J, Kaupmees R, Abbasi N, Muska K, Mengü I and Timmo K 2023 Bandgap fluctuations, hot carriers, and band-to-acceptor recombination in Cu<sub>2</sub>ZnSn(S,Se)<sub>4</sub> microcrystals *Phys. Status Solidi* **17** 1–5
- [40] Bleuse J, Perret S, Curé Y, Grenet L, André R and Mariette H 2020 Optical determination of the band gap and band tail of epitaxial Ag<sub>2</sub>ZnSnSe<sub>4</sub> at low temperature *Phys. Rev. B* **102** 195205
- [41] Fang H H, Adjokatse S, Shao S, Even J and Loi M A 2018 Long-lived hot-carrier light emission and large blue shift in formamidinium tin triiodide perovskites *Nat. Commun.* **9** 243
- [42] Chepur D V, Bercha D M, Turyanitsa I D and Slivka V Y 1968 Peculiarities of the energy spectrum and edge absorption in the chain compounds AVBVCVII *Phys. Status Solidi* **30** 461–8
- [43] Krustok J, Collan H and Hjelt K 1997 Does the low-temperature Arrhenius plot of the photoluminescence intensity in CdTe point towards an erroneous activation energy? *J. Appl. Phys.* **81** 1442–5
- [44] Krustok J, Collan H, Hjelt K, Mädasson J and Valdna V 1997 Photoluminescence from deep acceptor-deep donor complexes in CdTe *J. Lumin.* **72–74** 103–5
- [45] Krustok J, H S J, Collan H, Yakushev M, Mädasson J and Bucher E 1999 Origin of the deep center photoluminescence in CuGaSe<sub>2</sub> and CuInS<sub>2</sub> crystals *J. Appl. Phys.* **86** 364–9
- [46] Krustok J, Raudoja J, Krunk M, Mändar H and Collan H 2000 Nature of the native deep localized defect recombination centers in the chalcopyrite and orthorhombic AgInS<sub>2</sub> *J. Appl. Phys.* **88** 205–9
- [47] Krustok J, Raudoja J, Schön J H, Yakushev M and Collan H 2000 Role of deep donor-deep acceptor complexes in CIS-related compounds *Thin Solid Films* **361** 406–10
- [48] Williams F 1968 Donor—acceptor pairs in semiconductors *Phys. Status Solidi* **25** 493–512



## Appendix 3

### Publication III

**M. Dolcet Sadurni**, K. Timmo, V. Mikli, J. Krustok, M. Danilson, A. Suchodolskis, C. Radu, A. Bocirnea, A. Galca, M. Grossberg-Kuusik, M. Kauk-Kuusik, "Effects of cationic substitution on the properties of  $Sb_{1-x}Bi_xSe_3$  ( $x = 0-1$ ) compounds" *Journal of Alloys and Compounds* 1037 (2025) 182292, <https://doi.org/10.1016/j.jallcom.2025.182292>.





Contents lists available at ScienceDirect

Journal of Alloys and Compounds

journal homepage: [www.elsevier.com/locate/jalcom](http://www.elsevier.com/locate/jalcom)

## Effects of cationic substitution on the properties of $\text{Sb}_{1-x}\text{Bi}_x\text{SeI}$ ( $x = 0-1$ ) compounds

Marc Dolcet Sadurni<sup>a,\*</sup>, Kristi Timmo<sup>a</sup>, Valdek Mikli<sup>a</sup>, Jüri Krustok<sup>a</sup>, Mati Danilson<sup>a</sup>, Artūras Suchodolskis<sup>b</sup>, Cristian Radu<sup>c,d</sup>, Amelia Elena Bocirnea<sup>c</sup>, Aurelian Catalin Galca<sup>c,e</sup>, Maarja Grossberg-Kuusik<sup>a</sup>, Marit Kauk-Kuusik<sup>a</sup>

<sup>a</sup> Department of Materials and Environmental Technology, Tallinn University of Technology, Ehitajate Tee 5, Tallinn 19086, Estonia

<sup>b</sup> Department of Optoelectronics, Center for Physical Sciences and Technology, Sauletekio Av. 3, Vilnius 10257, Lithuania

<sup>c</sup> National Institute of Materials Physics, Atomistilor 405A, Magurele, Ilfov 077125, Romania

<sup>d</sup> Faculty of Physics, University of Bucharest, Atomistilor 405, Magurele, Ilfov 077125, Romania

<sup>e</sup> International Centre for Advanced Training and Research in Physics, Atomistilor 409, Magurele, Ilfov 077125, Romania

### ARTICLE INFO

#### Keywords:

Antimony selenoiodide  
Bismuth selenoiodide  
Solid solution  
Pnictogen chalcogenides

### ABSTRACT

Pnictogen chalcogenide semiconductors are emerging materials with broad potential in energy-related applications, including solar cells, photocatalysis, photodetectors, batteries, supercapacitors, thermoelectric and piezoelectric generators. Their compositional flexibility allows fine tuning of structural and optoelectronic properties. In this study, microcrystalline powders of  $\text{Sb}_{1-x}\text{Bi}_x\text{SeI}$  ( $x = 0-1$ ) were synthesized from binary precursors by a solid-state method in evacuated quartz ampoules. Energy dispersive spectroscopy confirmed the successful substitution of Sb with Bi in  $\text{Sb}_{1-x}\text{Bi}_x\text{SeI}$ . The formation of solid solutions was also supported by Raman spectroscopy and X-ray diffraction (XRD). All materials exhibited needle-shaped crystal morphologies and orthorhombic crystal structure ( $Pnma$ ), regardless of the Bi/Sb ratio. XRD patterns shifted toward smaller angles with increasing Bi content, indicating lattice expansion. Calculated lattice parameters ( $b$  and  $c$ ) increased linearly with Bi incorporation, while the lattice parameter ( $a$ ) remained constant. Raman spectra exhibited characteristic peaks at  $182\text{ cm}^{-1}$  for Bi-Se vibration and  $209\text{ cm}^{-1}$  for Sb-Se vibration, with intensity ratios reflecting Bi content. UV-Vis-NIR diffuse reflectance spectroscopy revealed a direct band gap that decreased from 1.7 eV (SbSeI) to 1.29 eV (BiSeI). Room-temperature photoluminescence measurements exhibited a single emission band, shifting from 1.75 eV to 1.41 eV with increasing Bi content. Ultraviolet photoelectron spectroscopy indicated a shift in the valence band maximum from 0.44 eV (SbSeI) to 1.1 eV (BiSeI). These findings highlight the tunability of  $\text{Sb}_{1-x}\text{Bi}_x\text{SeI}$  compounds, offering pathways for optimizing their properties for specific optoelectronic applications.

### 1. Introduction

Heavy pnictogen chalcogenides are a recently rediscovered family of inorganic ternary semiconductors that are earth-abundant and non-toxic. These materials exhibit unique optoelectronic properties, such as ferroelectricity [1], high carrier mobilities, and strong anisotropic charge transport [2]. Due to their properties, pnictogen chalcogenides have attracted significant interest for use in photovoltaics [3–5] and other energy harvesting applications [6–9].

SbSeI and BiSeI share an orthorhombic crystal structure (space group  $Pnma$ ) and exhibit a quasi-1D arrangement, consisting of aligned chains

held together by weak van der Waals forces. This structural anisotropy enables efficient charge carrier transport along the chain axis, making them attractive for optoelectronic and thermoelectric applications [10]. SbSeI has a band gap energy of approximately 1.72 eV [11], while BiSeI exhibits a lower band gap of around 1.29 eV [12]. Although these materials are classified as indirect band gap semiconductors, the predicted difference between the direct and indirect band gaps is approximately  $\sim 0.2$  eV for SbSeI [13] and  $\sim 0.1$  eV for BiSeI [14]. Both materials also exhibit high absorption coefficients ( $\sim 10^5\text{ cm}^{-1}$ ) [15], supporting their potential for efficient light harvesting and energy conversion.

Advanced computational techniques have been used in several

\* Corresponding author.

E-mail address: [madolc@taltech.ee](mailto:madolc@taltech.ee) (M. Dolcet Sadurni).

<https://doi.org/10.1016/j.jalcom.2025.182292>

Received 15 May 2025; Received in revised form 2 July 2025; Accepted 15 July 2025

Available online 16 July 2025

0925-8388/© 2025 Elsevier B.V. All rights are reserved, including those for text and data mining, AI training, and similar technologies.

theoretical studies of the electronic structure of SbSeI and BiSeI [13,14,16]. However, experimental investigations have thus far focused only on the band structure of SbSeI [17–20], with no experimental data reported for BiSeI. Understanding the band structure is crucial to selecting appropriate materials for photovoltaic applications. The optical band gap defines the theoretical efficiency limit of a solar cell, while appropriate band alignment with other cell layers is essential for achieving optimal device performance. According to the Shockley-Queisser (SQ) limit, the optimal band gap for a single-junction solar cell under AM1.5 G illumination is approximately 1.34 eV, corresponding to a theoretical maximum efficiency of around 33 % [21]. In multi-junction solar cells, wider band gaps are required to maximize efficiency across the solar spectrum [22]. For indoor photovoltaics (IPV), where artificial lighting such as white light emitting diodes (LEDs) is used, an optimal band gap of 1.7–1.9 eV is desired [23], making materials like SbSeI particularly promising for these applications. A viable strategy for tailoring the band gap of absorber materials is the synthesis of solid solutions from two parent compounds, enabling compositional optimization to achieve desired optoelectronic properties. Partial substitution of pnictogen cations [16,24–27], as well as chalcogen [28] and halide anions [29], has been demonstrated in various pnictogen chalcogenides. In the earlier study by Viskunets *et al.* [27], the formation of a continuous solid solution of  $Sb_{1-x}Bi_xSeI$  with a step  $x = 0.1$  was confirmed by XRD and differential thermal analysis (DTA), with all compositions crystallizing in an orthorhombic structure. Additionally, photoconductivity and optical absorption properties of these solid solutions were investigated in [26].

The present work aims to use  $Sb_{1-x}Bi_xSeI$  solid solutions as absorber materials for various photovoltaic (PV) applications - from lower band gap compositions suitable for single-junction solar cells to wider band gaps tailored for tandem devices and IPV systems. However, while the tunable band gap (1.72–1.29 eV) makes these materials a promising and environmentally friendly candidate for next-generation energy harvesting technologies, further detailed analysis is still required.

In this study,  $Sb_{1-x}Bi_xSeI$  ( $x = 0, 0.2, 0.4, 0.6, 0.8, \text{ and } 1$ ) solid solutions were synthesized by a solid-state reaction method to investigate the effect of Bi content on their structural, optical, and electronic properties. Increasing Bi content led to a nonlinear narrowing of the band gap, accompanied by a similar trend in the RT-PL peak emission energy and a transition in conductivity type. The relative intensity changes of the Sb–Se and Bi–Se Raman modes correlated with Bi content, enabling reliable estimation of metal composition in the solid solution using Raman spectroscopy. Changes in energy level alignment were also examined, and to the best of current knowledge, this study presents one of the first experimental band diagrams for the  $Sb_{1-x}Bi_xSeI$  system.

## 2. Methodology

$Sb_{1-x}Bi_xSeI$  microcrystalline powders with different values of  $x$  ( $x = 0, 0.2, 0.4, 0.6, 0.8$  and  $1$ ) were synthesized via a solid-state reaction route from self-prepared  $Sb_2Se_3$  (5 N),  $Bi_2Se_3$  (4 N),  $SbI_3$  (3 N) and commercially available  $BiI_3$  (Aldrich, 2 N). The masses of precursors containing Sb and Bi were calculated and weighed to achieve a total mass of 1 g with the desired Bi/Sb ratio, then mixed and ground in an agate mortar to ensure homogeneity and facilitate the reaction. The mixtures were poured into quartz ampoules (6.5 cm long, 1.2 cm diameter), degassed under dynamic vacuum, and sealed. The six ampoules were heated from room temperature (RT) to 225 °C within 3 h and maintained at that temperature for 24 h. Subsequently, the temperature increased from 225 °C to 440 °C within 5 h, remaining below the melting temperature of SbSeI ~452 °C [30]. The samples were held at 440 °C for 256 h, followed by natural cooling in air to RT (Fig. S1). Additionally, the samples with Bi content  $x = 0.6, 0.8$  and  $1$  were recrystallized at 480 °C for 472 h to enhance crystallinity and eliminate secondary phases, including  $Bi_2Se_3$  and  $BiI_3$  as identified by X-ray

diffraction (XRD) after the initial annealing. The higher recrystallization temperature was selected for Bi-rich ( $x > 0.5$ ) compositions due to the significantly higher melting point of BiSeI ( $T_M=545$  °C [31]) compared to SbSeI. After the synthesis, shiny, grey microcrystals were formed and settled at the bottom of the ampoules, including larger needle-like crystals.

A high-resolution scanning electron microscope (HR-SEM Zeiss Merlin) was used to examine the morphology of the microcrystals. Two detectors were utilized for this analysis: a high-efficiency in-lens secondary electron detector, which provided high-contrast surface images, and an energy-selective backscattered electron detector, which enabled compositional contrast imaging. HR-SEM Zeiss Merlin equipped with a Bruker Esprit 1.82 energy dispersive X-ray (EDX) system with an EDX-Flash 3001 detector for compositional analysis of the microcrystals. High-resolution transmission electron microscopy (HR-TEM) images were acquired using a JEOL JEM-2100F transmission electron microscope equipped with a JEOL JED-2300T Dry SDD energy dispersive X-ray (EDX-TEM) unit. The acceleration voltage was set to 200 keV. To characterize the crystal structure and phase composition of the  $Sb_{1-x}Bi_xSeI$  solid solutions, XRD was performed using a Rigaku Ultima IV diffractometer. The diffractometer was operated at 40 kV and 40 mA with monochromatic  $Cu K\alpha$  radiation ( $\lambda = 1.5406$  Å) detected by a silicon strip detector (D/teX Ultra). Phase analysis and lattice parameters were calculated using the PDXL2 Rigaku software. To further investigate the phase composition of microcrystals, room-temperature micro-Raman (RT  $\mu$ -Raman) spectroscopy was employed. Raman spectra were collected using a 532 nm laser with a power intensity of 0.42 mW and a spot size of 10–20  $\mu m$  in diameter on a Horiba LabRam HR 800 spectrometer equipped with a multichannel CCD detection system in a backscattering configuration. The same equipment was used to measure room temperature micro-photoluminescence (RT-PL) in the visible spectral range. The optical band gaps of the materials were determined by analyzing the ultraviolet–visible–near-infrared (UV–Vis–NIR) diffuse reflectance data measured by a Shimadzu UV-3600 two-beam spectrometer equipped with a multi-purpose compartment MPC-3100 with an integrating sphere of the diameter of 60 mm. Measurements were recorded between 260 and 2600 nm. The X-ray photoelectron spectroscopy (XPS) measurements were performed using a Kratos Ultra DLD setup in ultrahigh vacuum conditions, with the base pressure of  $10^{-9}$  mbar, with a monochromatized Al  $K\alpha$  anode, having an energy of 1486.6 eV. The surface charging effects were compensated by using both an electron flood gun during measurement as well as ulterior correction to the C-C contamination bond at 284.6 eV. Ultraviolet photoelectron spectroscopy (UPS) was performed using an Axis Ultra DLD photoelectron spectrometer (Kratos Analytical) equipped with a helium discharge lamp. The He(I) resonance line ( $h\nu = 21.21$  eV) was used to obtain UPS spectra, allowing the determination of the work function and valence band maximum energies of the materials. An ambient Scanning Kelvin Probe system (SKP5050, KP Technology Ltd, UK) equipped with a 2 mm gold-covered vibrating tip was used to evaluate the photosensitivity and conductivity type of all six materials. A semiconductor red laser with a wavelength of 670 nm and a power of 1 mW was employed to observe changes in surface potential with illumination.

## 3. Results and discussion

### 3.1. Characterization of the morphology and composition of $Sb_{1-x}Bi_xSeI$ ( $x = 0-1$ ) microcrystals

The morphology of the synthesized materials was examined using SEM. Fig. 1 presents top-view SEM images of  $Sb_{1-x}Bi_xSeI$  ( $x = 0-1$ ) microcrystals, revealing structures consisting predominantly of cylindrical or prismatic, needle-shape crystals of varying sizes. The crystals range in length from several tenths of a micrometer to over a millimeter, with diameters ranging from 10  $\mu m$  to several hundred micrometers. These findings align with previous studies [32], based on the growth

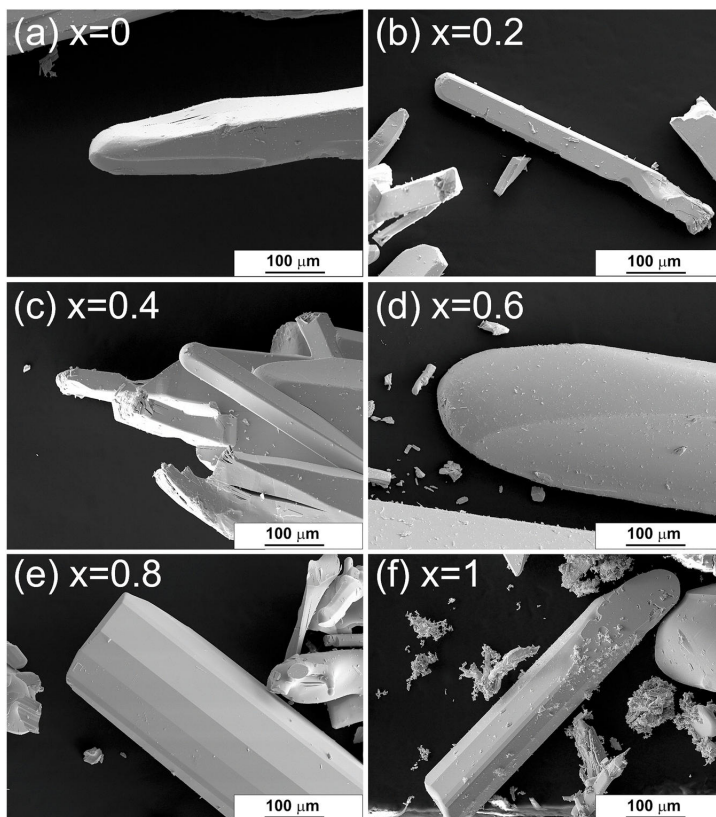


Fig. 1. SEM images of microcrystals of  $Sb_{1-x}Bi_xSeI$  ( $x = 0-1$ ).

mechanism of  $A^V B^VI C^{VII}$  crystals, where needle-shape structures exhibit a faster growth rate along the  $b$ -axis. A closer examination revealed that these needles consist of multiple parallel-aligned layers connected along the  $a$ -axis. In addition, clusters of smaller, irregularly shaped crystals partially covered with nanometer-sized crystals (see Fig. 1f) were observed. Incorporating Bi into the solid solutions resulted in more rounded needle-shaped crystals with a greater number of facets ( $x = 0.8, 1$ ).

For the elemental compositional analysis of the  $Sb_{1-x}Bi_xSeI$  compounds, the samples were embedded in epoxy resin and polished for cross-sectional examination of the crystal's bulk. EDX measurements were performed across multiple regions and crystals within each sample (Fig. S2), revealing consistent elemental distributions that confirmed high compositional uniformity. According to the EDX data (shown in Table 1), the target elemental composition (SbBi = 33.33 %, Se = 33.33 %, I = 33.33 %) was closely achieved throughout the entire series and the substitution of Sb by Bi was confirmed.

Raman spectra of  $Sb_{1-x}Bi_xSeI$  solid solutions were measured from single microcrystals and are presented in Fig. 2.

The Raman spectra of  $Sb_{1-x}Bi_xSeI$  crystals were fitted using Lorentzian functions, and the corresponding peaks, displayed in different colors, are shown in Fig. 2. The Raman spectra of SbSeI and BiSeI are consistent with previous reports, exhibiting the highest frequency modes at  $182\text{ cm}^{-1}$  ( $\Gamma_{1(Bi)}$ ) and  $209\text{ cm}^{-1}$  ( $\Gamma_{1(Sb)}$ ), corresponding to the Bi-Se and Sb-Se bonds, respectively, which is in good agreement with [33, 34]. Additionally, peaks at 95, 115, 137, 167, 187 and  $213\text{ cm}^{-1}$  were identified and attributed to SbSeI. For BiSeI, peaks at 75, 96, 106, 115,

Table 1  
Elemental composition of  $Sb_{1-x}Bi_xSeI$  ( $x = 0-1$ ) determined by EDX.

$Sb_{1-x}Bi_xSeI$	$x = Bi/(Sb+Bi)$ outcome	Sb (at%)	Bi (at%)	Se (at%)	I (at%)
SbSeI	0	34.1 ± 0.7	-	32.6 ± 0.4	33.3 ± 0.4
$Sb_{0.8}Bi_{0.2}SeI$	0.20	27.0 ± 0.5	6.7 ± 0.1	32.7 ± 0.4	33.6 ± 0.5
$Sb_{0.6}Bi_{0.4}SeI$	0.40	20.5 ± 0.5	13.7 ± 0.3	31.3 ± 0.4	34.5 ± 0.5
$Sb_{0.4}Bi_{0.6}SeI$	0.62	13.0 ± 0.3	21.1 ± 0.5	32.3 ± 0.4	33.6 ± 0.5
$Sb_{0.2}Bi_{0.8}SeI$	0.81	6.6 ± 0.2	27.4 ± 0.6	32.5 ± 0.4	33.4 ± 0.5
BiSeI	1	-	34.2 ± 0.5	32.6 ± 0.3	33.2 ± 0.3

137, 153, 159, 182 and  $186\text{ cm}^{-1}$  were observed, aligning well with previous reports [28,35,36]. Peaks at lower wavenumbers ( $75$  and  $96\text{ cm}^{-1}$ ) are attributed to Bi-I bonds and those at 153, 159, 182,  $186\text{ cm}^{-1}$  to Bi-Se bonds. The cationic substitution of Sb with Bi in the  $Sb_{1-x}Bi_xSeI$  microcrystals clearly influences the Raman modes. Variations in the Bi content in  $Sb_{1-x}Bi_xSeI$  resulted in changes in the relative intensities of the  $\Gamma_{1(Bi)}$  and  $\Gamma_{1(Sb)}$  vibrational modes. The presence of two distinct modes, rather than a single average mode, in the solid solutions of  $x = 0.2-0.8$  indicates Raman bimodal behavior, similar to that observed in the  $Bi_{1-x}Sb_xSI$  system [24] and as reported for  $Sb_{0.5}Bi_{0.5}SeI$  [25]. As the Bi content increases, the relative intensities of the two main



Fig. 2. Normalized Raman spectra of  $Sb_{1-x}Bi_xSeI$  ( $x = 0-1$ ) microcrystals (dots). Fitted spectra (black line) using Lorentzian functions.

peaks of SbSeI and BiSeI change (see Fig. 3), allowing the estimation of the content of metal atoms in the solid solution with relatively high accuracy by Raman spectroscopy. To verify that microcrystal orientation does not affect the Raman measurements, a polarization-dependent study was conducted by varying the microcrystal alignment relative to incident polarized laser. The relative intensities of the Bi-Se and Sb-Se peaks remained constant, confirming the polarization independence of the measurements (Fig. S3).

XRD patterns of  $Sb_{1-x}Bi_xSeI$  were recorded and are presented in Fig. 4a. The reflections obtained were compared with data cards of SbSeI (ICSD # 01-076-1354), BiSeI (ICSD # 01-070-4693),  $Sb_{0.7}Bi_{0.3}SeI$  (ICDD # 00-065-0522), and  $Sb_{0.3}Bi_{0.7}SeI$  (ICDD # 00-066-0065). All peaks align with their expected positions. The position of the reflections gradually shifted to lower angles as the Bi content in the solid solutions increased. For example, the diffraction peak belonging to the reflection of 112 shifted from  $29.4^\circ$  to  $28.9^\circ$  (Fig. 4b). A similar behaviour was also observed for  $BiSb_{1-x}I_x$  solid solutions [37].

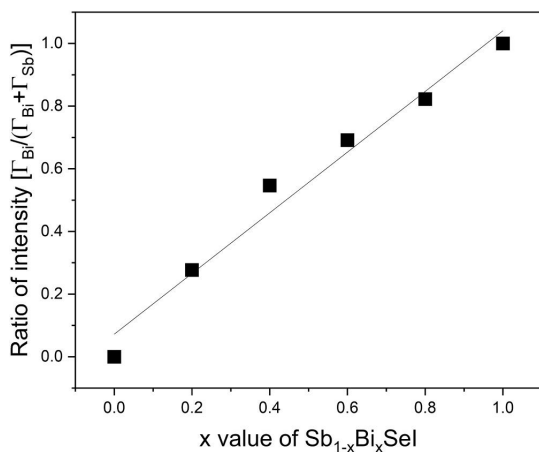


Fig. 3. Ratio of the intensities of the main Raman peaks corresponding to the Sb-Se ( $209\text{ cm}^{-1}$ ) and Bi-Se ( $182\text{ cm}^{-1}$ ) modes.

The lattice parameters for all materials were calculated and presented in Fig. S4. The orthorhombic space group  $Pnma$  was identified for BiSeI, SbSeI and all intermediate solid solutions. A 3.4 % increase in unit cell volume was observed upon full substitution of Sb with Bi, consistent with the larger atomic radius of Bi compared to Sb and is in good agreement with previous studies [14,19,25]. The expansion is anisotropic: the unit cell parameters  $b$  and  $c$  increase with higher Bi content, while the parameter  $a$  remains nearly constant (see Fig. S4). Both parameters  $a$  and  $b$  follow the Vegard's law, exhibiting a linear dependence on Bi content.

The morphology, crystal structure and elemental composition of solid solutions were also characterized by HR-TEM, TEM-EDX and XPS (Table S1).

From the morphological perspective, all samples exhibit large microcrystals (Fig. 5a) that tend to be elongated and have straight edges (facets), formed by specific crystallographic planes. The HR-TEM image reveals that the ribbons align along the long axis of the rods (Fig. 5b). A magnified image of the area shown in Fig. 6b demonstrates a continuous crystalline layer without visible grain boundaries or structural defects such as dislocations (Fig. 5c). The diffraction points indicated in Fig. 5d correspond to the following lattice planes and interplanar distances:  $(010) - 4.22\text{ \AA}$ ,  $(11-1) - 3.57\text{ \AA}$ ,  $(10-1) - 6.72\text{ \AA}$ . The orientation of the crystallite is such that the zone axis  $[101]$  is parallel to the electron beam for  $x = 0.8$ . The selected area diffraction (SAED) pattern revealed a single set of diffraction spots for all solid solutions, confirming their high crystallinity. Fig. 5d illustrates the lattice planes corresponding to  $Sb_{1-x}Bi_xSeI$  with  $x = 0.8$ .

An orthorhombic crystal structure with  $Pnma$  space group was found for all solid solutions by SAED, in agreement with XRD results. The lattice parameters of the  $Sb_{1-x}Bi_xSeI$  powders with  $x = 0.2, 0.4, 0.6$  and  $0.8$  were determined using SAED and compared to XRD (Fig. S4). While the SAED measurements provided detailed structural information from individual single crystals, slight discrepancies were observed with XRD results. These differences arise from the fact that SAED was conducted on microcrystals, whereas XRD data were obtained from ground powder samples.

TEM-EDX analysis has been done on microcrystals from solid solutions. The EDX maps reveal that all elements are homogeneously distributed in the areas analysed (Fig. 6). The TEM-EDX results are consistent with the expected stoichiometric ratio ( $(Bi,Sb):Se:1 = 1:1:1$ ) and agree with the SEM-EDX results (Table S1). However, discrepancies between SEM and TEM measurements emerge as the Bi molar fraction increases. Specifically, the Bi content measured by TEM-EDX is higher than that measured by SEM-EDX. This discrepancy can be attributed to the differences in acceleration voltage: 20 keV for SEM-EDX and 200 keV for TEM-EDX. The higher sensitivity of SEM-EDX at 2.3 keV (Bi M line) compared to TEM-EDX can explain the variation in Bi content. Consequently, SEM-EDX results are considered more reliable because of their greater sensitivity in this energy range. The elemental composition of the solid solutions was also investigated by X-ray photoelectron spectroscopy measurements. The XPS results are included in Table S1 for comparison. As expected, some discrepancies arise between EDX and XPS data due to the fundamentally different probing depths of the techniques - EDX being bulk-sensitive, while XPS probes only the top  $\sim 5-10\text{ nm}$  of the surface. Moreover, the quantitative interpretation of XPS data is limited by several factors, including surface geometry, peak intensity, the reliability of relative sensitivity factors, surface volume homogeneity, and potential sample degradation during analysis. Additional challenges arise from the heterogeneous nature of the polycrystalline samples, variations in surface composition, and possible contamination [38]. Despite these limitations, the XPS data qualitatively confirms the presence of all constituent elements and shows reasonable agreement with the stoichiometric trends observed by EDX. These results support the overall elemental composition and confirm the consistency of the solid solution series.

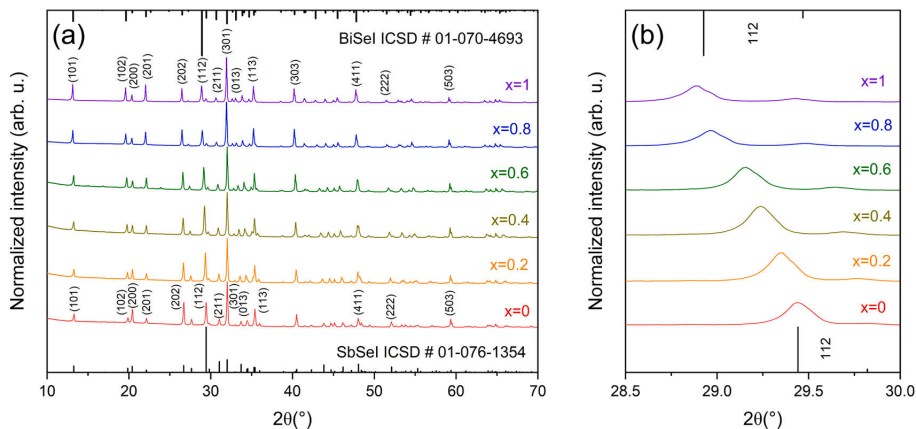


Fig. 4. (a) XRD pattern of  $\text{Sb}_{1-x}\text{Bi}_x\text{SeI}$  ( $x = 0-1$ ) powders. (b) The enlarged XRD pattern shows a shift of the distance between (112) planes.

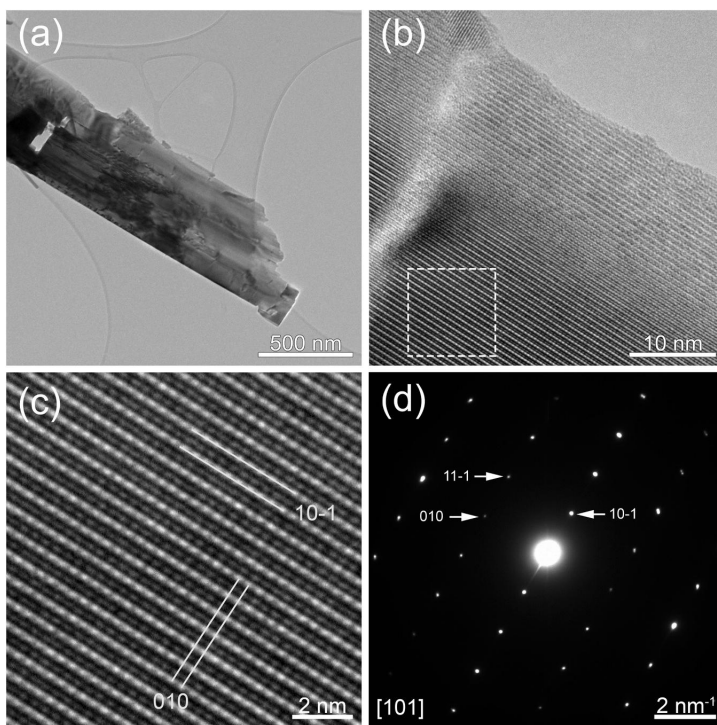


Fig. 5. (a) Low magnification TEM image, (b) HR-TEM image indicating the area that was magnified in (c) where the lattice planes (10-1) and (010) were illustrated and (d) SAED corresponding to  $\text{Sb}_{1-x}\text{Bi}_x\text{SeI}$  with  $x = 0.8$ .

### 3.2. Characterization of optical properties of $\text{Sb}_{1-x}\text{Bi}_x\text{SeI}$ ( $x = 0-1$ ) microcrystals

RT photoluminescence analysis revealed a single, asymmetric emission peak for all solid solutions, as shown in Fig. 7. The observed band shape is characteristic of band-to-band recombination, where the high energy side is mainly determined by the Fermi distribution, while low energy side reflects the density of states function. A more detailed discussion of this shape is provided in [12]. The peak maxima, determined

by fitting the spectra with Split Pseudo-Voigt functions, shifted non-linearly from 1.75 eV for SbSeI to 1.41 eV for BiSeI. These values are consistent with previously reported optical band gap energies for SbSeI [11] and BiSeI [12].

UV-Vis-NIR diffuse reflectance spectroscopy was conducted on the samples in the form of a pressed microcrystalline powder, following the methodology described in [12]. The diffuse reflectance data were analyzed using the Kubelka-Munk function (Eq. 1) to determine the optical band gaps of the solid solutions,

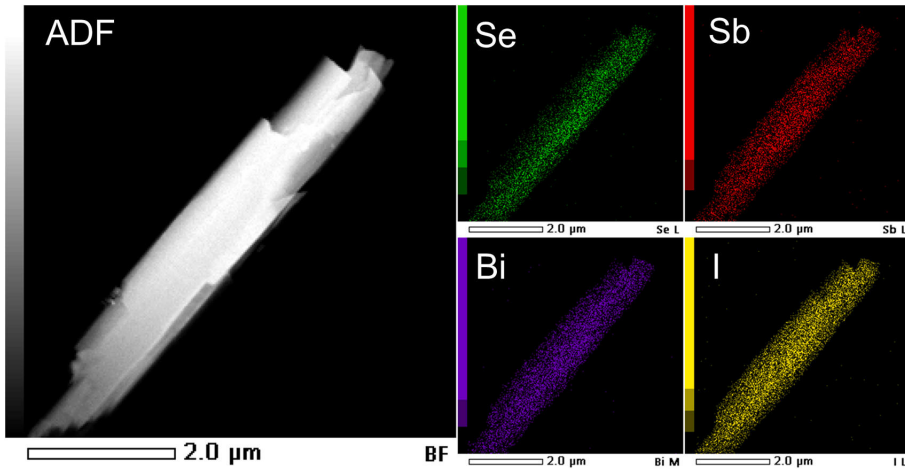


Fig. 6. Dark-field STEM image and EDX elemental mapping ( $x = 0.4$ ).

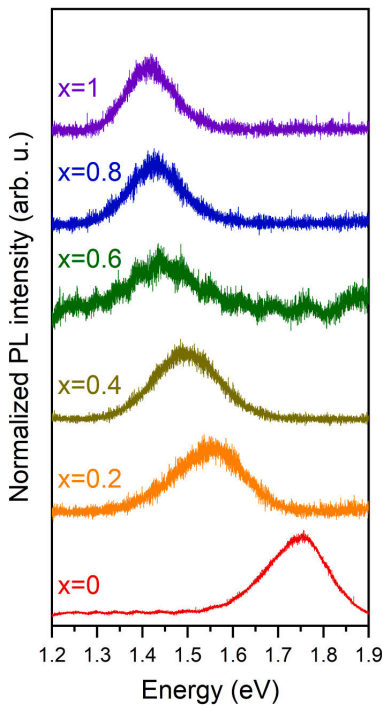


Fig. 7. Room temperature photoluminescence spectra of  $\text{Sb}_{1-x}\text{Bi}_x\text{SeI}$  ( $x = 0-1$ ) microcrystals.

$$F(R_\infty) = \frac{(1 - R_\infty)^2}{2R_\infty} \sim \alpha, \quad (1)$$

where  $R_\infty$  is the absolute diffuse reflectance. For optically thick samples,  $F(R_\infty)$  can be approximated as the absorption coefficient  $\alpha$ . When plotted against the photon energy, this function enables for band gap determination by identifying linear regions that intersect the energy axis (see Fig. 8). The optical band gaps were extracted using the Tauc

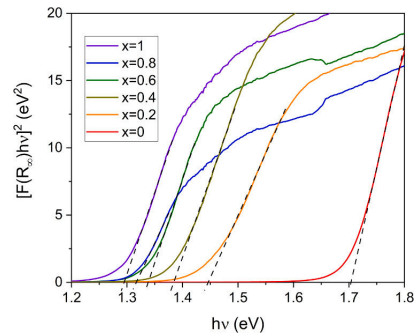


Fig. 8. Optical band gap determination from Tauc plots: extrapolation of the linear least squares fit of  $[F(R_\infty)h\nu]^2$  vs  $h\nu$  for  $\text{Sb}_{1-x}\text{Bi}_x\text{SeI}$  ( $x = 0-1$ ) microcrystals.

relation:

$$(F(R_\infty)h\nu)^{1/n} = A(h\nu - E_g), \quad (2)$$

where  $A$  is a constant,  $h$  the Planck's constant,  $\nu$  the photon frequency and  $E_g$  is the optical band gap. The value of factor  $n$  is  $1/2$  for direct transitions and 2 for indirect transitions. Band gaps of all solid solutions were estimated using  $n = 1/2$ , assuming the presence of direct band gaps.

The optical band gap of  $\text{Sb}_{1-x}\text{Bi}_x\text{SeI}$  solid solutions can be precisely tuned by adjusting the Bi/Sb ratio. The experimentally measured band gap values range from 1.7 eV for SbSeI to 1.29 eV for BiSeI (Fig. 8) are in good agreement with previously reported values 1.72 eV [11] and 1.29 eV [35,39], respectively. In an earlier study, an almost linear decrease of  $E_g$  was detected with increasing  $x$  value [26]. In contrast, our samples exhibit a nonlinear decrease in band gap with increasing Bi content, as shown in Fig. 9, indicating a characteristic band bowing effect. Similar nonlinear behaviour has been reported in other chalcogenide solid solutions, such as  $\text{Bi}_{1-x}\text{Sb}_x\text{SI}$  [24], as well as in  $\text{Sb}_2(\text{S}_x\text{Se}_{1-x})_3$  [40] or  $\text{Ag}_x\text{Cu}_{1-x}\text{GaSe}_2$  [41]. This nonlinear behaviour is often attributed to local structural distortions upon substitution, including atom displacements, clustering, or localized states in the band gap. It can also arise from increased spin-orbit coupling when heavier atoms (Bi) replace lighter (Sb) ones. The optical bowing effect in semiconductor

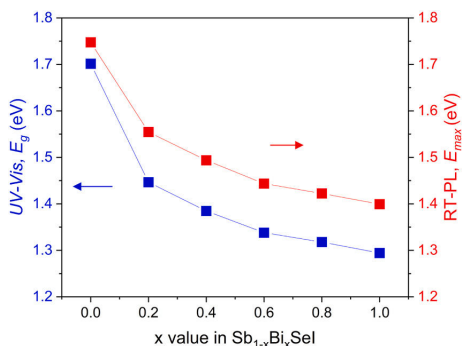


Fig. 9. Optical band gap values (blue squares) along with the maximum emission energy ( $E_{max}$ ) from photoluminescence spectra (red squares) for  $Sb_{1-x}Bi_xSe_1$  ( $x = 0-1$ ) microcrystals as a function of the Bi/Sb ratio.

alloys is linked to differences in atomic electronegativities and internal structural relaxation - specifically, changes in bond lengths and angles [24,40].

Fig. 9 shows the optical band gap values and RT- PL peak energies ( $E_{max}$ ) as a function of the Bi/Sb ratio in  $Sb_{1-x}Bi_xSe_1$  ( $x = 0-1$ ). A similar nonlinear trend is observed for both parameters. In  $SbSe_1$ , the PL peak energy is only 0.05 eV above the band gap, whereas Bi incorporation leads to a consistent offset, with the PL emission remaining approximately 0.11 eV higher than the direct band gap across all Bi-containing compositions. This behaviour, previously reported for  $BiSe_1$  [12], is commonly observed in different semiconductors [42,43].

To investigate the impact of Bi incorporation on the band structure of  $Sb_{1-x}Bi_xSe_1$ , a UPS study was conducted across the entire series. Selected microcrystals from each solid solution were analyzed.

The work function ( $\phi$ ) of the  $Sb_{1-x}Bi_xSe_1$  compounds was determined from the secondary-electron cutoff energy obtained in UPS measurements using He(I) excitation, as described by Eq. (3)

$$\Phi = h\nu - E_{cutoff} \quad (3)$$

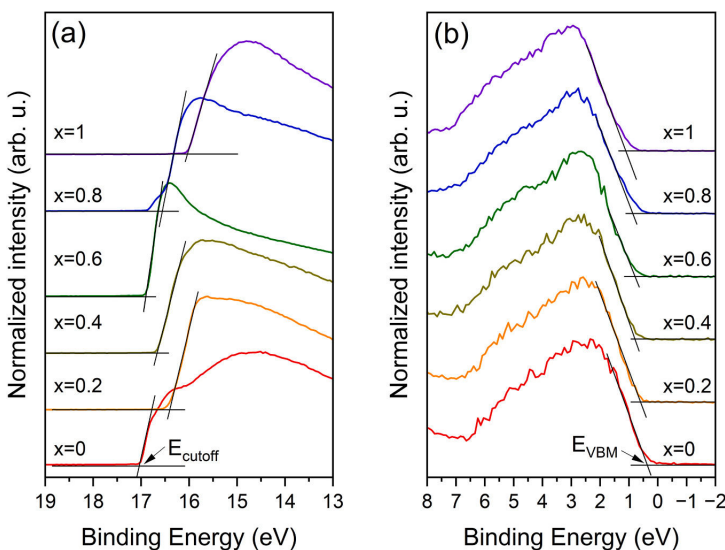


Fig. 10. Ultraviolet photoelectron spectra (UPS) of  $Sb_{1-x}Bi_xSe_1$  ( $x = 0-1$ ) shown in the binding energy scale. (a) High binding energy region highlighting the secondary electron cutoff ( $E_{cutoff}$ ). (b) Low binding energy region showing the valence band onset used to determine the valence band edge ( $E_{VBM}$ ).

where  $\Phi$  is the work function,  $h\nu$  represents the excitation energy of the He(I) line (21.21 eV), and  $E_{cutoff}$  corresponds to the secondary-electron cutoff energy, marking the end of secondary-electron emission at the high binding energy side of the spectrum (Fig. 10a). The work function is defined as the minimum energy required to remove an electron from the Fermi level ( $E_F$ ) to the vacuum level ( $E_{VAC}$ ) [44].

The valence band edge ( $E_{VBM}$ ) was determined from the UPS spectrum in binding energy scale by linearly extrapolating the intersection of the low-binding-energy onset to the baseline (Fig. 10b). Here,  $E_{VBM}$  denotes the energy difference between the valence band maximum and the  $E_F$ . Combined with the optical band gap values obtained from UV-VIS-NIR measurements, these data were used to estimate the

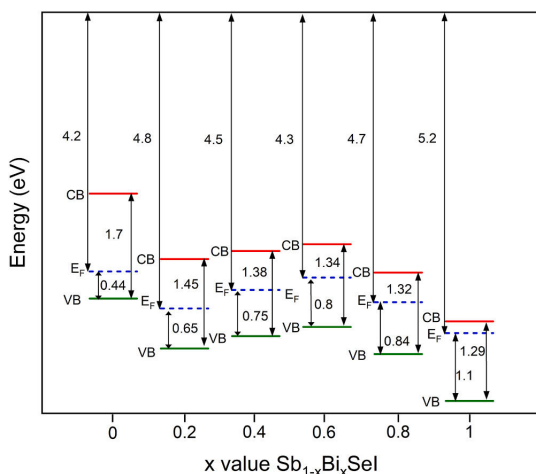


Fig. 11. Experimentally determined band diagram of  $Sb_{1-x}Bi_xSe_1$  ( $x = 0-1$ ) solid solutions, illustrating the compositional dependence of work function, valence band edge, and band gap energy.

position of the valence band relative to the vacuum level and to construct the experimental energy band diagram of the  $\text{Sb}_{1-x}\text{Bi}_x\text{SeI}$  system (Fig. 11).

The UPS study showed that increasing the Bi content in  $\text{Sb}_{1-x}\text{Bi}_x\text{SeI}$  shifted the  $E_{\text{VBM}}$  from 0.44 eV to 1.1 eV, indicating a movement of the Fermi level toward the conduction band. Similar shift in  $E_{\text{VBM}}$  has been reported in other solid solution systems, such as CZT(S,Se) [45]. A transition in conductivity type from *p*-type to *n*-type was observed when the Bi content exceeded 0.2 ( $x = 0.2$ ), see Table S2. Despite reports of *n*-type conductivity for SbSeI in the literature, the present findings suggest that the conductivity type is strongly influenced by composition. Comparable work function and band gap values are reported in [20], although the obtained  $E_{\text{VBM}}$  is considerably lower in that study. Although experimental data for BiSeI are limited, the theoretical studies predict a comparable band gap (1.29 eV) and  $E_{\text{VBM}}$ , differing by only 0.1 eV from the values determined in this work [14]. Scanning Kelvin Probe measurements performed on all six solid solutions revealed a clear photosensitive response under red laser illumination. For Sb-rich compositions ( $x = 0, 0.2, 0.4$ ), the contact potential difference (CPD) increased upon illumination, whereas a decrease in CPD was observed for Bi-rich compositions ( $x = 0.6, 0.8, 1$ ) (Fig. S5). This contrasting behaviour indicates a possible transition in conductivity type from *p*-type to *n*-type as the Bi content surpasses that of Sb, consistent with the findings from UPS analysis.

#### 4. Conclusions

Solid solutions of  $\text{Sb}_{1-x}\text{Bi}_x\text{SeI}$  ( $x = 0-1$ ) have successfully synthesized from  $\text{Sb}_2\text{Se}_3$ ,  $\text{Bi}_2\text{Se}_3$ ,  $\text{SbI}_3$  and  $\text{BiI}_3$  precursors, forming microcrystals with needle-shape structures. EDX analysis confirmed the progressive substitution of Sb by Bi across the series. The formation of predominantly single phase of  $\text{Sb}_{1-x}\text{Bi}_x\text{SeI}$  solid solutions was confirmed by RT-Raman spectroscopy and XRD, which revealed an orthorhombic crystal structure (*Pnma*) for all compositions. The relative intensity changes in Sb-Se and Bi-Se Raman modes correlated with Bi content in  $\text{Sb}_{1-x}\text{Bi}_x\text{SeI}$ , offering a spectroscopic indicator of composition. Optical characterization demonstrated that increasing Bi incorporation reduced nonlinearly the band gap from 1.7 eV (SbSeI) to 1.29 eV (BiSeI), positioning the material within the optimal energy range for photovoltaic absorbers. RT-PL exhibited a nonlinear shift in peak emission energy ( $E_{\text{max}}$ ), from 1.75 eV to 1.41 eV across the series. UPS revealed a downward shift in  $E_{\text{VBM}}$  with higher Bi content, accompanied by a transition from *p*-type to *n*-type conductivity as indicated by both UPS and Scanning Kelvin Probe measurements. These findings highlight the tunable optoelectronic properties of  $\text{Sb}_{1-x}\text{Bi}_x\text{SeI}$ , underscoring their potential in diverse photovoltaic applications. In particular, the composition  $\text{Sb}_{0.4}\text{Bi}_{0.6}\text{SeI}$  with  $E_g = 1.34$  eV, is well suited for use as an absorber layer in single junction solar cells. Conversely, SbSeI, with its higher band gap, is a promising candidate for indoor photovoltaic devices or as top absorber in tandem solar cell architecture.

#### CRedit authorship contribution statement

**Maarja Grossberg-Kuusik:** Funding acquisition, Writing – review & editing. **Marit Kauk-Kuusik:** Writing – review & editing, Supervision, Project administration, Funding acquisition. **Cristian Radu:** Investigation, Formal analysis. **Aurelian Catalin Galca:** Investigation, Formal analysis. **Amelia Elena Bocirnea:** Formal analysis, Investigation. **Marc Dolcet Sadurni:** Writing – original draft, Methodology, Investigation, Formal analysis, Data curation. **Kristi Timmo:** Writing – review & editing, Supervision, Project administration, Investigation, Formal analysis, Data curation. **Mati Danilson:** Investigation, Formal analysis. **Artūras Suchodolskis:** Investigation, Formal analysis. **Valdek Mikli:** Investigation, Formal analysis. **Jūri Krustok:** Writing – review & editing, Investigation, Formal analysis.

#### Declaration of Competing Interest

The authors declare that they have no known competing financial interests or personal relationships that could have appeared to influence the work reported in this paper.

#### Acknowledgements

This work was supported by European Union through the European Regional Development Fund, Project TK210, and by the Estonian Research Council grant PRG1023. NIMP authors acknowledge funding from *Autoritatea Națională pentru Cercetare* (Romanian National Authority for Research) through the Core Programme PC3-PN23080303 project, and from *Unitatea Executivă pentru Finanțarea Învățământului Superior, a Cercetării, Dezvoltării și Inovării* (UEFISCDI) through ERANET-M-3-ERANET-Ligthcell (Contract No. 19/15.03.2024) project. The XPS measurements were performed using the Romanian National Interest Setup "System of complex XPS/ESCA installations and research using synchrotron radiation".

#### Appendix A. Supporting information

Supplementary data associated with this article can be found in the online version at doi:10.1016/j.jallcom.2025.182292.

#### References

- E. Fatuzzo, G. Harbecke, W.J. Merz, R. Nitsche, H. Roetschi, W. Ruppel, Ferroelectricity in SbSI, *Phys. Rev.* 127 (1962) 2036–2037, <https://doi.org/10.1103/PhysRev.127.2036>.
- R.E. Brandt, J.R. Poindexter, P. Gorai, R.C. Kurchin, R.L.Z. Hoye, L. Nienhaus, M. W.B. Wilson, J.A. Polizzotti, R. Sereika, R. Zaltauskas, L.C. Lee, J.L. Macmanus-Driscoll, M. Bawendi, V. Stevanović, T. Buonassisi, Searching for "defect-Tolerant" photovoltaic materials: combined theoretical and experimental screening, *Chem. Mater.* 29 (2017) 4667–4674, <https://doi.org/10.1021/acs.chemmater.6b05496>.
- T. Kobayashi, R. Nishikubo, Y. Chen, K. Marumoto, A. Saeki, Wavelength-recognizable SbSI:Sb<sub>2</sub>S<sub>3</sub> photovoltaic devices: elucidation of the mechanism and modulation of their characteristics, *Adv. Funct. Mater.* 34 (2024) 1–10, <https://doi.org/10.1002/adfm.202311794>.
- I. Caño, J.W. Turnley, P. Benítez, C. López-Álvarez, J.M. Asensi, D. Payno, J. Puigdollers, M. Placidi, C. Cazorla, R. Agrawal, E. Saucedo, Novel synthesis of semiconductor chalcogenide anti-perovskites by low-temperature molecular precursor ink deposition methodologies, *J. Mater. Chem. C Mater.* 12 (2024) 3154–3163, <https://doi.org/10.1039/d3tc04410f>.
- R. Nie, S.I. Seok, Efficient antimony-based solar cells by enhanced charge transfer, *Small Methods* 4 (2020) 1–10, <https://doi.org/10.1002/smdt.201900698>.
- P. Chauhan, J. Singh, A. Kumar, Two-dimensional Janus antimony chalcogenides for efficient energy conversion applications, *J. Mater. Chem. A Mater.* 12 (2024) 16129–16142, <https://doi.org/10.1039/d4ta02974g>.
- H. Song, S. Hajra, S. Panda, S. Hwang, N. Kim, J. Jo, N. Vittayakorn, K. Mistewicz, H. Joon Kim, Antimony sulfide-based energy harvesting and self-powered temperature detection, *Energy Technol.* 12 (2024) 1–9, <https://doi.org/10.1002/ente.202301125>.
- P. Govindaraj, K. Venugopal, Intrinsic ultra-low lattice thermal conductivity in orthorhombic BiSI: an excellent thermoelectric material, *J. Alloy. Compd.* 929 (2022) 167347, <https://doi.org/10.1016/j.jallcom.2022.167347>.
- P. Kumar, W. Wahyudi, A. Sharma, Y. Yuan, G.T. Harrison, M. Gedda, X. Wei, A. El-Labban, S. Ahmad, V. Kumar, V. Tung, T.D. Anthopoulos, Bismuth-based mixed-anion compounds for anode materials in rechargeable batteries, *Chem. Commun.* 58 (2022) 3354–3357, <https://doi.org/10.1039/d1cc06456h>.
- W. Khan, S. Hussain, J. Minar, S. Azam, Electronic and thermoelectric properties of ternary chalcogenide semiconductors: first principles study, *J. Electron. Mater.* 47 (2018) 1131–1139, <https://doi.org/10.1007/s11664-017-5884-z>.
- M. Dolcet Sadurni, K. Timmo, V. Mikli, O. Volobujeva, I. Mengü, J. Krustok, M. Grossberg-Kuusik, M. Kauk-Kuusik, Preparation and characterization of SbSeI thin films, *J. Sci. Adv. Mater. Devices* 9 (2024) 100664, <https://doi.org/10.1016/j.jsamd.2023.100664>.
- M. Dolcet Sadurni, J. Krustok, K. Timmo, V. Mikli, R. Kondrotas, M. Grossberg-Kuusik, M. Kauk-Kuusik, Radiative recombination model for BiSeI microcrystals: unveiling deep defects through photoluminescence, *J. Phys. Energy* 6 (2024) 045004, <https://doi.org/10.1088/2515-7655/ad8377>.
- K.T. Butler, S. McKechnie, P. Azarhoosh, M. Van Schilfgarde, D.O. Scanlon, A. Walsh, Quasi-particle electronic band structure and alignment of the V-VI-VII semiconductors SbSI, SbSBr, and SbSeI for solar cells, *Appl. Phys. Lett.* 108 (2016), <https://doi.org/10.1063/1.4943973>.
- A.M. Ganose, K.T. Butler, A. Walsh, D.O. Scanlon, Relativistic electronic structure and band alignment of BiSI and BiSeI: candidate photovoltaic materials, *J. Mater. Chem. A Mater.* 4 (2016) 2060–2068, <https://doi.org/10.1039/c5ta09612j>.

- [15] E. Wlazlak, A. Blachecki, M. Bisztyga-Szklarz, S. Klejna, T. Mazur, K. Mech, K. Pilarczyk, D. Przyuczyna, M. Suchecki, P. Zawal, K. Szaciowski, Heavy pnictogen chalcogenides: the synthesis, structure and properties of these rediscovered semiconductors, *Chem. Commun.* 54 (2018) 12133–12162, <https://doi.org/10.1039/c8cc05149f>.
- [16] C. López, I. Caño, D. Rovira, P. Benítez, J.M. Asensi, Z. Jehl, J.L. Tamarit, E. Saucedo, C. Cazorla, Machine-learning aided first-principles prediction of earth-abundant pnictogen chalcogenide solid solutions for solar-cell devices, *Adv. Funct. Mater.* 2406678 (2024) 1–14, <https://doi.org/10.1002/adfm.202406678>.
- [17] R. Nie, M. Hu, A.M. Risqi, Z. Li, S.H. Seok, Efficient and stable antimony selenoiodide solar cells, *Adv. Sci.* 8 (2021) 1–8, <https://doi.org/10.1002/advs.202003172>.
- [18] K.W. Jung, Y.C. Choi, Compositional engineering of antimony chalcogenides via a two-step solution process for solar cell applications, *ACS Appl. Energy Mater.* (2021), <https://doi.org/10.1021/acsaem.1c02676>.
- [19] I. Caño, A. Navarro-Güell, E. Maggi, M. Barrio, J.L. Tamarit, S. Svatek, E. Antolín, S. Yan, E. Barrena, B. Galiana, M. Placidi, J. Puigdollers, E. Saucedo, SbSeI and SbSeBr micro-columnar solar cells by a novel high pressure-based synthesis process, *J. Mater. Chem. A Mater.* (2023) 17616–17627, <https://doi.org/10.1039/d3ta03179a>.
- [20] Y.C. Choi, K.W. Jung, One-step solution deposition of antimony selenoiodide films via precursor engineering for lead-free solar cell applications, *Nanomaterials* 11 (2021), <https://doi.org/10.3390/nano11123206>.
- [21] W. Shockley, H.J. Queisser, Detailed balance limit of efficiency of p-n junction solar cells, *J. Appl. Phys.* 32 (1961) 510–519, <https://doi.org/10.1063/1.1736034>.
- [22] G.K. Grandhi, D. Hardy, M. Krishnaiah, B. Vargas, B. Al-Anesi, M.P. Suryawanshi, D. Solis-Ibarra, F. Gao, R.L.Z. Hoye, P. Vivo, Wide-bandgap perovskite-inspired materials: defect-driven challenges for high-performance optoelectronics, *Adv. Funct. Mater.* (2023) 2307441, <https://doi.org/10.1002/adfm.202307441>.
- [23] S. Hwang, T. Yasuda, Indoor photovoltaic energy harvesting based on semiconducting  $\pi$ -conjugated polymers and oligomeric materials toward future IoT applications, *Polym. J.* 55 (2023) 297–316, <https://doi.org/10.1038/s41428-022-00727-8>.
- [24] R.A. Groom, A. Jacobs, M. Cepeda, R. Drummey, S.E. Latturmer, Structural and optical properties of Sb-substituted bisi grown from sulfur/iodine flux, *Inorg. Chem.* 56 (2017) 12362–12368, <https://doi.org/10.1021/acs.inorgchem.7b01839>.
- [25] R. Sereika, R. Zaltauskas, S. Bandaru, F. Liu, A. Cerskus, Two-transition behavior in  $\text{Bi}_{0.5}\text{Sb}_{0.5}\text{SeI}$  crystals, *J. Phys. Chem. Solids* 154 (2021), <https://doi.org/10.1016/j.jpcs.2021.110031>.
- [26] Д.П. Белозкий, Н.В. Гавриленко, Д.М. Катеринюк, Я.И. Кушир, В.Ф. Лашини, Н.В. Монк, Фотопроводимость и оптические свойства кристаллов и пленок  $\text{SbSeI-BiSeI}$ , *Неорганические Материалы* 9 (7) (1973) 1142–1145.
- [27] Л. Віскупень, Л. Піскач, І. Олексюк, І. Яковлюк, Система  $\text{Ma SbSeI} - \text{BiSeI}$ , *Науковий вісник Східноєвропейського національного університету імені Лесі Українки, Хімічні науки* № 24 (2013) 22–24.
- [28] G. Kanchana, D. Arivuoli, Spectroscopic investigation of  $\text{BiSeI}$ ,  $\text{SbSeI}$  compounds and  $\text{BiSbS}_2\text{Se}_{1-x}\text{I}_x$  solid solutions, *Indian J. Eng. Mater. Sci.* 8 (2001) 373–376.
- [29] A. Audzijonis, L. Zigas, A. Kvedaravičius, R. Zaltauskas, The experimental and theoretical investigation of vibration spectra in ferroelectric semiconductor  $\text{SbSBr}_{1-x}\text{I}_x$  crystals, *Phys. B Condens Matter* 404 (2009) 3941–3946, <https://doi.org/10.1016/j.physb.2009.07.162>.
- [30] Z.S. Aliev, E.C. Ahmadov, D.M. Babanly, I.R. Amiraslanov, M.B. Babanly, The  $\text{Bi}_2\text{Se}_3\text{-Bi}_2\text{Te}_3\text{-BiI}_3$  system: synthesis and characterization of the  $\text{BiTe}_{1-x}\text{Se}_x\text{I}$  solid solutions, *CALPHAD* 66 (2019) 4–9, <https://doi.org/10.1016/j.calphad.2019.101650>.
- [31] U. Petasch, H. Go, È.H. Oppermann, È. Das, Untersuchungen zum quasibina È ren System  $\text{Bi}_2\text{Se}_3/\text{BiI}_3$ , 624 (1998), [https://doi.org/10.1002/\(SICI\)1521-3749\(199811\)624](https://doi.org/10.1002/(SICI)1521-3749(199811)624).
- [32] A.K. Pathak, M.D. Prasad, S.K. Batabyal, One-dimensional  $\text{SbSI}$  crystals from  $\text{Sb}$ ,  $\text{S}$ , and  $\text{I}$  mixtures in ethylene glycol for solar energy harvesting, *Appl. Phys. A Mater. Sci. Process* 125 (2019) 1–8, <https://doi.org/10.1007/s00339-019-2476-1>.
- [33] S.K. Balakrishnan, P.C. Parambil, E. Edri, Mechanistic insight into the topotactic transformation of trichalcogenides to chalcogenides, *Chem. Mater.* 34 (2022) 3468–3478, <https://doi.org/10.1021/acs.chemmater.2c00306>.
- [34] S.K. Balakrishnan, P.C. Parambil, L. Houben, M. Asher, O. Yaffe, E. Edri, Revealing hidden phases and self-healing in antimony trichalcogenides and chalcogenides, *Cell Rep. Phys. Sci.* 4 (2023) 101298, <https://doi.org/10.1016/j.xcrp.2023.101298>.
- [35] L. Xu, M. Yang, Q. Lu, Y. Ren, Y. Chen, J. Guo, M. Cai, X. Miao, F. Teng, H. Fan, C. Zhang, X. He, P. Hu, 2D  $\text{BiSeI}$  nanosheets for broadband self-powered photoelectrochemical photodetector, *Phys. Status Solidi Rapid Res. Lett.* 18 (2024) 1–9, <https://doi.org/10.1002/pssr.202300183>.
- [36] X. Yan, W.L. Zhen, H.J. Hu, L. Pi, C.J. Zhang, W.K. Zhu, High-performance visible light photodetector based on bisel single crystal, *Chin. Phys. Lett.* 38 (2021), <https://doi.org/10.1088/0256-307X/38/6/068103>.
- [37] H. Kunioku, M. Higashi, R. Abe, Low-temperature synthesis of bismuth chalcogenides: candidate photovoltaic materials with easily, continuously controllable band gap, *Sci. Rep.* 6 (2016) 1–7, <https://doi.org/10.1038/srep32664>.
- [38] J.F. Moulder, W.F. Stickle, P.E. Sobol, K.D. Bomben, *Handbook of X-ray photoelectron spectroscopy*, Perkin-Elmer Corporation, *Phys. Electron. Div.* (1992).
- [39] B. Xiao, M. Zhu, L. Ji, B. Bin Zhang, J. Dong, J. Yu, Q. Sun, W. Jie, Y. Xu, Centimeter size  $\text{BiSeI}$  crystal grown by physical vapor transport method, *J. Cryst. Growth* 517 (2019) 7–11, <https://doi.org/10.1016/j.jcrysgro.2019.04.003>.
- [40] E.A. Rueda Pérez, E. Regalado-Pérez, A. Cerdán-Pasarán, R.G. Avilez García, N. R. Mathews,  $\text{Sb}_2(\text{S,Se}_{1-x})$  thin films by electrodeposition: role of deposition potential on the formation of the solid solution and photovoltaic performance via device simulation, *Curr. Appl. Phys.* 47 (2023) 44–53, <https://doi.org/10.1016/j.cap.2022.12.011>.
- [41] V.V. Rákittin, M.V. Gapanovich, D.S. Lutsenko, V.B. Nazarov, A.V. Stanchik, V. F. Gremenok, A.V. Kabyliatski, Studying the effect of composition on the crystal structure, optical properties, and photogenerated current carriers lifetimes in  $\text{Ag}_x\text{Cu}_{1-x}\text{GaSe}_2$  ( $0 \leq x \leq 1$ ) solid solutions, *High. Energy Chem.* 58 (2024) 492–498, <https://doi.org/10.1134/S0018143924700474>.
- [42] G. Martinez, B.A. Piot, M. Haki, M. Potemski, Y.S. Hor, A. Materna, S.G. Strzelecka, A. Hruban, O. Caha, J. Novák, A. Dubroka, Drašar, M. Orlita, Determination of the energy band gap of  $\text{Bi}_2\text{Se}_3$ , *Sci. Rep.* 7 (2017) 1–5, <https://doi.org/10.1038/s41598-017-07211-x>.
- [43] M. Lang, C. Zimmermann, C. Krämmer, T. Renz, C. Huber, H. Kalt, M. Hetterich, Luminescence properties of  $\text{Cu}_2\text{ZnSn}(\text{S,Se})_4$  solar cell absorbers: state filling versus screening of electrostatic potential fluctuations, *Phys. Rev. B* 95 (2017) 1–9, <https://doi.org/10.1103/PhysRevB.95.155202>.
- [44] J.W. Kim, A. Kim, Absolute work function measurement by using photoelectron spectroscopy, *Curr. Appl. Phys.* 31 (2021) 52–59, <https://doi.org/10.1016/j.cap.2021.07.018>.
- [45] T. Olar, I. Lauerhmann, H. Xie, M. Neuschitzer, E. Saucedo, W. Calvet, A. Steigert, B. Ümsür, B. Chacko, V. Parvan, M. Gorgoi, B. Senkovskiy, M.C. Lux-Steiner, Assessment of chemical and electronic surface properties of the  $\text{Cu}_2\text{ZnSn}(\text{S,Se})_4$  after different etching procedures by synchrotron-based spectroscopies, *Energy Procedia* 84 (2015) 8–16, <https://doi.org/10.1016/j.egypro.2015.12.289>.

## Supplementary material

### Effects of cationic substitution on the properties of $\text{Sb}_{1-x}\text{Bi}_x\text{SeI}$ ( $x = 0-1$ ) compounds

Marc Dolcet Sadurni<sup>a,\*</sup>, Kristi Timmo<sup>a</sup>, Valdek Mikli<sup>a</sup>, Jüri Krustok<sup>a</sup>, Mati Danilson<sup>a</sup>, Artūras Suchodolskis<sup>b</sup>, Cristian Radu<sup>c,d</sup>, Amelia Elena Bocirnea<sup>c</sup>, Aurelian Catalin Galca<sup>c,e</sup>, Maarja Grossberg-Kuusik<sup>a</sup>, Marit Kauk-Kuusik<sup>a</sup>

<sup>a</sup>Department of Materials and Environmental Technology, Tallinn University of Technology, Ehitajate tee 5, 19086, Tallinn, Estonia

<sup>b</sup>Department of Optoelectronics, Center for Physical Sciences and Technology, Sauletekio av. 3, 10257, Vilnius, Lithuania

<sup>c</sup>National Institute of Materials Physics, Atomistilor 405A, 077125, Magurele, Ilfov, Romania

<sup>d</sup>Faculty of Physics, University of Bucharest, Atomistilor 405, 077125, Magurele, Ilfov, Romania

<sup>e</sup>International Centre for Advanced Training and Research in Physics, Atomistilor 409, 077125, Magurele, Ilfov, Romania

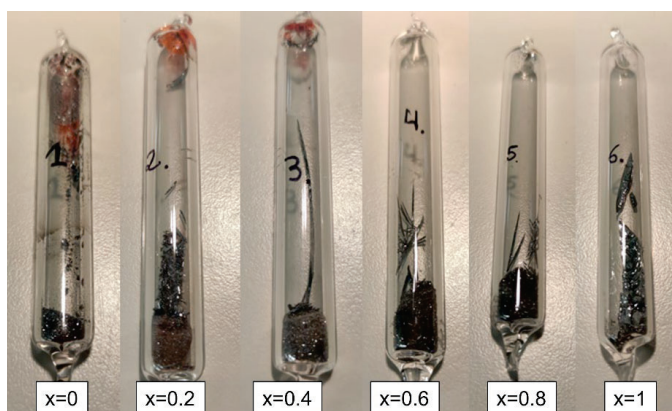


**Fig S1.**  $\text{Sb}_{1-x}\text{Bi}_x\text{SeI}$  ( $x = 0-1$ ) materials in sealed quartz ampoules after synthesis. Materials with Bi content of  $x = 0, 0.2$  and  $0.4$  were heated up to  $440\text{ }^\circ\text{C}$  while the ones containing higher amounts of Bi ( $x = 0.6, 0.8, 1$ ) were heated up to  $480\text{ }^\circ\text{C}$ .

The transparent sealed ampoules contain the synthesized microcrystalline materials, which have settled at the bottom. The material appears visibly grey and shiny. Needle-like crystals are clearly discernible to the naked eye, ranging from small crystallites to longer structures extending up to several centimeters in length. In the samples with compositions  $x = 0, 0.2$  and  $0.4$ , a distinct reddish coloration is observed near the top of the ampoule, suggesting the presence of residual  $\text{SbI}_3$ .

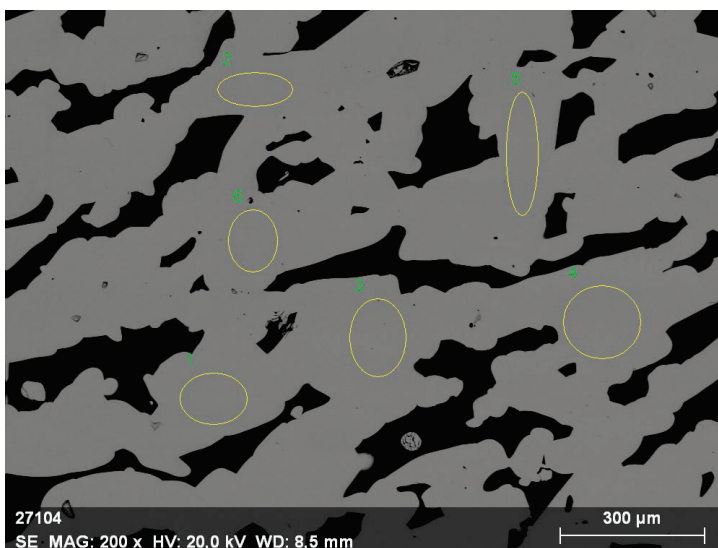


**Fig S2.** SEM-EDX image of  $\text{Sb}_{0.2}\text{Bi}_{0.8}\text{SeI}$  polished sample. The elemental composition was estimated by averaging measurements from different regions across multiple crystals.

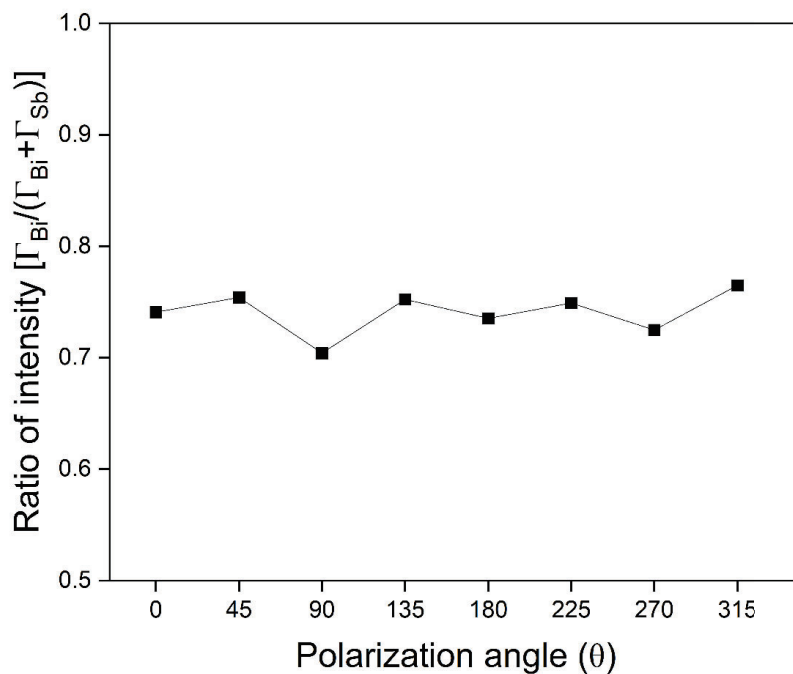


**Fig S3.** Ratio of the Raman peak intensities corresponding to Bi–Se and Sb–Se bonds as a function of polarization angle. The constant ratio confirms that the measurements are independent of microcrystal orientation.

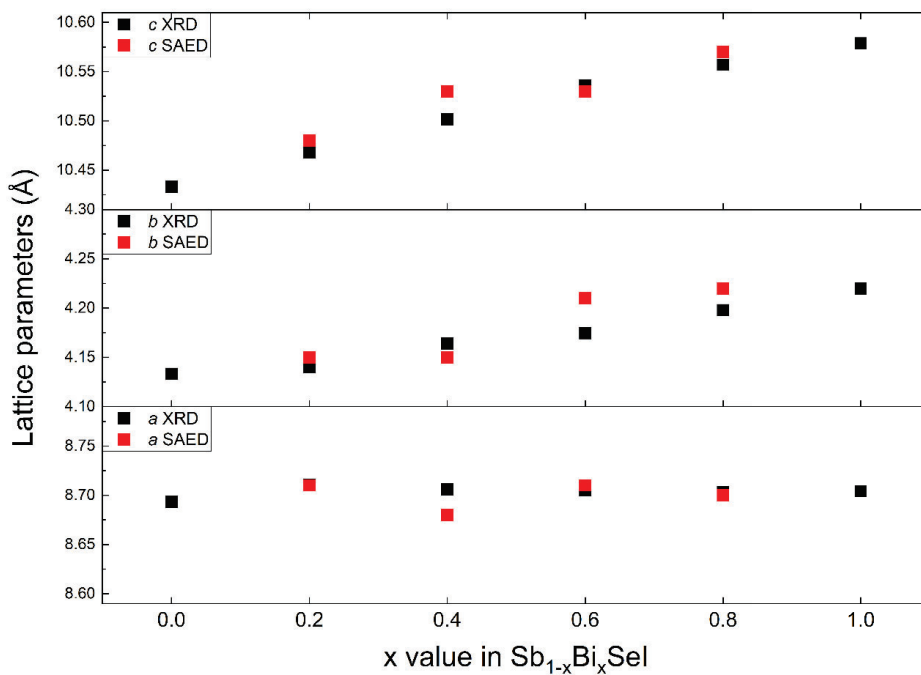


**Fig S4.** Comparison of lattice parameters obtained from X-ray diffraction (XRD) and selected area electron diffraction (SAED). The consistency between both methods confirms the structural reliability of the synthesized material.

**Table S1.** Elemental composition of Sb<sub>1-x</sub>Bi<sub>x</sub>SeI (x = 0.2, 0.4, 0.6 and 0.8) determined by TEM, SEM-EDX and XPS.

Composition		Sb at. %	Bi at. %	Se at. %	I at. %
Sb <sub>0.8</sub> Bi <sub>0.2</sub> SeI	TEM-EDX	27.1	8.4	32.6	31.8
	SEM-EDX	27.0±0.6	6.7±0.1	32.7±0.4	33.6±0.5
	XPS	28.1	8.3	36.1	27.5
	Stoichiometric	26.67	6.66	33.33	33.33
Sb <sub>0.6</sub> Bi <sub>0.4</sub> SeI	TEM-EDX	18.6	17.0	33.6	30.6
	SEM-EDX	20.5±0.5	13.7±0.3	31.3±0.4	34.5±0.5
	XPS	22.4	17.4	31.7	27.5
	Stoichiometric	20.00	13.33	33.33	33.33
Sb <sub>0.4</sub> Bi <sub>0.6</sub> SeI	TEM-EDX	12.3	24.7	32.3	30.6
	SEM-EDX	13.0±0.3	21.1±0.5	32.3±0.4	33.6±0.5
	XPS	17.8	26.1	29.5	26.6
	Stoichiometric	13.33	20.00	33.33	33.33
Sb <sub>0.2</sub> Bi <sub>0.8</sub> SeI	TEM-EDX	6.1	32.9	30.8	30.2
	SEM-EDX	6.6±0.2	27.5±0.6	32.5±0.4	33.4±0.5
	XPS	7.6	33.3	33.3	25.8
	Stoichiometric	6.66	26.67	33.33	33.33

**Table S2.** Work function and  $E_{VBM}$  obtained by UPS,  $E_g$  from UV-Vis-NIR, derived  $E_F-E_{CBM}$  values and conductivity type of  $Sb_{1-x}Bi_xSeI$  ( $x = 0-1$ ).

	$\Phi$ (eV)	$E_{VBM}$ (eV)	$E_g$ (eV)	$E_F-E_{CBM}$ (eV)	Conductivity type
SbSeI	4.2	0.44	1.70	1.26	p-type
$Sb_{0.2}Bi_{0.8}SeI$	4.8	0.65	1.45	0.80	p-type
$Sb_{0.4}Bi_{0.6}SeI$	4.5	0.75	1.38	0.63	n-type
$Sb_{0.6}Bi_{0.4}SeI$	4.3	0.80	1.34	0.54	n-type
$Sb_{0.8}Bi_{0.2}SeI$	4.7	0.84	1.32	0.48	n-type
BiSeI	5.2	1.10	1.29	0.19	n-type

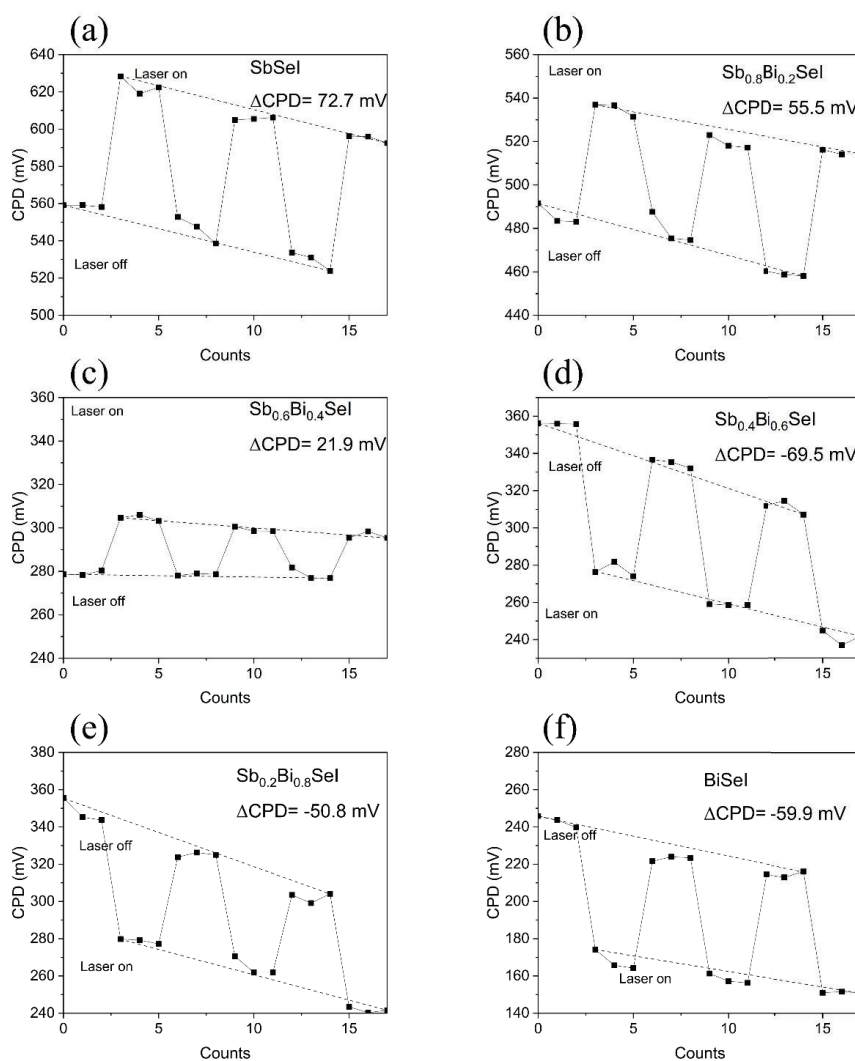


**Fig S5.** Contact potential difference of  $Sb_{1-x}Bi_xSeI$  ( $x = 0-1$ ) measured under dark and illuminated conditions using the scanning Kelvin Probe technique.

For scanning Kelvin Probe measurements polycrystalline samples were ground using an agate mortar to ensure a clean and uniform surface. Due to the potential hygroscopic nature of these materials arising from their iodine content, measurements were performed immediately after grinding to minimize moisture absorption, which could otherwise affect the results. The freshly ground powder was uniformly spread on carbon tape fixed to an aluminium plate. A glass slide was used to evenly distribute the powder, forming a flat and consistent layer to optimize measurement accuracy. Measurements were conducted under dark and laser-illuminated conditions ( $\lambda = 670$  nm).

# Curriculum vitae

## Personal data

Name: Marc Dolcet Sadurni  
Date of birth: 22.08.1994  
Place of birth: Sort/Spain  
Citizenship: Spanish

## Contact data

E-mail: [madolc@taltech.ee](mailto:madolc@taltech.ee)

## Education

2022–2026 Tallinn University of Technology, PhD  
2020–2022 Tallinn University of Technology & Tartu University, Materials and Processes for Sustainable Energetics, MSs, *cum laude*  
2022 Chalmers University of Technology, Gothenburg, Sweden. Exchange student  
2012–2017 Universitat Autònoma de Barcelona, Physics, BSc  
2016 University of Wroclaw, Wroclaw, Poland. Exchange student  
2010–2012 IES l'Arboç, High school

## Language competence

English Fluent  
Catalan Native  
Spanish Native  
Estonian Beginner

## Professional employment

2022–2026 Tallinn University of Technology, Early-stage researcher  
2024–2025 Erasmus Student Network Estonia, President  
2023–2024 Erasmus Student Network TalTech IC, President  
2018–2020 Institut de Microelectrònica de Barcelona (IMB-CNM-CSIC), Research technician  
2017–2018 Institut de Microelectrònica de Barcelona (IMB-CNM-CSIC), Graduate internship

## Defended dissertations

2022 Master's degree, Supervisor: Dr. Kristi Timmo, Impact of sulfur annealing on the  $\text{Cu}_2\text{ZnSnS}_4$  monograin powder properties and solar cell parameters, Tallinn University of Technology  
2017 Bachelor's degree, Supervisor: Dr. Marc Salleras, Integration of a heat exchanger in a  $\mu$ -TEG, Universitat Autònoma de Barcelona

## Supervised dissertations

2024 Mane Hovhannisyan, Bachelor's degree, Supervisor: Early-stage researcher, Marc Dolcet, Dr. Kristi Timmo, Synthesis and characterization of  $(\text{Bi,Sb})\text{SeI}$  thin films, Tallinn University of Technology

### Participation in conferences

2025	15 <sup>th</sup> European Kesterite+ and ReNew-PV Workshop, Berlin, Germany. Oral presentation
2024	14 <sup>th</sup> European Kesterite+ and ReNew-PV Workshop, Verona, Italy. Poster presentation
2024	European Materials Research Society (E-MRS) Spring Meeting, Strasbourg, France. Oral presentation
2023	13 <sup>th</sup> European Kesterite+ Workshop, Barcelona, Spain. Oral and poster presentations
2023	European Materials Research Society (E-MRS) Spring Meeting, Strasbourg, France. Invited oral presentation
2023	Graduate School of Functional Materials and Technologies (GSFMT), Tartu, Estonia. Oral and poster presentations
2020	International Conference on Thermoelectrics (VCT), online. Oral presentation
2019	Iberian Thermoelectric Workshop (ITW), Ciudad Real, Spain. Poster presentation
2019	European Materials Research Society (E-MRS) Spring Meeting, Nice, France. Poster presentation

### Summer schools

2025	Summed-PV Summer school in Life Cycle assessment, Salerno, Italy
2024	Next Generation High Efficiency Photovoltaics International School and Workshop, Palma, Spain

### Honors and awards

2025	Golden Badge of Merit: „FIDELIS STUDIOŠUS“, Tallinn University of Technology
2025	Summed-PV best project award. Summer School in Photovoltaics and Raw Materials
2025	Tallinn's most outstanding conference for Northern European Platform 2024, City of Tallinn & Estonian convention of bureau
2025	Student of the Year finalist, Tallinn University of Technology
2022	Adlerbertska Foreign Student Hospitality Foundation scholarship, Chalmers University of Technology
2022	Erasmus+ scholarship, Chalmers University of Technology
2020–2022	Dora scholarship. Tallinn University of Technology
2021	Specialty scholarship. Tallinn University of Technology
2021	Performance scholarship. Tallinn University of Technology
2018	Outstanding Poster Award, 37 <sup>th</sup> International Conference on Thermoelectrics (ICT), Caen, France "Integration of a heat exchanger on an all Si-based thermoelectric micro/nanogenerator"
2016	Erasmus+ scholarship, University of Wrocław

## List of publications

1. **M. Dolcet Sadurni**, K. Timmo, V. Mikli, J. Krustok, M. Danilson, A. Suchodolskis, C. Radu, A. E. Bocirnea, A. C. Galca, M. Grossberg-Kuusk, and M. Kauk-Kuusik, "Effects of cationic substitution on the properties of  $Sb_{1-x}Bi_xSe$  ( $x = 0-1$ ) compounds" *Journal of Alloys and Compounds* 1037 (2025), 182292, <https://doi.org/10.1016/j.jallcom.2025.182292>
2. **M. Dolcet Sadurni**, J. Krustok, K. Timmo, V. Mikli, R. Kondrotas, M. Grossberg-Kuusk, and M. Kauk-Kuusik, "Radiative recombination model for BiSe microcrystals: unveiling deep defects through photoluminescence" *Journal of Physics: Energy* 6 (2024), 045004, <https://doi.org/10.1088/2515-7655/ad8377>
3. **M. Dolcet Sadurni**, K. Timmo, V. Mikli, O. Volobujeva, I. Mengü, J. Krustok, M. Grossberg-Kuusk, and M. Kauk-Kuusik, "Preparation and characterization of SbSe thin films" *Journal of Science: Advanced Materials and Devices* 9 (2024), 100664, <https://doi.org/10.1016/j.jsamd.2023.100664>
4. K. Timmo, **M. Dolcet Sadurni**, M. Pilvet, K. Muska, M. Altosaar, V. Mikli, F. Atlan, M. Guc, V. Izquierdo-Roca, M. Grossberg-Kuusk, and M. Kauk-Kuusik, "Efficiency enhancement of  $Cu_2ZnSnS_4$  monograin layer solar cells via absorber post-growth treatments" *Solar Energy Materials and Solar Cells* 250 (2023), 112090, <https://doi.org/10.1016/j.solmat.2022.112090>
5. D. Estrada-Wiese, **M. Dolcet Sadurni**, R. Soriano, J. Santander, M. Salleras, L. Fonseca, and A. Tarancón, "Improved design of an all-Si based thermoelectric microgenerator" in *Smart Systems Integration (SSI)* (2021), pp. 1–4, <https://doi.org/10.1109/SSI52265.2021.9466984>
6. J. M. S. Gordillo, G. G. Diez, M. P. Pujadó, M. Salleras, D. Estrada-Wiese, **M. Dolcet Sadurni**, L. Fonseca, A. Morata, and A. Tarancón, "Thermal conductivity of individual Si and SiGe epitaxially integrated nanowires by scanning thermal microscopy" *Nanoscale* 13 (2021), 7252–7265, <https://doi.org/10.1039/d1nr00344e>
7. L. Fonseca, I. Donmez-Noyan, **M. Dolcet Sadurni**, D. Estrada-Wiese, J. Santander, M. Salleras, G. Gadea, M. Pacios, J. M. Sojo, A. Morata, and A. Tarancón, "Transitioning from Si to SiGe nanowires as thermoelectric material in silicon-based microgenerators" *Nanomaterials* 11 (2021), 517, <https://doi.org/10.3390/nano11020517>
8. M. Salleras, I. Donmez-Noyan, **M. Dolcet Sadurni**, J. Santander, D. Estrada-Wiese, J. M. Sojo, G. Gadea, A. Morata, A. Tarancón, and L. Fonseca, "Managing heat transfer issues in thermoelectric microgenerators" in *Heat Transfer – Design, Experimentation and Applications* (2021), <https://doi.org/10.5772/intechopen.96246>
9. L. Fonseca, **M. Dolcet Sadurni**, A. Stranz, and M. Salleras, "Compact design of an all-silicon thermoelectric microgenerator" in *Smart Systems Integration Conference* (2019), pp. 242–247

10. I. D. Noyan, G. Gadea, M. Salleras, M. Pacios, C. Calaza, A. Stranz, **M. Dolcet Sadurni**, A. Morata, A. Tarancón, and L. Fonseca, "SiGe nanowire arrays based thermoelectric microgenerator" *Nano Energy* 57 (2019), 492–499, <https://doi.org/10.1016/j.nanoen.2018.12.050>
11. I. Donmez, **M. Dolcet Sadurni**, A. Stranz, M. Salleras, L. Fonseca, G. Gadea, and A. Tarancón, "Improved micronanogenerators based on silicon compatible materials and processing" *Journal of Physics: Conference Series* 1407 (2019), 012097
12. I. D. Noyan, **M. Dolcet Sadurni**, M. Salleras, A. Stranz, C. Calaza, G. Gadea, M. Pacios, A. Morata, A. Tarancón, and L. Fonseca, "All-silicon thermoelectric micro/nanogenerator including a heat exchanger for harvesting applications" *Journal of Power Sources* 413 (2019), 125–133, <https://doi.org/10.1016/j.jpowsour.2018.12.029>

## Elulookirjeldus

### Isikuandmed

Nimi: Marc Dolcet Sadurni  
Sünniaeg: 22.08.1994  
Sünnikoht: Sort/Hispaania  
Kodakondsus: Hispaania

### Kontaktandmed

E-post: [madolc@taltech.ee](mailto:madolc@taltech.ee)

### Hariduskäik

2022–2026 Tallinna Tehnikaülikool, PhD  
2020–2022 Tallinna Tehnikaülikool ja Tartu Ülikool, Materjalid ja protsessid jätkusuutlikus energeetikas, MSc, *cum laude*  
2022 Chalmersi Tehnikaülikool, Göteborg, Rootsi. Vahetusüliõpilane  
2012–2017 Barcelona Autonoomne Ülikool, Füüsika, BSc  
2016 Wrocław Ülikool, Wrocław, Poola. Vahetusüliõpilane  
2010–2012 IES l'Arboç, keskkool

### Keelteoskus

Inglise keel kõrgtase  
Katalaani keel emakeel  
Hispaania keel emakeel  
Eesti keel algtase

### Teenistuskäik

2022–2026 Tallinna Tehnikaülikool, nooremteadur  
2024–2025 Erasmus Student Network Estonia, president  
2023–2024 Erasmus Student Network TalTech IC, president  
2018–2020 Barcelona Mikroelektronika Instituut (IMB-CNM-CSIC), teadustehnik  
2017–2018 Barcelona Mikroelektronika Instituut (IMB-CNM-CSIC), praktikant

### Kaitstud väitekirjad

2022 Magistritöö, juhendaja: Dr. Kristi Timmo, Väavli aururõhu töötluste mõju  $\text{Cu}_2\text{ZnSnS}_4$  monoterapulbrite omadustele ja päikesepatarei väljundparameetritele, Tallinna Tehnikaülikool  
2017 Bakalaureusetöö, juhendaja: Dr. Marc Salleras, Soojuseradiaatori integreerimine  $\mu\text{-TEG-I}$ , Barcelona Autonoomne Ülikool

### Juhendatud väitekirjad

2024 Mane Hovhannisyan, Bakalaureusetöö, juhendajad: Nooremteadur, Marc Dolcet Sadurni, Dr. Kristi Timmo, (Bi,Sb)SeI õhukeste kilede süntees ja karakteriseerimine, Tallinna Tehnikaülikool

### **Osalemine konverentsidel**

2025	15 <sup>th</sup> European Kesterite+ and ReNew-PV Workshop, Berliin, Saksamaa. Suuline ettekanne
2024	14 <sup>th</sup> European Kesterite+ and ReNew-PV Workshop, Verona, Itaalia. Posterettekanne
2024	European Materials Research Society (E-MRS) Spring Meeting, Strasbourg, Prantsusmaa. Suuline ettekanne.
2023	13 <sup>th</sup> European Kesterite+ Workshop, Barcelona, Hispaania. Suuline ja posterettekanne
2023	European Materials Research Society (E-MRS) Spring Meeting, Strasbourg, Prantsusmaa. Kutsutud suuline ettekanne
2023	Graduate School of Functional Materials and Technologies (GSFMT), Tartu, Eesti. Suuline ja posterettekanne.
2020	International Conference on Thermoelectrics (VCT), veebis. Suuline ettekanne
2019	Iberian Thermoelectric Workshop (ITW), Ciudad Real, Hispaania. Posterettekanne
2019	European Materials Research Society (E-MRS) Spring Meeting, Nice, Prantsusmaa. Posterettekanne

### **Suvekoolid**

2025	Summed-PV suvekool elutsükli hindamise teemal, Salerno, Itaalia
2024	Next Generation High Efficiency Photovoltaics rahvusvaheline kool ja töötuba, Palma, Hispaania

### **Autasud**

2025	Kuldne teenetemärk „FIDELIS STUDIOSUS“, Tallinna Tehnikaülikool
2025	Summed-PV parima projekti auhind, fotovoltseadmete ja toorainete suvekool
2025	Tallinna silmapaistvaim konverents Northern European Platform 2024, Tallinna linn ja Eesti Konverentsibüroo
2025	Aasta üliõpilase finalist, Tallinna Tehnikaülikool
2022	Adlerbertska välisüliõpilaste stipendium, Chalmersi Tehnikaülikool
2022	Erasmus+ stipendium, Chalmersi Tehnikaülikool
2020–2022	Dora stipendium, Tallinna Tehnikaülikool
2021	Erialastipendium, Tallinna Tehnikaülikool
2021	Edukusstipendium, Tallinna Tehnikaülikool
2018	Parima postri auhind, 37. rahvusvaheline termoelektri konverents (ICT), Caen, Prantsusmaa „Soojusvaheti integreerimine täielikult räni-põhisele termoelektrilisele mikro-/nanogeneraatorile“
2016	Erasmus+ stipendium, Wrocław Ülikool

## Teaduspublikatsioonid

1. **M. Dolcet Sadurni**, K. Timmo, V. Mikli, J. Krustok, M. Danilson, A. Suchodolskis, C. Radu, A. E. Bocirnea, A. C. Galca, M. Grossberg-Kuusk, and M. Kauk-Kuusik, "Effects of cationic substitution on the properties of  $Sb_{1-x}Bi_xSe$  ( $x = 0-1$ ) compounds" *Journal of Alloys and Compounds* 1037 (2025), 182292, <https://doi.org/10.1016/j.jallcom.2025.182292>
2. **M. Dolcet Sadurni**, J. Krustok, K. Timmo, V. Mikli, R. Kondrotas, M. Grossberg-Kuusk, and M. Kauk-Kuusik, "Radiative recombination model for BiSe microcrystals: unveiling deep defects through photoluminescence" *Journal of Physics: Energy* 6 (2024), 045004, <https://doi.org/10.1088/2515-7655/ad8377>
3. **M. Dolcet Sadurni**, K. Timmo, V. Mikli, O. Volobujeva, I. Mengü, J. Krustok, M. Grossberg-Kuusk, and M. Kauk-Kuusik, "Preparation and characterization of SbSe thin films" *Journal of Science: Advanced Materials and Devices* 9 (2024), 100664, <https://doi.org/10.1016/j.jsamd.2023.100664>
4. K. Timmo, **M. Dolcet Sadurni**, M. Pilvet, K. Muska, M. Altosaar, V. Mikli, F. Atlan, M. Guc, V. Izquierdo-Roca, M. Grossberg-Kuusk, and M. Kauk-Kuusik, "Efficiency enhancement of  $Cu_2ZnSnS_4$  monograin layer solar cells via absorber post-growth treatments" *Solar Energy Materials and Solar Cells* 250 (2023), 112090, <https://doi.org/10.1016/j.solmat.2022.112090>
5. D. Estrada-Wiese, **M. Dolcet Sadurni**, R. Soriano, J. Santander, M. Salleras, L. Fonseca, and A. Tarancón, "Improved design of an all-Si based thermoelectric microgenerator" in *Smart Systems Integration (SSI)* (2021), pp. 1–4, <https://doi.org/10.1109/SSI52265.2021.9466984>
6. J. M. S. Gordillo, G. G. Diez, M. P. Pujadó, M. Salleras, D. Estrada-Wiese, **M. Dolcet Sadurni**, L. Fonseca, A. Morata, and A. Tarancón, "Thermal conductivity of individual Si and SiGe epitaxially integrated nanowires by scanning thermal microscopy" *Nanoscale* 13 (2021), 7252–7265, <https://doi.org/10.1039/d1nr00344e>
7. L. Fonseca, I. Donmez-Noyan, **M. Dolcet Sadurni**, D. Estrada-Wiese, J. Santander, M. Salleras, G. Gadea, M. Pacios, J. M. Sojo, A. Morata, and A. Tarancón, "Transitioning from Si to SiGe nanowires as thermoelectric material in silicon-based microgenerators" *Nanomaterials* 11 (2021), 517, <https://doi.org/10.3390/nano11020517>
8. M. Salleras, I. Donmez-Noyan, **M. Dolcet Sadurni**, J. Santander, D. Estrada-Wiese, J. M. Sojo, G. Gadea, A. Morata, A. Tarancón, and L. Fonseca, "Managing heat transfer issues in thermoelectric microgenerators" in *Heat Transfer – Design, Experimentation and Applications* (2021), <https://doi.org/10.5772/intechopen.96246>
9. L. Fonseca, **M. Dolcet Sadurni**, A. Stranz, and M. Salleras, "Compact design of an all-silicon thermoelectric microgenerator" in *Smart Systems Integration Conference* (2019), pp. 242–247

10. I. D. Noyan, G. Gadea, M. Salleras, M. Pacios, C. Calaza, A. Stranz, **M. Dolcet Sadurni**, A. Morata, A. Tarancón, and L. Fonseca, "SiGe nanowire arrays based thermoelectric microgenerator" *Nano Energy* 57 (2019), 492–499, <https://doi.org/10.1016/j.nanoen.2018.12.050>
11. I. Donmez, **M. Dolcet Sadurni**, A. Stranz, M. Salleras, L. Fonseca, G. Gadea, and A. Tarancón, "Improved micronanogenerators based on silicon compatible materials and processing" *Journal of Physics: Conference Series* 1407 (2019), 012097
12. I. D. Noyan, **M. Dolcet Sadurni**, M. Salleras, A. Stranz, C. Calaza, G. Gadea, M. Pacios, A. Morata, A. Tarancón, and L. Fonseca, "All-silicon thermoelectric micro/nanogenerator including a heat exchanger for harvesting applications" *Journal of Power Sources* 413 (2019), 125–133, <https://doi.org/10.1016/j.jpowsour.2018.12.029>

ISSN 2585-6901 (PDF)  
ISBN 978-9916-80-507-7 (PDF)